STRUCTURAL AND FUNCTIONAL OPTICAL COHERENCE TOMOGRAPHY IMAGING OF THE COLON

by

Weston Anthony Welge

A Dissertation Submitted to the Faculty of the

COLLEGE OF OPTICAL SCIENCES

In Partial Fulfillment of the Requirements
For the Degree of

DOCTOR OF PHILOSOPHY

In the Graduate College

THE UNIVERSITY OF ARIZONA

2016

THE UNIVERSITY OF ARIZONA
GRADUATE COLLEGE

As members of the Dissertation Committee, we certify that we have read the dissertation prepared by Weston Anthony Welge,
titled Structural and Functional Optical Coherence Tomography Imaging of the Colon
and recommend that it be accepted as fulfilling the dissertation requirement for the Degree of Doctor of Philosophy.

Date: 25 May 2016
Jennifer K. Barton

Date: 25 May 2016
Arthur F. Gmitro

Date: 25 May 2016
Jim Schwiegerling

Final approval and acceptance of this dissertation is contingent upon the candidate's submission of the final copies of the dissertation to the Graduate College.
I hereby certify that I have read this dissertation prepared under my direction and recommend that it be accepted as fulfilling the dissertation requirement.

Date: 25 May 2016
Dissertation Director: Jennifer K. Barton

STATEMENT BY AUTHOR

This dissertation has been submitted in partial fulfillment of requirements for an advanced degree at the University of Arizona and is deposited in the University Library to be made available to borrowers under rules of the Library.

Brief quotations from this dissertation are allowable without special permission, provided that an accurate acknowledgment of the source is made. Requests for permission for extended quotation from or reproduction of this manuscript in whole or in part may be granted by the head of the major department or the Dean of the Graduate College when in his or her judgment the proposed use of the material is in the interests of scholarship. In all other instances, however, permission must be obtained from the author.

SIGNED: Weston Anthony Welge

ACKNOWLEDGEMENTS

Several people – colleagues, mentors, students, and friends – have added immense value to my graduate and research experience.

I owe much to my advisor, **Jennifer Barton**, for providing me with extraordinary freedom in my research, support and advice (and some gentle pressure) to keep me on track, and valuable critiques that have improved my ability to propose and communicate ideas. I am also grateful for our many conversations about research, academia, and industry. I hope I can eventually grow to be as effective a mentor as Jennifer.

I thank my fellow graduate students in the Tissue Optics lab – **Molly Kennan**, **Tyler Tate**, **Andrew Wall**, and **Jen Watson** – for sharing and critiquing ideas and providing moral support. I owe much of what I have learned about many aspects of biomedical technology development from you all.

Without the support of **Art Gmitro**, **Andy Rouse**, **Ted Trouard**, and **Urs Utzinger**, I would not have had the valuable opportunity to practice teaching. To the students in those classes, thank you for graciously allowing me to learn and make mistakes as an instructor.

Several undergraduate students have assisted me with my projects. I am grateful to have had the chance to work with you and I hope that you have learned from and enjoyed the experience as much as I have.

Faith Rice has been invaluable in her assistance with logistics and animal procedures. I don't know which is more complicated: mouse imaging or university bureaucracy, but Faith has helped me survive both.

Several faculty have helped me develop as an engineer, teacher, scholar, and professional. Whether through training, advice, or casual conversation, the following (not already mentioned above) have inspired and influenced me: **Harry Barrett**, **Jenny Hoit**, **Edwin Maas**, **Marek Romanowski**, **Jim Schwiegerling**, and **Brad Story**.

Among my friends, **Andrew DeMarco** deserves thanks for constantly questioning me (and therefore making me question myself) during our discussions of our research, providing perhaps the most critical eye toward my work, and supporting me through the many frustrating times in graduate school.

Finally, I thank my wife, **Kim Neely**, for her endless love and support.

DEDICATION

To Kim

TABLE OF CONTENTS

LIST OF FIGURES 8

LIST OF TABLES 10

LIST OF SOURCE CODE 11

ABSTRACT 12

CHAPTER 1 INTRODUCTION 14
- 1.1 Motivation 14
  - 1.1.1 Colon cancer 14
  - 1.1.2 Screening methods 16
- 1.2 Optical coherence tomography 17
  - 1.2.1 Interferometry 18
  - 1.2.2 Source characteristics and coherence 22
  - 1.2.3 Time-domain OCT 25
  - 1.2.4 Spectral-domain OCT 26
  - 1.2.5 Swept-source OCT 29
- 1.3 Doppler optical coherence tomography 30
  - 1.3.1 Doppler effect 31
  - 1.3.2 Review of Doppler OCT methods 34
  - 1.3.3 Derivation of Kasai autocorrelation 36

CHAPTER 2 PRESENT STUDY 43
- 2.1 Integration of a custom endoscope with a commercial OCT system . . 44
- 2.2 Endoscopic *in vivo* functional OCT imaging of colon vasculature . . . 46
- 2.3 Endoscopic *in vivo* structural OCT imaging of colonic crypts 48

CHAPTER 3 FUTURE WORK 49

APPENDIX A 53
- A.1 Accepted manuscript: Integrating a custom endoscope 53
- A.2 Sample-arm optical design 69
  - A.2.1 Procedure for endoscope construction 89
- A.3 Hardware for synchronization to galvanometer signal 93
  - A.3.1 Inverting differentiator and rectifier circuit 95
  - A.3.2 Arduino configuration and software 99

TABLE OF CONTENTS – *Continued*

A.3.3 Motor driver configuration and software 102
A.4 Switching between endoscope and handheld probe modes 107
A.5 Procedure for OCS1050SS imaging using endoscope 117
A.6 Numerical dispersion correction 121
A.6.1 Theory 121
A.6.2 Calibration 130
A.6.3 Numerical dispersion compensation software 146

APPENDIX B 185
B.1 Submitted manuscript: Endoscopic Doppler OCT imaging 185
B.2 Kasai autocorrelation 214
B.2.1 Method and parameters 214
B.2.2 Kasai autocorrelation software 219
B.3 Preliminary use of other Doppler OCT methods and future work . . . 231

APPENDIX C 239
C.1 Conference proceedings: Colon crypt imaging using OCT 239

REFERENCES 246

LIST OF FIGURES

1.1 Michelson interferometer 21
1.2 Polychromatic interference as a function of OPD 22

A.1 Rod prism mechanical drawing 70
A.2 Endoscope optical diagram 71
A.3 Endoscope spot diagram 71
A.4 Endoscope construction jig 90
A.5 Synchronization hardware system diagram 94
A.6 x-galvanometer control signal 96
A.7 Inverting differentiator and rectifier circuit 97
A.8 Output of inverting differentiator and rectifier 98
A.9 Inverting differentiator, rectifier, and clipper circuit 99
A.10 Arduino output signal 102
A.11 3540i program: rotational motion for volumetric imaging 103
A.12 3540i program: linear motion for volumetric imaging 104
A.13 3540i program: linear motion for Doppler imaging 105
A.14 Imaging Module interior 108
A.15 Imaging Module translation stage screws 109
A.16 Fiber-lens mount removed 110
A.17 Fiber-lens mount replaced 111
A.18 Measuring reference-arm power 112
A.19 Power meter 113
A.20 Tilt-adjustment screws 115
A.21 Aligned reference-arm power signal 116
A.22 Dispersion correction of a mirror 128

A.23 PSF before and after dispersion correction 129
A.24 Circular shift to fix asymmetric sweep spectra 130
A.25 Comparison of shifting A-scans 131

B.1 Mouse ear angiogram 236
B.2 Complex differential variance values versus A-scan period 238

LIST OF TABLES

1.1 Sign convention for derivation of the Doppler frequency shift 32

A.1 Additional motor parameters and timing analysis 106
A.2 Power supply settings 117

LIST OF SOURCE CODE

A.1 `motionControlR5.ino` 100
A.2 `generateCalibrationFile.m` 132
A.3 `correctDispersionVolumetric.m` 147
A.4 `correctDispersionLongBscan.m` 167
B.1 `KasaiLongitudinal.m` 220
B.2 `KasaiProcessing.m` 220
B.3 `addROILines.m` 230

ABSTRACT

Colorectal cancer (CRC) remains the second deadliest cancer in the United States, despite steady reduction in mortality rate over the last three decades. Colonoscopy is the gold-standard screening modality with high sensitivity and specificity to mature polyps. However, the miss rate for small ($< 5\,\text{mm}$) lesions is estimated to be as high as 26%. Because the five-year survival rate for CRC detected at the local stage is 90%, there is a clear need for a screening procedure that is sensitive to these small lesions.

Optical coherence tomography (OCT) has become a major biomedical imaging modality since its invention in 1991. As the optical analog to ultrasound, OCT provides information in both lateral and depth dimensions with resolution $< 10\,\mu\text{m}$ and an imaging depth of about 1.5 mm in scattering tissue.

In this dissertation, I describe my efforts to develop new uses of OCT for improved early detection of adenoma in the azoxymethane mouse model of CRC. In recent years, commercial OCT systems have reached imaging speeds sufficiently high for *in vivo* volumeric imaging while laterally sampling the tissue at the Nyquist limit. First, I describe the design of a miniature endoscope and the integration of this probe with a commercial OCT system. Then I describe the development of two OCT imaging methods, one structural and one functional, that could be used for future work in diagnostic or therapeutic studies. The structural method produces *en face* images of the colon surface showing the colonic crypts, the first such demonstration of crypt visualization in the mouse. Changes in the crypt pattern are correlated with adenoma and are one of the earliest morphological changes. The functional method uses a Doppler OCT algorithm and image processing to detect the colon microvasculature. This technique can be used for vessel counting and blood flow measurements. Angiogenesis occurs at the beginning of tumorigenesis, and the

tumor-originated arterioles are incapable of regular vasodilation. This Doppler OCT technique could potentially detect tumors at the earliest stages by measuring the change in local blood flow velocity in response to vasodilatory stimuli.

CHAPTER 1

Introduction

1.1 Motivation

1.1.1 Colon cancer

Colorectal cancer (CRC) is the second deadliest cancer in the United States, with an estimated 50,000 deaths in 2015 [1]. Over the last twenty years, the incidence of CRC has gradually declined for adults over the age of 50. This positive statistic is largely credited by improved knowledge of risk factors and an increase in screening. Age is one of the largest risk factors of developing CRC, with adults over the age of 50 accounting for more than 90% of diagnoses. As a result of this statistic, the American Cancer Society (ACS) recommends adults undergo regular screening for CRC at the age of 50.

Despite the high accuracy of some screening methods such as colonoscopy and increasing screening rates, the overall mortality rate remains high. When CRC is detected at the local stage, the 5-year survival rate is 90%; however, this rate drops to just 13% when CRC is detected at the distant stage [1]. These facts underscore the importance of early detection. Current screening methods are generally accurate for detection of mature epithelial adenomatous polyps, but struggle to detect juvenile adenoma that are too small to easily detect with standard colonoscopy. Therefore, there is a need for detecting small polyps that have the potential to progress into cancerous adenocarcinoma.

Our lab has investigated the use of optical coherence tomography (OCT) in the mouse colon for several years [2, 3, 4, 5, 6, 7, 8, 9, 10, 11, 12]. We have demonstrated that OCT is capable of detecting adenoma less than 1 mm in diameter. OCT provides depth information which cannot be obtained using standard white-light endoscopy. This depth information enables measurement of the thickness of the colon mucosa, the epithelial layer of the colon where adenoma form. Furthermore, adenoma appear hypointense in OCT. This led to the discovery that adenoma present a different slope of light attenuation with depth compared to non-adenomatous colon tissue. The combination of mucosal thickness and the slope of the light attenuation can serve as a quantitative measure for automated adenoma detection [4]. While promising, this work determined that accurate detection of adenoma requires a doubling of mucosa thickness.

Our lab has also investigated the correlation between aberrant crypt foci (ACF) and adenoma using dual-modality systems consisting of OCT and fluorescence imaging [12, 6]. ACF are neoplastic lesions thought to be the earliest morphological change in the natural history of colon carcinogenesis [13]. Time-serial imaging of the colonic crypts could possibly detect adenoma at the earliest stages of development, as well as study the efficacy of chemopreventive and chemotherapeutic agents that may halt the progression of ACF to adenoma in the azoxymethane (AOM) mouse model of colorectal cancer. Fluorescence imaging using methylene blue was used for imaging colonic crypts while OCT provided complementary depth-resolved data. However, the use of fluorescent dye for contrast and different properties of the imaging modalities (e.g., field of view and resolution) are not ideal. Using OCT alone for ACF imaging would be more convenient. We have previously demonstrated crypt imaging using OCT with an ultrahigh-resolution achromatic endoscope [10]. At the time, however, three-dimensional imaging of the mouse colon with high sampling density was difficult. Newer OCT systems have achieved imaging speeds fast enough for imaging the colon crypts by highly sampling the mucosa and without the use of ultrahigh-resolution endoscopes that are difficult to construct.

1.1.2 Screening methods

The American Cancer Society currently recommends several screening methods for CRC, and these can generally be categorized as stool tests or imaging procedures [1]. Stool tests are the least invasive and most convenient procedures for patients. These procedures typically do not require an office visit. Fecal occult blood test or fecal immunochemical test are recommended once every 3 years. These methods test for presence of human blood in the feces and can be conducted in the home. This allows for detection of bleeding in the digestive tract, which can sometimes be caused by polyps in the colon. These tests typically have high sensitivity and low specificity or vise versa [14]. Patients are expected to schedule a colonoscopy if these fecal tests are positive for abnormal bleeding. The ACS recommends a stool DNA test once every 3 years [1]. This test requires the patient to send a stool sample by mail to a lab for DNA testing. With a robust set of DNA tests, the area under the receiver operating characteristic (ROC) curve[1] can exceed 90% [15]. Despite the favorable performance of these stool tests, they ultimately can only detect the presence of cancer, but not localize the lesions.

Imaging procedures for CRC screening are capable of both detection and localization of suspicious lesions, but are more invasive for the patient. Virtual (CT) and standard colonoscopy are both ACS-recommended imaging procedures. Virtual colonoscopy is the fastest imaging method, requires the least patient preparation, and has similar sensitivity to regular colonoscopy [16]. Virtual colonoscopy is particularly valuable to patients in rural areas who may not have easy access to gastroenterologists. However, CT imaging exposes the patient to ionizing radiation and detected polyps cannot be removed without a separate colonoscopy procedure.

---

[1] The area under the ROC curve is a quantitative measure of the performance of a binary classifier. The metric is interpreted as the percent probability that the classifier will correctly identify the positive and negative samples when presented with a randomly selected truly positive and truly negative sample pair.

Colonoscopy is the most effective screening method for CRC and is the only method capable of taking biopsies for making a diagnosis. Due to the invasive nature of introducing a flexible endoscope into the colon and the common usage of anesthesia, the ACS recommends colonoscopy once every decade. Colonoscopy is also labor-intensive as it requires the physician to navigate through a large organ while closely inspecting for polyps. For mature adenoma, colonoscopy has high sensitivity, but small or flat lesions are particularly difficult to detect. The miss rate for polyps less than 5 mm in diameter is estimated to be between 15% [17] and 26% [18, 19]. Therefore, there is room for improving detection of small and flat lesions to improve early detection of CRC and reduce the death rate.

1.2 Optical coherence tomography

Optical coherence tomography (OCT) is a minimally invasive imaging modality that produces depth-resolved, cross-sectional images of tissue. Pulse-echo ultrasound is an appropriate analogy to quickly understand the general function of OCT. OCT images are generated by detecting reflections in a sample due to changes in refractive index using near-infrared, broadband light. As in ultrasound, the time delay of reflections can be measured to determine the locations of reflectors in depth. Where ultrasound and OCT differ, however, is in the detection of the "echo" signals. Ultrasound directly measures the time for the echo pulse to return and infers the location of scatterers by knowing the speed of sound in tissue. This direct measurement of time cannot be used in optical imaging to resolve small differences in traveled distance because the speed of light is too fast for electronic timing. Low-coherence interferometry is instead used to measure the optical path length to the reflectors in the sample.

There are three different architectures of OCT that use different methods of generating the same images: time-domain OCT, spectral domain OCT, and swept-source (or optical frequency domain) OCT. While the purpose of each type is the same, they are characterized by different imaging speeds and performance.

In this chapter, I provide an introduction to interferometry and coherence as relevant to OCT. Next, I describe the light source and detector characteristics. Finally, I briefly describe and compare the three types of OCT architectures.

1.2.1 Interferometry

OCT systems typically use Michelson interferometers. In such a system, the beam from the light source is split by a beamsplitter into two paths: a sample arm with a mirror located at a known distance from the beamsplitter and a reference arm with the beam focused on to the tissue sample. The reflected light recombines at the beamsplitter and is detected by a detector. The combination of the sample and reference beams form interference fringes. In this section, I describe monochromatic and polychromatic two-beam interferometry using plane waves.

The plane wave is the simplest solution of the Helmholtz wave equation and is given by

$$\boldsymbol{U}(\boldsymbol{r}, t) = Ae^{i(\boldsymbol{k}\cdot\boldsymbol{r} - \omega t + \phi)}\hat{\boldsymbol{a}}, \tag{1.1}$$

where A is the real-valued amplitude, $\boldsymbol{r} = r\hat{\boldsymbol{r}} = x\hat{\boldsymbol{x}} + y\hat{\boldsymbol{y}} + z\hat{\boldsymbol{z}}$ is the position vector, $\boldsymbol{k} = k\hat{\boldsymbol{k}} = k(\alpha\hat{\boldsymbol{x}} + \beta\hat{\boldsymbol{y}} + \gamma\hat{\boldsymbol{z}})$ is the wave vector pointing in the direction of propagation with amplitude $k = \frac{2\pi n}{\lambda}$ for wavelength λ and refractive index n and α, β, and γ are direction cosines, ω is the angular frequency, t is time, ϕ is the phase, and $\hat{\boldsymbol{a}} = a_x\hat{\boldsymbol{x}} + a_y\hat{\boldsymbol{y}} + a_z\hat{\boldsymbol{z}}$ is the unit vector describing the state of polarization of the wave. While plane waves do not physically exist due to their infinite extent, they are useful approximations for collimated light or light far from a source. Moreover, real electromagnetic waves can be decomposed into an infinite sum of plane waves traveling in different directions. In homogeneous, isotropic media, the polarization is perpendicular to the wave propagation. Electromagnetic waves contain transverse electric field and magnetic field components that are both orthogonal to one another and to the direction of propagation. We typically focus on only the electric field because electronic detectors often primarily interact with the electric field and the magnetic field can be uniquely determined if the electric field and material electromagnetic properties are known. The electric field is

$$\boldsymbol{E}(\boldsymbol{r},t) = \mathrm{Re}\{\boldsymbol{U}(\boldsymbol{r},t)\} = A\cos(\boldsymbol{k}\cdot\boldsymbol{r} - \omega t + \phi)\hat{\boldsymbol{a}}. \tag{1.2}$$

The principle of superposition states that the electromagnetic fields add in linear media (with each polarization component adding individually). If we consider two monochromatic plane waves with the sample amplitude

$$\boldsymbol{U}_1(\boldsymbol{r},t) = A\exp\left[i(\boldsymbol{k}_1\cdot\boldsymbol{r} - \omega_1 t + \phi_1)\right] \tag{1.3}$$

$$\boldsymbol{U}_2(\boldsymbol{r},t) = A\exp\left[i(\boldsymbol{k}_2\cdot\boldsymbol{r} - \omega_2 t + \phi_2)\right], \tag{1.4}$$

the linear summation of the two waves is

$$\begin{aligned}
\boldsymbol{U}(\boldsymbol{r},t) &= \boldsymbol{U}_1(\boldsymbol{r},t) + \boldsymbol{U}_2(\boldsymbol{r},t) && (1.5)\\
&= 2A\left[\cos\left(\frac{1}{2}(\boldsymbol{k}_\Sigma\cdot\boldsymbol{r} - \omega_\Sigma t + \phi_\Sigma)\right)\cos\left(\frac{1}{2}(\boldsymbol{k}_\Delta\cdot\boldsymbol{r} + \omega_\Delta t + \phi_\Delta)\right)\right. && (1.6)\\
&\quad\left. + i\left[\sin\left(\frac{1}{2}(\boldsymbol{k}_\Sigma\cdot\boldsymbol{r} - \omega_\Sigma t + \phi_\Sigma)\right)\cos\left(\frac{1}{2}(\boldsymbol{k}_\Delta\cdot\boldsymbol{r} - \omega_\Delta t + \phi_\Delta)\right)\right]\right], && (1.7)
\end{aligned}$$

where the Σ subscript denotes the sum of the two variables and the subscript Δ denotes the difference. The electric field is simply

$$\boldsymbol{E}(\boldsymbol{r},t) = 2A\cos\left(\frac{1}{2}(\boldsymbol{k}_\Sigma\cdot\boldsymbol{r} - \omega_\Sigma t + \phi_\Sigma)\right)\cos\left(\frac{1}{2}(\boldsymbol{k}_\Delta\cdot\boldsymbol{r} + \omega_\Delta t + \phi_\Delta)\right). \tag{1.8}$$

The first cosine has very high frequency, much too high to be detected by electronic sensors, and is the direction of propagation. The second cosine has a lower frequency that can be very low when the two beams have similar wavelengths. These low-frequency oscillations can be directly detected and are known as the interference fringes. The fringes are perpendicular to $\boldsymbol{k}_\Delta$.

Optical detectors respond to the irradiance of the sum of the electromagnetic waves, which is proportional to the square magnitude of the electric fields ($\boldsymbol{I}(\boldsymbol{r},t) =$

$\frac{1}{2}c\epsilon_0|\boldsymbol{E}(\boldsymbol{r},t)|^2$). If we generalize to two waves with different amplitudes A_1 and A_2 and the same wavelength ($\lambda_1 = \lambda_2 = \lambda$ and $\omega_1 = \omega_2 = \omega$), the irradiance corresponding to the two-wave interference example is

$$\begin{aligned} I(z,t) &= CU(z,t)U^*(z,t) && (1.9)\\ &= C\left(A_1 e^{-i(\boldsymbol{k}_1\cdot\boldsymbol{r}-\omega t+\phi_1)} + A_2 e^{-i(\boldsymbol{k}_2\cdot\boldsymbol{r}-\omega t+\phi_2)}\right) && (1.10)\\ &\times\left(A_1 e^{i(\boldsymbol{k}_1\cdot\boldsymbol{r}-\omega t+\phi_1)} + A_2 e^{i(\boldsymbol{k}_2\cdot\boldsymbol{r}-\omega t+\phi_2)}\right) && (1.11)\\ &= C\left(A_1^2 + A_2^2 + A_1A_2\left[e^{i(\boldsymbol{k}_\Delta\cdot\boldsymbol{r}+\phi_\Delta)} + e^{-i(\boldsymbol{k}_\Delta\cdot\boldsymbol{r}+\phi_\Delta)}\right]\right) && (1.12)\\ &= I_1 + I_2 + 2\sqrt{I_1I_2}\cos\left(\boldsymbol{k}_\Delta\cdot\boldsymbol{r}+\phi_\Delta\right), && (1.13) \end{aligned}$$

where $C = \frac{1}{2}c\epsilon_0$, c is the speed of light in vacuum, ϵ_0 is the permittivity of free space, and $I = CA^2$. The phase term ϕ_Δ accounts for any phase differences in the two beams.[2] We see that the interference fringes are time-independent when the two beams are the same wavelength. Therefore, the fringes form a standing wave.

Optical coherence tomography systems typically utilize Michelson interferometers. As seen in Fig. 1.1, Michelson interferometers use a beam splitter to send the input beam to two arms of the interferometer. The reflected light recombines at the beam splitter and a portion of the combined light continues to an optical detector. Here both of the beams travel in the same direction ($\boldsymbol{k}_1 = \boldsymbol{k}_2 = k$), but the total distance traveled differs ($z_1 \neq z_2$). Scalar notation can replace the previous vector notation if we define the optical axis to be along the direction of propagation. In this situation, the irradiance incident on the detector is

$$I(\Delta z) = \underbrace{I_1 + I_2}_{\text{DC}} + \underbrace{2\sqrt{I_1I_2}\cos\left(2k\Delta z + \Delta\phi\right)}_{\text{AC}}, \tag{1.14}$$

where $\Delta z = z_1 - z_2$ and the factor of 2 inside the cosine is due to the round trip path of the light. As in Eq. (1.13), the interference does not vary in time because the

---

[2] If considering polarization in Eq. (1.13), the amplitude of the cosine would be scaled by $p_{12} = |\hat{\boldsymbol{a}}_1\cdot\hat{\boldsymbol{a}}_2|$ and an additional phase term $\phi_p = \arg(\hat{\boldsymbol{a}}_1\cdot\hat{\boldsymbol{a}}_2)$ would be included in the argument of the cosine.

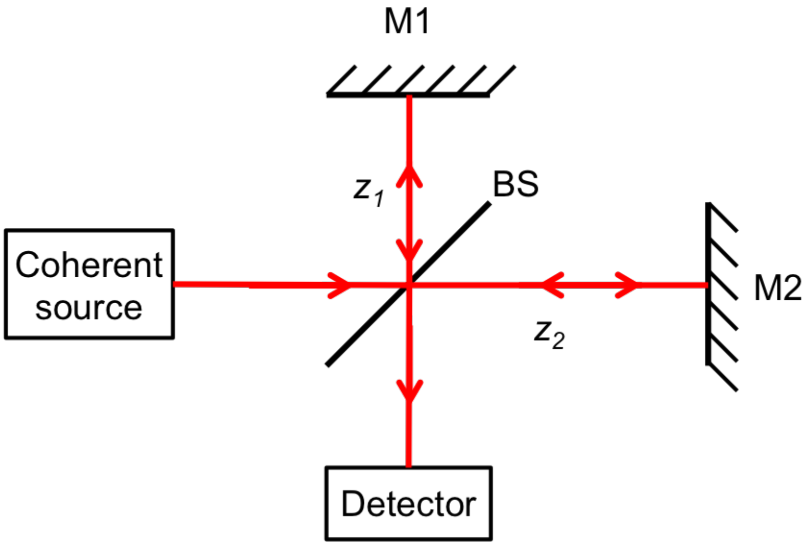

Figure 1.1: Michelson interferometer. The source beam is split by the beam splitter (BS) and reflects off of mirrors (M1) and (M2) in the two interferometer arms. The light recombines at BS and a portion of the combined light reaches the detector and the rest of the light travels back to the source. The mirrors are in general located at different distances from the beam splitter z_1 and z_2.

beams are of the same frequency. If neither interferometer arms contain dispersive media, then the phase offset $\Delta\phi = 0$. If the interferometer arms contain media other than air, then the optical path difference ($OPD = n_1 z_1 - n_2 z_2$) is used in place of Δz. The sum of the irradiances of the individual beams form a DC offset. This signal is modulated by the cosine term that varies as the path length changes with a frequency equal to k. A detector that is sensitive to small changes in intensity can therefore measure with very high precision very small changes in path length. However, monochromatic interference can only measure relative path differences and cannot measure the actual distance from the beam splitter to the reflector in one of the interferometer arms. To measure absolute distances, a broadband, or low-coherence, source is instead used.

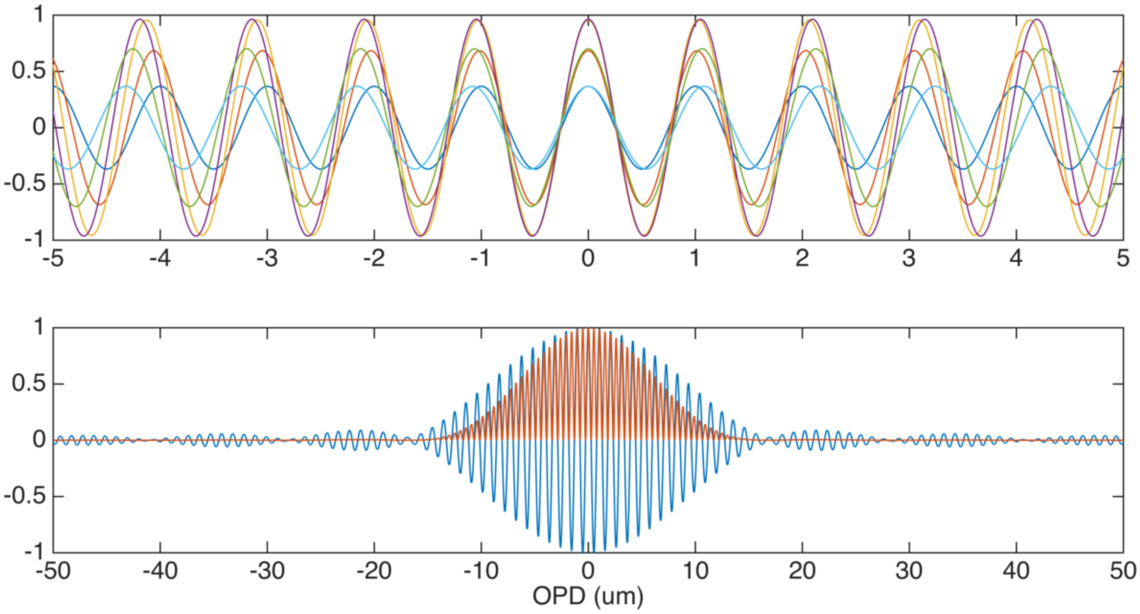

Figure 1.2: Simulation illustrating the effects of multiple wavelengths summed together. The top plot contains cosines with wavelengths from 1000 nm to 1080 nm with a Gaussian power spectrum and the bottom plot shows the normalized sum (blue) and the square of the normalized sum (orange).

1.2.2 Source characteristics and coherence

To determine locations of reflectors in depth, the light source must be polychromatic. This can be intuitively understood by considering that at zero OPD, the cosine term in Eq. (1.14) is at its maximum, regardless of wavelength. But when multiple wavelengths are used simultaneously, the fringes have high visibility only at and near zero OPD, as shown in Fig. 1.2. The relationship between the OPD over which light with a particular bandwidth produces visible fringes and the bandwidth of the source spectrum is known as temporal coherence.

To describe this mathematically, we return to Eq. (1.14) with a few modifications:

$$I(k, \Delta z)dk = G(k)dk\left(I_1 + I_2 + 2\sqrt{I_1 I_2}\cos(2k\Delta z)\right), \tag{1.15}$$

where $G(k)$ is the normalized real-valued power spectrum of the source as a function of wavenumber and dispersion is ignored ($\Delta\phi = 0$). If we assume uniform detector sensitivity to all wavelengths in $G(k)$, then the total irradiance seen by the detector is

$$I(\Delta z) = \int_0^\infty G(k)\left(I_1 + I_2 + 2\sqrt{I_1 I_2}\cos(2k\Delta z)\right) dk. \tag{1.16}$$

The first two terms are still constant over Δz and simply bias the detector current. If we inspect the interferometric term, we see it is similar to a Fourier transform. Because the source spectrum physically contains only positive frequencies, we can extend the integral in Eq. (1.16) to infinite limits by multiplying by a step function without any loss of information, thus forming a Fourier transform of the power spectrum.

$$\begin{aligned}\int_0^\infty 2\sqrt{I_1 I_2}G(k)\cos(2k\Delta z)dk &= 2\,\mathrm{Re}\left\{\int_{-\infty}^\infty 2\sqrt{I_1 I_2}G(k)\,\mathrm{step}(k)e^{i2k\Delta z}dk\right\} && (1.17)\\ &= 2\,\mathrm{Re}\left\{\mathcal{F}\left\{G(k)\,\mathrm{step}(k)\right\}\right\} && (1.18)\\ &= \gamma(\Delta z)\cos(2\pi k_0\Delta z + \beta(\Delta z)) && (1.19)\end{aligned}$$

The Fourier transform of the power spectrum $\gamma(\Delta z)$ is known as the coherence function of the source and is the axial PSF in OCT. A broad power spectrum corresponds to a narrow coherence function. The width of the coherence function is known as the coherence length and is the axial resolution in OCT. The irradiance oscillates with a frequency proportional to the central wavenumber (with a phase shift $\beta(\Delta z)$ for non-symmetric spectra). As demonstrated heuristically in Fig. 1.2, the fringe visibility is a function of the coherence function.

$$V(\Delta z) = \frac{I_{\max} - I_{\min}}{I_{\max} + I_{\min}} = \frac{2\sqrt{I_1 I_2}}{I_1 + I_2}\gamma(\Delta z) \tag{1.20}$$

Fringes have significant visibility only at or around $\Delta z = 0$ when using broad-bandwidth sources. Because such sources have short coherence lengths, OCT is a form of low-coherence interferometry.[20]

The axial resolution of OCT is defined by the source coherence length. The coherence length can be defined as the full-width at half-maximum (FWHM) of $\gamma(\Delta z)$.

If the power spectrum is Gaussian, then the Fourier transform is also Gaussian and the coherence length l_c is given by

$$l_c = \frac{2\ln(2)}{\pi}\frac{\lambda_0^2}{\Delta\lambda}, \tag{1.21}$$

where λ_0 is the central wavelength and $\Delta\lambda$ is the $1/e$ bandwidth of the normalized power spectrum. A Gaussian, Lorentzian, or other smoothly decaying power spectrum is preferable to a rectangular spectrum because the Fourier transform will not have side lobes that could be mistaken for nearby reflectors in the sample.

By contrast, the lateral resolution depends on the imaging optics as in a typical imaging system. In a diffraction limited system, the lateral resolution is approximated by the Rayleigh criterion:

$$\Delta x = \frac{0.61\lambda_0}{NA}, \tag{1.22}$$

where λ_0 is the center wavelength and NA is the numerical aperture in object space. Thus there is a trade-off between axial depth of field and lateral resolution. Typically relatively low NA values are used in OCT to maintain approximately constant lateral resolution over the imaging depth.

The wavelengths chosen for OCT tend to be in the near infrared as this is a region with favorable scattering and absorption by typical molecules (oxyhemoglobin, deoxyhemoglobin, water, etc.) in biological samples. The absorption coefficient ranges from $0.1\,\mathrm{mm}^{-1}$ to $1.0\,\mathrm{mm}^{-1}$ over the wavelength range of 600 nm to 1300 nm. Outside of the visible and near-infrared regions, absorption of water tends to be several orders of magnitude greater. Scattering decreases monotonically with wavelength. The combined effect of scattering, absorption, and axial and lateral resolution make choosing an ideal wavelength choice impossible. Longer wavelengths have greater depth of imaging, but axial resolution worsens exponentially. The ideal central wavelength will depend on the target tissue and task.

1.2.3 Time-domain OCT

Time-domain OCT (TDOCT) was the original OCT architecture invented in 1991.[20] The optical system is a Michelson interferometer with a broadband light source, a reference arm mirror that oscillates along the optical axis, and a single-element photodetector. As described in Section 1.2.2, a broadband source has a narrow coherence function $\gamma(OPD)$, so interference fringes are visible at and near zero OPD. By oscillating the reference mirror over a distance of around 1 mm to 2 mm, the location of zero OPD is effectively shifted throughout the depth of imaging in the sample. Reflections from scatterers in the sample will only be detected when the mirror is placed such that the reflectors are near the zero OPD point. Therefore, one full scan (forward or reverse) of the reference arm mirror generates a single A-scan. This method is called time-domain because OPD is scanned as a function of time.

The mathematical representation of an A-scan in TDOCT is nearly identical to Eq. (1.19), though it is typically expressed as a function of time and frequency, rather than distance and wavenumber. Also, the carrier frequency ν_0 is shifted by ν_D due to the Doppler effect imposed by the scanning mirror, where

$$\nu_D = \frac{2v\nu_0}{c} \tag{1.23}$$

and v is the velocity of the reference mirror. In practice, the fringes from the carrier (plus Doppler) frequency are removed by using a lock-in amplifier set to the Doppler-shifted carrier frequency. The reference mirror ideally scans at a constant velocity over the desired imaging depth so that the envelope signal is not reduced due to frequency mismatches between the carrier and lock-in amplifier when the mirror experiences acceleration at the ends of travel. The resulting signal is the envelope of the fringes, which have the shape of the coherence function. The amplitude of the envelope is proportional to the sample reflectance at the depth location of zero OPD (plus the reflectances of adjacent reflectors within the coherence length around the zero OPD point).

A two-dimensional image (B-scan) is generated by scanning the beam across the tissue in one direction. Scanning in x and y on a sample generates a three-dimensional volumetric image (C-scan).

TDOCT is fundamentally restricted by the mechanical scan time of the reference mirror. The maximum realistic scanning frequency is on the order of kilohertz, which greatly reduces the feasibility of TDOCT for collecting volumetric data with high spatial sampling. Piezoelectric scanners can achieve greater frequencies, but cannot travel on the order of millimeters, greatly reducing the depth of field. Furthermore, Fourier-domain OCT methods, described in Secs. 1.2.4 and 1.2.5, have superior SNR compared to TDOCT.[21, 22, 23] As a result of these limitations, TDOCT has been largely supplanted by Fourier-domain methods; however, the invention of multiple-reference OCT (MR-OCT) has renewed interest in TDOCT. This architecture, invented in 2013 [24], uses a partially reflecting mirror in the reference arm before the distal highly reflective mirror to generate beams with several different path lengths as light reflects from each face of the windows. This allows for sampling at several depths in the sample simultaneously. A piezoelectric actuator modulates the mirror at the end of the reference arm, which shifts the path lengths of all of the reflected beams. The result is a fast-scanning, extremely low-cost OCT system [24, 25, 26, 27, 28, 29].

1.2.4 Spectral-domain OCT

Spectral-domain OCT (SDOCT) is one of two Fourier-domain OCT methods that measure a fringe signal in wavenumber space and then generate an A-scan by applying the Fourier transform to measured signal. Using a stationary reference-arm mirror, each reflected wave from the sample combines to generate a cosine with a frequency proportional to the OPD of the reflector and weighted by the sample reflectance at that depth. A superposition of these sinusoidal signals, biased by a constant value proportional to the total reflectances of the reference mirror and all reflections in the sample arm, reaches the detector arm. SDOCT uses a spectrometer to sample the interference fringes as a function of wavelength (later computationally recorded linearly in wavenumber). Because each spectral bin on a spectrometer has a narrow bandwidth and long coherence length, fringe visibility is sufficiently high over the entire scattering-limited imaging depth in tissue without having to move the reference arm to move the position of zero OPD in the sample.

The principle of Fourier-domain OCT can be easily understood by representing the sample as a collection of N discrete reflectors of infinitesimal extent (Dirac delta functions) weighted by their reflectance.

$$U_s(z,k) = \sqrt{G(k)}\exp(i(2kz-\omega t))\sum_{n=1}^{N} r_n\delta(z-z_n) \tag{1.24}$$

$$U_r(z,k) = \sqrt{G(k)}r_r\exp(i(2kz_r-\omega t)) \tag{1.25}$$

The measured detector signal is proportional to the square modulus of the sum of the sample and reference arms averaged over the detector exposure time (the $1/\sqrt{2}$ assumes a 50:50 beamsplitter).

$$I_D(k) \propto \left\langle \left| \sqrt{\frac{G(k)}{2}}r_r\exp(i(2kz_r-\omega t)) + \sqrt{\frac{G(k)}{2}}\sum_{n=1}^{N} r_n\exp(i(2kz_n-\omega t)) \right|^2 \right\rangle$$

$$= \frac{G(k)}{2}\left(R_r + \sum_{n=1}^{N} R_n\right) \tag{1.26a}$$

$$+ G(k)\sum_{n=1}^{N}\sqrt{R_rR_n}\cos(2k(z_r-z_n)) \tag{1.26b}$$

$$+ G(k)\sum_{n\neq m=1}^{N}\sqrt{R_nR_m}\cos(2k(z_n-z_m)) \tag{1.26c}$$

The irradiance is described in three terms. The sum of all reflectances adds a time-invariant bias as a function of wavenumber to the interferogram (Eq. (1.26a)). The term in Eq. (1.26b) is the fringe signal due to interference from the reference and sample arms and contains the sample reflectance $\sqrt{R_n}$, which is the desired function to extract in OCT. The final term (Eq. (1.26c)) is from interference of scatterers in the sample arm separated by less than the source coherence length and is undesired.

Taking the inverse Fourier transform of Eq. (1.26) results in

$$\begin{aligned}
I_D(z) \propto\ & \frac{\gamma(z)}{2}\left(R_r + \sum_{n=1}^{N} R_n\right) \\
& + \frac{1}{2}\gamma(z) * \sum_{n=1}^{N} \sqrt{R_r R_n}\left[\delta(z + 2(z_r - z_n)) + \delta(z - 2(r_r - z_n))\right] \\
& + \frac{1}{2}\gamma(z) * \sum_{n \neq m=1}^{N} \sqrt{R_n R_m}\left[\delta(z + 2(z_n - z_m)) + \delta(z - 2(z_n - z_m))\right] \\
=\ & \frac{\gamma(z)}{2}\left(R_r + \sum_{n=1}^{N} R_n\right) && \text{(1.27a)} \\
& + \frac{1}{2}\sum_{n=1}^{N} \sqrt{R_r R_n}\left[\gamma(2(z_r - z_n)) + \gamma(-2(r_r - z_n))\right] && \text{(1.27b)} \\
& + \frac{1}{2}\sum_{n \neq m=1}^{N} \sqrt{R_n R_m}\left[\gamma(2(z_n - z_m)) + \gamma(-2(z_n - z_m))\right] && \text{(1.27c)}
\end{aligned}$$

The OCT A-scan, represented by Eq. (1.27), is a function of OPD. Due to the Hermitian symmetry of the Fourier transform, the transform of a cosine has delta functions at positive and negative distances. Without additional hardware or processing, half of the resulting information is redundant; the negative distances are typically omitted from display. The DC term in Eq. (1.27a) presents as an artifact at the zero OPD point. The autocorrelation signal (Eq. 1.27c) produces artifactual signal near zero OPD. The desired reflectivity profile from Eq. (1.27b) presents as the rest of the signal in the A-scan. The coherence function $\gamma(z)$ is the axial PSF and is convolved with the Fourier transform of the measured fringe data.

Imaging speed of SDOCT is significantly greater than TDOCT owing to the fast acquisition time of line cameras compared to mechanical motion of a reference arm mirror. SDOCT also has fundamental SNR improvements over TDOCT owing to the fact that all of the light is used, whereas TDOCT systems are only sensitive to light collected from depths within the coherence length of the zero OPD location.[21, 22, 23]

1.2.5 Swept-source OCT

The operation of swept-source OCT (SSOCT), also known as optical frequency domain imaging (OFDI), is nearly identical to SDOCT. The main difference in the system architecture is that a swept-source laser is used instead of a broadband continuous source. A swept-source laser has a narrow instantaneous linewidth and sweeps over a wide range of wavelengths. Early swept sources used spinning or scanning mirrors and, as a result, the sweep speed was limited by mechanical motion and the need for each narrow frequency band to reach saturation before exiting the cavity [30, 31]. The invention of the Fourier domain mode locked (FDML) laser [32] greatly increased sweep rates. FDML lasers use a long fiber cavity to carry the entire chirped signal and is synchronized such that the beam passes through a tunable filter (e.g., Fabry-Perot filter) with the changing tuning frequency. This prevents light from being blocked with each pass and allows the power to build up to saturation over multiple passes through the cavity. While the filter is still mechanical, Fabry-Perot filters use much faster piezoelectric actuators. Because light is not lost with each pass through the cavity, build-up time of the beam only occurs when the laser is powered on. Therefore, the build-up time no longer limits the sweep rate of the laser. This has enabled sweep rates as high as 20 MHz [33]. Semiconductor lasers, such as the vertical-cavity surface-emiting laser (VCSEL), have also become increasingly common as frequency-tunable sources for OCT [34]. These sources are currently slower than FDML and polygon-mirror based lasers, but can be produced for much less cost and quality can be tightly controlled.

Some benefits of SSOCT are the fact that photodetectors are simpler to use in the near-infrared wavelengths typically used in OCT and the imaging speed is faster than SDOCT because modern frequency-tunable sources have faster sweep rates than line-scan camera frame rates [35].

1.3 Doppler optical coherence tomography

Doppler OCT, one of many functional OCT methods, generates images where the contrast depicts movement or flow due to the Doppler effect. The ability to detect flow in OCT enabled the visualization of blood and lymphatic vessels and estimation of flow velocity near the surface of tissue. This information has many clinical applications. Examples in ophthalmology include detection of diseases such as diabetic retinopathy, macular degeneration, and anterior ischemic optic neuropathy. Dermatologists can use vascular imaging for detection and monitoring of diseases such as port-wine stain, hemangioma, burns and lacerations, and eczema. Detection of vascular function and morphology may also be used in cancer for early detection, study of natural progression, and response to therapies.

Doppler OCT was first demonstrated independently by two groups in 1997 by applying the short-time Fourier transform (STFT) to data collected using time-domain OCT [36, 37]. Major developments in Doppler OCT include phase-resolved optical Doppler tomography in 2000 to decouple spatial and flow resolutions [38], measurement of the standard deviation of the Doppler shift to measure flow perpendicular to the beam in 2002 [39], development of optical microangiography for filtering out static tissue in the frequency domain in 2007 [40], several intensity-only based methods since 2005 [41, 42, 43], and computationally efficient methods of computing the phase shift between adjacent A-scans using complex data [44, 45]. Doppler OCT remains a highly active area of research in both technology/algorithm development and biomedical studies.

1.3.1 Doppler effect

The Doppler effect describes the change in frequency of a wave due to movement of the source, receiver, or any intermediate reflector. The effect is valid and mathematically equivalent for both acoustic and electromagnetic waves. In Doppler imaging, movement can be measured by detecting the change in source wave frequency as a result of moving particles in the sample.

A Doppler imaging system can be considered to consist of a point source S and a point receiver R separated by a distance d. In general, both S and R are moving at velocities $\boldsymbol{v}_S$ and $\boldsymbol{v}_R$, respectively. To simplify the derivation, first consider that S and R are moving parallel to one another in an arbitrary direction such that the velocity vectors can be represented as scalars. Deviation from this geometry is considered later. The signs of the algebraic terms below depend on the direction of movement of S and R relative to a laboratory frame. This derivation first assumes that S and R are moving in the positive direction. The results are generalized to any combination of movement directions in Table 1.1.

Consider a wave emitted by S at time 0 that reaches R at time t. The distance traveled by the wave can be equivalently described in terms of the velocity of the wave c and in terms of the distances between S and R:

$$\text{distance traveled} = ct = d + v_R t, \tag{1.28}$$

where $v_R t$ is the distance traveled by R over the time duration t.

At some future time τ, another wave is emitted by S (the source period is τ). Relative to time 0, S has traveled a distance $v_S\tau$. This wave will reach R at a time t'. The distance that this wave traveled is described similarly as Eq. (1.28).

$$c(t' - \tau) = d \overset{a}{-} v_S\tau \overset{b}{+} v_R t' \tag{1.29}$$

The signs denoted by a and b depend on the sign of the movement of S and R (positive or negative) and are described in Table 1.1. Future steps in this derivation

S_{dir}	R_{dir}	a	b
$+$	$+$	$-$	$+$
$-$	$-$	$+$	$-$
$+$	$-$	$-$	$-$
$-$	$+$	$+$	$+$

Table 1.1: Sign convention in (1.29) based on direction of movement of S and R.

maintain the signs used in (1.29). Solving for t' yields

$$t' = \frac{d + (c - v_S)\tau}{c - v_R}. \tag{1.30}$$

The time interval between the two received waves is $\tau' = t' - t$ and described in terms of distances as

$$\begin{aligned} \tau' &= \frac{d + (c - v_S)\tau}{c - v_R} - \frac{d}{c - v_R} \\ &= \frac{c - v_S}{c - v_R}\tau. \end{aligned} \tag{1.31}$$

The total number of emitted waves must equal the number of received waves.

$$f_S\tau = f_R\tau' \tag{1.32}$$

When the velocities of S and R are not equal, the frequency of the received waves will differ from the frequency of the emitted waves.

$$\begin{aligned} f_R &= \frac{\tau}{\tau'} f_S \\ &= \frac{c - v_R}{c - v_S} f_S \\ &= \left(1 - \frac{v_R}{c}\right)\left(1 - \frac{v_S}{c}\right)^{-1} f_S \end{aligned} \tag{1.33}$$

The inverse term in (1.33) can be simplified using the binomial theorem[3] and re-

---

[3] $(1+x)^n = 1 + nx + \frac{n(n-1)}{2!}x^2 + \ldots$

taining only the first two terms because $v_s \ll c$.

$$f_R \approx \left(1 - \frac{v_R}{c}\right)\left(1 + \frac{v_S}{c}\right) f_S \tag{1.34}$$

$$= \left(1 + \frac{v_S - v_R}{c} - \frac{v_R v_S}{c^2}\right) f_S \tag{1.35}$$

$$\approx \left(1 + \frac{v_S - v_R}{c}\right) f_S \tag{1.36}$$

The third term in (1.35) can be neglected because $v_R v_S \ll c^2$. Therefore, the Doppler frequency shift is expressed as

$$f_D \equiv f_R - f_S \tag{1.37}$$

$$= \frac{v}{c} f_S, \tag{1.38}$$

where $v = v_S - v_R$.

Now consider that the source and receiver are co-located (as is the case in OCT) and stationary. If the angle between the imaging probe and the direction of a moving target traveling at velocity $\boldsymbol{v}_T$ is θ, then the apparent velocity measured by the probe is the projection of the target velocity vector on the probe beam:

$$v = 2 v_T \cos\theta. \tag{1.39}$$

The factor of 2 comes from the double-pass nature of the transmitted and reflected beam.[4] Substituting (1.39) into (1.38) yields the Doppler formula for OCT:

$$f_D = \frac{2v\cos\theta}{c} f_S \tag{1.40}$$

$$= \frac{2v\cos\theta}{\lambda_S} \tag{1.41}$$

where λ_S is the wavelength of the source. Therefore, the entire spectrum will be shifted in frequency proportional to the projection of the scatterer velocity vector on the beam.

---

[4] For separate source and receiver with angles relative to the target θ_S and θ_R, the velocity at the receiver is $v = v_T(\cos\theta_S + \cos\theta_R)$.

1.3.2 Review of Doppler OCT methods

The first applications of Doppler OCT used TD-OCT systems and estimated the local frequency shift due to the Doppler effect using the short-time Fourier transform (STFT)[36, 37]. The STFT is a windowed Fourier transform and enables localized frequency analysis. While theoretically straightforward, the STFT is computation heavy, requiring a discrete Fourier transform to be computed at each discrete spatial location. Moreover, the STFT method has a fundamental tradeoff between spatial resolution in the resulting flow map and Doppler frequency resolution. This is a result of the fact that the frequency resolution is inversely proportional to the maximum extent of the window. Therefore, a short window has high spatial resolution, but low resolution to frequency shifts and vice versa.

The tradeoff between spatial resolution and velocity sensitivity was broken with the development of phase-resolved optical Doppler tomography (PR-ODT) in 2000 [38]. This method computes the phase difference between adjacent A-scans at each depth location. The Doppler frequency shift ω is related to the phase difference $\Delta\phi$ by

$$\omega = \frac{\Delta\phi}{T}, \tag{1.42}$$

where T is the time between the the acquisition of the compared pixels (A-scan rate). The proof of this is described in Section 1.3.3. Not only did this method decouple spatial and frequency resolutions, it also increased sensitivity to slower flow velocities because T is orders of magnitude greater for adjacent A-scans than it is for adjacent pixels in depth. Even slower velocities can be detected when adjacent B-scan pixels are used for computing the phase difference. Imaging speed also greatly improved as a result of PR-ODT [38, 46]. The phase difference in PR-ODT is computed using the autocorrelation of the complex analytic signal with lag T. While first proposed for OCT by Zhao et al. [46], the theoretical basis for this method was first described for Doppler ultrasound by Kasai et al. [47] 15 years prior. Early demonstrations of this method include TD-OCT for imaging port-wine stain [48] and skin vasculature [38, 49], SD-OCT for imaging the retina [50, 51], and SS-OCT for chick chorioallantoic membrane [52] and human skin [53].

Several groups have demonstrated Doppler OCT methods that use only the real-valued intensity, rather than the complex representation with encoded phase information [41, 42, 43, 54, 55, 56, 57]. In general, intensity-based methods are based on the statistical behavior of speckle that arises from local interference of partially coherent light. When the beam and scatterers are static, the speckle pattern is stationary. However, movement causes the speckle to vary in time. The variance of the speckle is proportional to velocity of the scatterer. A major advantage of methods using speckle decorrelation or variance is that they are sensitive to flow perpendicular to the beam. Furthermore, intensity-based measures are insensitive to phase noise of the source and may be more appropriate for SS-OCT because swept sources typically have greater phase instability compared to superluminescent diodes that are typically used in SD-OCT. Some intensity methods, such as intensity-based Doppler variance (IBDV) have been demonstrated to be less sensitive to bulk tissue motion than PR-ODT [43].

Doppler OCT algorithms have also been developed that use the complex OCT signal.. The joint spectral and time domain OCT (STdOCT) method localizes the Doppler frequency shift in depth by recognizing that the measured fringe signal from a moving scatterer can be expressed equivalently as a shift in OPD as a function of wavenumber and a stationary OPD with a beat frequency as a function of time [58]. This method requires only Fourier transforms to obtain information about flow velocity. Optical microangiography (OMAG) [59] applies a Fourier transform to the complex OCT signal using time as the variable of integration, rather than k, to determine the temporal frequency spectrum of the measured signal, where the frequency is proportional to the flow velocity. These data are high-pass filtered to remove low-frequency data that correspond to stationary tissue. The inverse

Fourier transform of these filtered data return an interferogram containing only information from moving scatterers. Finally, the Fourier transform over k is applied to generate images containing only moving scatterers (i.e., angiogram). Resonant Doppler OCT [60] uses an electro-optic phase modulator to add a time-varying phase to the OCT interferogram to compensate for the phase imparted by moving scatterers. When the modulator frequency matches the Doppler frequency, the fringe visibility is maximized. Fringes from static tissue will be blurred, so the resulting images will be angiograms. Because the modulator is tunable over a wide frequency range, this method is sensitive to a much wider range of flow velocities than other techniques, which are fundamentally limited to measuring Doppler frequencies at half of the A-scan rate (Nyquist limit). The complex differential variance (CDV) algorithm uses the ratio of the phase change to the amplitude over a small depth window between two or more A-scans at the same location [45]. The local phase change is sensitive to flow variations across the window. The amplitude only changes when flow velocity is high. However, the combination of phase and amplitude are not sensitive to bulk motion or sources of noise or synchronization errors in the source or data acquisition.

1.3.3 Derivation of Kasai autocorrelation

The theory and algorithms of Doppler OCT can be traced to the groundwork laid in the fields of ultrasound (US) and signal processing. OCT and US are described similarly through the mathematics of complex analytical signals. This section describes the basics of the complex representation of signals (RF in US and interferogram in OCT) and the statistical operations that estimate the Doppler frequency shift induced by a moving scatterer along the axis of the beam. Afterwards, the Kasai autocorrelation is derived [47]. This algorithms was originally designed for implementation in hardware; the autocorrelation in hardware is a straightforward operation and is faster than computing the autocorrelation in software, especially in 1985 when the method was developed.

The OCT interferogram can be described as a complex signal of the form

$$\Gamma(t) = \mathrm{Re}\left\{A(t)e^{i\omega_0 t}\right\} \tag{1.43a}$$

$$\Gamma(k) = \mathrm{Re}\left\{A(k)e^{ik_o OPD}\right\}, \tag{1.43b}$$

where Eq. (1.43a) is used in time-domain OCT and Eq. (1.43b) is used in Fourier-domain OCT.[5] These signals are comprised of a single-frequency complex exponential with frequency proportional to the OPD (and Doppler shifted due to the moving reference mirror in TD-OCT) and a complex envelope $A(\cdot)$ [61]. The envelope can be expressed as

$$A(t) = I(t) + iQ(t), \tag{1.44}$$

where $I(t)$ is the in-phase component and $Q(t)$ is the quadrature component, to use terminology from signal processing. In phasor notation, Eq. (1.44) is written as

$$A(t) = a(t)e^{i\theta(t)}. \tag{1.45}$$

Typically only the magnitude $a(t)$ of Eq. (1.45) is directly measured, where

$$a(t) = \sqrt{I^2(t) + Q^2(t)}. \tag{1.46}$$

The complex representation of $A(t)$ defines a phase

$$\theta(t) = \tan^{-1}\left(\frac{Q(t)}{I(t)}\right). \tag{1.47}$$

The instantaneous angular frequency $\omega(t)$ is defined as the time derivative of the phase [61]:

$$\omega(t) \equiv \dot{\theta}(t) = \frac{\dot{Q}(t)I(t) - \dot{I}(t)Q(t)}{I^2(t) + Q^2(t)}. \tag{1.48}$$

---

[5] For the rest of this section, the signals will be treated as functions of time. Wavenumber can be substituted for time in the case of Fourier-domain OCT methods.

The Doppler effect causes a shift of the source spectrum upon reflection or scattering off of a moving target. If the power spectrum of the complex envelope $A(t)$ is denoted $G(\omega)$, then the mean angular frequency is defined as

$$\bar{\omega} = \frac{\int_{\infty} d\omega\ \omega G(\omega)}{\int_{\infty} d\omega\ G(\omega)}. \tag{1.49}$$

Measuring or estimating $\bar{\omega}$ is the goal of Doppler imaging. By comparing $\bar{\omega}$ to the source mean frequency, the difference is proportional to the velocity of the scatterer, scaled by the angle between the beam and the scatterer velocity vector. Various Doppler algorithms attempt to estimate $\bar{\omega}$ because $G(\omega)$ is typically not directly measurable.

The Wiener-Khinchine theorem states that the power spectrum of a wide-sense stationary random process is related to the autocorrelation of the random process by the Fourier transform.

$$R(\tau) = \mathcal{F}^{-1}\left\{G(\omega)\right\} = \int_{\infty} d\omega\ G(\omega) e^{i\omega\tau}, \tag{1.50}$$

where

$$R(\tau) \equiv \left\langle A^{*}(t) A(t+\tau) \right\rangle. \tag{1.51}$$

The angular brackets in Eq. (1.51) denote the ensemble average.[6] Using Eq. (1.44),

---

[6] There is an important and subtle difference between time average and ensemble average that is relevant to this discussion. The time average is calculated by averaging the data collected from a single experiment over a period of time. The ensemble average is calculated at a particular point in time by averaging the stochastic output at that point in time over an infinite number of identical experiments. The ensemble average is popular in theoretical analysis because it involves the probability distribution function describing the stochastic process, which can often be accurately chosen based on the physics of the experiment. However, it is impossible to experimentally measure the ensemble average.

The ensemble and time averages are equal if and only if the system is *ergodic*. Ergodicity is difficult to verify experimentally. As such, authors often state that the ensemble and time averages are equal if the system is stationary, because that is easier to test and because an ergodic system

$R(\tau)$ can be expressed as

$$\begin{aligned} R(\tau) &= \langle [I(t) - iQ(t)]\,[I(t+\tau) + iQ(t+\tau)] \rangle \\ &= \langle I(t)I(t+\tau) + Q(t)Q(t+\tau) + i\,[I(t)Q(t+\tau) - Q(t)I(t+\tau)] \rangle \\ &= \langle I(t)I(t+\tau) \rangle + \langle Q(t)Q(t+\tau) \rangle + i\,[\langle I(t)Q(t+\tau) \rangle - \langle Q(t)I(t+\tau) \rangle] \\ &= R_{II}(\tau) + R_{QQ}(\tau) + i\,[R_{IQ}(\tau) - R_{QI}(\tau)]\,. \end{aligned} \tag{1.52}$$

The ensemble averaging can be applied to each term in the third line because the ensemble average is a linear operation.

The mean angular frequency can be expressed in terms of the autocorrelation and this can be seen by taking the time derivative of $R(\tau)$ using the definition from Eq. (1.50) and evaluating at $\tau = 0$.

$$R(\tau) = \int_{\infty} d\omega\ G(\omega) e^{i\omega\tau} \tag{1.53a}$$

$$R(0) = \int_{\infty} d\omega\ G(\omega) \tag{1.53b}$$

$$\frac{d}{d\tau} R(\tau) = \dot{R}(\tau) = i \int_{\infty} d\omega\ \omega G(\omega) e^{i\omega\tau} \tag{1.53c}$$

$$\dot{R}(0) = i \int_{\infty} d\omega\ \omega G(\omega). \tag{1.53d}$$

By inspection of Eq. (1.49), $\bar{\omega}$ can be expressed in terms of the autocorrelations in Eq. (1.53).

$$\bar{\omega} = \frac{\int_{\infty} d\omega\ \omega G(\omega)}{\int_{\infty} d\omega\ G(\omega)} = \frac{\dot{R}(0)}{iR(0)} \tag{1.54}$$

Equation (1.54) can be further expressed in terms of the in phase and quadrature

---

must also be stationary. In the special case that the stochastic process is Gaussian, however, ergodicity can be proven if the power spectrum is continuous or, equivalently, if the autocorrelation function vanishes as the temporal or spatial distance between the processes approaches infinity. Because noise is Gaussian in US and OCT (and most other optical imaging systems), the systems can be assumed to be ergodic. Therefore, the time average is an accurate approximation to the ensemble average [62].

components through algebraic manipulation of Eq. (1.52).

$$\begin{aligned}
R(0) &= \langle A^*(t)A(t)\rangle \\
&= \langle (I(t)-iQ(t))(I(t)+iQ(t)\rangle \\
&= \left\langle I^2(t)+Q^2(t)\right\rangle \\
&= R_{II}(0)+R_{QQ}(0) && (1.55)\\
\dot{R}(\tau) &= \frac{d}{d\tau}\left\langle (I(t)-iQ(t))(I(t+\tau)+iQ(t+\tau))\right\rangle \\
&= \frac{d}{d\tau}\left\langle I(t)I(t+\tau)+Q(t)Q(t+\tau)+i\left[I(t)Q(t+\tau)-Q(t)I(t+\tau)\right]\right\rangle \\
&= \frac{d}{d\tau}\left(R_{II}(\tau)+R_{QQ}(\tau)+i\left[R_{IQ}(\tau)-R_{QI}(\tau)\right]\right) \\
&= \dot{R}_{II}(\tau)+\dot{R}_{QQ}(\tau)+i\left[\dot{R}_{IQ}(\tau)-\dot{R}_{QI}(\tau)\right] && (1.56)\\
\dot{R}(0) &= \left\langle I(t)\dot{I}(t)\right\rangle+\left\langle Q(t)\dot{Q}(t)\right\rangle+i\left[\left\langle I(t)\dot{Q}(t)\right\rangle-\left\langle Q(t)\dot{I}(t)\right\rangle\right] \\
&= i\left[\left\langle I(t)\dot{Q}(t)\right\rangle-\left\langle Q(t)\dot{I}(t)\right\rangle\right] \\
&= i\left[\dot{R}_{IQ}(0)-\dot{R}_{QI}(0)\right] && (1.57)
\end{aligned}$$

The penultimate line of Eq. (1.57) does not contain $\dot{R}_{II}$ or $\dot{R}_{QQ}$ because they are odd functions and odd functions evaluated at zero are zero.[7] Substituting Eqs. (1.55) and (1.57) into Eq. (1.54) yields

$$\begin{aligned}
\bar{\omega} &= \frac{\dot{R}_{IQ}(0)-\dot{R}_{QI}(0)}{R_{II}(0)+R_{QQ}(0)} && (1.58a)\\
&= \frac{\left\langle I(t)\dot{Q}(t)\right\rangle-\left\langle Q(t)\dot{I}(t)\right\rangle}{\langle I^2(t)\rangle+\langle Q^2(t)\rangle} && (1.58b)\\
&= \left\langle \frac{I(t)\dot{Q}(t)-Q(t)\dot{I}(t)}{I^2(t)+Q^2(t)}\right\rangle && (1.58c)\\
&= \left\langle \dot{\theta}\right\rangle. && (1.58d)
\end{aligned}$$

Therefore, the mean angular frequency is equal to the ensemble average of the

---

[7] The autocorrelation of real functions are even and the derivative of even functions are odd.

instantaneous frequency. In the case of an ergodic random process such as the measured OCT signal, the ensemble average is approximated by the time average.

An alternative expression for $\bar{\omega}$ is derived from the phasor representation of the autocorrelation $R(\tau)$ and the definitions in Eq. (1.52).

$$R(\tau) = A(\tau)e^{i\phi(\tau)} \tag{1.59a}$$

$$A(\tau) = \sqrt{(R_{II}(\tau) + R_{QQ}(\tau))^2 + (R_{IQ}(\tau) - R_{QI}(\tau))^2} \tag{1.59b}$$

$$\phi(\tau) = \tan^{-1}\left(\frac{R_{IQ}(\tau) - R_{QI}(\tau)}{R_{II}(\tau) + R_{QQ}(\tau)}\right) \tag{1.59c}$$

Note that the amplitude $A(\tau)$ is even due to the squaring inside the square root and the phase $\phi(\tau)$ is odd because arctangent is an odd function. The derivative of an even function produces an odd function and vice versa. Also, an odd function evaluated at zero equals zero. Therefore, evaluating the autocorrelation and its time derivative at zero yields

$$R(0) = A(0) \tag{1.60}$$

$$\dot{R}(\tau) = \left(\dot{A}(\tau) + iA(\tau)\dot{\phi}(\tau)\right)e^{i\phi(\tau)} \tag{1.61}$$

$$\dot{R}(0) = iA(0)\dot{\phi}(0). \tag{1.62}$$

Substituting Eqs. (1.60) and (1.62) into Eq. (1.54) shows that the mean angular frequency is equal to the time derivative of the autocorrelation phase.

$$\bar{\omega} = \frac{\dot{R}(0)}{iR(0)} = \dot{\phi}(0) \tag{1.63}$$

If the phase is slowly varying over a small time duration T, the derivative can be approximated as

$$\dot{\phi}(0) \approx \frac{\phi(T) - \phi(0)}{T} = \frac{\Delta\phi}{T}. \tag{1.64}$$

The smallest value of T in Doppler OCT would be adjacent measurements, either adjacent pixels in depth in TD-OCT, or (more commonly) adjacent A-scans in Fourier-domain OCT methods. Therefore, an estimate of the mean angular frequency is obtained by calculating the phase of the autocorrelation of adjacent A-scans.

In TD-OCT systems, in-phase and quadrature components must be measured directly, typically achieved using a lock-in amplifier. This produces $A(t)$ in Eq. (1.44), which is used to compute the autocorrelation as in Eq. (1.51), where τ is either an adjacent pixel in depth when measuring high flow velocity is desired, or the adjacent A-scan (comparing equal depth pixels) when slower flow measurements are needed. In Fourier domain methods where the data is measured in wavenumber space, the inverse Fourier transform will return the complex A-scan data that can be used for computing the autocorrelation.

The arctangent operation used to compute the autocorrelation phase is unambiguously defined over the range of $[-\pi, \pi)$. From Eq. (1.40) relating the Doppler frequency shift and the velocity of the scatterer, and substituting $f_D \approx \bar{\omega}/2\pi$,

$$\begin{aligned} v &= \frac{c}{2n\cos\theta}\frac{f_D}{f_s} && (1.65)\\ &= \frac{\Delta\phi\lambda_0}{4\pi nT\cos\theta} && (1.66)\\ &= \frac{\Delta\phi}{2kT\cos\theta}. && (1.67) \end{aligned}$$

The maximum detectable velocity before phase wrapping approaches infinity as the scatterer moves increasingly perpendicularly to the beam, but the maximum unambiguous measurement of the velocity projection onto the beam is when $\Delta\phi = \pm\pi$, or

$$v_{\max} = \pm\frac{\lambda_0}{4nT}. \qquad (1.68)$$

Phase unwrapping techniques can be applied most effectively to a locally smooth velocity profile, but is unreliable when the change in phase between adjacent pixels approaches $\pm\pi$. The minimum detectable velocity depends on the noise of the system and is proportional to the minimum detectable phase shift $\Delta\phi$.

CHAPTER 2

Present Study

Our lab and others have demonstrated the value of OCT for cancer imaging in the gastrointestinal (GI) tract. The ability to image with $<10\,\mu\text{m}$ resolution in depth and laterally non-destructively enables early detection of abnormalities including dysplasia and inflammatory disease. For diagnostic imaging, OCT provides superior lateral resolution and introduces an entire new dimension of information with depth-resolved imaging compared to established modalities such as white-light endoscopy. For imaging on the cellular scale, OCT has inferior resolution to microscopy of thin stained sections, but certain cellular-level details can be inferred from OCT (e.g., cellular structure using polarization-sensitive OCT, molecular information deduced from absorption and scattering, etc.) and does not require excision of tissue. Complementary imaging modalities, such as fluorescence spectroscopy and microscopy, can be combined with OCT to obtain more information about the tissue while remaining non-destructive and fast. Recent advances in sources, detectors, and GPU-powered processing have enabled real-time three-dimensional OCT imaging *in vivo*. These advances are especially useful in GI imaging due to the large surface area of many GI organs.

Some practical challenges remain in translating OCT to human GI imaging. For example, the tissue must remain within the probe depth of field. In tubular organs with mostly uniform diameter, this could be achieved with a balloon catheter. Alternatively, the reference arm length can be modulated in real-time to adjust the working distance of the probe. Automated scanning is also necessary to produce non-distorted images unless post-processing is used to spatially resample the acquired data. Fortunately, imaging the distal mouse colon can be easily automated using a miniature side-viewing endoscope controlled by motors for helical scanning.

The goal of my research was to develop new technology and methods for early detection of adenoma in the colon. The azoxymethane mouse model of colorectal cancer was used for validation. A commercial swept-source OCT system with sufficiently high A-scan rate for 3D imaging was used. Imaging of the mouse colon required development and integration of a miniature scanning endoscope with this OCT system. I developed software for synchronizing motion of the endoscope to the control signals used to guide scanning in the original imaging probe and for numerically correcting dispersion introduced by the endoscope. I used the Kasai autocorrelation method for functional OCT imaging of the colon, producing the first *in vivo* vascular images of the mouse colon. Finally, by highly sampling the tissue, I produced images of the colonic crypts and compared them to established crypt patterns for studying the development of aberrant crypt foci.

2.1 Integration of a custom endoscope with a commercial OCT system

Over 40 companies currently produce OCT systems for research or medical applications [63]. The growth of the commercial OCT market has enabled researchers to use OCT without the optical, electrical, and mechanical engineering expertise required to design and build their own OCT system. While some of these companies produce probes for *in vivo* imaging, certain applications currently require custom imaging probes. The purpose of this project was to develop and integrate a miniature endoscope for imaging the mouse colon in a helical scanning geometry with the Thorlabs OCS1050SS swept-source OCT system. The work required to integrate the system is generalizable to most commercial OCT systems that do not give the user complete control over data acquisition and processing.

I designed a miniature endoscope with an outer diameter of about 2 mm based on a general design developed in our lab [4]. An optical fiber is connected to a silica spacer for expanding the beam exiting the fiber. Using the GRIN coefficients from GRINTech, I specified the pitch and length of a rod gradient index lens to provide a numerical aperture (NA) of 1.4 to match the NA of the fiber for maximum coupling efficiency of the returning light and a beam focus located 250 µm beyond the surface of the glass envelope that encloses the optics. A rod prism is attached to the distal end of the lens to deviate the light by 98° for imaging through the sides of the endoscope. The optical materials and fiber (Hi-1060, Corning Inc., Corning, NY) were chosen to operate in the 1000 nm to 1080 nm wavelength range of the OCS1050SS source. During imaging, the envelope remains stationary while the optics and the fiber are free to move for scanning the beam.

I developed the rest of the sample-arm architecture to allow the endoscope to scan in a helix, which is the most efficient geometry for a side-viewing endoscope to scan the entire wall of the colon for 3D imaging. A stepper motor motor interfaces with a fiber-optic rotary joint (FORJ) to rotate the endoscope. The FORJ contains a fiber-free region to allow one end of the fiber to rotate freely without twisting and damaging the fiber. The rotary joint and rotational motor are mounted on a linear translation stage that is moved by a linear actuator for moving the endoscope optics through the colon.

Both rotational and linear motors are synchronized to the OCT system using the electronic signal that controls the fast-scanning mirror in the commercial imaging probe. To avoid image distortion, one full rotation of the endoscope occurs during the period of a single sweep of the fast scanning mirror signal. The commercial system scans in a raster pattern and does not collect data during the rapid return sweep of the fast-scanning mirror. Therefore, the endoscope must complete one full rotation and come to a complete stop after each B-scan to prevent shifting of the images from B-scan to B-scan. The period of non-zero acceleration at the beginning and end of each rotation distort the left and right edges of each B-scan due to oversampling. However, with sufficiently high rotational acceleration, the oversampled regions can be limited to less than 5% of the image width. When high sampling (e.g., sampling at the Nyquist limit) is desired, the linear motor continuously move at a slow velocity without noticeably distorting the volumetric image.

Some electronics were necessary for synchronizing the motor drivers to the fast-scanning mirror control signal. I designed an inverting differentiator and rectifier circuit to generate a positive rectangular signal during the period of data acquisition. This signal was input to an Arduino Uno to give the user the ability to output a clean digital signal. Moreover, the user can control the duration of the digital signal or implement additional functionality in the future, if desired.

Due to mismatches in the material dispersion of the new sample arm and the commercial reference arm, the collected images experience significant axial resolution degradation. While this can be easily corrected by introducing a variable-thickness dispersive optic into the arm with less dispersion, neither arm in this system has room; the sample arm is all fiber and the reference arm is very compact. Therefore, I implemented a numerical dispersion compensation algorithm in MATLAB that is applied in post-processing. This algorithm, inspired by a previous method from our lab [4], is computationally simpler than previous techniques reported in the literature [64, 65, 66, 67].

The completed system is the first helical scanning endoscopic OCT system developed in our lab. The resulting published manuscript and specific details of this project are given in Appendix A. This paper attempts to describe a general method of integrating custom sample-arm optics with commercial OCT systems to help researchers make use of OCT for animal imaging without having to design their own OCT system.

2.2 Endoscopic *in vivo* functional OCT imaging of colon vasculature

The Doppler effect changes the frequency of light that is reflected by a moving particle. Doppler OCT algorithms allow for this frequency shift to be estimated, producing images that have contrast in regions of motion. The most common application of Doppler OCT is for imaging blood flow. Estimates of blood flow velocity and turbulence provides functional information to complement the structural information normally provided with OCT. Doppler OCT has been used extensively for imaging the retina, brain, and skin. Because these organs can be imaged with probes outside of the body, the imaging optics can be designed to minimize vibration. These probes also do not typically have moving optical fibers, which avoids issues of time-varying optical path length. Skin and brain can be mechanically stabilized, though the retina typically cannot be kept completely still. Motion compensation and image registration techniques may be necessary to produce high-quality vascular images of the retina.

Using the endoscopic system described in Appendix A, I implemented a Doppler OCT algorithm based on the two-dimensional Kasai autocorrelation [44, 47] to conduct endoscopic vascular imaging in the mouse colon. By greatly oversampling in the lateral direction during scanning, much of the motion artifacts induced by animal breathing and endoscope vibration can be minimized. Through a series of image processing steps, a map identifying blood vessels is generated. This map can be used for measuring vessel count, flow velocity, and vessel density. The method consists of an intensity threshold to remove signal-free regions from future processing, matched filtering using a circular template for extracting vessels in cross-sectional B-scans, and histogram segmentation for discriminating vessels with blood flow from static tissue. This was the first demonstration of Doppler OCT imaging in the colon to the best of my knowledge.

Further details of the image processing steps, the resulting images, and the software are presented in Appendix B. Also included is a manuscript submitted for publication.

2.3 Endoscopic *in vivo* structural OCT imaging of colonic crypts

Aberrant crypt foci (ACF) is thought to be the earliest morphological change in colon tissue prior to development of adenoma. Therefore, this is a potential biomarker for early detection of adenoma and for studying the efficacy of therapies. Narrowband imaging and chromoendoscopy are the prevailing methods of imaging the colon crypts and detecting ACF. While these methods provide high crypt contrast, it is difficult to correlate ACF with adenoma until the adenoma become sufficiently mature and large to see with these surface-imaging modalities. Otherwise, the tissue must be explanted for histopathological analysis to identify adenoma. OCT, on the other hand, can detect small adenoma by measuring thickening of the mucosa and changes in light attenuation with depth.

The OCS1050SS system has a sufficiently fast A-scan rate to spatially sample the colon surface at the Nyquist limit (2 samples per spot radius) necessary for visualizing small crypts of the mouse colon. Sum projections along the depth direction over a thickness of about 200 µm beginning about 50 µm beneath the lumen surface produces *en face* images with crypt contrast. Standard deviation projections over the entire depth of the tissue are also effective and enhancing crypt contrast. Preliminary results show that the crypt patterns in non-diseased tissue and in adenoma match the established crypt patterns identified by Kudo [68].

In Appendix C, I present my current results from a time-serial study imaging colon crypts in AOM- and saline-treated mice and a conference proceedings manuscript.

CHAPTER 3

Future Work

This dissertation describes the development of the instrumentation and software for producing volumetric structural images and Doppler B-scans in the mouse colon. I validated the system for both of these imaging applications and presented pilot data using a small number of mice. Future work in this area can go in many different directions. Among the most promising are:

1. volumetric imaging for highly accurate adenoma characterization,
2. crypt imaging for early adenoma detection, studying progression of the adenoma-adenocarcinoma sequence, and the role of aberrant crypt foci in the sequence, and
3. vascular imaging for early detection of dysplasia and studying microvascular hemodynamics.

The previous work in my lab can be extended through the use of volumetric imaging. Previously, we image the distal 30 mm of the mouse colon at 8–16 discrete angles. This allows for detection of most moderate-to-large adenoma, but estimating the tumor size can be difficult. Using a helical scan geometry with the fast OCS1050SS system produces fully sampled images of the distal colon. Tumor counts and tumor volume can now be measured with much greater precision. Furthermore, adenoma growth can be accurately measured over time because there is no risk of having a small adenoma begin development in a location that is not imaged. This improves our ability to study the natural history of adenoma and the efficacy of chemopreventive and chemotherapeutic agents.

The colonic crypts can be visualized by laterally sampling the colon surface at the Nyquist limit and generating *en face* sum projections. This method may be superior to the current standard crypt imaging modalities, chromoendoscopy and narrowband imaging, because OCT provides information beneath the tissue surface and does not require contrast agents. We have previously combined OCT and chromoendoscopy to study the correlation between aberrant crypt foci (ACF) and adenoma [6]. Now that OCT can be used for crypt imaging, the endoscope design is greatly simplified and surface and depth information are automatically co-localized. OCT can be used to study the relationship of ACF in the adenoma-adenocarcinoma sequence in a mouse model of colorectal cancer. We have previously defined a doubling of the mucosa thickness as a characteristic of adenoma [9]. The additional crypt data may enable earlier detection of adenoma if the crypt pattern noticeably changes prior to significant thickening of the mucosa. The crypt patterns could be used as an additional biomarker for monitoring efficacy of therapies and preventive treatments. Generating easy-to-read crypt images is currently based on trial and error. However, this may be automated in the future by implementing previously developed methods for extracting the crypts as three-dimensional structures [69]. Volumetric crypt images could lead to new, quantitative definitions of the various crypt patterns qualitatively defined by Kudo [68].

The ability to endoscopically image the microvasculature of the colon using Doppler OCT has, in my opinion, the greatest potential for early detection of epithelial dysplasia and was the motivation for my work on Doppler OCT. In the last decade, researchers have discovered that angiogenesis occurs at the beginning of tumorigenesis in the colon [70] and in pre-malignant tumors in other organs [71]. These new vessels are characterized by abnormal structure and function. The vessels are highly tortuous, contain regions of variable vessel diameter and dead ends. The arterioles also lack a uniform layer of smooth muscle. These abnormalities result in irregular blood flow velocity, excessive leakiness, and the inability to modulate flow by dilating or constricting arterioles [71, 72]. High-quality OCT angiography could be used to quantify tortuosity, although using this as a measure for discriminating normal and dysplastic tissue is a difficult problem.

The dysfunction due to the absence of smooth muscle may be an attractive biomarker of dysplasia. One purpose of the smooth muscle is to modulate flow resistance to regulate tissue temperature. For example, arterioles dilate in response to heat to increase blood flow and dissipate excess heat through convection. Hyperthermia studies have discovered that blood perfusion sometimes increases and sometimes decreases in response to heat about 3 °C above body temperature [73, 74]. Four reasons may partially explain these seemingly paradoxical results. First, what smooth muscle that does exist on tumor-originated arterioles still cannot be innervated properly [75]. Second, the tortuous vessel structure reduces flow velocity [76]. Third, the vessels surrounding tumors are normal and respond to heat by dilating. Therefore, if a tumor capillary bed is in parallel with a capillary bed in normal surrounding tissue, an increase of flow in the normal tissue will decrease flow in the tumor due to the decreased flow resistance in the healthy tissue. However, if the two capillary beds are in series, heat will increase flow velocity in the normal tissue and, therefore, the tumor as well [75]. Finally, the number of arterioles with immunoreactivity to vasoactive intestinal polypeptide, a potent vasodilator, is higher in juvenile adenoma and lower in mature adenoma compared to normal tissue [77]. The combined result of these four factors is that the change in blood flow rate in adenoma should be more heterogeneous than in normal tissue.

The heterogeneous response of arterioles in dysplastic tissue to heat or chemical vasodilators makes the vessel function a potential biomarker for detecting dysplasia at the earliest stages of development and may be detectable using Doppler OCT. Absolute flow velocity is difficult to measure with Doppler OCT because the angle of the flow with respect to the OCT beam must be estimated. Fortunately, detecting dysfunctional arterioles requires measuring only the change in flow in response to a vasodilator stimulus. Therefore, dysplastic tissue may be detectable with Doppler OCT by imaging before and after heating the tissue or injecting a vasodilator. One challenge with this method is ensuring that the pre- and post-heating images are co-located. Removing the endoscope to introduce a heating element, for example, will stretch and distort the colon lumen and make co-localization difficult. Another potential hurdle is that it is currently unknown whether the changes in blood flow in normal and dysplastic arterioles are sufficiently different for accurate classification. We also do not know how quickly these changes reach a level of maximum discriminability as most hyperthermia studies involve heating for 30 minutes or longer. For this to be a viable screening modality, the total procedure time must be kept to a minimum and comparable to the duration of a colonoscopy procedure. OCT could be used to image the colon over time to study the temporal response of the microvasculature to vasodilation or vasoconstriction stimuli to improve our knowledge of vascular functional physiology. Because arterioles in dysplastic tissue are dysfunctional regardless of the organ, OCT could potentially be used for detecting dysfunctional microvasculature in any organ that can be imaged with optical methods.

APPENDIX A

A.1 Accepted manuscript: Integrating a custom endoscope

W. A. Welge and J. K. Barton, "Expanding functionality of commercial optical coherence tomography systems by integrating a custom endoscope," *PLOS ONE* **10**(9): e0139396 (2015).

RESEARCH ARTICLE

Expanding Functionality of Commercial Optical Coherence Tomography Systems by Integrating a Custom Endoscope

Weston A. Welge[1]*, **Jennifer K. Barton**[1,2]*

1 College of Optical Sciences, The University of Arizona, Tucson, Arizona, United States of America,
2 Department of Biomedical Engineering, The University of Arizona, Tucson, Arizona, United States of America

* wwelge@email.arizona.edu (WAW); barton@email.arizona.edu (JKB)

Citation: Welge WA, Barton JK (2015) Expanding Functionality of Commercial Optical Coherence Tomography Systems by Integrating a Custom Endoscope. PLoS ONE 10(9): e0139396. doi:10.1371/journal.pone.0139396

Editor: John Green, University Hospital Llandough, UNITED KINGDOM

Received: July 9, 2015

Accepted: September 12, 2015

Published: September 29, 2015

Data Availability Statement: All relevant data are within the paper.

Funding: This research was supported by the National Cancer Institute (cancer.gov) and the National Heart, Lung, and Blood Institute (nhlbi.nih.gov) of the National Institutes of Health under award numbers R01CA109385 (JKB) and T32HL007955 (WAW), respectively, and the American Society for Laser Medicine and Surgery (aslms.org) Student Research Grant (WAW). The content is solely the responsibility of the authors and does not necessarily represent the official views of the National Institutes of Health. The funders had no role in study design, data

Abstract

Optical coherence tomography (OCT) is a useful imaging modality for detecting and monitoring diseases of the gastrointestinal tract and other tubular structures. The non-destructiveness of OCT enables time-serial studies in animal models. While turnkey commercial research OCT systems are plenty, researchers often require custom imaging probes. We describe the integration of a custom endoscope with a commercial swept-source OCT system and generalize this description to any imaging probe and OCT system. A numerical dispersion compensation method is also described. Example images demonstrate that OCT can visualize the mouse colon crypt structure and detect adenoma *in vivo*.

Introduction

Optical coherence tomography (OCT) is a scanning imaging modality that generates cross-sectional images with high lateral and axial resolution (typically < 15 μm) to depths of up to 2 mm. Originally adopted by the ophthalmic community, OCT has also been used to investigate the gastrointestinal tract [1–5]. At least 40 companies currently produce research or clinical OCT systems [6], including clinical endoscope/catheter-based systems for esophageal (Nine-Point Medical) and intravascular (St. Jude Medical) imaging.

Arguably the most challenging and expensive components of an OCT system are the light source and the "engine" responsible for system control, data acquisition, and data processing. Researchers who wish to use OCT may choose to purchase a commercial OCT system that provides the desired imaging speed, axial resolution (lateral resolution is determined by the probe optics), and imaging depth. Few companies produce endoscopic imaging probes for research applications, but several custom probe designs have been published in the literature. Probes can be broadly grouped by their design architecture, such as gradient index lens [7, 8] and fiber [9, 10], traditional lenses [11], ball lens [12], lens generated by melting photonic crystal fiber using the electric arc from a fiber splicer [13], injection of index-matching fluid to improve image quality [14], and lens-free [15]. The best choice of probe architecture (including

collection and analysis, decision to publish, or preparation of the manuscript.

Competing Interests: The authors have declared that no competing interests exist.

diameter, flexibility, scanning method, and optical characteristics) depends on the application, thus more variation in probe design is needed than in OCT engine configuration. Compared to the light source and engine, probes are typically easier and less expensive to construct.

This article describes the integration of a lab-built gradient index lens-based endoscope [16] with a commercial swept-source OCT system (OCS1050SS, Thorlabs, Newton, NJ, USA), which has a central wavelength of 1040 nm and spectral bandwidth of 80 nm. The overall system diagram is shown in Fig 1. The swept-source laser in this system produces an axial resolution of 12 μm in air, and the A-scan rate of the system is 16 kHz. The OCT system has an imaging range of 2.0 mm, A/D sample rate of 100 MS/s, and a 3 dB rolloff of 0.47 mm. The system generates fringe data linearly in wavenumber. This central wavelength provides a compromise of resolution and penetration depth in highly scattering tissue. Furthermore, this wavelength is useful for ophthalmic imaging due to fairly low water absorption. The bandwidth and A-scan rate are sufficient for video-rate imaging at good axial resolution. The choice of light source impacts the performance of the OCT system in several ways that are described below.

The details in this article, however, can be generalized to the integration of any custom imaging probe to any commercial OCT system that provides a connection to the sample arm optics and access to scan synchronization signals. When the user is unable to directly control the data acquisition and OCT control software, the system is best viewed as a black box. In other words, the sample arm optics and scanning motion must be designed around the constraints imposed by the OCT system.

Examples of such constraints are the imaging speed, data acquisition scheme, and optical materials. The A-scan rate is generally constant, but the B-scan rate may be variable. If the OCT system allows the user to adjust the physical scan length and/or sampling density, then the total time to acquire a single B-scan will change. The B-scan acquisition time constrains the custom sample arm scan length, velocity, and sampling density.

The data acquisition scheme encompasses the scanning geometry and any computational overhead involved in recording and processing data. For a raster scanning system, data are likely only acquired during one sweep direction of the fast scan axis. If there are brief time periods of no data acquisition between each subsequent B-scan, this constrains or complicates scanning geometries for the custom sample arm. On the other hand, if the commercial system acquires data by scanning the beam in a spiral, then data may be acquired constantly. This provides greater freedom for designing the new sample arm scanning geometry, but the images generated by the system would be distorted if the new sample arm scans in a non-spiral geometry. In general, whenever the scanning geometry changes, the image processing by the OCT system will generate distorted images. To properly display the images, the user must process the image data themselves.

Finally, the optical materials used in the system, such as fibers and lenses, may not be known to the user. This poses two problems. The first is matching the optical path length of the new sample arm to the commercial arm in order to generate OCT images. Building the custom endoscopic sample arm with a matching optical path length may require measuring the physical length of one of the commercial arms (sample arm would most often be easiest) and multiplying by the refractive indices of an appropriate fiber and lenses for the source spectrum. Designing the sample arm with the necessary optical path length may require trial and error. The second problem is dispersion. The broad bandwidth sources used by high-resolution OCT systems are particularly susceptible to the effects of dispersion mismatches between the sample and reference arms. The simplest way to mitigate dispersion is to ensure that the amount of dispersive materials are equal in the sample and reference arms. However, if the reference arm specifications are not completely known, it may be difficult to avoid mismatching the dispersion in the sample arm. A variable-thickness prism pair may be placed in an air gap in the

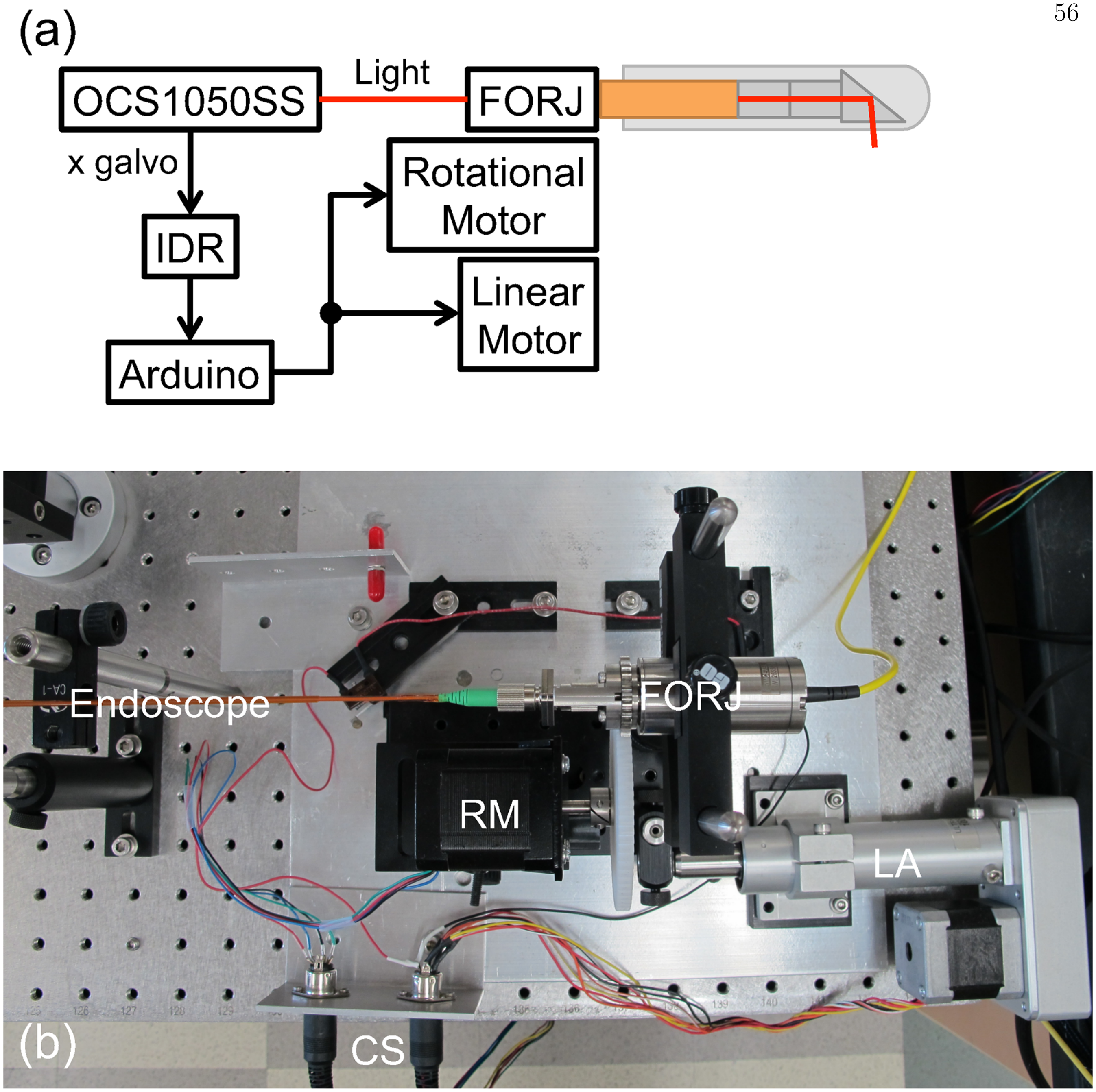

Fig 1. System diagram. (a) Thorlabs OCS1050SS swept-source OCT system is treated as a black box. The fiber optic rotary joint (FORJ) is connected to the OCS1050SS light source via a fiber optic patch cable. The electronic *x*-galvanometer scanner control signal from the OCS1050SS is connected to a custom inverting differentiator and rectifier (IDR) circuit that converts the sawtooth input wave to a square wave with a high signal during the period of data acquisition along the fast *x*-axis of the raster scan pattern. The IDR output is connected to an Arduino Uno that detects the rising edge and outputs a short digital pulse to signal the motor drivers to begin movement of the rotational and linear motors. The endoscope is connected directly to the FORJ. The rotational motor is connected to the FORJ through meshed gears. The rotational motor, FORJ, and endoscope are mounted on a linear translation stage that is controlled by the linear motor. The fast rotational motion and slow linear motion result in a helical scanning geometry. (b) A photograph of the sample arm, including the motors and translation stage. The rotational motor (RM) spins the fiber optic rotary joint (FORJ) and both are mounted on a linear translation stage that is moved by the linear actuator (LA). Motor drivers send control signals (CS) to the control the motors.

doi:10.1371/journal.pone.0139396.g001

sample arm or reference arm if room is available. The thickness can be adjusted through trial and error until axial-resolution degradation is minimized. However, there may not be space available to physically correct for mismatched dispersion and complete compensation is unlikely. If this is the case, numerical dispersion compensation methods can be applied to fix the axial blurring in post-processing. These methods require access to the raw fringe data.

We describe our method of integrating an endoscope with the OCS1050SS system as a specific example. Integration details are provided below in three parts: the sample arm optics, scanning synchronization, and numerical dispersion compensation. Highly sampled images of normal and adenomatous mouse colon are provided in the Results section. These images demonstrate how a system designed for microscope stage imaging can be modified to accommodate an endoscope capable of resolving colonic crypts and enable the measurement of adenoma size and tumor burden.

Materials and Methods

Light source

The light source affects OCT performance in many ways and the ideal light source will depend on the particular application. In OCT, the axial and lateral resolutions are decoupled (the lateral resolution depends on the imaging probe optics). If the source spectrum is approximately Gaussian, then the axial resolution Δz in a medium characterized by refractive index n depends on the central wavelength λ_0 and the bandwidth $\Delta\lambda$ according to

$$\Delta z = \frac{2\ln(2)}{\pi n}\frac{\lambda_0^2}{\Delta\lambda}. \tag{1}$$

The result of this computation is sometimes referred to as the coherence length of the source. For a broadband source that simultaneously emits at all wavelengths within its bandwidths (e.g., superluminescent diode), the coherence length and the axial resolution are the same. However, the coherence length of swept-source lasers—which have narrow bandwidths at each instance in time, but sweep over a large bandwidth—is often specified as the instantaneous coherence length and is therefore much larger than the axial resolution. Nevertheless, Eq (1) can still be used to compute the theoretical axial resolution of a swept-source laser for OCT.

The penetration depth of OCT is limited by light scattering and absorption, both of which depend on wavelength. Absorption by chromophores present in biological tissue (primarily oxyhemoglobin, deoxyhemoglobin, and water) varies greatly with wavelength, but is relatively low in the region of 600 nm to 1300 nm, where the absorption coefficient μ_a is approximately 0.1mm^{-1} to 1.0mm^{-1}. Scattering monotonically decreases with increasing wavelength and dominates in this spectral region with reduced scattering coefficient μ_s' approximately 10mm^{-1}

Table 1. Comparison of Estimated Penetration Depth and Axial Resolution in Colon Tissue for Four Common OCT Wavelengths.

λ_0 (nm)	δ (mm)	Δz (μm)
850	2.04	2.28
1050	2.65	3.48
1310	3.48	5.41
1550	4.29	7.57

λ_0, central wavelength; δ, estimated penetration depth; Δz, axial resolution in tissue with index of refraction 1.4 and assuming a constant bandwidth of 100 nm.

doi:10.1371/journal.pone.0139396.t001

to 100mm^{-1} [17]. When $\mu_s' \gg \mu_a$, the diffusion approximation can be used to accurately estimate the penetration depth. The penetration depth is defined as the distance by which the light intensity drops to $1/e$ of the incident intensity and is defined as

$$\delta = \frac{1}{\sqrt{3\mu_a(\mu_a + \mu_s')}}. \tag{2}$$

Common commercial swept-source lasers for OCT applications have central wavelengths at or near 850, 1050, 1310, 1550nm [18]. Table 1 shows a comparison of penetration depth and axial resolution at these wavelengths. Reduced scattering coefficient can be estimated as

$$\mu_s' = a\left(\frac{\lambda}{500}\right)^{-b}, \tag{3}$$

where λ is the central wavelength in nanometers, a is the value of μ_s' at λ = 500nm, and b is the scattering power [19]. Experimental values for a and b in bowel tissue are 1.65mm^{-1} and 1.240, respectively [19]. The absorption spectrum is not so easy to estimate at arbitrary wavelengths and the literature is sparse in describing tissue absorption at wavelengths longer than 1000mm. We approximate $\mu_a \approx 0.1\mu_s'$ in the calculations for δ in Table 1. The axial resolution assumes a spectral bandwidth of 100nm.

Water is a particularly important absorber in biological tissue. Most tissue has a higher concentration of water than of other significant absorbers. At wavelengths shorter than 1100 nm, both oxygenated and deoxygenated blood have higher absorption coefficients than water, but water dominates at higher wavelengths [19]. Water absorption has a local minimum near 1050 nm, making that wavelength an attractive choice for imaging through the eye.

The best choice of light source wavelength depends on the application. Generally, in highly scattering tissues there exists a tradeoff between imaging depth and axial resolution given limited choice of source bandwidths. Other considerations include that standard optical fibers exhibit zero dispersion at 1310 nm, which may simplify dispersion correction, and the broad availability of fiber optical components optimized for 1310 nm and 1550 nm. For our application, the satisfactory penetration depth and high resolution available at 1050 nm led to the choice of this wavelength source.

Sample arm optics

The sample arm replaced the tabletop microscope setup standard with the Thorlabs OCT system. The design was previously reported [16], and an overview is given here. The Zemax (Zemax, Kirkland, WA, USA) optical design and spot diagram are shown in Fig 2. The new optics are connected to the fiber optic output connector on the OCT instrument. The optics consist of a fiber optic patch cable, fiber optic rotary joint (FORJ), and a 2mm-diameter, side-viewing endoscope in a commonly used configuration [7]. The endoscope consists of a single-mode optical fiber (HI 1060, Corning, Corning, NY, USA) cemented to a BK7 glass spacer, followed by a gradient-index lens (0.14 pitch, 0.5 lens NA, Grintech, GmbH, Jena, Germany) and a 41° rod prism (Photop Technologies, Sunnyvale, CA, USA), all encapsulated with a glass cylindrical window (custom, University of Arizona Glass Shop) attached to a polyimide tube (MicroLumen, Oldsmar, FL, USA). The length of the spacer (1.97mm) and the pitch of the gradient-index lens were chosen to achieve a numerical aperture (NA) to match the NA of the fiber at 0.14. The endoscope provides a lateral resolution of 6 μm, with the focus of the beam located approximately 250 μm outside the window. The total length of the endoscope is 295 mm. The FORJ (Princetel, Hamilton, NJ, USA) enables free rotation of the endoscope. The length of the fiber optic patch cable was chosen so that the optical path length of the custom probe was the same as

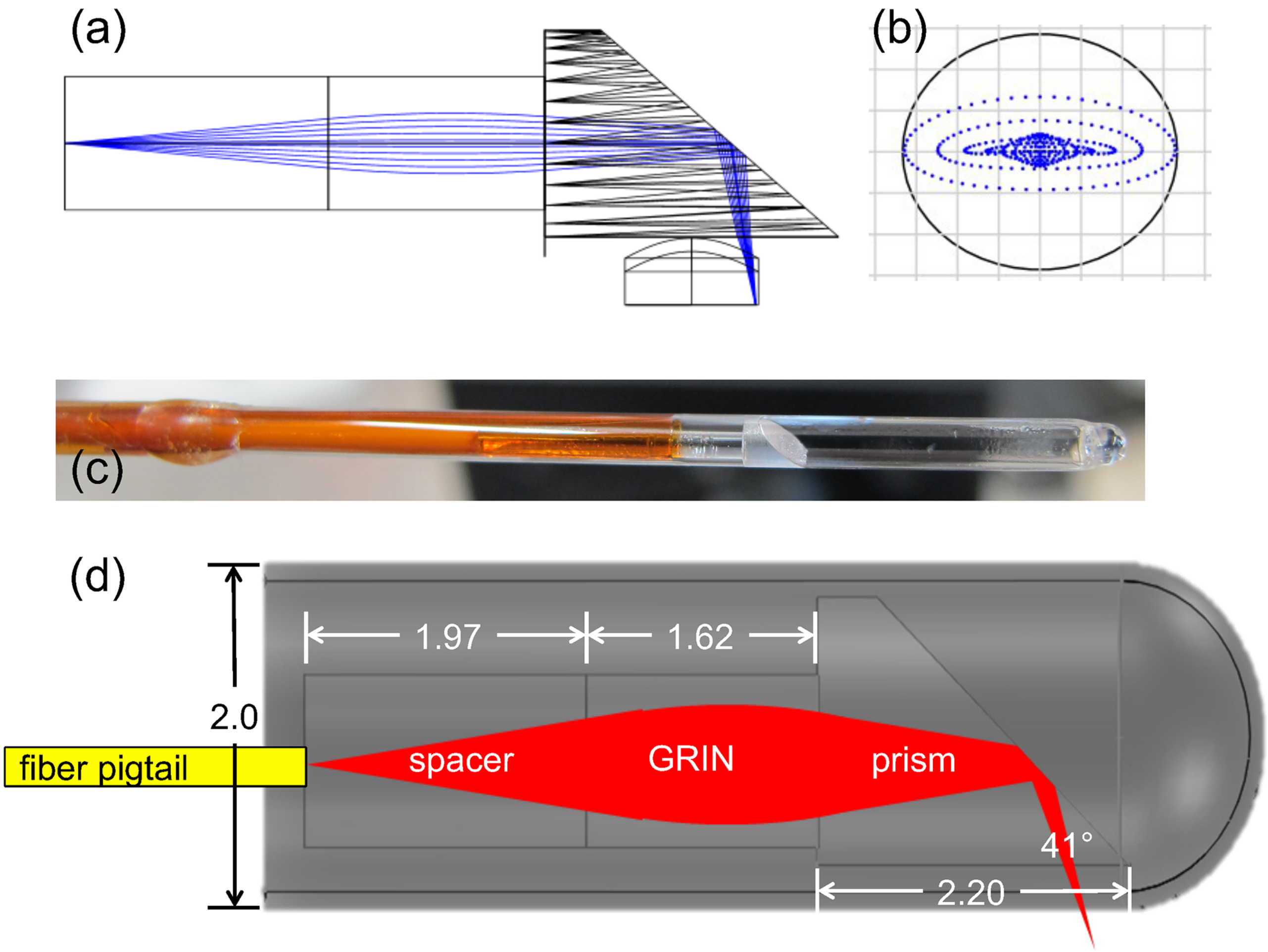

Fig 2. Endoscope. (a) Optical layout showing rays traced through the glass spacer, gradient-index lens, 41° prism, glass window, and tissue. (b) Spot diagram at beam focus. The cylindrical glass window induces astigmatism, but the traced spot is still smaller than the diffraction limited spot radius of 6.14 μm (denoted by the black circle). (c) Photograph of the distal portion of the endoscope. (d) Diagram showing dimensions in mm. Both the spacer and GRIN lens have a diameter of 1.0 mm. The prism is cylindrical with a rectangular exit face. The radius of the circular entrance face is 0.85mm with the square exit face cut a distance of 0.7mm from the center of the circular entrance face. The wall thickness of the glass envelope is 100 μ and a length of about 35 mm. The GRIN lens is characterized by a numerical aperture of 0.5 and a pitch of 1.4.

doi:10.1371/journal.pone.0139396.g002

the original sample arm (and thus would match the OCT system reference arm length). The OCS1050SS reference arm length can be adjusted by about 2 cm. The desired length of the new sample arm was estimated by measuring the physical length of the commercial probe fiber and estimating the path through the probe. Starting from this estimate and the known optical path lengths through the FORJ and endoscope, the correct patch cable length was determined through trial and error. An image will be generated with the OCT system once the optical path length of the sample arm and reference arm match within the coherence length of the source.

The endoscope collects data in a helical scanning geometry using a fast rotational stepper motor (Lin Engineering, Morgan Hill, CA, USA) and a slow linear actuator (Ultra Motion, Cutchogue, NY, USA), each controlled by a motor driver (3540i, Applied Motion Products, Watsonville, CA, USA). The beam always passes through the cylindrical glass window during data collection. The window and polyimide sheath are held stationary while the internal optics move independently. A spur gear attached to the rotational stepper motor meshes with the gear teeth on the FORJ for rotational motion. The FORJ, rotational motor, and internal endoscope optics are all mounted on a linear translation stage connected to the linear actuator for longitudinal motion. A popular alternative that avoids the use of a FORJ is to attach the prism to a rotational micromotor at the distal tip of the endoscope [20]. A downside of this approach is that the micromotor wires inherently obstruct part of the field of view. Another design scans using a piezoelectric transducer [21], which is relatively complex, but could be made side-viewing by placing a cone mirror at the distal tip of the endoscope.

Scanning synchronization

The scanning motion of the sample arm can be synchronized to the commercial OCT scanning signals to avoid changing the data acquisition rate and image processing. In this way, the sample arm appears "unchanged" from the perspective of the OCT system. Many commercial systems steer the imaging beam in the sample arm with a scanning x-y galvanometer mirror system. The OCS1050SS sample arm uses a raster scan pattern. Thus to synchronize the new helically scanning endoscope, the rotational motor was synchronized to the fast x-axis of the galvanometer system such that one full rotation corresponded to the period of data acquisition of one sweep of the original x-galvanometer mirror.

The speed of the linear motor controls the pitch of the helix. If this linear motion is slow, the endoscope linear motor can move continuously without significant image distortion, thus restricting the burden of synchronization to the rotational motion. Therefore, the slow y-galvanometer signal was not used. Linear motion speed and time were empirically adjusted such that the motor moved the desired distance within the total 3D image acquisition time of the OCT instrument.

There may be a difference between the signal waveform type and amplitude generated by the commercial OCT system (an analog ± 10V sawtooth in our case), and that needed by the endoscope motor drivers (a digital TTL signal). If so, additional electronics will be needed to synchronize the motors and OCT control signals. We used an analog inverting differentiator and rectifier circuit and a microcontroller (Arduino Uno) to generate a short, 5V digital pulse signal immediately after the x-galvanometer control signal indicated the beginning of a sweep (by beginning a ramp from 10V to −10V). The inverting differentiator and rectifier circuit schematic is shown in Fig 3. The inverting differentiator output is given by

$$v_{\mathrm{out}}(t) = -RC\frac{dv_{\mathrm{in}}(t)}{dt}, \tag{4}$$

where $R = 2\ \mathrm{M}\Omega$, $C = 20\ \mathrm{nF}$, $v_{\mathrm{in}}(t) = V_{\mathrm{galvo}}$, and $v_{\mathrm{out}}(t)$ is the output of the LT1097 operational amplifier. The rectifier holds any negative output voltage from the inverting differentiator at 0V. The gain and rectifier ensure that the circuit output range is within the 0V to 5V range supported by the Arduino input/output pins.

The Arduino was programmed to output a 25 ms digital pulse upon detecting a rising edge from the inverting differentiator and rectifier circuit. Fig 4 shows an oscilloscope trace showing the g-galvanometer signal, inverting differentiator and rectifier output, and Arduino output. The inverting differentiator and rectifier output was connected to an external interrupt pin on the Arduino. A rising-edge triggers an interrupt service routine that simply sets an output pin to 5V, which is connected to the input of the motor drivers. By inspection of the generated assembly code, the total delay between the triggering of the interrupt and setting the output pin high was 4 μs. The duration of each rotation (B-scan) was about 140 ms, so this delay results in a loss of 0.002% of data. This is minor in our case, but the error increases with high B-scan rates. As such, the delay introduced by any control electronics should be carefully checked to ensure that it does not result in a significant loss of data.

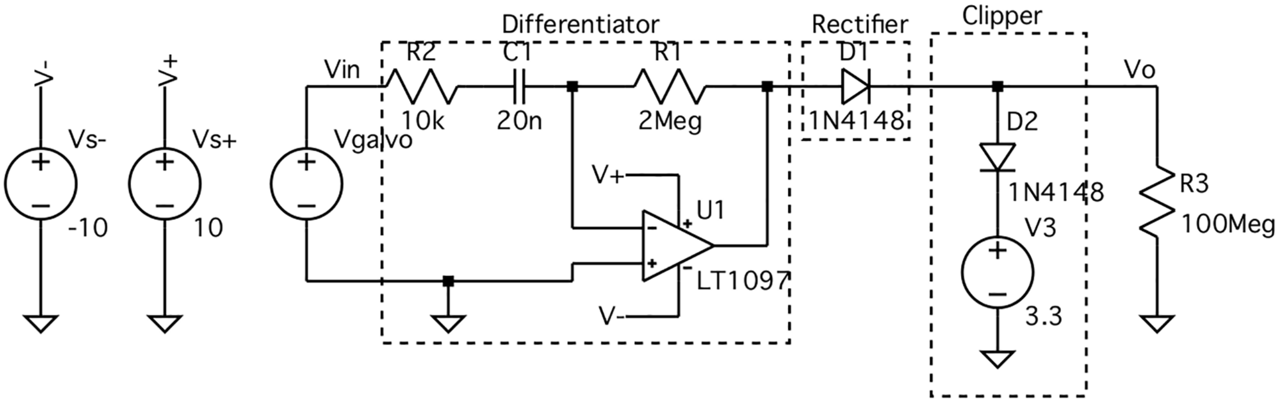

Fig 3. Inverting differentiator and rectifier circuit schematic. This circuit converts the *x*-galvanometer waveform (V_{galvo}) from a sawtooth wave with a peak-to-peak voltage of ±10V to a square wave that is 4V during the slow sweep of the *x*-galvanometer mirror and 0V otherwise. The V_{galvo} waveform is characterized by three parts. Data are acquired during the low-magnitude negative slope portion of the wave. The rapid return of the *x*-galvanometer mirror occurs during the high-magnitude positive slope portion. In between these two sweeps, the raw OCT fringe data is saved to the PC and the V_{galvo} waveform is kept constant (zero slope). The purpose of this circuit is to detect the beginning of the negative slope portion of the waveform and communicate this to an Arduino Uno, which can safely read input voltages from 0V to 5V. Resistor R2 attenuates high-frequency ringing in the Differentiator. The Rectifier diode holds the negative portion of the Differentiator output at 0V. The optional Clipper prevents the output V_o from exceeding 4.3V (the sum of the bias voltage V3 and the forward voltage drop of D2). The input impedance of the Arduino I/O pins is represented by R3.

doi:10.1371/journal.pone.0139396.g003

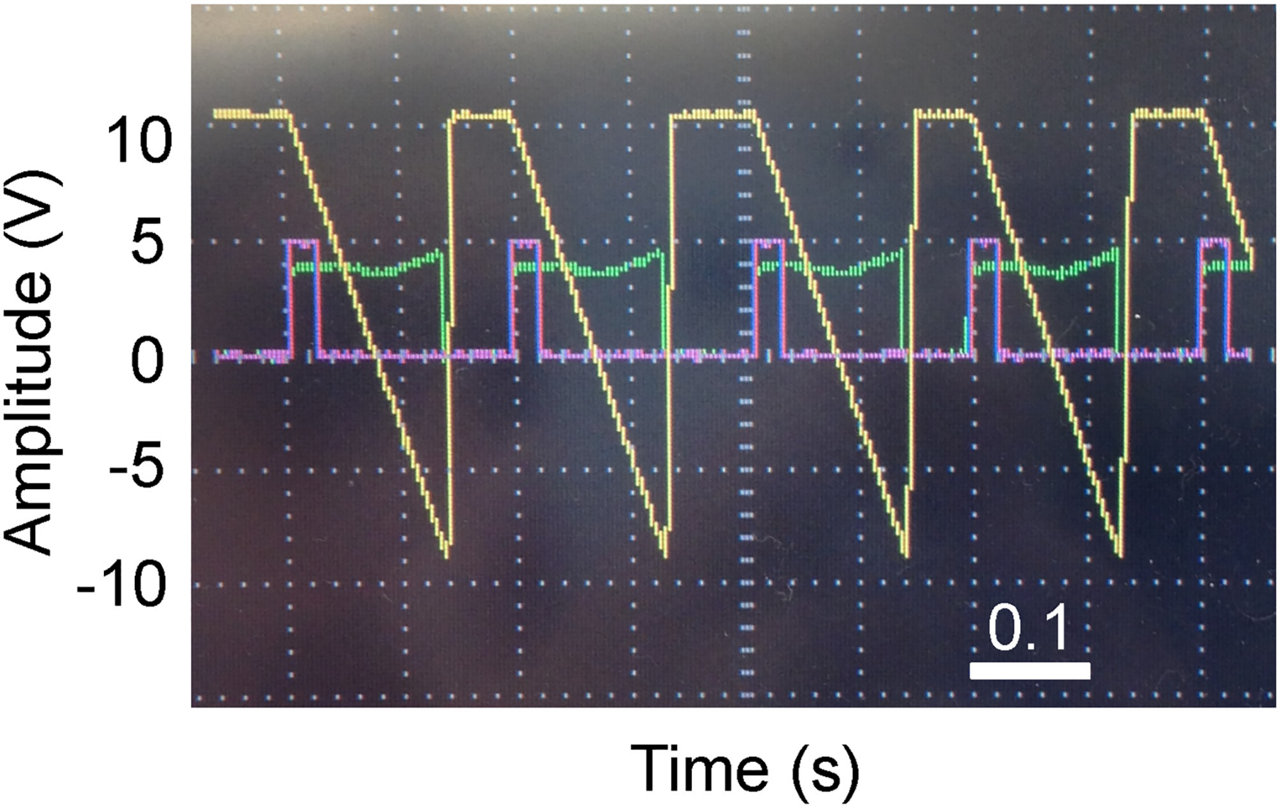

Fig 4. Oscilloscope traces of motor control signals. A few cycles of the electronic signals used in motor synchronization are displayed. The *x*-galvanometer control signal is yellow, the output of the inverting differentiator and rectifier circuit is green, and the Arduino output that serves as the digital pulse to trigger the motors is purple.

doi:10.1371/journal.pone.0139396.g004

In addition to motion synchronization, the velocity and acceleration of the motors controlling the endoscope can be chosen to minimize image distortion and produce the desired sampling density. In a raster scan, data are not collected during the rapid return sweep of the fast x-axis. Therefore, each B-scan will be aligned with respect to one another when the rotational motion of the endoscope comes to a complete stop after each rotation. The angles during which the endoscope experiences rotational acceleration and deceleration will be oversampled. This distortion can be fixed by resampling the data if information about the position or instantaneous rotational velocity are known. This information can be collected using, for example, a closed-loop encoder or Hall effect sensor with the rotational motor. Care must be taken that the entire 360° scan is accomplished within one x-axis data acquisition sweep (B-scan). In the OCS1050SS system, as in most swept-source OCT systems, the A-scan rate is constant. The lateral sampling density is therefore determined by the rotational velocity.

For very fast systems, starting and stopping the rotational motion for each B-scan may be unfeasible. An alternate rotational scanning method would be to continuously rotate the endoscope at a constant rotational velocity. Each B-scan would be rotationally misaligned from one another based on the time duration where data are not collected between B-scans. If this time is constant, then a constant circular shift can be applied to the raw fringe data to align the B-scans. If this time varies, as was the case with the OCS1050SS, then each B-scan could be aligned after determining the rotational offset by measuring the rotational orientation of the endoscope with a Hall effect sensor or by computing the maximum correlation of adjacent B-scans.

Numerical dispersion compensation

Dispersion is a phenomenon by which the speed of light in a medium depends on the wavelength. If the total group index of all media in the sample and reference arms mismatch, the axial resolution will be degraded. Dispersion is often corrected physically by matching media in the sample and reference arms, and/or by placing compensating optics such as a variable-thickness prism pair in the optical path of one of the arms. Complete physical compensation may be impossible due to space and access constraints of commercial systems. In such cases, numerical dispersion compensation methods can be applied to correct axial resolution degradation.

Several methods exist for numerical dispersion correction in OCT [22–25]. The simple method below, adapted from [26], requires that the fringe data be uniformly sampled by wavenumber prior to correction. This method is computationally simpler than the methods described in [22–25], but is only appropriate for samples that introduce minimal dispersion (i.e. this method is appropriate for correcting dispersion introduced by the OCT system). The measured fringe signal in frequency-domain OCT contains two DC terms corresponding to the reflectance of the sample and reference mirror plus a modulation term that is proportional to

$$\cos(k(\omega)z + \phi_{disp}(k)) = \mathrm{Re}\left\{\exp[i(k(\omega)z + \phi_{\mathrm{disp}}(k)])\right\}, \tag{5}$$

where $k(\omega) = \omega n(\omega)/c$ is the wavenumber as a function of angular frequency ω, z is the depth in the sample measured relative to the location of zero optical path difference, and $\phi_{\mathrm{disp}}(k)$ is the phase due to dispersion as a function of wavenumber. Recognizing that, in the absence of dispersion, the modulation frequency is linearly proportional to the optical path difference ($k(\omega)z = \omega OPD(\omega)/c$), a line is fit to the measured phase as a function of k and subtracted from the phase, effectively isolating $\phi_{\mathrm{disp}}(k)$, which is nonlinear.

Algorithm 1. Numerical dispersion compensation.

Require: $f_{k,i}^{(\mathrm{M})}$ is the fringe data corresponding to the *k*th pixel of the *i*th A-scan taken from a mirror. Each mirror A-scan is collected at the same position. $f_{k,i}^{(\mathrm{S})}$ is the fringe data from the tissue sample. All fringes are linearly sampled by wavenumber *k*.

```
function DispersionCompensation ($f_{k,i}^{(\mathrm{M})}$,$f_{k,i}^{(\mathrm{S})}$)
  $\bar{f}_k^{(\mathrm{M})} \leftarrow \frac{1}{N}\sum_{i=1}^{N} f_{k,i}^{(\mathrm{M})}$    ▷ $\bar{f}_k^{(M)} \propto cos(k \cdot OPD + \phi_{disp}(k))$
  for $i = 1$ to $N$ do    ▷ Spectral subtraction
    $f'^{(\mathrm{M})}_{k,i} \leftarrow f^{(\mathrm{M})}_{k,i} - \bar{f}^{(\mathrm{M})}_k$
  end for
  $\tilde{f}^{(\mathrm{M})}_{k,i} \leftarrow f'^{(\mathrm{M})}_{k,i} + i\mathcal{H}\left\{f'^{(\mathrm{M})}_{k,i}\right\}$    ▷ $\tilde{f}^{(\mathrm{M})}_{k,i}$ is the analytic representation of $f'^{(\mathrm{M})}_{k,i}$
  $\phi^{(\mathrm{M})}_{k,i} \leftarrow arg\left\{\tilde{f}^{(\mathrm{M})}_{k,i}\right\}$
  $\bar{\phi}^{(\mathrm{M})}_k \leftarrow \frac{1}{N}\sum_{i=1}^{N} \phi^{(\mathrm{M})}_{k,i}$
  Compute robust linear regression of $\phi^{(\mathrm{M})}_k$, returning coefficients $\beta$ (slope) and $\alpha$ (intercept).
  for $k = 1$ to $K$ do    ▷ Isolate phase due to dispersion
    $\phi^{(\mathrm{disp})}_k \leftarrow \bar{\phi}^{(\mathrm{M})}_k - \beta k - \alpha$
  end for
  $\bar{f}^{(\mathrm{S})}_k \leftarrow \frac{1}{N}\sum_{i=1}^{N} f^{(\mathrm{S})}_{k,i}$    ▷ Estimate source spectrum
  for $i = 1$ to $N$ do
    for $k = 1$ to $K$ do
      $f^{(\mathrm{S})}_{k,i} \leftarrow f^{(\mathrm{S})}_{k,i} - \bar{f}^{(\mathrm{S})}_k$    ▷ Subtract spectrum
      $\hat{f}^{(\mathrm{S})}_{k,i} \leftarrow f^{(\mathrm{S})}_{k,i} \cdot exp\left(-i\phi^{(\mathrm{disp})}_k\right)$    ▷ Remove dispersion
    end for
  end for
  return $\hat{f}^{(\mathrm{S})}_{k,i}$    ▷ Dispersion-corrected sample fringe data
end function
```

doi:10.1371/journal.pone.0139396.t002

The method we used in practice is described in Alg. 1. The system dispersion was determined from a sequence of 2000 A-scans collected at the same location on a mirror. The raw fringes were averaged together to obtain a smooth fringe measurement. The instantaneous phase (the argument of the modulation term) was extracted by taking the angle of the Hilbert transform of the averaged fringe signal. A linear fit was computed using iteratively reweighted least squares with bisquare weighting (`robustfit` function in MATLAB (2014a, Mathworks, Natick, MA, USA)). The system dispersion $\phi_{\mathrm{disp}}(k)$ is the difference of the instantaneous phase and the linear fit. DC signal removal was performed on sample images by subtracting the source spectrum from the sample fringes. The spectrum was estimated by averaging all fringes in a B-scan. Finally, the degradation due to dispersion was corrected by multiplying the sample fringe data after DC removal by $\exp(-i\phi_{\mathrm{disp}})$. Because the swept source in the OCS1050SS has asymmetric forward and reverse sweep spectra, the entire dispersion compensation algorithm was applied independently to the fringes corresponding to the even and odd A-scans.

Mouse colon imaging

The integrated endoscope was used to image the distal 15mm of colon of a mouse model of colorectal cancer. A/J mice (The Jackson Laboratory, Bar Harbor, ME, USA) were administered the carcinogen azoxymethane (AOM, Sigma-Aldrich, St. Louis, MO, USA) in the cancer group and saline in the control group. Cancer mice were administered 10mg/kg of AOM subcutaneously weekly for five weeks to induce development of colon adenoma, in accordance with a protocol approved by The University of Arizona Institutional Animal Care and Use Committee. Control mice were administered 0.2mL of saline subcutaneously at the same rate. Mice were anesthetized for imaging with intraperitoneal injection of 100mL/kg ketamine and 10mL/kg xylazine. Both mice weighed 20g. Lubrication was applied to the endoscope glass envelope and anus prior to insertion. The endoscope was inserted 30mm into the mouse. Mice were placed on heating pads during imaging to maintain normal body temperature. The mice were not mechanically immobilized during imaging. No maintenance anesthesia was required. The mice recovered after imaging and were monitored for signs of pain or distress.

The 3D OCT volumes consisted of 2400 B-scans and each B-scan consisted of 2000 A-scans. With an A-scan rate of 16 khZ, the B-scan frame rate for 2000 A-scans per B-scan would be 8 frames per second, however the actual frame rate varies due to the variable time for the PC to save the fringe data to disc and is closer to 7.5 frames per second. The rotational velocity of the motor was 2.5rev/s. With a gear ratio of 0.347 linking the rotational motor to the FORJ, this rotational velocity corresponds to an endoscopic rotational velocity of 0.87rev/s. The circumference of the tissue in contact with the glass envelope was about 6.3 mm. At 2000 A-scans samples per B-scan, the lateral sample separation was 3.1 μm. This is approximately half the focused beam radius, therefore the lateral direction is approximately Nyquist sampled. The endoscope moved linearly constantly at a velocity of 41 μm/s. At this speed, imaging of the distal 15mm of the colon took about 6 minutes per mouse. At 2400 B-scans per volume, the sample separation in the longitudinal direction (pitch of the helix) was 6.3 μm, which corresponds to a sampling rate about half the Nyquist criterion.

The adenoma in the AOM-treated mouse were identified by visual inspection of the OCT B-scans using criteria defined by Hariri et al. [4]. These criteria include localized thickening of the mucosa and greater signal attenuation with depth compared to surrounding regions.

Results and Discussion

We present example OCT images of the distal 15mm of colon for a control mouse (Fig 5) and an AOM mouse (Fig 6). The distortion at the left and right sides of the images are due to oversampling from the acceleration and deceleration of the rotational motor. Both cross-sectional images (Figs 5a and 6a) demonstrate that the system can resolve the epithelium, colonic mucosa, submucosa, muscularis propria, and some tissue beyond the colon wall. The adenoma in Fig 6a appears as a bulbous mass that protrudes from the colonic mucosa.

The *en face* standard-deviation projections in Figs 5b and 6b reveal the colonic crypts (enlarged views in Figs 5c and 6c). The crypts in the healthy mouse are characterized by mostly uniform density and size. By contrast, the crypts on the adenoma in the AOM-treated mouse are elongated and irregular. These results are similar to those previously reported by our group using chromoendoscopy on the same mouse model of colon cancer [27]. Previous endoscopic OCT systems that provided only two-dimensional data visualized murine colonic crypts only intermittently and required ultrahigh resolution [11]. Colonic crypts have been visualized in the larger rabbit using an ultrahigh-resolution light source (200nm bandwidth) [28] or a high-speed (100 kHz) swept-source laser [29]. The projections in Figs 5b and 6b demonstrate that colonic crypts in a mouse colon can be visualized with a relatively simple endoscope and moderately fast commercial swept-source laser system.

Some artifacts are present in the *en face* standard-deviation projections. Respiratory motion and peristalsis of the colon cause axial motion of the tissue. This can cause variability in the

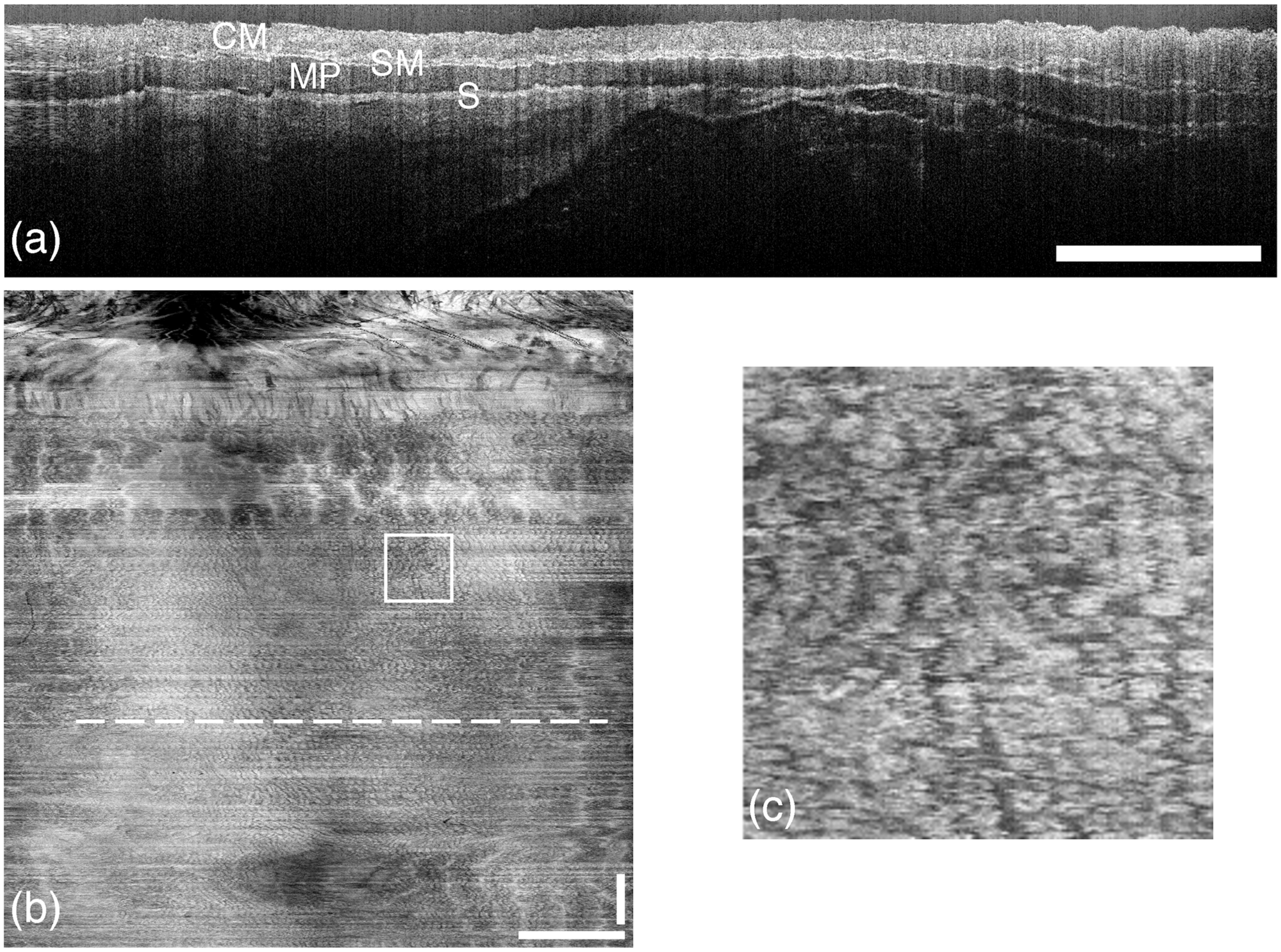

Fig 5. OCT images of saline-treated mouse colon. (a) Cross-sectional image (B-scan) showing high contrast between the many layers of the colon wall (labelled are colonic mucosa (CM), submucosa (SM), muscularis propria (MP), and serosa (S)). The horizontal axis is circumferential and the vertical axis is depth. (b) *En face* standard-deviation projection of the colon with the anus located at the top. The crypt structure can be seen throughout. (c) Enlarged region denoted by the square inset in (b) showing the crypts. The colon circumference (horizontal axis in (a) and (b)) is 6.3mm and the length (vertical axis in (b)) is 15 mm. The horizontal dashed line in (b) indicates the location of the B-scan displayed in (a). All scale bars are 1mm.

doi:10.1371/journal.pone.0139396.g005

overall brightness of a B-scan due to roll off (when the tissue moves away from the endoscope) or reduced contrast due to Doppler shifts.

Compared to our previously reported interim results [16], the images presented here are of higher quality. While the optical design of the endoscope is identical, we corrected some flaws in the construction of the new endoscope by improving the alignment of the optics and reducing the amount of optical glue used cement the components. This improved the power throughput of the endoscope. The axial resolution was also improved through the use of numerical dispersion compensation. The circuit was also redesigned to be more robust and to trigger faster.

Some evidence suggests that aberrant crypt foci may precede dysplasia [30]. Magnifying chromoendoscopy using methylene blue as a contrast agent is the most common method of imaging aberrant crypt foci [31]. The results reported here suggest that OCT may be an attractive contrast-agent-free alternative to chromoendoscopy to investigate the relationship between aberrant crypt foci and cancer development.

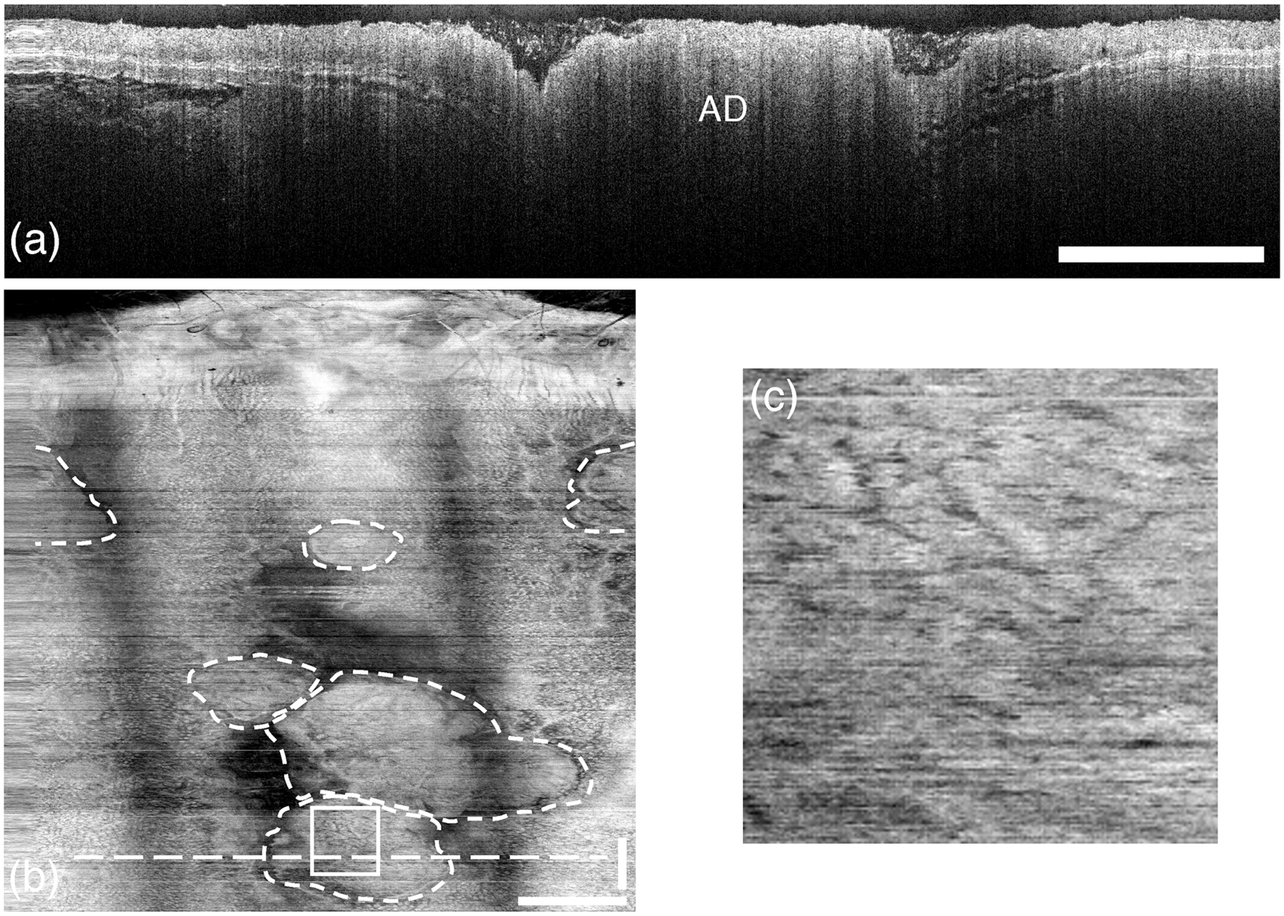

Fig 6. OCT images of AOM-treated mouse colon. (a) Cross-sectional image (B-scan) showing adenoma (AD), characterized by rapid attenuation and loss of tissue boundary visibility. The horizontal axis is circumferential and the vertical axis is depth. (b) *En face* standard-deviation projection of the colon with the anus located at the top. Adenoma are bounded by dashed curves. Crypt structure can also be visualized. (c) Enlarged region denoted by the square inset in (b) showing crypts. Notice the non-uniform crypt density and crypt elongation compared to Fig 5c. The colon circumference (horizontal axis in (a) and (b)) is 6.3mm and the length (vertical axis in (b)) is 15 mm. The horizontal dashed line in (b) indicates the location of the B-scan displayed in (a). All scale bars are 1mm.

doi:10.1371/journal.pone.0139396.g006

Acknowledgments

We thank Photini Faith Rice for her assistance with drug treatment and animal imaging.

Author Contributions

Conceived and designed the experiments: WAW JKB. Performed the experiments: WAW. Analyzed the data: WAW. Contributed reagents/materials/analysis tools: WAW JKB. Wrote the paper: WAW JKB.

References

1. Tsai TH, Lee HC, Ahsen OO, Liang K, Giacomelli MG, Potsaid BM, et al. Ultrahigh speed endoscopic optical coherence tomography for gastroenterology. Biomed Opt Express. 2014 Nov; 5(12):4387–4404. Available from: http://www.ncbi.nlm.nih.gov/pmc/articles/PMC4285613/. doi: 10.1364/BOE.5.004387 PMID: 25574446
2. Hatta W, Uno K, Koike T, Iijima K, Asano N, Imatani A, et al. A prospective comparative study of optical coherence tomography and EUS for tumor staging of superficial esophageal squamous cell carcinoma.

Gastrointest Endosc. 2012 Sep; 76(3):548–555. Available from: http://www.sciencedirect.com/science/article/pii/S0016510712022675. doi: 10.1016/j.gie.2012.05.012 PMID: 22898413

3. Zhou C, Tsai TH, Lee HC, Kirtane T, Figueiredo M, Tao YK, et al. Characterization of buried glands before and after radiofrequency ablation by using 3-dimensional optical coherence tomography (with videos). Gastrointest Endosc. 2012 Jul; 76(1):32–40. Available from: http://www.sciencedirect.com/science/article/pii/S0016510712001319. doi: 10.1016/j.gie.2012.02.003 PMID: 22482920
4. Hariri LP, Qiu Z, Tumlinson AR, Besselsen DG, Gerner EW, Ignatenko N, et al. Serial endoscopy in azoxymethane treated mice using ultra-high resolution optical coherence tomography. Cancer Biol Ther. 2007 Nov; 6(11):1753–1762. Available from: http://www.landesbioscience.com/journals/cbt/article/4852/. doi: 10.4161/cbt.6.11.4852 PMID: 17986850
5. Suter MJ, Gora MJ, Lauwers GY, Arnason T, Sauk J, Gallagher KA, et al. Esophageal-guided biopsy with volumetric laser endomicroscopy and laser cautery marking: a pilot clinical study. Gastrointest Endosc. 2014 Jun; 79(6):886–896. Available from: http://www.sciencedirect.com/science/article/pii/S0016510713025613. doi: 10.1016/j.gie.2013.11.016 PMID: 24462171
6. Swanson E. Clinical translation in OCT: Role of research, funding, and entrepreneurism (Presentation Video). Proc SPIE. 2014; 8934:89342E–89342E–1. Available from: http://dx.doi.org/10.1117/12.2064185. doi: 10.1117/12.2064185
7. Tearney GJ, Brezinski ME, Fujimoto JG, Weissman NJ, Boppart SA, Bouma BE, et al. Scanning single-mode fiber optic catheter-endoscope for optical coherence tomography. Opt Lett. 1996 Apr; 21(7):543–545. Available from: http://ol.osa.org/abstract.cfm?URI=ol-21-7-543. doi: 10.1364/OL.21.000543 PMID: 19865466
8. Bonnema GT, Cardinal KO, Williams SK, Barton JK. A concentric three element radial scanning optical coherence tomography endoscope. J Biophoton. 2009 Jul; 2(6–7):353–356. Available from: http://onlinelibrary.wiley.com/doi/10.1002/jbio.200910024/abstract. doi: 10.1002/jbio.200910024
9. Reed WA, Yan MF, Schnitzer MJ. Gradient-index fiber-optic microprobes for minimally invasive in vivo low-coherence interferometry. Opt Lett. 2002 Oct; 27(20):1794–1796. Available from: http://ol.osa.org/abstract.cfm?URI=ol-27-20-1794. doi: 10.1364/OL.27.001794 PMID: 18033366
10. Lorenser D, Yang X, Kirk RW, Quirk BC, McLaughlin RA, Sampson DD. Ultrathin side-viewing needle probe for optical coherence tomography. Opt Lett. 2011 Oct; 36(19):3894. Available from: https://www.osapublishing.org/ol/abstract.cfm?uri = ol-36-19-3894. doi: 10.1364/OL.36.003894 PMID: 21964133
11. Tumlinson AR, Považay B, Hariri LP, McNally J, Unterhuber A, Hermann B, et al. In vivo ultrahigh-resolution optical coherence tomography of mouse colon with an achromatized endoscope. J Biomed Opt. 2006; 11(6):064003–064003–8. Available from: http://dx.doi.org/10.1117/1.2399454. doi: 10.1117/1.2399454 PMID: 17212526
12. Zhao M, Huang Y, Kang JU. Sapphire ball lens-based fiber probe for common-path optical coherence tomography and its applications in corneal and retinal imaging. Opt Lett. 2012 Dec; 37(23):4835–4837. Available from: http://ol.osa.org/abstract.cfm?URI=ol-37-23-4835. doi: 10.1364/OL.37.004835 PMID: 23202062
13. Choi HY, Ryu SY, Na J, Lee BH, Sohn IB, Noh YC, et al. Single-body lensed photonic crystal fibers as side-viewing probes for optical imaging systems. Opt Lett. 2008 Jan; 33(1):34–36. Available from: http://ol.osa.org/abstract.cfm?URI=ol-33-1-34. doi: 10.1364/OL.33.000034 PMID: 18157249
14. Quirk BC, McLaughlin RA, Pagnozzi AM, Kennedy BF, Noble PB, Sampson DD. Optofluidic needle probe integrating targeted delivery of fluid with optical coherence tomography imaging. Opt Lett. 2014 May; 39(10):2888–2891. Available from: http://ol.osa.org/abstract.cfm?URI=ol-39-10-2888. doi: 10.1364/OL.39.002888 PMID: 24978229
15. Xie Y, Martini N, Hassler C, Kirch R, Seifert A, Stieglitz T, et al. In vivo monitoring of glial scar proliferation on chronically implanted neural electrodes by fiber optical coherence tomography. Frontiers in Neuroengineering. 2014; 7(34). Available from: http://www.frontiersin.org/neuroengineering/10.3389/fneng.2014.00034/abstract. doi: 10.3389/fneng.2014.00034 PMID: 25191264
16. Welge WA, Barton JK. Spiral-scanning, side-viewing optical coherence tomography endoscope for three-dimensional fully sampled in vivo imaging of the mouse colon. Proc SPIE. 2013; 8575:85750R–85750R–6. Available from: http://dx.doi.org/10.1117/12.2002655. doi: 10.1117/12.2002655
17. Fercher AF, Drexler W, Hitzenberger CK, Lasser T. Optical coherence tomography—principles and applications. Rep Prog Phys. 2003 Feb; 66(2):239–303. Available from: http://iopscience.iop.org/0034-4885/66/2/204. doi: 10.1088/0034-4885/66/2/204
18. Drexler W, Liu M, Kumar A, Kamali T, Unterhuber A, Leitgeb RA. Optical coherence tomography today: speed, contrast, and multimodality. J Biomed Opt. 2014; 19(7):071412–071412. Available from: http://dx.doi.org/10.1117/1.JBO.19.7.071412. doi: 10.1117/1.JBO.19.7.071412 PMID: 25079820

19. Jacques SL. Optical properties of biological tissues: a review. Phys Med Biol. 2013 Jun; 58(11):R37. Available from: http://iopscience.iop.org/0031-9155/58/11/R37. doi: 10.1088/0031-9155/58/11/R37 PMID: 23666068

20. Tsai TH, Potsaid B, Tao YK, Jayaraman V, Jiang J, Heim PJS, et al. Ultrahigh speed endoscopic optical coherence tomography using micromotor imaging catheter and VCSEL technology. Biomed Opt Express. 2013 Jun; 4(7):1119–1132. Available from: http://www.ncbi.nlm.nih.gov/pmc/articles/PMC3704093/. doi: 10.1364/BOE.4.001119 PMID: 23847737

21. Zhang N, Tsai TH, Ahsen OO, Liang K, Lee HC, Xue P, et al. Compact piezoelectric transducer fiber scanning probe for optical coherence tomography. Opt Lett. 2014 Jan; 39(2):186–188. Available from: http://ol.osa.org/abstract.cfm?URI=ol-39-2-186. doi: 10.1364/OL.39.000186 PMID: 24562102

22. Wojtkowski M, Srinivasan VJ, Ko TH, Fujimoto JG, Kowalczyk A, Duker JS. Ultrahigh-resolution, high-speed, Fourier domain optical coherence tomography and methods for dispersion compensation. Opt Express. 2004; 12(11):2404. Available from: http://www.opticsinfobase.org/oe/fulltext.cfm?uri = oe-12-11-2404&id=80147. doi: 10.1364/OPEX.12.002404 PMID: 19475077

23. Cense B, Nassif N, Chen T, Pierce M, Yun SH, Park B, et al. Ultrahigh-resolution high-speed retinal imaging using spectral-domain optical coherence tomography. Opt Express. 2004 May; 12(11):2435–2447. Available from: http://www.opticsexpress.org/abstract.cfm?URI=oe-12-11-2435. doi: 10.1364/OPEX.12.002435 PMID: 19475080

24. Fercher AF, Hitzenberger CK, Sticker M, Zawadzki R, Karamata B, Lasser T. Dispersion compensation for optical coherence tomography depth-scan signals by a numerical technique. Opt Commun. 2002 Apr; 204(1â??6):67–74. Available from: http://www.sciencedirect.com/science/article/pii/S0030401802011379. doi: 10.1016/S0030-4018(02)01137-9

25. Marks DL, Oldenburg AL, Reynolds JJ, Boppart SA. Digital algorithm for dispersion correction in optical coherence tomography for homogeneous and stratified media. Appl Opt. 2003 Jan; 42(2):204–217. Available from: http://ao.osa.org/abstract.cfm?URI=ao-42-2-204. doi: 10.1364/AO.42.000204 PMID: 12546500

26. Winkler AM, Rice PFS, Drezek RA, Barton JK. Quantitative tool for rapid disease mapping using optical coherence tomography images of azoxymethane-treated mouse colon. J Biomed Opt. 2010; 15 (4):041512–041512–10. Available from: http://dx.doi.org/10.1117/1.3446674. doi: 10.1117/1.3446674 PMID: 20799790

27. Keenan MR, Leung SJ, Rice PS, Wall RA, Barton JK. Dual optical modality endoscopic imaging of cancer development in the mouse colon. Laser Surg Med. 2015; 47(1):30–39. Available from: http://dx.doi.org/10.1002/lsm.22307. doi: 10.1002/lsm.22307

28. Herz P, Chen Y, Aguirre A, Fujimoto J, Mashimo H, Schmitt J, et al. Ultrahigh resolution optical biopsy with endoscopic optical coherence tomography. Opt Express. 2004 Jul; 12(15):3532–3542. Available from: http://www.opticsexpress.org/abstract.cfm?URI=oe-12-15-3532. doi: 10.1364/OPEX.12.003532 PMID: 19483882

29. Adler DC, Chen Y, Huber R, Schmitt J, Connolly J, Fujimoto JG. Three-dimensional endomicroscopy using optical coherence tomography. Nat Photon. 2007 Dec; 1(12):709–716. Available from: http://www.nature.com/nphoton/journal/v1/n12/full/nphoton.2007.228.html#a1. doi: 10.1038/nphoton.2007.228

30. Takayama T, Katsuki S, Takahashi Y, Ohi M, Nojiri S, Sakamaki S, et al. Aberrant Crypt Foci of the Colon as Precursors of Adenoma and Cancer. N Engl J Med. 1998 Oct; 339(18):1277–1284. Available from: http://dx.doi.org/10.1056/NEJM199810293391803. doi: 10.1056/NEJM199810293391803 PMID: 9791143

31. Alrawi SJ, Schiff M, Carroll RE, Dayton M, Gibbs JF, Kulavlat M, et al. Aberrant Crypt Foci. Anticancer Res. 2006 Jan; 26(1A):107–119. Available from: http://ar.iiarjournals.org/content/26/1A/107.

A.2 Sample-arm optical design

The optical diagram of the endoscope is shown in Fig. A.2 and the spot diagram is shown in Fig. A.3. The full prescription file follows the figures. The endoscope consists of pigtailed silica spacer (fiber not modeled), gradient-index (GRIN) lens, and silica rod prism $n = 1.45$ with a mirrored surface. The rod prism angle is 41° with respect to the exit face. The mechanical drawing of the rod prism is shown in Fig. A.1. This causes the reflected light to exit at an angle of 98° instead of 90°, as would be the case with a 45° prism. This effectively reduces the stray light reflected from the exit face of the prism from returning to the detector and causing a ghosting artifact in the final OCT image.The GRIN lens coefficients were provided by the manufacturer (GRINTech, Jena, Germany).

The spot diagram shows that astigmatism is present. This is due to the cylindrical glass envelope that encompasses the distal tip of the endoscope. However, the astigmatism is minor and does not cause the spot to grow significantly beyond the diffraction limit.

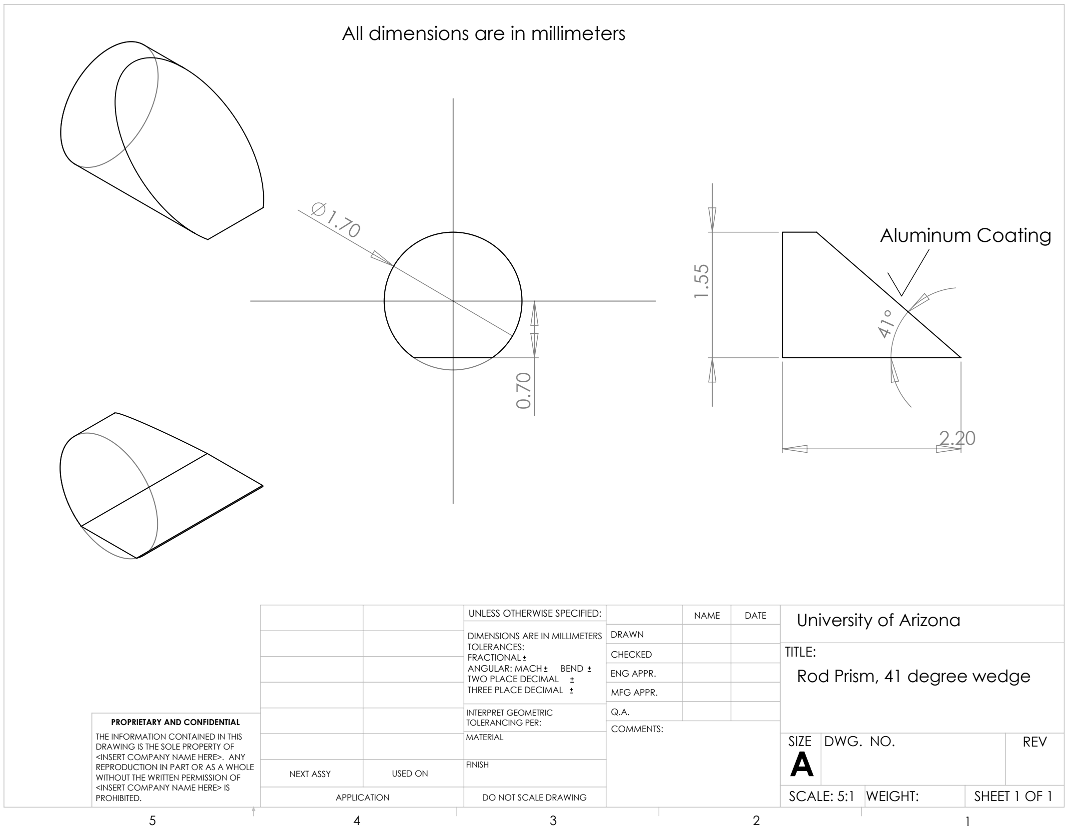

Figure A.1: Rod prism mechanical drawing.[78]

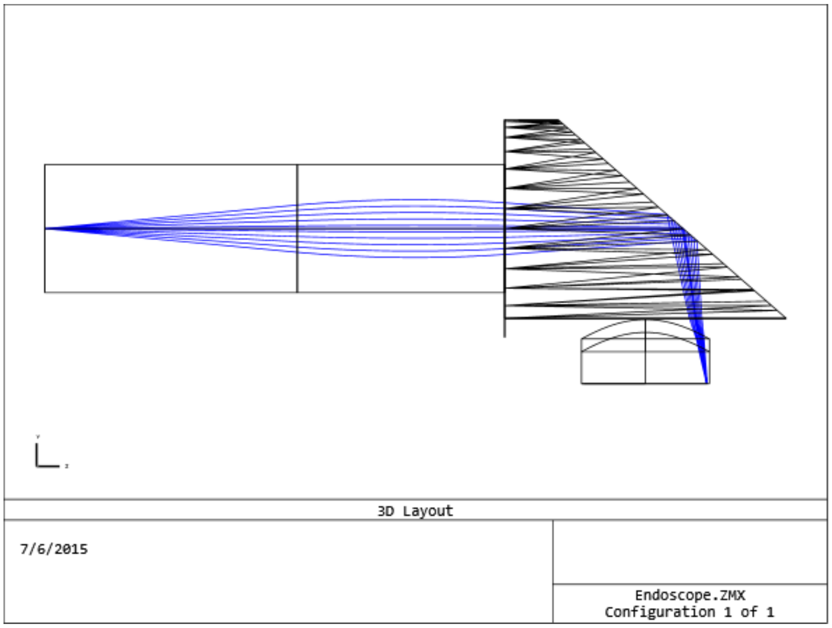

Figure A.2: Endoscope optical diagram.

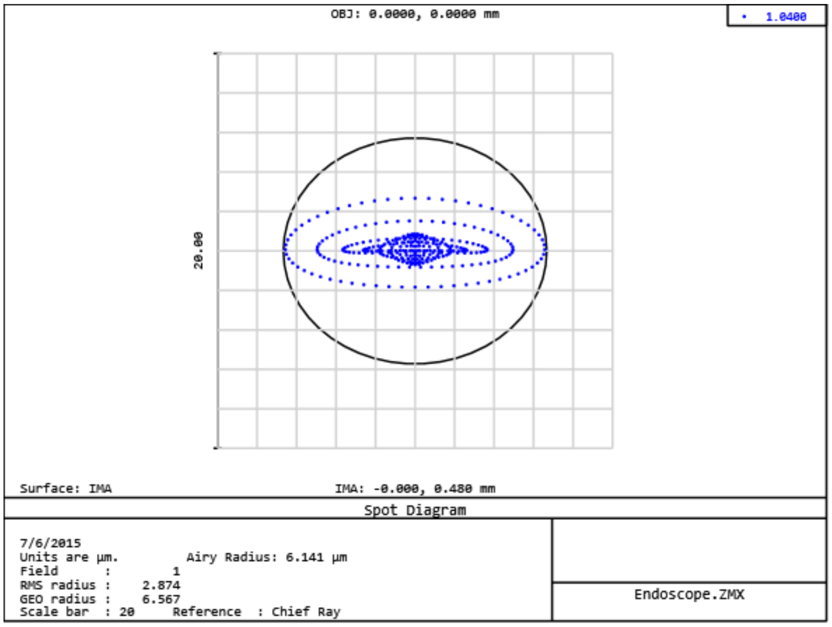

Figure A.3: Endoscope spot diagram. The diffraction-limited spot is denoted by the black circle.

```
System/Prescription Data

File : R:\People\Weston\Endoscope\OCS1050SS Conversion from laptop\
   OCS1050SS Conversion\Endoscope.ZMX
Title:
Date : 4/4/2016


GENERAL LENS DATA:

Surfaces : 8
Stop : 1
System Aperture : Object Space NA = 0.14
Fast Semi−Diameters : On
Telecentric Object Space: On
Field Unpolarized : On
Convert thin film phase to ray equivalent : On
J/E Conversion Method : X Axis Reference
Glass Catalogs : SCHOTT
Ray Aiming : Off
Apodization : Uniform, factor = 0.00000E+000
Reference OPD : Exit Pupil
Paraxial Rays Setting : Ignore Coordinate Breaks
Method to Compute F/# : Tracing Rays
Print Coordinate Breaks : On
Multi−Threading : On
OPD Modulo 2 Pi : Off
Temperature (C) : 2.00000E+001
```

Pressure (ATM) : 1.00000E+000

Adjust Index Data To Environment : Off

Effective Focal Length : −4.66205e−010 (in air at system temperature and pressure)

Effective Focal Length : −4.66205e−010 (in image space)

Back Focal Length : −2.234828

Total Track : 4.105

Image Space F/# : 1.64862e−019

Paraxial Working F/# : 2.054876

Working F/# : 4.839678

Image Space NA : 0.1135966

Object Space NA : 0.14

Stop Radius : 1

Paraxial Image Height : 0.1731067

Paraxial Magnification : 0

Entrance Pupil Diameter : 2.82785e+009

Entrance Pupil Position : 1e+010

Exit Pupil Diameter : 0.2967732

Exit Pupil Position : −1.267466

Field Type : Object height in Millimeters

Maximum Radial Field : 0

Primary Wavelength [m] : 1.04

Angular Magnification : 0

Lens Units : Millimeters

Source Units : Watts

Analysis Units : Watts/cmˆ2

Afocal Mode Units : milliradians

MTF Units : cycles/millimeter

```
Include Calculated Data in Session File : On

Fields : 1
Field Type :  Object height in Millimeters
 #  X−Value  Y−Value  Weight
 1  0.000000  0.000000  1.000000

Vignetting Factors
 #  VDX  VDY  VCX  VCY  VAN
 1  0.000000  0.000000  0.000000  0.000000  0.000000

Wavelengths : 1
Units: m
 #  Value  Weight
 1  1.040000  1.000000

SURFACE DATA SUMMARY:

Surf  Type  Radius  Thickness  Glass  Diameter  Conic  Comment
 OBJ STANDARD Infinity 0  0 0
 STO STANDARD Infinity 1.974 N−BK7 1 0 Spacer
   2 GRINSUR5 Infinity 1.621 GTAG 1 0 GRIN (cr2616−1)
   3 STANDARD Infinity 0  1 0
   4 NONSEQCO Infinity 0  1.7 0 Entry port
   5 STANDARD Infinity 0.16  2.2 0 Exit port
   6 TOROIDAL Infinity 0.1 1.500000, 64.110000 1 0 Glass envelope
   7 TOROIDAL Infinity 0.25 1.400000, 0.000000 1 0
 IMA STANDARD Infinity   0.9648317 0
```

SURFACE DATA DETAIL:

Surface OBJ STANDARD

Surface STO STANDARD Spacer
Aperture : Floating Aperture
Maximum Radius : 0.5

Surface 2 GRINSUR5 GRIN (cr2616−1)
Delta t : 0.02
N0 : 1.629
Nr2 : −0.376
Nr4 : 0.062
Nz1 : 0
Nz2 : 0
Nz3 : 0
Nz4 : 0
X Tangent : 0
Y Tangent : 0
Aperture : Floating Aperture
Maximum Radius : 0.5

Surface 3 STANDARD
Aperture : Floating Aperture
Maximum Radius : 0.5

```
Surface 4 NONSEQCO Entry port
Draw Ports? : 3
Decenter X : 0
Decenter Y : −0.701
Decenter Z : 1.1
Tilt About X : 90
Tilt About Y : 0
Tilt About Z : 0
Order : Decenter then tilt

There are 1 objects:

Object 1 : Welge__Rod_Prism.ZPO
Object Type : CAD Part: Zemax Part Designer (NSC_ZPDO)
Face 0 : Face 0
Face Is : Reflective
Coating : (none)
Scattering : None
Face 1 : Face 1
Face Is : Object Default
Coating : (none)
Scattering : None
Face 2 : Face 2
Face Is : Object Default
Coating : (none)
Scattering : None
Face 3 : Face 3
```

```
Face Is : Object Default
Coating : (none)
Scattering : None
Reference Object : 0
Inside Of : 0
XYZ Position :  0 −0.7 0
Tilt About XYZ :  0 0 0
Pos. Mtrx. R11 R12 R13 X :  1.00000000E+000  0.00000000E+000  0.00000000E
    +000  0.00000000E+000
Pos. Mtrx. R21 R22 R23 Y :  0.00000000E+000  1.00000000E+000  0.00000000E
    +000  −7.00000000E−001
Pos. Mtrx. R31 R32 R33 Z :  0.00000000E+000  0.00000000E+000  1.00000000E
    +000  0.00000000E+000
Material : N−BK7
Index at 1.040000 m = 1.50695401


Surface 5 STANDARD Exit port

Surface 6 TOROIDAL Glass envelope
Extrapolate? : 0
Radius of Rotation : −0.9
Coefficient on yˆ2 : 0
Coefficient on yˆ4 : 0
Coefficient on yˆ6 : 0
Coefficient on yˆ8 : 0
Coefficient on yˆ10 : 0
Coefficient on yˆ12 : 0
```

```
Coefficient on y^14 : 0
Number of terms : 0
Normalization Radius : 100
Aperture : Floating Aperture
Maximum Radius : 0.5

Surface 7 TOROIDAL
Extrapolate? : 0
Radius of Rotation : −0.9
Coefficient on y^2 : 0
Coefficient on y^4 : 0
Coefficient on y^6 : 0
Coefficient on y^8 : 0
Coefficient on y^10 : 0
Coefficient on y^12 : 0
Coefficient on y^14 : 0
Number of terms : 0
Normalization Radius : 100
Aperture : Floating Aperture
Maximum Radius : 0.5

Surface IMA STANDARD

EDGE THICKNESS DATA:

Surf  X−Edge  Y−Edge
 OBJ  0.000000  0.000000
 STO  1.974000  1.974000
```

```
   2  1.621000  1.621000
   3  0.000000  0.000000
   4  0.000000  0.000000
   5  0.008331  0.160000
   6  0.100000  0.100000
   7  0.401669  0.250000
 IMA  0.000000  0.000000

SOLVE AND VARIABLE DATA:

 Semi Diameter 1 : Fixed
 Semi Diameter 2 : Fixed
 Semi Diameter 3 : Fixed
 Semi Diameter 4 : Fixed
 Semi Diameter 5 : Fixed
 Semi Diameter 6 : Fixed
 Semi Diameter 7 : Fixed

INDEX OF REFRACTION DATA:

System Temperature: 20.0000 Celsius
System Pressure : 1.0000 Atmospheres
Absolute air index: 1.000269 at wavelength 1.040000 m
Index data is relative to air at the system temperature and pressure.
Wavelengths are measured in air at the system temperature and pressure.

Surf  Glass  Temp  Pres  1.04000000
   0    20.00  1.00  1.0000000000
```

```
  1  N−BK7  20.00  1.00  1.5069540061 step 0.5 available
  2  GTAG  20.00  1.00  1.6194916378
  3   20.00  1.00  1.0000000000
  4   20.00  1.00  1.0000000000
  5   20.00  1.00  1.0000000000
  6  <MODEL> 20.00  1.00  1.4910172041
  7  <MODEL> 20.00  1.00  1.4000000000
  8   20.00  1.00  1.0000000000

THERMAL COEFFICIENT OF EXPANSION DATA:

Surf  Glass  TCE ∗ 10E−6
 0   0.0000000000
 1  N−BK7  7.1000000000 step 0.5 available
 2  GTAG  0.0000000000
 3   0.0000000000
 4   0.0000000000
 5   0.0000000000
 6  <MODEL>  0.0000000000
 7  <MODEL>  0.0000000000
 8   0.0000000000

GLOBAL VERTEX COORDINATES, ORIENTATIONS, AND ROTATION/
    OFFSET MATRICES:

Reference Surface: 1

Surf  R11  R12  R13  X  Tilt X
```

```
                 R21  R22  R23  Y  Tilt Y
                 R31  R32  R33  Z  Tilt Z

0  1.0000000000  0.0000000000  0.0000000000  0.000000000E+000  0.000000000E
   +000
       0.0000000000  1.0000000000  0.0000000000  0.000000000E+000
          0.000000000E+000
       0.0000000000  0.0000000000  1.0000000000  0.000000000E+000
          0.000000000E+000

1  1.0000000000  0.0000000000  0.0000000000  0.000000000E+000  0.000000000E
   +000  Spacer
       0.0000000000  1.0000000000  0.0000000000  0.000000000E+000
          0.000000000E+000
       0.0000000000  0.0000000000  1.0000000000  0.000000000E+000
          0.000000000E+000

2  1.0000000000  0.0000000000  0.0000000000  0.000000000E+000  0.000000000E
   +000  GRIN (cr2616−1)
       0.0000000000  1.0000000000  0.0000000000  0.000000000E+000
          0.000000000E+000
       0.0000000000  0.0000000000  1.0000000000  1.974000000E+000
          0.000000000E+000

3  1.0000000000  0.0000000000  0.0000000000  0.000000000E+000  0.000000000E
   +000
       0.0000000000  1.0000000000  0.0000000000  0.000000000E+000
          0.000000000E+000
```

```
          0.0000000000  0.0000000000  1.0000000000  3.595000000E+000
              0.000000000E+000

  4  1.0000000000  0.0000000000  0.0000000000  0.000000000E+000  0.000000000E
      +000  Entry port
          0.0000000000  1.0000000000  0.0000000000  0.000000000E+000
              0.000000000E+000
          0.0000000000  0.0000000000  1.0000000000  3.595000000E+000
              0.000000000E+000

NSC Object 1: Welge__Rod_Prism.ZPO
          1.0000000000  0.0000000000  0.0000000000  0.000000000E+000
              0.000000000E+000
          0.0000000000  1.0000000000  0.0000000000  −7.000000000E−001
              0.000000000E+000
          0.0000000000  0.0000000000  1.0000000000  3.595000000E+000
              0.000000000E+000

  5  1.0000000000  0.0000000000  0.0000000000  0.000000000E+000  9.000000000E
      +001  Exit port
          0.0000000000  0.0000000000  −1.0000000000  −7.010000000E−001
              0.000000000E+000
          0.0000000000  1.0000000000  0.0000000000  4.695000000E+000
              0.000000000E+000

  6  1.0000000000  0.0000000000  0.0000000000  0.000000000E+000  9.000000000E
      +001  Glass envelope
          0.0000000000  0.0000000000  −1.0000000000  −8.610000000E−001
```

```
          0.000000000E+000
      0.0000000000  1.0000000000  0.0000000000  4.695000000E+000
          0.000000000E+000

  7  1.0000000000  0.0000000000  0.0000000000  0.000000000E+000  9.000000000E
     +001
      0.0000000000  0.0000000000  −1.0000000000  −9.610000000E−001
          0.000000000E+000
      0.0000000000  1.0000000000  0.0000000000  4.695000000E+000
          0.000000000E+000

  8  1.0000000000  0.0000000000  0.0000000000  0.000000000E+000  9.000000000E
     +001
      0.0000000000  0.0000000000  −1.0000000000  −1.211000000E+000
          0.000000000E+000
      0.0000000000  1.0000000000  0.0000000000  4.695000000E+000
          0.000000000E+000


GLOBAL SURFACE CENTER OF CURVATURE POINTS:

Reference Surface: 1

Surf  X  Y  Z
  0  –  –  –
  1  –  –  –  Spacer
  2  –  –  –  GRIN (cr2616−1)
  3  –  –  –
```

```
  4 – – – Entry port
  5 – – – Exit port
  6 – – – Glass envelope
  7 – – –
  8 – – –

ELEMENT VOLUME DATA:

For centered elements with plane or spherical circular faces, exact
volumes are computed by assuming edges are squared up to the larger
of the front and back radial aperture.

For all other elements, approximate volumes are numerically integrated
to 0.1% accuracy. Zero volume means the volume cannot be accurately computed.

Single elements that are duplicated in the Lens Data Editor
for ray tracing purposes may be listed more than once yielding
incorrect total mass estimates.

                                   Volume cc  Density g/cc  Mass g
Element surf 1 to 2  0.001550  2.510000  0.003891
Element surf 2 to 3  0.001273  3.600000  0.004583
Element surf 6 to 7  0.000079  0.000000  0.000000
Element surf 7 to 8  0.000217  0.000000  0.000000
Total Mass:  0.008475

F/# DATA:
```

```
F/# calculations consider vignetting factors and ignore surface apertures.

     Wavelength:  1.040000
# Field  Tan  Sag
1 0.0000 mm: 4.5088  5.2561

CARDINAL POINTS:

Object space positions are measured with respect to surface 1.
Image space positions are measured with respect to the image surface.
The index in both the object space and image space is considered.

                                        Object Space  Image Space
W =  1.040000 (Primary)
Focal Length :  0.004640  −0.004640
Focal Planes :  0.999183  −2.234828
Principal Planes :  0.994543  −2.230188
Anti−Principal Planes :  1.003823  −2.239468
Nodal Planes :  0.994543  −2.230188
Anti−Nodal Planes :  1.003823  −2.239468

PHYSICAL OPTICS PROPAGATION SETTINGS SUMMARY:

 OBJ STANDARD
Use Rays To Propagate To Next Surface : Off
Recompute Pilot Beam : Off
Do Not Rescale Beam Size Using Ray Data: Off
Use Angular Spectrum Propagator : Off
```

```
Use X−Axis Reference : Off
Output Pilot Radius : Best Fit
 STO STANDARD Spacer
Use Rays To Propagate To Next Surface : Off
Recompute Pilot Beam : Off
Do Not Rescale Beam Size Using Ray Data: Off
Use Angular Spectrum Propagator : Off
Use X−Axis Reference : Off
Output Pilot Radius : Best Fit
   2 GRINSUR5 GRIN (cr2616−1)
Use Rays To Propagate To Next Surface : On
Recompute Pilot Beam : Off
Do Not Rescale Beam Size Using Ray Data: Off
Use Angular Spectrum Propagator : Off
Use X−Axis Reference : Off
Output Pilot Radius : Best Fit
   3 STANDARD
Use Rays To Propagate To Next Surface : Off
Recompute Pilot Beam : Off
Do Not Rescale Beam Size Using Ray Data: Off
Use Angular Spectrum Propagator : Off
Use X−Axis Reference : Off
Output Pilot Radius : Best Fit
   4 NONSEQCO Entry port
Use Rays To Propagate To Next Surface : On
Recompute Pilot Beam : Off
Do Not Rescale Beam Size Using Ray Data: Off
Use Angular Spectrum Propagator : Off
```

```
Use X−Axis Reference : Off
Output Pilot Radius : Best Fit
   5 STANDARD Exit port
Use Rays To Propagate To Next Surface : Off
Recompute Pilot Beam : Off
Do Not Rescale Beam Size Using Ray Data: Off
Use Angular Spectrum Propagator : Off
Use X−Axis Reference : Off
Output Pilot Radius : Best Fit
   6 TOROIDAL Glass envelope
Use Rays To Propagate To Next Surface : Off
Recompute Pilot Beam : Off
Do Not Rescale Beam Size Using Ray Data: Off
Use Angular Spectrum Propagator : Off
Use X−Axis Reference : Off
Output Pilot Radius : Best Fit
   7 TOROIDAL
Use Rays To Propagate To Next Surface : Off
Recompute Pilot Beam : Off
Do Not Rescale Beam Size Using Ray Data: Off
Use Angular Spectrum Propagator : Off
Use X−Axis Reference : Off
Output Pilot Radius : Best Fit
 IMA STANDARD
Use Rays To Propagate To Next Surface : Off
Recompute Pilot Beam : Off
Do Not Rescale Beam Size Using Ray Data: Off
Use Angular Spectrum Propagator : Off
```

```
Use X−Axis Reference : Off
Output Pilot Radius : Best Fit

FILES USED:

Zemax File
  R:\People\Weston\Endoscope\OCS1050SS Conversion from laptop\OCS1050SS
       Conversion\Endoscope.ZMX
Session File
  R:\People\Weston\Endoscope\OCS1050SS Conversion from laptop\OCS1050SS
       Conversion\Endoscope.SES
Lens Configuration File
  R:\People\Weston\Endoscope\OCS1050SS Conversion from laptop\OCS1050SS
       Conversion\Endoscope.CFG
Glass Catalogs
  C:\Users\wwelge\Documents\Zemax\GLASSCAT\SCHOTT.AGF
Coating Data
  C:\Users\wwelge\Documents\Zemax\COATINGS\COATING.DAT
NSC Object Files
  C:\Users\wwelge\Documents\Zemax\OBJECTS\CAD Files\Welge__Rod_Prism
      .ZPO.ZEN
NSC Scatter Profiles
  C:\Users\wwelge\Documents\Zemax\PROFILES\SCATTER_PROFILE.DAT
ABg Data
  C:\Users\wwelge\Documents\Zemax\ABG_DATA\ABG_DATA.DAT
Gradient Index Data
  C:\Users\wwelge\Documents\Zemax\GLASSCAT\SGRIN.DAT
Zemax Part Designer Files
```

C:\Users\wwelge\Documents\Zemax\OBJECTS\Part Designer Objects\Welge__Rod_Prism.ZPO

A.2.1 Procedure for endoscope construction

Materials:

- Polyimide tubing (ID: 1.45 mm; wall thickness: 57 µm; Part number: B0013H0X8E, Small Parts, Seattle, WA)
- GRIN lens assembly (Corning Hi 1060 fiber pigtail, silica spacer, GRIN lens (part number: GT-LFRL-100-014-50-NC, GRINTech, Jena, Germany), Assembly number: GT-SMFP-SP1.94-100-0175-50, GRINTech) with pigtail reconnectorized to shorten length to about 1 m
- Rod prism (custom (Fig. A.1), Photop, Sunnyvale, CA)
- Cylindrical glass envelope (OD: 2 mm, wall thickness: 100 µm, University of Arizona glass shop
- Norland Optical Adhesive 63 (Norland Products, Cranbury, NJ)
- F120 epoxy (Thorlabs, Newton, NJ)
- Endoscope construction jig (shown in Fig. A.4)
- UV epoxy-curing source
- Glass cover slip
- Disposable gloves
- Small needle (24+ gauge)
- UV-blocking safety glasses

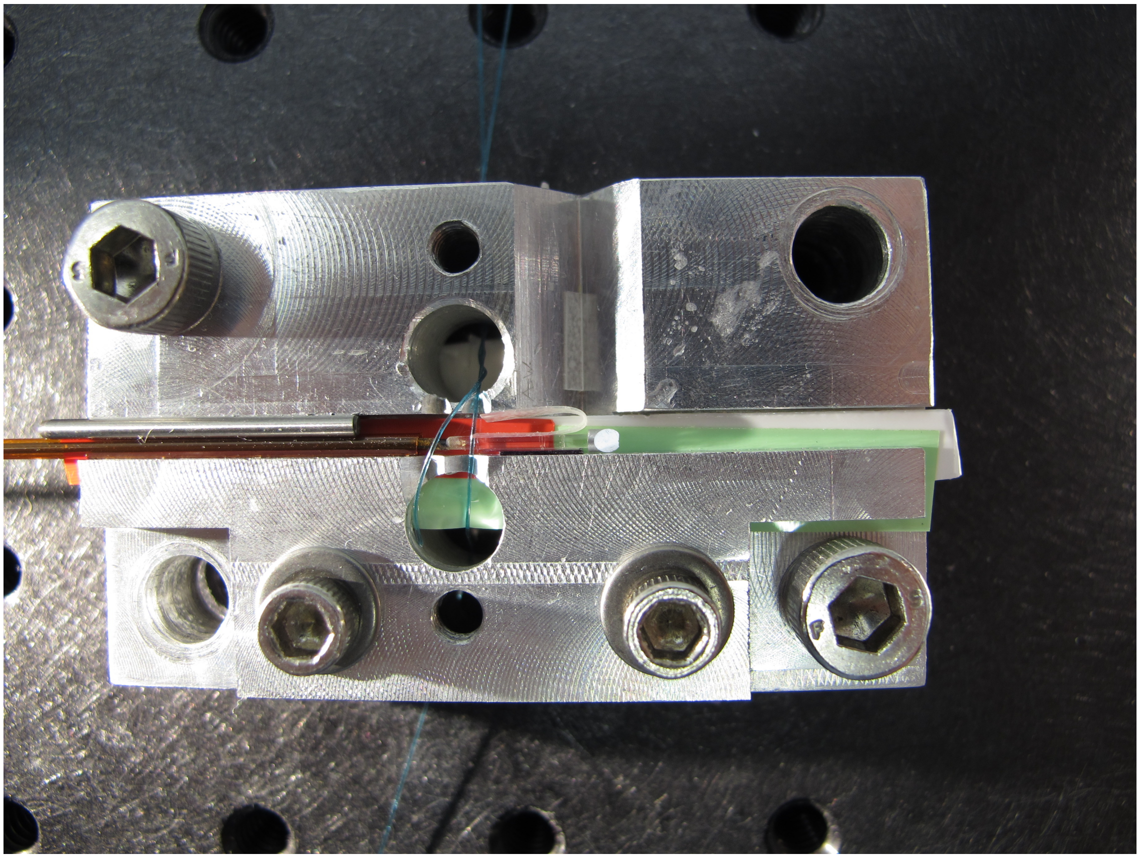

Figure A.4: Endoscope construction jig. The metal pin holds the endoscope flush with one surface of the jig. Colored shim stock is used for proper height alignment of the prism to the GRIN lens. The clear folded shim and small black shim center the optics horizontally with respect to the prism entrance face.

Endoscope construction

1. Cut polyimide tubing such that 1 mm to 2 mm of the GRIN lens extends out of the tubing when the proximal end of the tubing is flush with the fiber strain-relief boot.
2. Wear gloves for the rest of the procedure.
3. Thread GRIN lens assembly through polyimide tube while adding F120 epoxy to the fiber jacket so that the entire length of the fiber is glued to the polyimide tube.
4. Add a thick coating of F120 epoxy to the junction of the polyimide tube and the fiber strain-relief boot. This epoxy will help prevent the fiber or tubing from breaking due to high rotational acceleration.
5. Let epoxy cure at room temperature for at least 1 hour. Do not proceed to the next step until the the epoxy at the junction of the tubing and strain-relief boot is cured.
6. Inspect GRIN face and entrance port of rod prism with a microscope or stereoscope and clean if necessary.
    (a) First try to blow the debris free with a canned-air duster.
    (b) Inspect optical surfaces again. If debris remains, continue to the next step.
    (c) Clean with lens cleaner or reagent-grade solvent using the brush technique. Fold a small piece of lens paper in half such that the fold is about as wide as the optic. Hold the tissue with carbon-tipped tweezers parallel to the surface of the lens. Apply a drop of lens cleaner or solvent to the wide-fold portion of the lens paper and gently brush this surface across the optic surface.

   (d) Inspect optic surface again and repeat brush technique if necessary.

7. Place the GRIN assembly in the construction jig such that one of the wires can secure the distal end of the polyimide tube and the second wire can secure the GRIN lens.

8. Cut small pieces of appropriate shim stock to elevate the rod prism 44 µm above the bottom edge of the GRIN. The prism should be placed on the shim stock such that the flat exit face is in contact with the shim stock. This height aligns the GRIN lens to the rotational center of mass of the the rod prism to reduce vibrations when rotating the endoscope.

9. Place a drop of of the NOA 63 epoxy on a glass cover slip.

10. Pick up a small amount of epoxy using the small needle tip and carefully touch the epoxy on the needle tip to the GRIN lens face. A small bead (< half the GRIN diameter) should be deposited to the GRIN lens.

11. Using the tweezers, gently slide the elevated rod prism until it is firmly in contact with the GRIN lens.

12. Put on UV-blocking safety glasses and cure the GRIN-prism junction with the UV-curing source for 60 s.

13. Inspect the bonded junction for any epoxy that may have been pushed out of the junction. If any epoxy is present, gently remove by wiping the junction with lens paper moistened with acetone.

14. Remove the assembly from the construction jig. If the optics are bonded to the shim stock or jig, carefully attempt to remove this extraneous epoxy with lens paper moistened with acetone.

15. Let epoxy permanently cure at room temperature for 24 h.

A.3 Hardware for synchronization to galvanometer signal

A system diagram showing the synchronization hardware is shown in Fig. A.5. The x-galvanometer scan signal (fast-axis in probe raster scan) is the trigger for endoscope motion. The fast rotational motor is synchronized to begin rotation at the beginning of the x-galvanometer sweep for data acquisition and the rotational motor comes to a complete stop at the end of the data acquisition period. Therefore, the endoscope rotates during the entire period of data acquisition and is stationary for the short time period during which the fast-axis of the galvanometer returns to the beginning position for the next sweep. The linear actuator is also synchronized to the x-galvanometer signal; however, the linear actuator moves continuously during data acquisition and is therefore only triggered at the beginning of a 3D scan.

When fringe data, rather than image data, are recorded by the Thorlabs imaging software, there is an additional period for writing the larger fringe data to the hard drive during which the x-galvanometer signal is constant. These variable-length plateaus can be seen in Fig. A.6. Because the duration of the plateaus cannot be predicted, proper synchronization of the endoscope motion must be linked to the beginning of the negative-slope region. This was accomplished using a custom circuit that performs the negative time derivative of the x-galvanometer signal. The output voltage range of the derivative operation was also limited to 0 V to 5 V so the signal could be safely input to an Arduino Uno. Further details of the circuit are given in Sec. A.3.1.

An Arduino was used to produce a user-defined digital pulse for triggering the motor drivers for both the rotational and linear motors. This results in a more robust synchronization system because the motor drivers are limited in the types of inputs that can be used for triggering motion. The motor driver software (SI Programmer, Applied Motion Products, Watsonville, CA) allows for conditional expressions based on four possible states of the I/O pins: high, low, rising edge, and

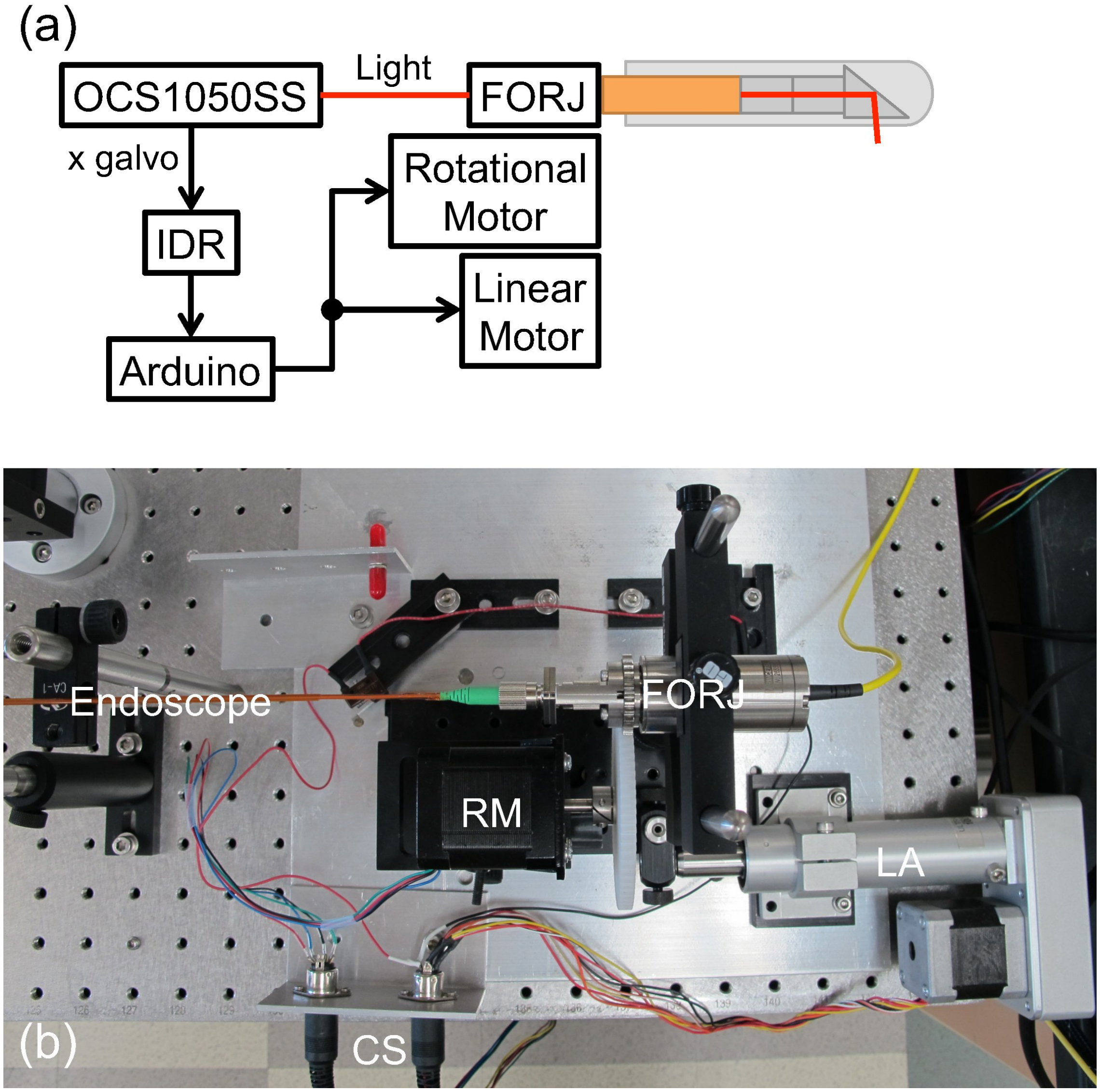

Figure A.5: Synchronization hardware system diagram (a) and photo (b). IDR: inverting differentiator and rectifier circuit; FORJ: fiber-optic rotary joint; RM: rotational stepper motor; LA: linear actuator; CS: control signals.[3]

falling edge. The rising edge from the custom circuit corresponding to the beginning of the negative slope data-acquisition period should be capable of triggering the motor driver; however, I found that this was unreliable. The motor would trigger at seemingly random times. The motor worked properly only on a high digital signal. Ideally the custom circuit produces a constant pulse during the data acquisition period and is 0 V otherwise. The motor drivers only sample the input voltage on the I/O pin when the motor is not in motion. Since the rising edge of the x-galvanometer signal is just approximately 7% of the total scan period for the imaging parameters used when fully spatially sampling the circumference of the mouse colon, it is likely that the motor will finish one full rotation before the end of the data acquisition period and then immediately begin another rotation if the rotational velocity and acceleration are not set to appropriate values. This tight tolerance is exacerbated when saving 3D image (rather than fringe) data. When saving image data, which is much smaller in size, there is no plateau region on the x-galvanometer signal and the beam scans continuously. The Arduino relieves the problem of synchronizing on a high signal because the user can use code to output a digital pulse of a user-defined time duration. I chose to output a 10 ms pulse, which was much shorter than the data-acquisition period, to ensure that motion triggering occurred only at the beginning of data acquisition. The details of the Arduino setup and code are given in Sec. A.3.2. Finally, the motor driver configuration and software is described in Sec. A.3.3.

A.3.1 Inverting differentiator and rectifier circuit

The purpose of the electronics is to convert the x-galvanometer sawtooth wave to a digital pulse that is high during data acquisition and low otherwise. The sawtooth peak-to-peak amplitude changes based on the x length specified by the user in the Thorlabs OCT imaging software. The length of the data acquisition period is determined by the number of x pixels defined by the user in the imaging software.

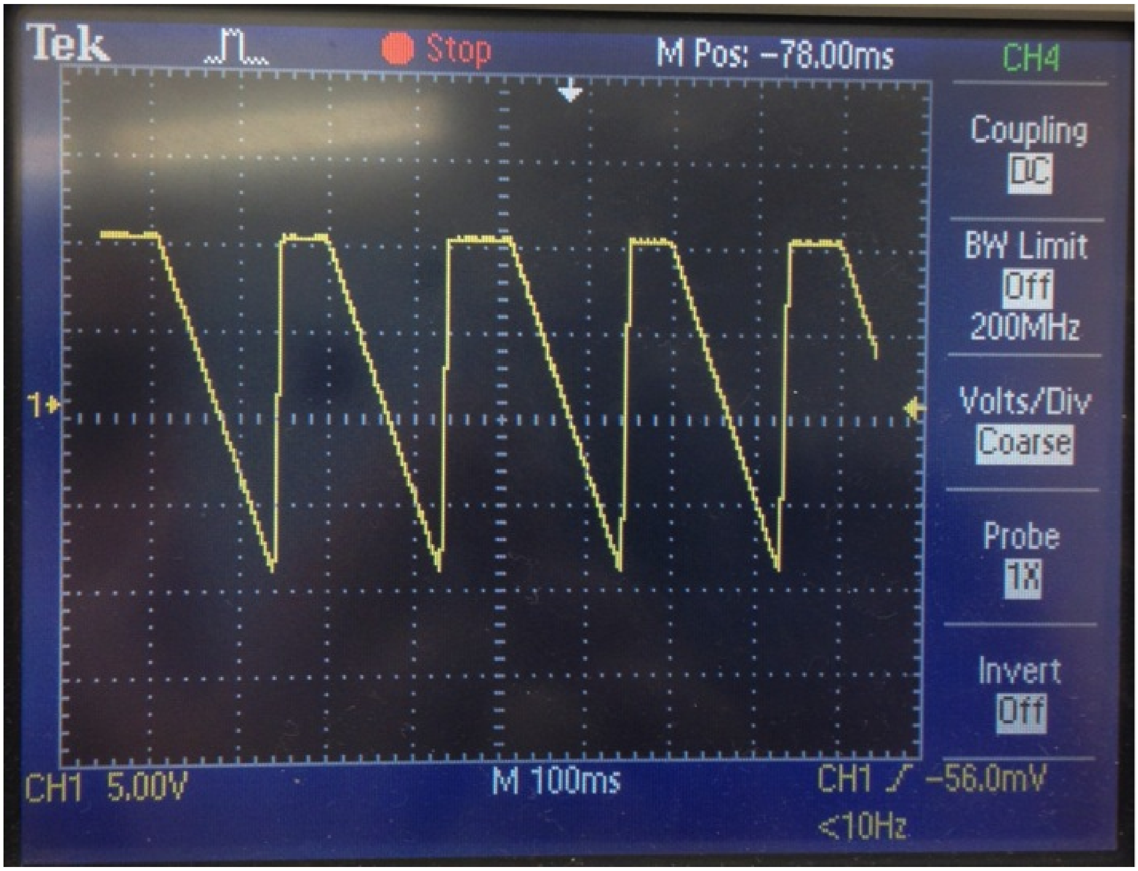

Figure A.6: x-galvanometer control signal. Data is acquired during the region of negative slope. The highly positive slope regions correspond to the rapid return sweep of the raster scan. The zero-slope regions fluctuate in duration and correspond to the time during which the PC writes the raw fringe data to the hard drive.

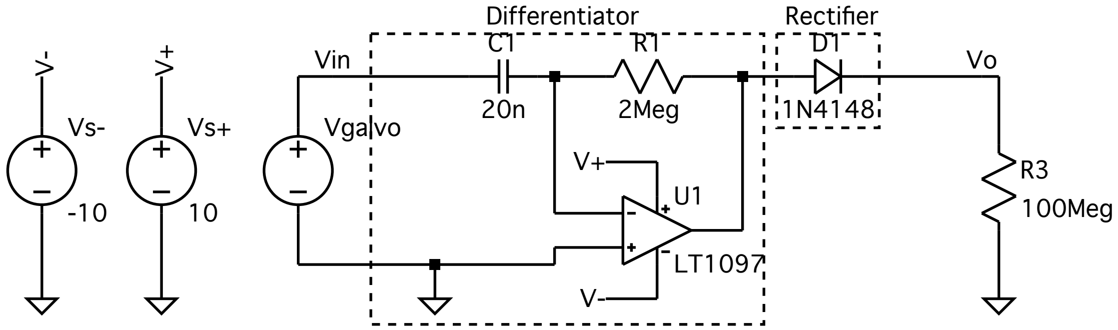

Figure A.7: Inverting differentiator and rectifier circuit for converting x-galvanometer sawtooth wave to a digital pulse train that is positive during the negative-slope region of the input signal and zero otherwise.

The A-scan rate of the system is a constant 16 kHz, so the B-scan duration is simply the number of x pixels divided by 16,000. Because the amplitude and period can vary, it is important that the electronics be robust to any user settings. The circuit schematic is shown in Fig. A.7. The x-galvanometer signal (Vgalvo) comes from an SMA connector on the rear of the OCS1050SS PC. The output (Vo) is connected to pin 2 of the Arduino Uno.

The data is always collected during the negative-slope portion of the x-galvanometer signal, so an inverting differentiator circuit was implemented. This circuit uses an operational amplifier to produce an ideal output $V_o(t)$ that is given by

$$V_o(t) = -RC\frac{dV_i(t)}{dt}, \tag{A.1}$$

where R is the resistance of a resistor connecting the op amp output to the inverting input and C is the capacitance of a capacitor in series with the V_i and the inverting input of the op amp.

On its own, the inverting differentiator would output a large negative square wave during the rapid positive-slope region of the input wave corresponding to the return sweep of the x-galvanometer mirror. To suppress this negative voltage, a diode is used as a rectifier. For op-amp output voltages greater than the diode forward-bias

Figure A.8: Output of inverting differentiator and rectifier.

voltage drop ($\approx 0.7\,\mathrm{V}$), the output voltage matches Eq. (A.1). Otherwise, the diode acts like an open circuit and the output voltage is 0 V. The output is shown in Fig. A.8 as the green trace.

The circuit in Fig. A.7 will output a maximum voltage of about 4.5 V when the OCT software parameters are set to 2000 x pixels and 6 mm x length. There is no need to change the x length parameter in endoscope mode. If this length is greatly reduced, it is possible for the resulting x-galvanometer waveform to have a negative slope magnitude large enough to exceed 5 V output. The circuit can be made more robust by adding a clipper circuit as shown in Fig. A.9. The circuit can also be made less susceptible to noise by adding a resistor in series with C1 and a capacitor

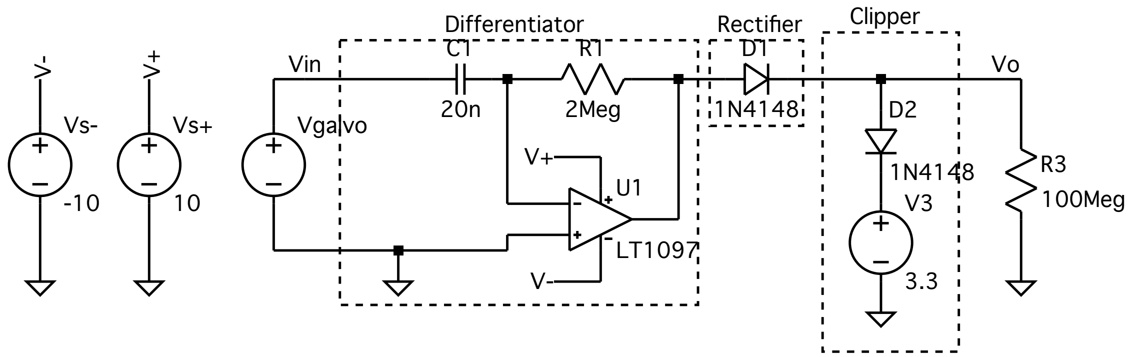

Figure A.9: Inverting differentiator, rectifier, and clipper circuit. The addition of a clipper prevents the output from exceeding 5 V and potentially damaging an Arduino, which can safely accept 0 V to 5 V input voltages.

in parallel with R1. These additional component values can be chosen to minimize the amplifier gain to high-frequency noise and reduce output oscillations.

A.3.2 Arduino configuration and software

An Arduino Uno was used in the synchronization hardware to give greater user control over the synchronization procedure. The code used at the time of this writing is provided in Code A.1. The Arduino is connected to the output of the inverting differentiator and rectifier circuit through I/O pin 2. An external interrupt is triggered when a rising edge is detected on this pin. The interrupt service routine sets a flag that is polled on each pass through the main function loop. When this flag is detected as high, the Arduino outputs a 5 V pulse on pin 4 for 10 ms. The duration of this pulse is arbitrary, but deliberately kept shorter than the data acquisition period because another rotational will be triggered if the signal is still high after the rotational motor completes one full rotation. Figure A.10 shows an oscilloscope trace of the Arduino output with the x-galvanometer control signal and inverting differentiator and rectifier circuit output. The trace shows that the Arduino output pulse occurs at the beginning of the negative-slope region corresponding to data acquisition.

Code A.1: `motionControlR5.ino`

```
// Motion Control

// Author: Weston A. Welge
// Date: April 18, 2016

/* Outputs a 10−ms digital pulse when a rising
    edge is detected on pin 2.

    Connections:
    Pin 2: Inverting differentiator and rectifier (IDR) circuit
              output
    Pin 4: Input 4 on 3540i motor drivers for both linear
              and rotational motors
    gnd: Ground pin connected to ground on 3540i and IRD
*/

// Connect both rotational and linear I/O ports to motorTrigger
const byte motorTrigger = 4;
const byte interruptPin = 2;
volatile byte state = LOW;

void setup() {
  pinMode(motorTrigger, OUTPUT);
  attachInterrupt(digitalPinToInterrupt(interruptPin), trigger, RISING);
}

```

```
void loop() {
  if (state == HIGH) {
    digitalWrite(motorTrigger, state);
    delay(10); // in milliseconds
    state = LOW;
  }
  digitalWrite(motorTrigger, state);
}

void trigger() {
  state = HIGH;
}
```

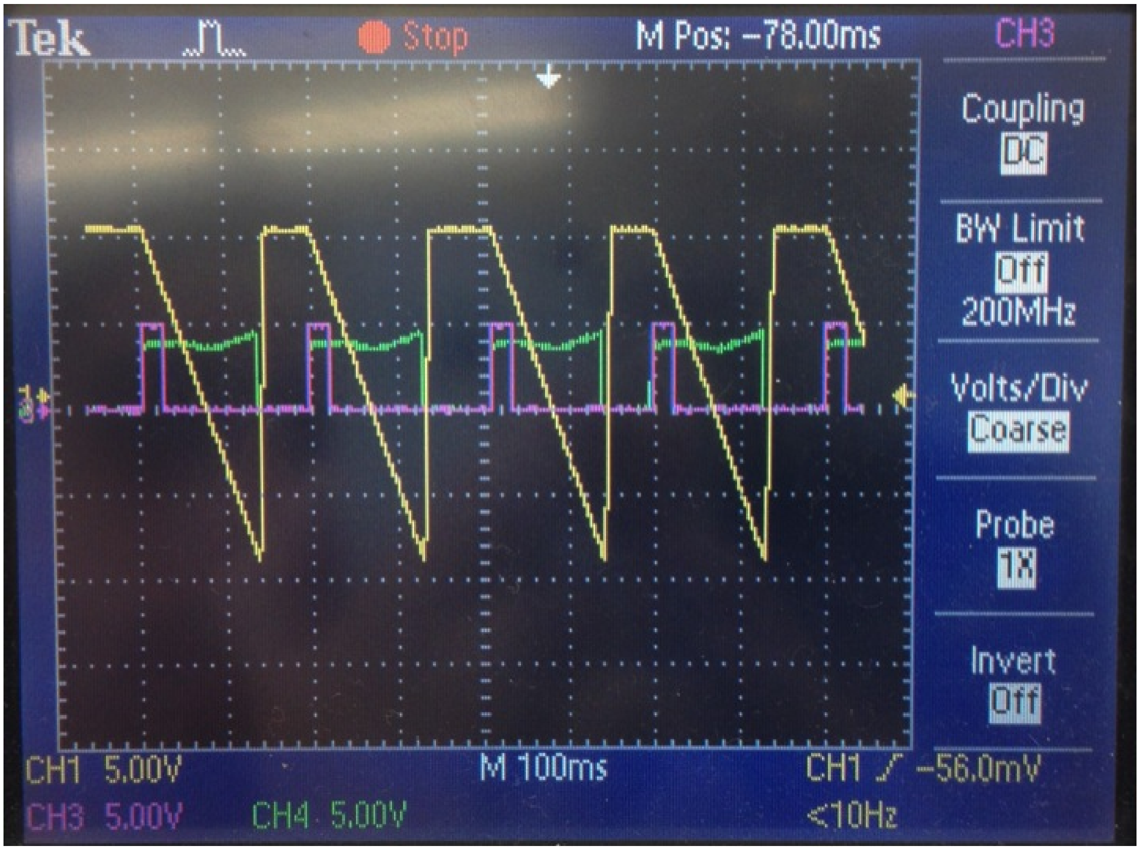

Figure A.10: Arduino output signal (purple) for triggering the linear and rotational motors. The inverting differentiator and rectifier circuit (green) and x-galvanometer signal (yellow) are also traced.

This Arduino program is used for both volumetric and longitudinal imaging. Simply ensure that the rotational motor driver is powered off during longitudinal imaging. The Arduino code is executed automatically after powering on the device.

A.3.3 Motor driver configuration and software

Both the rotation stepper motor (416-07-05D, Lin Engineering, Morgan Hill, CA) and linear actuator (4-A.083-HT17-2-B/3, Ultra Motion, Cutchogue, NY) are controlled by the same model motor driver (3540i, Applied Motion Products, Watsonville, CA). The motor drivers are programmed using the Si Pro-

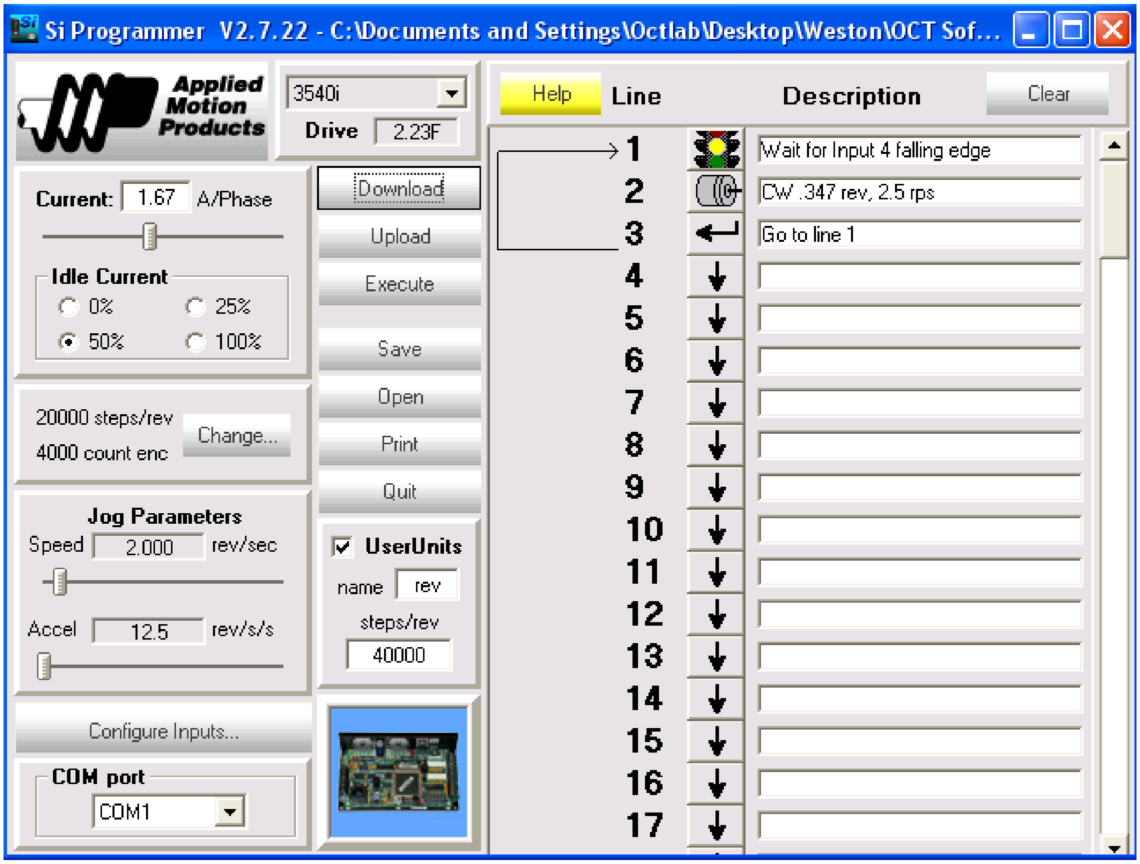
Si Programmer V2.7.22 - C:\Documents and Settings\Octlab\Desktop\Weston\OCT Sof...

3540i

Drive 2.23F

Current: 1.67 A/Phase

Idle Current

○ 0%
○ 25%
● 50%
○ 100%

20000 steps/rev

4000 count enc

Jog Parameters

Speed 2.000 rev/sec

Accel 12.5 rev/s/s

☑ UserUnits

name rev

steps/rev 40000

COM port COM1

Line	Description
1	Wait for Input 4 falling edge
2	CW .347 rev, 2.5 rps
3	Go to line 1
4	
5	
6	
7	
8	
9	
10	
11	
12	
13	
14	
15	
16	
17	

Figure A.11: Si Programmer program for rotational motion for volumetric imaging.

grammer software from Applied Motion. Three main programs are used for endoscopic imaging with the OCS1050SS: rotational motion for volumetric imaging (`RotationalMotionNoOutput.SI5`, Fig. A.11), linear motion for volumetric imaging (`LinearMotionR9.SI5`, Fig. A.12), and linear motion for Doppler imaging (`DopplerLinearMotionR1.SI5`, Fig. A.13).

The Arduino Uno output (pin 4) is connected to the Input 4 pin on both drivers. Each of the programs triggers when the Arduino outputs a high signal on the motor driver inputs (due to the circuit configuration on the motor drivers, falling edge and low signals on the Si Programmer correspond to digital high pulses).

In addition to the commands shown in Figs. A.11, A.12, and A.13, motor acceler-

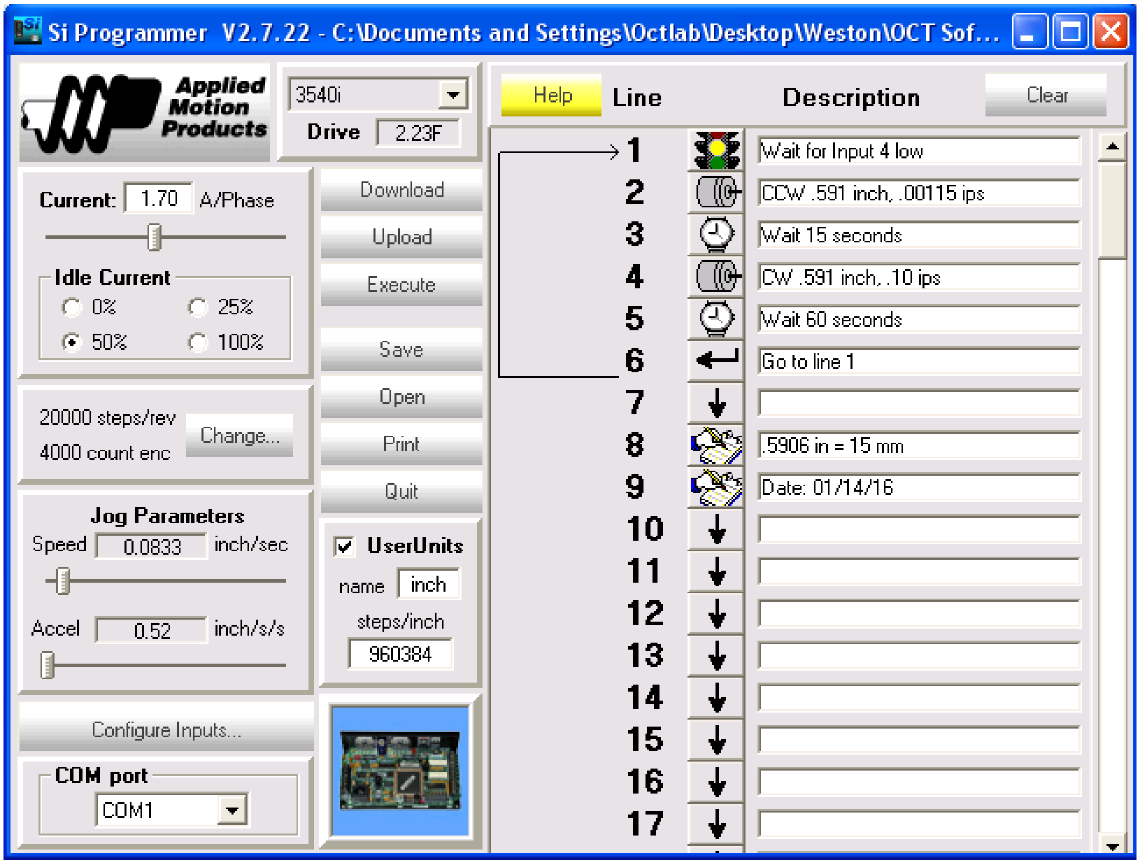

Si Programmer V2.7.22 - C:\Documents and Settings\Octlab\Desktop\Weston\OCT Sof...

3540i

Drive 2.23F

Current: 1.70 A/Phase

Idle Current
○ 0% ○ 25%
● 50% ○ 100%

20000 steps/rev
4000 count enc

Jog Parameters
Speed 0.0833 inch/sec
Accel 0.52 inch/s/s

☑ **UserUnits**
name inch
steps/inch 960384

COM port COM1

Line	Description
1	Wait for Input 4 low
2	CCW .591 inch, .00115 ips
3	Wait 15 seconds
4	CW .591 inch, .10 ips
5	Wait 60 seconds
6	Go to line 1
7	
8	.5906 in = 15 mm
9	Date: 01/14/16
10	
11	
12	
13	
14	
15	
16	
17	

Figure A.12: Si Programmer program for linear motion for volumetric imaging.

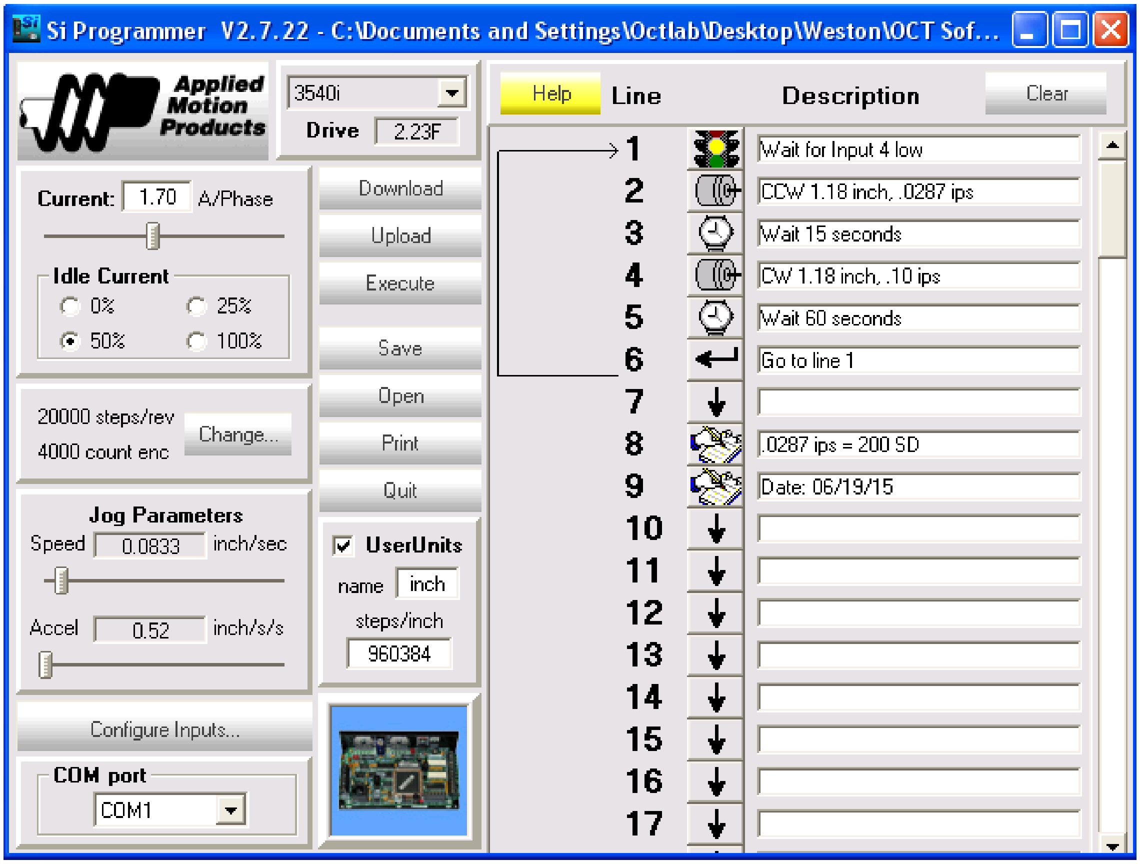

Si Programmer V2.7.22 - C:\Documents and Settings\Octlab\Desktop\Weston\OCT Sof...

3540i

Drive 2.23F

Current: 1.70 A/Phase

Idle Current

○ 0% ○ 25%

● 50% ○ 100%

20000 steps/rev

4000 count enc

Jog Parameters

Speed 0.0833 inch/sec

Accel 0.52 inch/s/s

☑ UserUnits

name inch

steps/inch

960384

COM port

COM1

Line	Description
1	Wait for Input 4 low
2	CCW 1.18 inch, .0287 ips
3	Wait 15 seconds
4	CW 1.18 inch, .10 ips
5	Wait 60 seconds
6	Go to line 1
7	
8	.0287 ips = 200 SD
9	Date: 06/19/15
10	
11	
12	
13	
14	
15	
16	
17	

Figure A.13: Si Programmer program for linear motion for Doppler (longitudinal) imaging.

Program	Parameter			Analysis		
	Distance	Speed	Accel	Accel	At Speed	Total
Rotation Volumetric	0.3472	2.5	300	0.008	0.131	0.147
Linear Volumetric	0.5906	0.00115	2.08	0.001	515.639	515.640
Linear Doppler	1.18	0.02869	2	0.014	41.121	41.148

Table A.1: Motor parameters not shown in program figures and timing analysis. Distances are in the `UserUnits` defined in each program (revolutions for rotational motion and inches for linear motion). Timing analysis is in seconds. Accel: acceleration and deceleration.

ation is also user-defined in the movement commands (Feed to Length commands). The values displayed in these figures are also rounded to 3 decimal places. The exact values are shown in Table A.1.

In essense, the rotational motor completes one full rotation and comes to a complete stop for each B-scan during volumetric imaging, and the linear actuator moves constantly at a slow velocity. The rotation program moves 0.347 revolutions because there is a gear ratio of 0.347 between the larger spur gear attached to the rotational stepper motor and the spur gear on the body of the fiber-optic rotary joint. The rotational motor comes to a complete stop every B-scan because there is a period of no data acquisition between each B-scan that corresponds to the rapid return sweep of the x-galvanometer mirror in the original OCS1050SS imaging probe. The acceleration and deceleration are set to high values to minimize the duration of non-constant rotational velocity during each B-scan. The non-constant velocity causes oversampling artifacts on the left and right ends of each B-scan. The rotational motor velocity on the Si Programmer and the x pixels and x length on the Thorlabs OCT software can be adjusted to control the spatial sampling during rotation. When the settings in Fig. A.11 are used with 2000 x pixels and 6.00 mm x length, the spatial sampling along the circumferential direction of the colon is approximately 2 samples per spot radius ($\Delta x = 2\pi(1\text{ mm})/2000 = 3.1\,\mu\text{m}$, where the colon radius is approximately 1 mm). The linear actuator velocity is set to sample with a helical pitch of approximately 1 sample per spot radius (Δy = 15 mm/2400 =6.3 µm), when imaging 15 mm of the colon with 2400 B-scans per volume (200 y pixels and 12 volumes per mouse).

During Doppler imaging, the linear velocity is chosen to produce about 80 samples per spot diameter (2000 x pixels and 216 y pixels with each frame concatenated to form a single B-scan over a distance of 30 mm). As in volumetric imaging, the linear motion is triggered at the beginning of imaging and continuously moves for the duration of imaging.

A.4 Switching between endoscope and handheld probe modes

The Thorlabs OCS1050SS can operate using the original handheld probe or the custom endoscope for imaging. At the time of this writing, the optical tube mount containing filters located in the reference arm of the Imaging Module must be removed to match the optical path lengths of the reference arm to the sample arm consisting of the endoscope, fiber-optic rotary joint, and patch cable. This section describes the method for switching from the commercial probe mode to the endoscope mode. The steps for converting from the endoscope to the handheld probe are simply the reverse of the following instructions.

1. Remove the top cover of the Imaging Module. Figure A.14 shows the interior of the Imaging Module after removing the cover.
2. Increase reference arm optical path length by turning the Optical Delay adjustment screw counterclockwise until the screw is no longer in contact with the translation stage. This step ensures that the translation stage spring is fully relaxed before detaching the translation stage from the Imaging Module chassis.

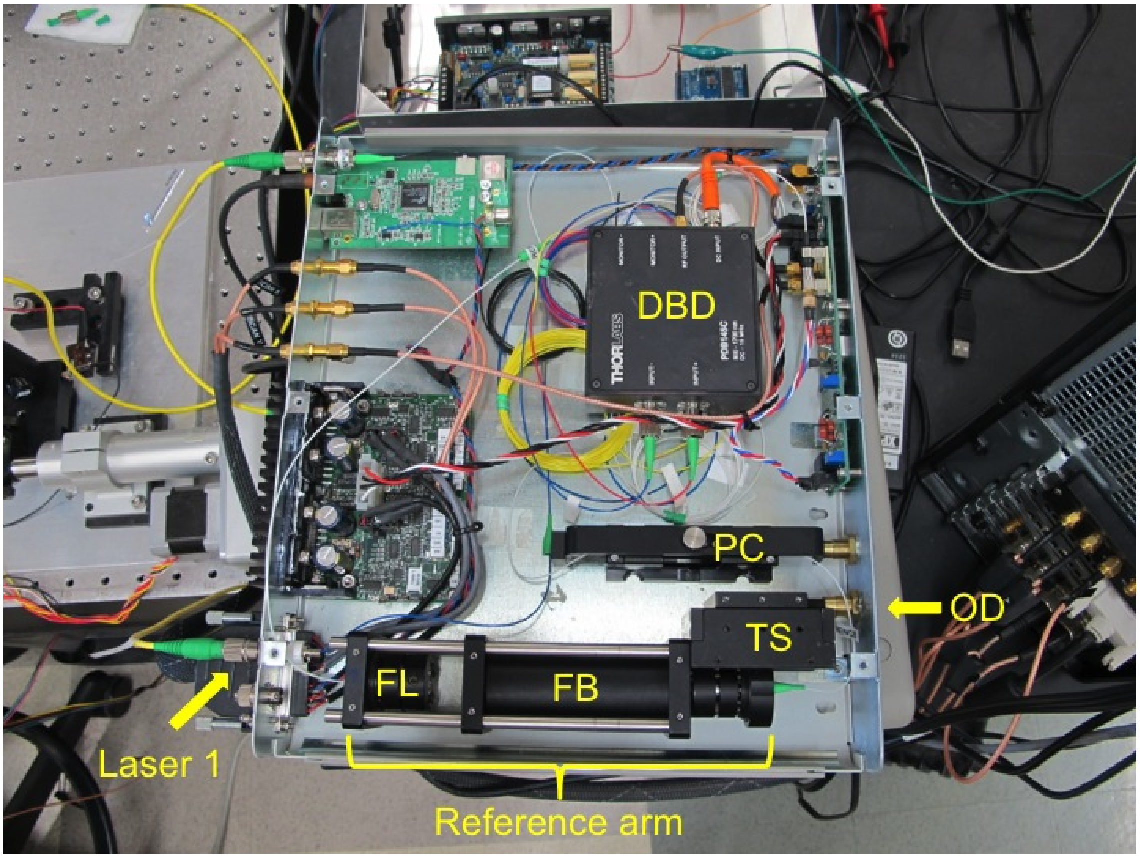

Figure A.14: Imaging Module interior after removing top cover with parts referenced in this section labeled in yellow. FL: fiber-laser mount; FB: filter barrel; TS: translation stage; OD: optical delay adjustment screw; PC: polarization controller; DBD: dual-balanced detector.

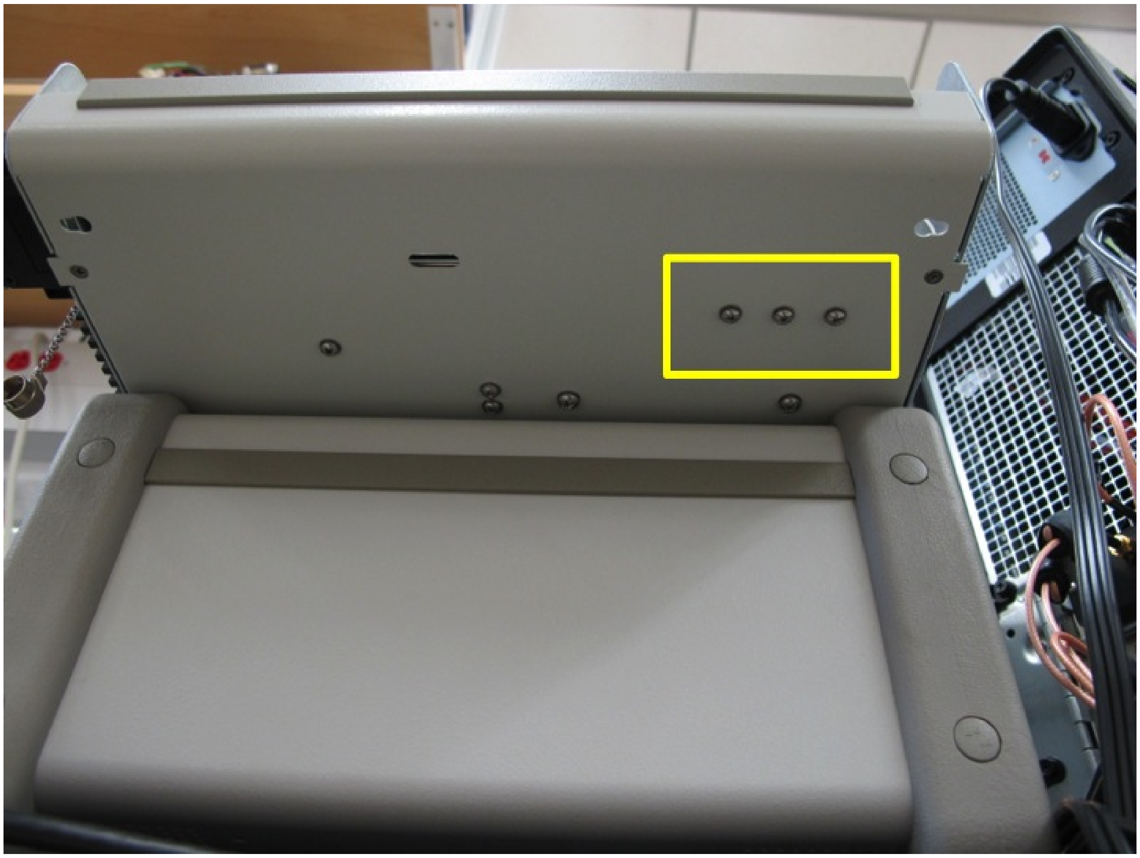

Figure A.15: Imaging Module translation stage screws.

3. Remove the three screws from the bottom of the Imaging Module chassis that secure the translation stage.The Imaging Module can partially hang over the Swept Source Engine to remove the screws, but be careful to not strain the fiber connecting the Imaging Module and Swept Source Engine. The screws are highlighted in Fig. A.15.

4. Loosen the 4 set screws attaching the fiber-lens mount labeled in Fig. A.14 to the cage frame. When rotating the reference arm to reach the screws on the bottom, be careful to not damage the blue interior fiber connected to the Laser 1 port by bending too much. Also, the reference arm fiber connecting the fiber-lens mount near the translation stage to the polarization controller is

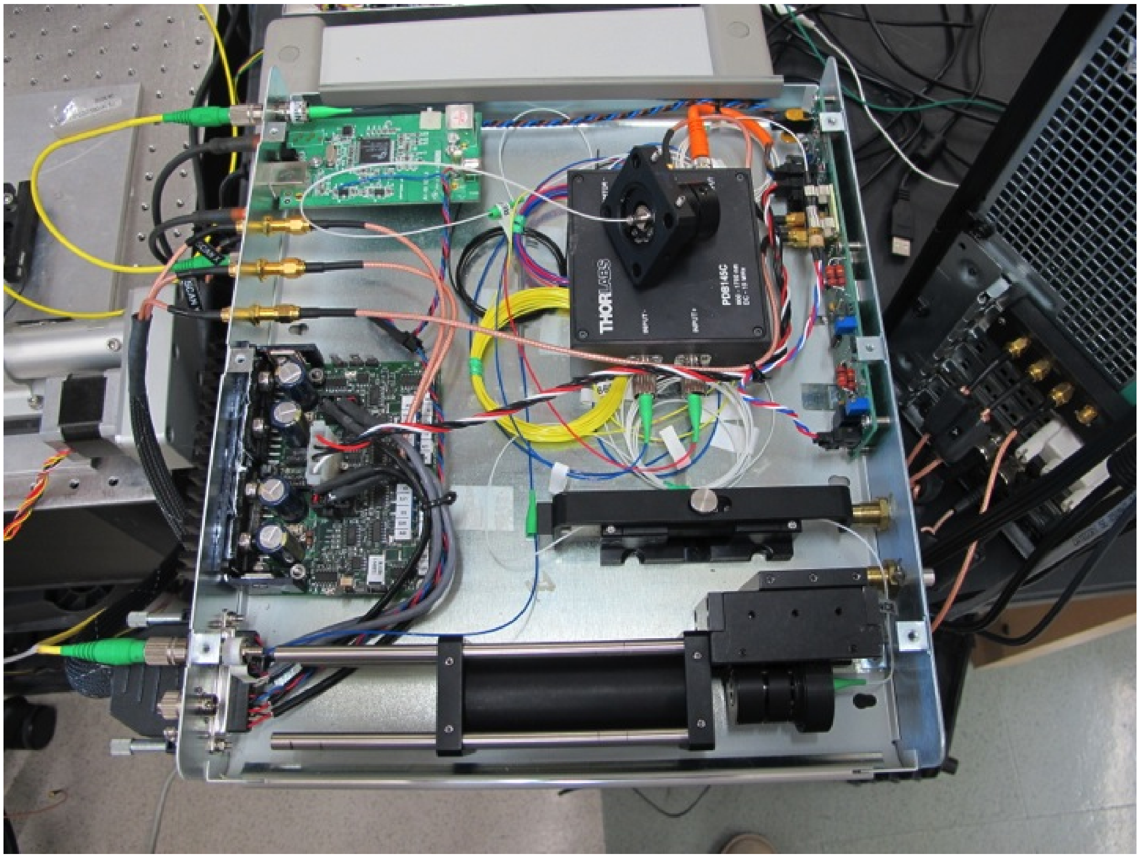

Figure A.16: Fiber-lens mount removed and placed atop the dual-balanced detector.

very short, so be careful to not attempt to physically remove the reference arm from the Imaging Module. Set the removed fiber-lens mount aside as shown in Fig. A.16; it will be replaced momentarily.

5. Loosen the 4 set screws attaching the filter barrel labeled in Fig. A.14 to the cage frame. Remove the filter barrel and store until the OCT system needs to be returned to handheld probe mode.

6. Replace the fiber-lend mount removed in Step 4 to the cage mount. Place the mount at the location shown in Fig. A.17. This location is also marked on the cage bars with permanent marker. To assist in maintaining alignment, the

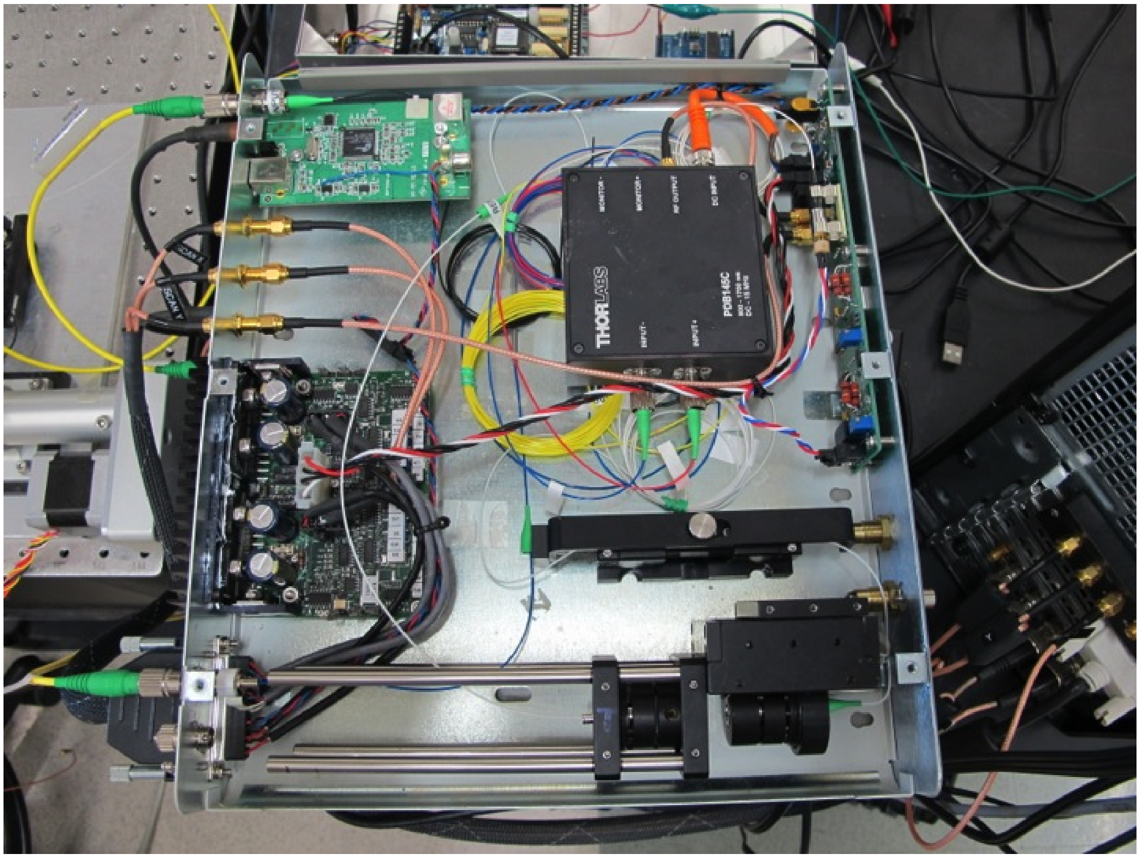

Figure A.17: Fiber-lens mount replaced after removing filter barrel.

side of the fiber-lens mount that should always be facing upward is marked with a “T” from a permanent marker.

7. Secure the reference arm to the Imaging Module chassis with the three screws removed in Step 3. Shorten the reference arm optical path length by turning the Optical Delay screw clockwise until it is near the end of its travel length.
8. Disconnect the sample-arm fiber from the Laser 1 port on the rear of the Imaging Module.
9. Disconnect one of the input fibers (“Input −” or “Input +”) from the dual-balanced detector and connect the fiber to the input of a New Focus fiber

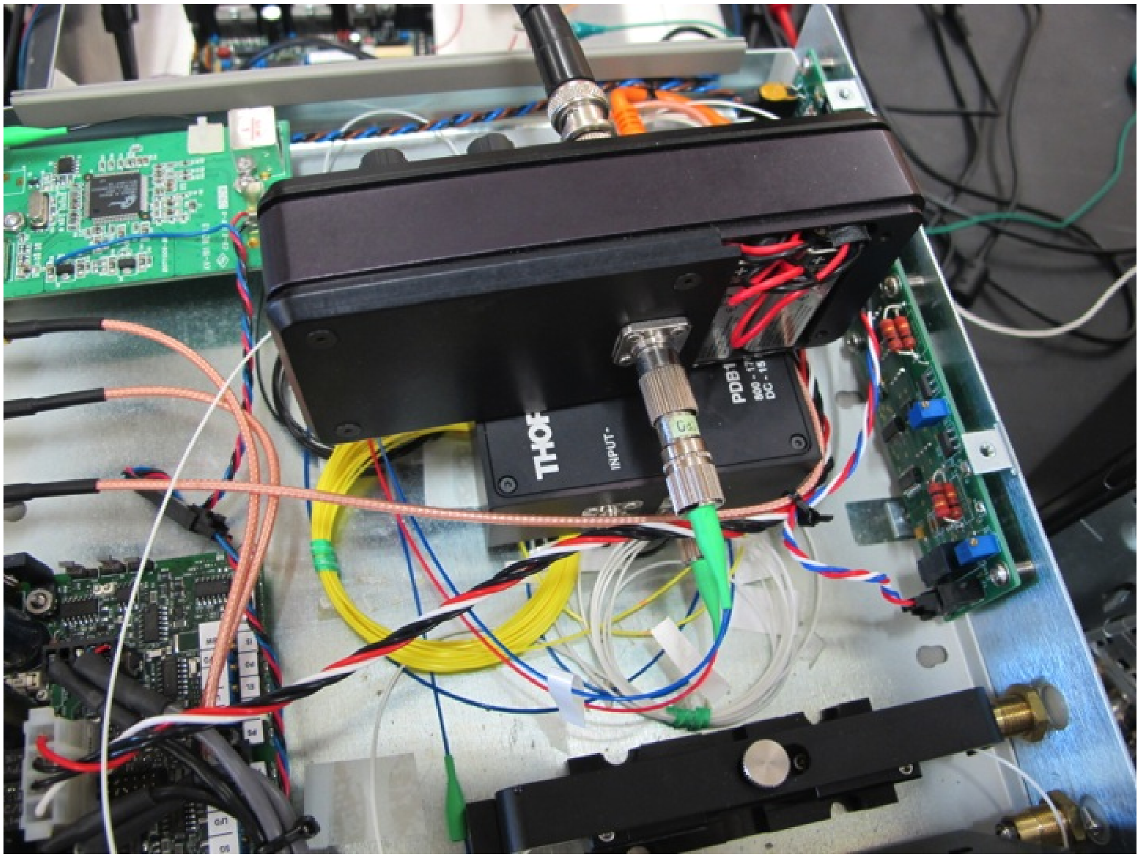

Figure A.18: Measuring reference-arm power using the “Input −” fiber.

power meter. The dual-balanced detector input fibers are short, so the power meter should rest on its side on top of the detector as shown in Fig. A.18. Make sure to use an appropriate power meter for the wavelength range of the OCS1050SS (1000 nm to 1080 nm), such as the model shown in Fig. A.19. Set the frequency range to the maximum range (DC to max). Initially set the gain to its maximum (3×10^4). Use a BNC connector to connect the output of the power meter to an oscilloscope.

10. Turn on Swept Source Engine and turn on imaging laser. If no signal is displayed on the oscilloscope, try reducing the power meter gain. The power meter outputs no voltage when the signal gain is high enough to saturate most

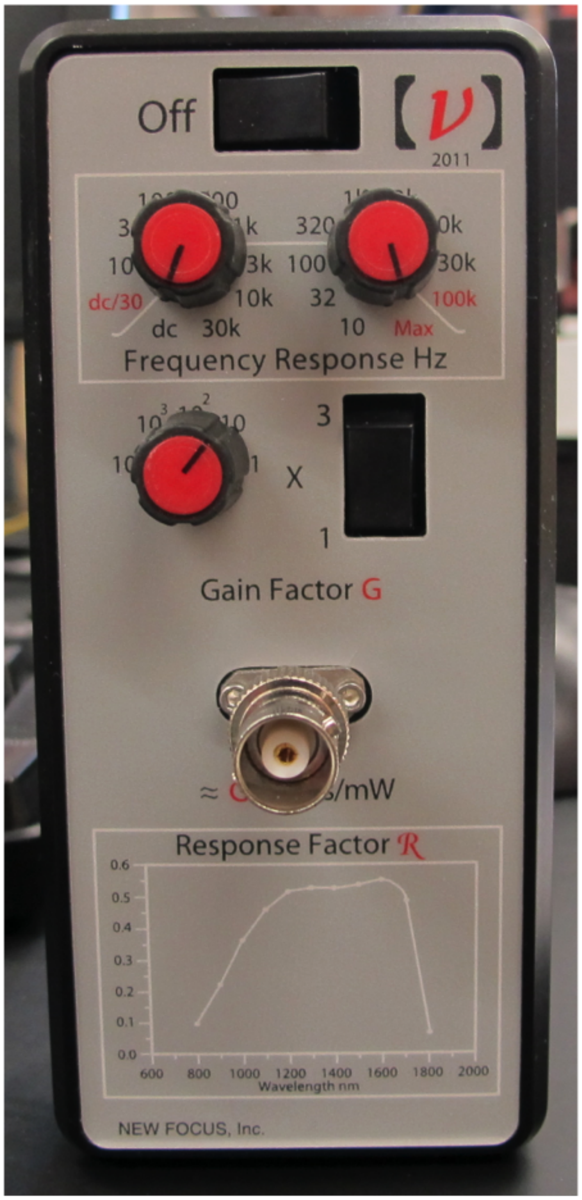

Figure A.19: New Focus power meter for measuring reference-arm throughput.

of the measured signal.

11. Adjust the vertical and horizontal tilt on the fiber-lens mount that was moved closer to the translation stage to maximize light throughput. Figure A.20 shows the two screws that adjust the tilt. You can tug the barrel in both vertical and horizontal directions while watching the oscilloscope to determine the direction of tilt adjustment to increase throughput. Typically, each screw will require less than one quarter turn to maximize throughput. You will need to reduce the gain on the power meter throughout this process to avoid saturation. Stop once you cannot increase power throughput any more. A well-aligned reference arm should produce the signal shown in Fig. A.21. The forward and reverse sweeps should be approximately mirrored horizontally.

12. Disconnect power meter and replace the appropriate fiber to the dual-balanced detector.

13. Connect the endoscope patch cable to the Laser 1 port on the Imaging Module and verify that light is exiting the endoscope. The cover can now be replaced on the Imaging Module.

14. Launch the Thorlabs imaging software and begin 2D imaging. Place a target near the endoscope window (e.g., mirror or cotton wrap). Adjust the Optical Delay screw until the sample is near the top of the screen and ensure that the sample or endoscope window signals are not overlapping due to wrap-around. With the endoscope and patch cable used at the time of this writing, the Optical Delay screw is typically tightened as far as it can travel. Note that the OCT image will be highly degraded in depth due to dispersion mismatch between the reference and sample arms. This is corrected in post-processing with a Matlab script described in Sec. A.6.

The conversion process is now complete. Converting from endoscope to handheld

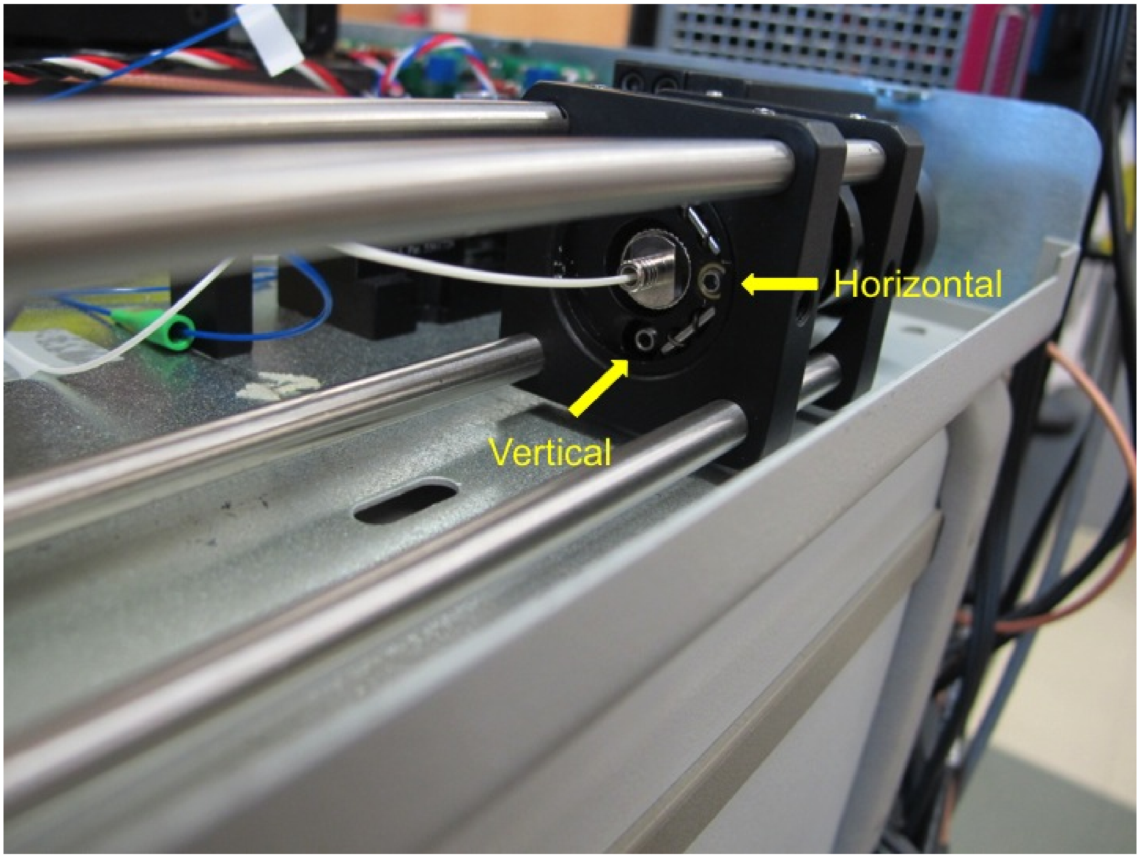

Figure A.20: Screws for adjusting vertical and horizontal tilt on fiber-lens mount.

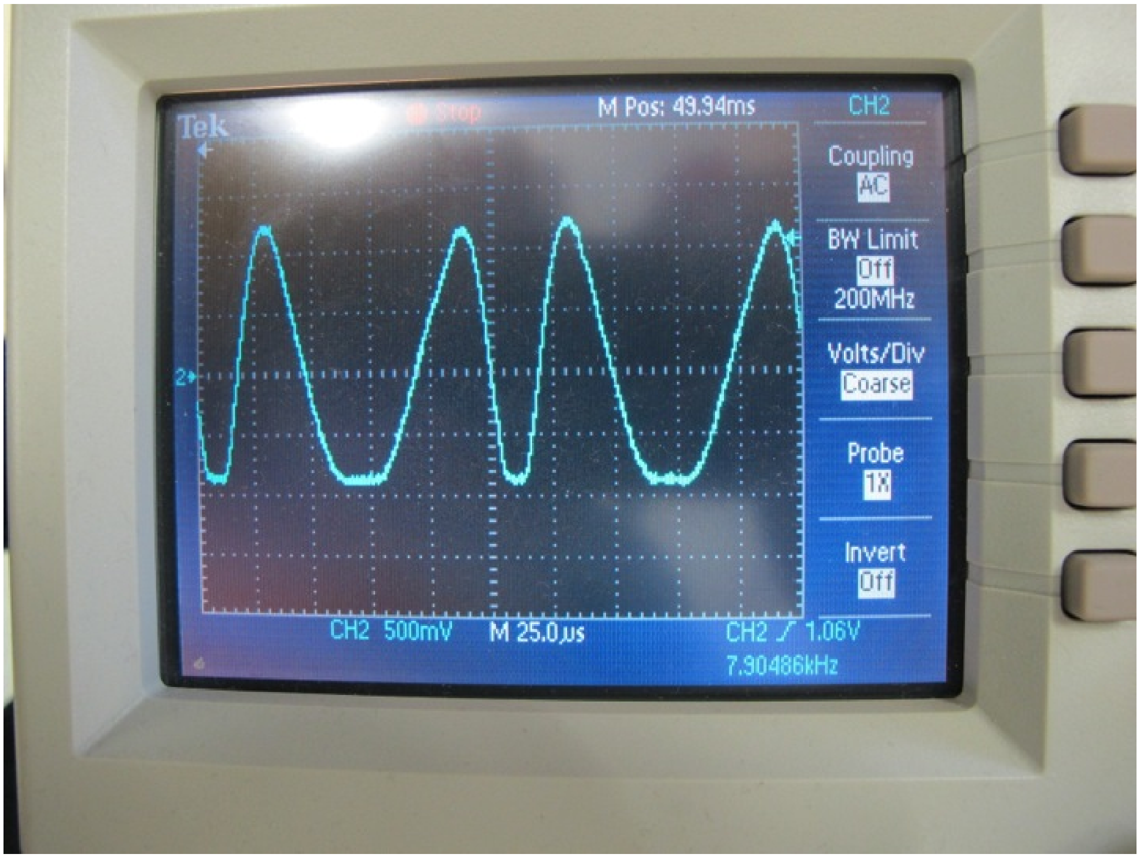

Figure A.21: Aligned reference-arm time-varying power signal with detector gain set to 30.

Component	Voltage
IDR	
LT1097 pin 7	10 V
LT1097 pin 4	−10 V
3450i motor drivers	
Rotational motor	25 V
Linear actuator	25 V

Table A.2: Power supply settings for endoscopic imaging with OCS1050SS. IDR: inverting differentiator and rectifier circuit.

probe mode is nearly identical. Remember to turn the Optical Delay screw counterclockwise until it is not in contact with the translation stage before detaching the translation stage from the chassis. The ideal location of the fiber-lens mount for handheld probe mode is also marked on the cage rods. The fiber-lens mount tilts will need to be adjusted to maximize throughput after returning the filter barrel to the reference arm and moving the mount to the end of the cage bars. The OCT image displayed in real-time 2D imaging will not require any post-processing for correction. When converting to handheld probe mode, adjust the Optical Delay until the image signal intensity is maximized and make sure the sample is located near the focus on the probe beam.

A.5 Procedure for OCS1050SS imaging using endoscope

This section describes the steps for operating the Thorlabs OCS1050SS in endoscope mode for volumetric (helical scanning) imaging and longitudinal imaging. The appropriate power supply settings are shown in Table A.2.

1. Power on PC.
2. Power on OCS1050SS by flipping the power switch on the Swept Source Engine.

3. Launch Thorlabs Swept Source OCT Imaging System software.
4. Connect 3540i programming cable (DB-9 to cat 3) to linear actuator motor driver.
5. Open Si Programmer software.
6. Power on 3540i linear actuator driver.
7. **(volumetric)** Power on 3540i rotational motor driver.
8. Power on inverting differentiator and rectifier circuit.
9. Power on Arduino Uno by connecting to PC via USB or using a DC power supply.
10. Turn on OCT laser by pressing Laser Enable button on Swept Source Engine. Optional: Turn on aiming laser by pressing Aim Enable button on Imaging Module.
11. Choose .FRG fringe file type (necessary for numerical dispersion compensation) and file name to save by selecting Recording>Setup... on the OCT software. Safe software to the local hard drive and later copy to the server.
12. Select the 3D Mode tab and enter the desired imaging parameters. To adjust number of A-scans to average, select the 2D Mode tab and change the value for Average number (this will apply to 3D imaging). The images reported in Sec. A.1 were collected without averaging.
13. To begin imaging, click Execute on Si Programmer, then press the green arrow button on the OCT software.
14. After the linear actuator returns to the home position, select Stop on the Si Programmer to prevent transient electric signals from triggering motion before the next image acquisition.

15. To image again, select a new filename from Recording>Setup... on the OCT software, select Execute on Si Programmer, and select the green arrow on the OCT software.

After the imaging session is complete:

1. Power off motor drivers.
2. Power off inverting differentiator and rectifier circuit.
3. Power off Arduino Uno.
4. Close Si Programmer and Thorlabs OCT software.
5. Turn off OCT laser and aiming laser by pressing the appropriate buttons on the Imaging Module and Swept Source Engine, then turn off the power to the OCS1050SS by pressing the power button on the Swept Source Engine.
6. If necessary, clean endoscope glass window with a Kimwipe and Edmund Scientific Tech Spec lens cleaner.
7. Copy any imaging files to the server and delete copies on the local hard drive.

Longitudinal and volumeric imaging in general use two different programs for the linear actuator. The following steps explain how to reprogram the 3540i motor driver.

1. With the motor driver powered off, connect the programming cable to the driver.
2. Launch the Si Programmer software.
3. Power on the motor driver. The Drive box on the Si Programmer should now display a number.

4. To view the code currently loaded on the driver, select Upload. This will also update the motor parameters (Current, UserUnits, Current).
5. Load an existing program with Open (`DopplerLinearMotionR1` for Doppler longitudinal imaging, `linearMotionR9` for volumetric linear motion, `rotationalMotionR4` for volumetric rotational motion).
6. Select Download to load the program onto the motor driver.
7. To execute the code while connected to the PC, select Execute. When not connected to the PC, the program will automatically run as soon as the driver is powered on.[1]

The images will need to be numerically dispersion corrected to improve the axial resolution. The method and software are described in Sec. A.6. The following steps describe how to use the dispersion compensation software.

1. Launch MATLAB on a PC with at least 8 GB of RAM (the software has been verified to work properly using MATLAB 2014b, 2015a, and 2015b).
2. Change working directory to `R:\Software\OCS1050SS Dispersion compensation software\`
3. Run appropriate program (`correctDispersionLongBscan.m` or `correctDispersionVolumetric.m`). You will be prompted to select the `.FRG` file to correct and a directory to save the corrected images.
4. Volumetric data are saved as one TIFF image per frame, along with a file `list.txt` that shows the order of the frames. To save the entire volume as a single TIFF stack, load ImageJ, select File>Import>Stack From List...

---

[1] The motor driver can process much faster when disconnected from the PC. This is necessary for the rotational motion program to run properly during volumetric imaging.

and chose the `list.txt` file. Then save the resulting stack with File>Save As>TIFF....

A.6 Numerical dispersion correction

The sample-arm optics used at the time of this writing have a mismatch of dispersive media with respect to the reference arm. This causes a significant increase in the axial PSF and severely degrades image quality. The simplest method of fixing a dispersion mismatch in OCT is to introduce a variable-thickness prism pair in the arm with less dispersion and adjust the thickness of the glass until the axial resolution degradation is corrected. This is not possible in the OCS1050SS because the reference arm contains very little room for additional optics. Instead, I correct the dispersion numerically by post-processing the raw fringe data. The numerical compensation fully corrects for axial image degradation. Because the method requires processing the data after imaging, it can be difficult to interpret the image data acquired in real time. The following sections describe the theory of the dispersion compensation (Sec. A.6.1), how to generate the calibration file necessary for correction (Sec. A.6.2), and the MATLAB script (Sec. A.6.3).

A.6.1 Theory

Dispersion is the phenomenon by which the index of refraction in a medium depends on wavelength (or, equivalently, the speed of light in a medium changes with wavelength). The frequency of the sinusoidal fringes in OCT are proportional to the OPD of a reflector. Therefore, the resulting A-scans are over OPD and not simply depth. When different wavelengths of light experience different indices of refraction in the sample and/or the optical system, the OPD differs with wavelength. Therefore, the location of the scatterer in the sample appears to be at different depths for different wavelengths. The result is that the scatterer is “blurred” in depth in the OCT image. While refractive index is in general a function of wavelength, it is not typically a problem in narrow-band interferometers. However, bandwidths of typical OCT sources are often broad enough that dispersion must be considered.

Mathematically, the dispersion relation relates the wavenumber, refractive index, wavelength, and phase velocity as

$$k = \frac{2\pi n(\omega)}{\lambda_0} = \frac{n(\omega)\omega}{c} = \frac{\omega}{v_p}, \tag{A.2}$$

where ω is angular frequency, λ_0 is the vacuum wavelength, c is the speed of light in vacuum, and v_p is the phase velocity. The phase velocity $v_p = \frac{c}{n(\omega)}$ refers to the velocity of an individual monochromatic plane wave component of a general wave consisting of multiple wavelengths.[2]

When two or more wavelengths of light overlap in space and time, the light can be represented as a linear superposition of plane waves. An example superposition of two plane waves of different wavelengths can be described as

$$\begin{aligned} U(z,t) &= \cos(k_1 z - \omega_1 t) + \cos(k_2 z - \omega_2 t) \qquad &\text{(A.3)} \\ &= 2\cos(k_\Delta z - \omega_\Delta t)\cos(k_\Sigma z - \omega_\Sigma t), \qquad &\text{(A.4)} \end{aligned}$$

where $k_\Delta = k_1 - k_2$, $k_\Sigma = k_1 + k_2$, $\omega_\Delta = \omega_1 - \omega_2$, and $\omega_\Sigma = \omega_1 + \omega + 2$. The first cosine in Eq. (A.4) describes a slowly varying envelope and the second cosine describes a rapidly oscillating phase (sometimes called the carrier). In this example, the phase velocity describes the speed at which the phase propagates and is given by

$$v_p = \frac{\omega_\Sigma}{k_\Sigma}. \tag{A.5}$$

The slowly varying envelope propagates at the group velocity:

$$v_g = \frac{\omega_\Delta}{k_\Delta}. \tag{A.6}$$

---

[2] Note that the phase velocity can exceed the vacuum speed of light when $n(\omega) < 1$, however this does not imply that any physical component of light is actually exceeding c. This is simply the result of describing a wave as a linear superposition of plane waves and plane waves cannot exist in reality due to their infinite extent in space and time.

In general, the group velocity is defined as

$$v_g \equiv \frac{d\omega}{dk}. \tag{A.7}$$

In a non-dispersive media, the phase and group velocities are both equal to c. However, light passing through dispersive media experiences a change in group velocity as a function of wavelength because $k = \frac{2\pi n(\omega)}{\lambda_0}$ is a function of ω. As polychromatic light passes through dispersive media, the monochromatic plane waves that comprise the total wave travel at different velocities and change their phase relative to one another.

In OCT, light travels through two interferometer arms that contain, in general, different amounts of dispersion. When the light from each arm reaches the detector, the total phase offset due to dispersion can be represented as $\phi(k)$, so the wave amplitude at the detector is

$$U_D(k) = U_r(k)e^{i\phi_r(k)} + U_s(k)e^{i\phi_s(k)}, \tag{A.8}$$

where

$$\phi(k) = 2\int_0^z k(\omega,\zeta)d\zeta \tag{A.9}$$

represents the total accumulated phase (or phase retardance) from traveling a distance $2z$ in dispersing media. The intensity on the detector is

$$I_D(k) \propto \mathrm{DC} + S(k)\cos(2kOPD + \phi_{\mathrm{disp}}(k)), \tag{A.10}$$

where

$$\phi_{\mathrm{disp}}(k) = \phi_r(k) - \phi_s(k) \tag{A.11}$$

is the phase due to dispersion mismatch in the interferometer. The phase due to dispersion is, by definition, non-linear as a function of k (if it were linear, then the group velocity would be constant, which implies that the individual plane wave components are not traveling at different velocities).

The effect of ϕ_{disp} can be conceptualized from the Fourier shift theorem. In Fourier-domain OCT systems, the measured signal can be represented as a function of wavenumber as in Eq. (A.10). An A-scan is generated by taking the inverse Fourier transform of the measured fringe signal.

$$\begin{aligned} A(z) &= \mathcal{F}^{-1}\left\{\cos(2kOPD + \phi_{\text{disp}}(k))\right\} && \text{(A.12)} \\ &= \delta(z \pm (2OPD + \phi_{\text{disp}}(k))) && \text{(A.13)} \end{aligned}$$

Because $\phi_{\text{disp}}(k)$ is non-linear in k, the amount of shift of the delta function changes with each plane wave component. Therefore, rather than simply shifting the delta function representing the location of a reflector, the delta function is “stretched” or broadened.

Various methods have been proposed for numerically correcting dispersion in OCT[64, 65, 66, 67]. Dispersion can be expressed as a Taylor series.

$$\begin{aligned} \phi(k) = \phi(k_0) + \left.\frac{d\phi(k)}{dk}\right|_{k_0}(k_0 - k) + \frac{1}{2}\left.\frac{d^2\phi(k)}{dk^2}\right|_{k_0}(k_0 - k)^2 + \dots \\ + \frac{1}{n!}\left.\frac{d^n\phi(k)}{dk^n}\right|_{k_0}(k_0 - k)^n \qquad \text{(A.14)} \end{aligned}$$

The first term describes the initial phase offset from the source (relative to the center wavenumber k_0) and the second term is the group velocity. The third term describes the group velocity dispersion, which describes how the envelope evolves over length in a dispersive media. The higher-order terms describe non-linear dispersion.

Fercher [67] developed a dispersion compensation method that uses correlation of the chirped OCT signal with a phase term corresponding to only the quadratic term of the dispersion function. This relies on the property that the autocorrelation of quadratic functions yields a delta function, as well as the linearity of the correlation and convolution operators. If a degraded OCT signal can be adequately described as containing primarily quadratic dispersion, then

$$J_{\text{Disp}}(z; L) = J(z) * Q(z; L), \qquad \text{(A.15)}$$

where $J(z)$ is the axial PSF without degradation due to dispersion and $Q(z; L)$ is the quadratic dispersion term for a dispersive media of length L. If $Q(z; L)$ can be described analytically, such as with the Sellmeier formula for determining $n(\lambda)$, then the quadratic dispersion can be effectively removed in post-processing by correlating the empirical complex A-scan with the convolution of the PSF and analytic quadratic phase term.

$$\begin{aligned} A_{\mathrm{DispComp}}(z) &= A(z) \otimes [J(z) * Q(z)] && \text{(A.16)} \\ &= [R(z) * J(z) * Q(z)] \otimes [J(z) * Q(z)] && \text{(A.17)} \\ &= R(z) * [J(z) \otimes J(z)] * [Q(z) \otimes Q(z)] && \text{(A.18)} \\ &= R(z) * [J(z) \otimes J(z)] * \delta(z) && \text{(A.19)} \\ &= R(z) * J(z) \otimes J(z) && \text{(A.20)} \end{aligned}$$

In the above equations, $R(z)$ is the reflectivity profile as a function of depth. The delta function changes with depth, so the convolution of the other functions with $\delta(z)$ does not change the arguments of the other functions to $z = 0$. This method is computationally simple, but only corrects for the quadratic term of dispersion and requires an analytic representation of that quadratic term. These limit its usefulness to biological imaging or in applications with significant higher-order dispersion.

Cense [64] briefly describes a method of numerical dispersion compensation that seems to me to be based on the Fourier shift theorem. They average a series of A-scans collected from a strong reflective surface beneath dispersive media (fovea of a model and real human eye). This strong reflector acts as an estimate of the coherence function or axial PSF of the system. They shift the A-scan pixels until the reflector is centered at the zero OPD point (top of the image) and then take the Fourier transform. They apply the argument operator to the resulting fringe data, which returns a phase based on the shift amount by the Fourier shift theorem.

$$\mathcal{F}\left\{A(z - z_0)\right\} = I(k)e^{-i2\pi k z_0} \tag{A.21}$$

The phase $2\pi k z_0$ is fit with a 9-degree polynomial. This polynomial forms a correction term of an exponential with opposite sign and is multiplied to the original fringe data to remove dispersion. They report great improvement in the axial PSF, though I was unable to replicate the results. The shift theorem does not fully apply in this case because the dispersion term is non-constant.

Wojtkowski [65] uses a merit function based on the sharpness or width of a mirror object approximation to the axial PSF. They iteratively determine a weighting term for the second- and third-order dispersion terms in the Taylor series expansion and apply the correction to the original fringe data and re-compute the merit function, defined as the number of pixels in depth above a threshold. The method is theoretically simple, but determining the appropriate weights for the global minimum can be difficult to achieve. I attempted to first minimize the quadratic weight because this term should contribute the most degradation, followed by the third-order weight. I also used the `fmincon` function in MATLAB to determine the coefficients to minimize the merit function. Finally, I used the MATLAB genetic algorithms tools to attempt to find the global minimum in the solution space. In each case, I was unable to significantly reduce axial broadening without introducing significant asymmetric oscillations on the final OCT image.

The method I implemented is similar to the method described by Marks [66] and Winkler [4]. Marks describes a method for using empirical measures of the dispersion $k(\omega)$ in the delay line of a time-domain OCT system and a dispersive slab of medium. His method assumes chirping of the interferogram as a result of the delay mechanism, which does not apply to Fourier-domain OCT methods. His method is generalized to sample media consisting of multiple slabs with their own dispersion functions. The method described here assumes the sample introduces negligible dispersion and is not appropriate for all biological samples. I correct dispersion in a similar manner to Winkler; however, the calibration method is different.

If a mirror is used as the sample and is at some distance other than zero OPD, the measured interferogram (linear in wavenumber) is given by Eq. (A.10). The goal is to measure the system dispersion $\phi_{\text{disp}}(k)$. If data are first acquired with the sample arm disconnected, a realistic measure of the DC term is saved.[3] Next, data are acquired with the sample arm connected and a mirror as the sample. The DC term is effectively removed by subtracting the reference-arm-only signal from this interferogram. The argument of the cosine can be extracted by unwrapping the angle of the Hilbert transform of the interferogram.

$$\text{unwrap}\left[\arg\left(\mathcal{H}\left\{\cos(2kOPD + \phi_{\text{disp}}(k))\right\}\right)\right] = 2kOPD + \phi_{\text{disp}}(k) \tag{A.22}$$

The nonlinear effects of dispersion cause the interferogram to chirp. Next, a robust linear regression (`robustfit` function in Matlab) is applied to the cosine argument to estimate the linear $2kOPD$ part. The phase due to distortion is isolated by subtracting the empirical cosine argument from the linear fit. This resulting vector is saved as the calibration file for the system. This should only need to be recomputed when a new endoscope is used with the system.

The system dispersion is removed from the originally recorded fringe data by multiplying by a correction vector after removing the source spectrum. The source spectrum is effectively removed by averaging all A-scans along the lateral direction and subtracting this average from each A-scan in the B-scan. The resulting interferogram is multiplied by $\exp(-i\phi_{\text{disp}}(k))$ to remove system dispersion.[4] In practice, $\phi_{\text{disp}}(k)$ is determined by averaging many stationary A-scans of a mirror sample, as described in the Sec. A.6.2.

An example of a mirror B-scan consisting of 2000 stationary A-scans before and after dispersion correction is shown in Fig. A.22. The corrected image is much closer to a delta-function approximation of a highly reflective surface. A comparison of

---

[3] The sample-arm intensity component of the DC term is typically much lower than the reference intensity when imaging biological samples.

[4] If the signal has wrapped around the the zero OPD point, then the correction term should be $\exp(+i\phi_{\text{disp}}(k))$.

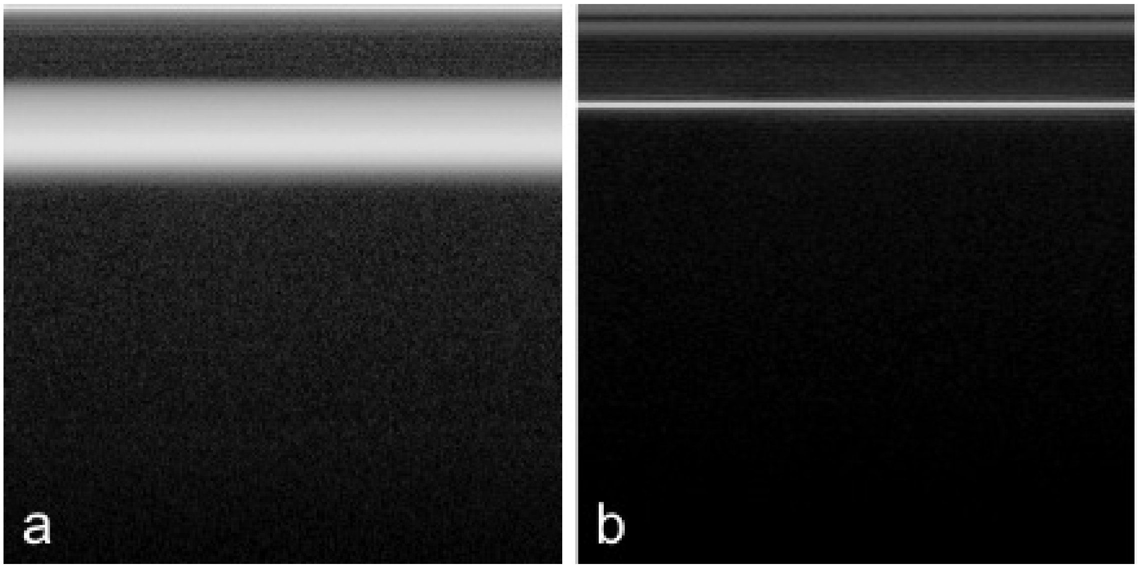

Figure A.22: Dispersion correction of 512 stationary A-scans of a mirror. (a) B-scan before dispersion correction; (b) B-scan after dispersion correction.

the PSF before and after correction is shown in Fig. A.23. The correction causes a broadening of the signal near zero OPD corresponding to the "autocorrelation" portion of the signal (i.e., the signal that arises from interference from scatterers located within the coherence length of the source). However, the PSF has been significantly narrowed by removing system dispersion.

Due to the asymmetric spectra of the swept source in forward and reverse sweeps, the correction is applied independently to the even and odd A-scans. Additionally, the corrected A-scans are circularly shifted to align the peaks of the power spectra and produce a better image. Figure A.24 shows a magnified region of the mirror in Fig. A.22 showing the asymmetry (a) and the improved image quality after circularly shifting every other A-scan by 3 pixels (b). When imaging biological samples, I noticed improved image quality when allowing each A-scan to circularly shift over a range of ±10 pixels to maximize the cross-correlation with the adjacent A-scans. This sometimes causes noticeable misalignment in the endoscope envelope signal, but it allows greater visualization of small features in the tissue. Figure A.25 shows

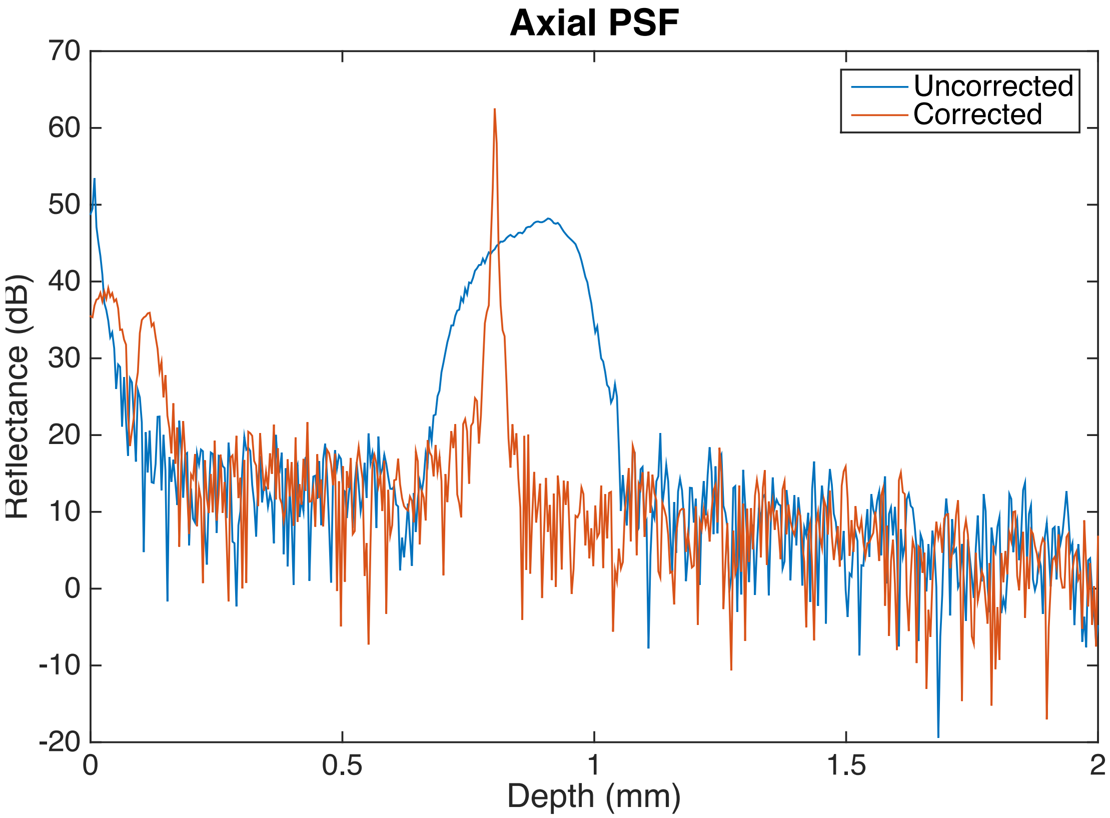

Figure A.23: PSF before and after dispersion correction using a mirror as the sample.

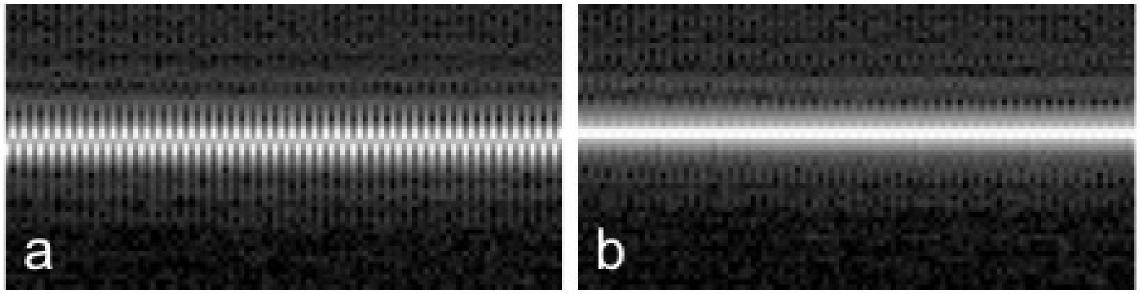

Figure A.24: Comparison of dispersion-corrected image of a mirror (a) before and (b) after circularly shifting by 3 pixels to align the peaks of the skewed and asymmetric sweep spectra of the source.

a magnified region of mouse colon to compare OCT image quality with and without vertically shifting A-scans. Allowing each A-scan to circularly shift by up to ±10 pixels to maximize the cross-correlation of the following A-scan produces superior image quality compared to simply shifting every odd A-scan by a fixed number of pixels.

A.6.2 Calibration

If the biological sample can be assumed to impart negligible dispersion over the length of the sample arm, then a calibration file needs to be generated only once for a given sample-arm optical system (endoscope, patch cable, fiber-optic rotary joint, etc.). To generate the calibration file, place a mirror at the focus of the endoscope and tilt the mirror appropriately to maximize the reflected intensity without saturation. Intensity and saturation can be monitored using the 1D imaging mode of the Thorlabs software. The Thorlabs software can only save raw fringe data when recording 3D imaging data. Only one frame of data is needed, so set the number of y pixels to the lowest allowable value. Do not move the endoscope during imaging. To minimize noise, many fringes should be averaged together. I typically average the fringes from 2000 A-scans (x pixels in the Thorlabs software). Ensure that no part of the dispersion-degraded signal from the mirror wraps around the zero OPD

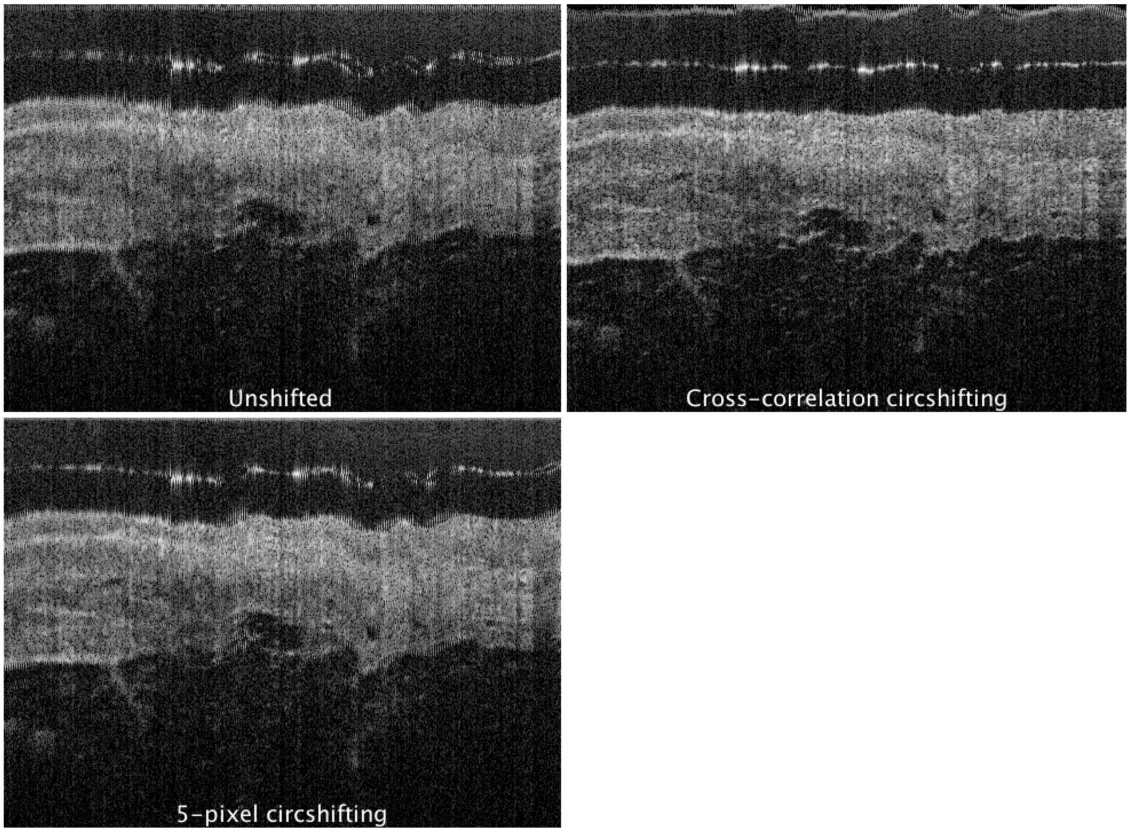

Figure A.25: Comparison of shifting A-scans to correct for asymmetric source sweep spectra. Shifting by a fixed number of pixels, as in Fig. A.24 is not as effective in biological samples as maximizing cross-correlation over a limited range of shift amounts (±10 pixels here).

point at the top of the image. Also, to reduce any interaction of the mirror signal with the DC and autocorrelation signals, it is best to adjust the reference arm until the top portion of the mirror signal is at least about 20% down from the top of the image.

To generate the calibration file, run the `generateCalibrationFile.m` Matlab script, the code is listed below in Code A.2. The program will ask the user to select the fringe (`*.FRG`) file from imaging the mirror. Next, select which frame to use for calibration. In general, any frame in the file should work, but if a particular frame is distorted due to data acquisition problems, then the user can retry and choose a different frame. The script will save a calibration file in the same directory as the loaded fringe file with "`_calibration.mat`" appended to the end of the fringe file name. Three figures will also be generated. The first figure is a plot of the first even A-scan interferogram, the average of all even interferograms in the image (estimate of the even-sweep source spectrum), and the first even interferogram with the even-sweep spectrum subtracted. Subtracting the spectrum should result in a fringe signal that is mostly symmetric about the $y = 0$ line. The second figure shows the OCT B-scan of the mirror before and after numerical dispersion compensation. If the corrected image is even further broadened, the mirror was on the "wrong" side of the zero OPD point. To fix this, either adjust the mirror-endoscope distance and/or reference arm delay to move the object to the other side of the zero OPD point, or, if this is not possible, change the signs in the argument of the exponential functions in lines 94 and 95 in `generateCalibrationFile.m`. The signs in `correctDispersionVolumetric.m` (lines 113 and 114) and `correctDispersionLongBscan.m` (lines 65 and 66) will also need to be changed. The third figure shows the mean measured phase, the linear fit to the phase, and the phase residual that forms the dispersion correction term.

Code A.2: `generateCalibrationFile.m`

```
1  function generateCalibrationFile
2  
```

```
% Generate numerical dispersion calibration file for using custom
% sample-arm optics (endoscopes) with the Thorlabs OCS1050SS swept-
    source
% OCT system.

% To generate a calibration file, save 3D fringe (.FRG) data of a
    mirror
% object using the endoscope. Ensure that the object's entire extent
    is on
% one side of the zero OPD point (do not let the object wrap across
    the top
% of the screen). Many A-scans are recommended for averaging out
    noise
% (e.g., 2000 A-scans per B-scan). Collect data without moving the
% endoscope or mirror. Only one frame of the volume is needed for
% generating the calibration file. You can choose any frame that is
    not
% distorted from data acquisition or any other source of error other
    than
% dispersion.

% generateCalibrationFile.m
% Author: Weston A. Welge
% Date: April 14, 2016

% Extract file header information
[file_head,frame_head,filter] = Open_File;
[pathstr,name,~] = fileparts(file_head.location);
```

```matlab

% Generate calibration file location+name
calname = [name '_calibration.mat'];
calfile = fullfile(pathstr, calname);

% Print number of frames in the file (should always be 16).
fprintf('Number of frames in this file: %d\n', file_head.nFr);

% Let user choose which of the 16 frames to use (probably want to always
% choose the same one).
frame_sel = input('Select first frame to process: ');

% Check to make sure selected frame exists
assert(frame_sel > 0 & frame_sel < file_head.nFr);

% Move file pointer to the beginning of the raw fringe data
fseek(file_head.fid, (frame_sel-1)*frame_head.length_bytes,'cof');

% Extract fringe data as 'frame_2D'. Should be a 2048x2000 matrix.
% 'frame_info' and 'elapsed_time' can be ignored.
[frame_2DRaw,~,~] = Load_Frame(file_head,...
       frame_sel, frame_head);

frame_2D = Fringe_apodization(frame_2DRaw,'Gaussian');

% Extract argument of interferogram cosine for even and odd A-scans
% separately due to asymmetric sweep spectra of source.
```

```
frameE = frame_2D(:,2:2:end);
frameO = frame_2D(:,1:2:end);
% Average all A-scans to estimate source spectrum as function of k.
avgFrameE = mean(frameE,2);
avgFrameO = mean(frameO,2);
% Subtract spectrum from each A-scan to remove DC component near 0
    OPD.
frameNoSpectrumE = frameE - repmat(avgFrameE,1,size(frameE,2));
frameNoSpectrumO = frameO - repmat(avgFrameO,1,size(frameO,2));
% Extract cosine argument (phase)
phaseTotalE = unwrap(angle(hilbert(frameNoSpectrumE)));
phaseTotalO = unwrap(angle(hilbert(frameNoSpectrumO)));
% Average phases to reduce noise
avgPhaseE = mean(phaseTotalE,2);
avgPhaseO = mean(phaseTotalO,2);

wavenumber = linspace(2*pi/1080E-9,2*pi/1000E-9,size(frame_2D,1));

% Plot single fringe, estimated spectrum, and single fringe with
    spectrum
% removed. The fringe with spectrum removed should appear mostly
    symmetric
% about the x axis.
figure
plot(wavenumber*10^-6,frameE(:,1))
hold on
plot(wavenumber*10^-6,avgFrameE)
plot(wavenumber*10^-6,frameNoSpectrumE(:,1))
```

```
hold off
xlabel('Wavenumber (rad/um)');
ylabel('Intensity (a.u.)');
legend('Single fringe','Average of all fringes (spectrum estimate)', ...
    'Single fringe with spectrum removed');

% Determine linear coefficients by fitting line to averaged phase
k = 1:size(frame_2D,1); % wavenumber indices
a = robustfit(k',avgPhaseE);
phaseSystemE = avgPhaseE - a(2)*k' - a(1);
a = robustfit(k',avgPhaseO);
phaseSystemO = avgPhaseO - a(2)*k' - a(1);

% Correct fringes by multiplying by correction factor (exp(+-i*phi_disp)).
% If the corrected image appears worse, the likely cause is that the mirror
% was flipped about the zero OPD point. Try changing the sign of the
% exponential argument or collect a new image with the reference arm
% adjusted to place the mirror on the other side of the zero OPD point.
correctedFringeE = frameE.*repmat(exp(1i*phaseSystemE),1,size(frameE,2));
correctedFringeO = frameO.*repmat(exp(1i*phaseSystemO),1,size(frameO,2));

% Generate OCT images before and after dispersion correction for
```

```
   visual
% inspection
OCT_IMG_linear = abs(ifft(frame_2D));
OCT_IMG_linearCorrE = abs(ifft(correctedFringeE));
OCT_IMG_linearCorrO = abs(ifft(correctedFringeO));
OCT_IMG_linearCorr = zeros(size(OCT_IMG_linear));
OCT_IMG_linearCorr(:,1:2:end) = OCT_IMG_linearCorrO;
OCT_IMG_linearCorr(:,2:2:end) = OCT_IMG_linearCorrE;
OCT_max = max(OCT_IMG_linear(:));
OCT_maxCorr = max(OCT_IMG_linearCorr(:));
dB_range = 50; % Dynamic range to display
OCT = (20*log10(OCT_IMG_linear./OCT_max)+dB_range)/dB_range*255;
OCTCorr = (20*log10(OCT_IMG_linearCorr./OCT_maxCorr)+dB_range)/
   dB_range*255;
OCT(OCT<0) = 0;
OCTCorr(OCTCorr<0) = 0;
OCT = uint8(OCT);
OCTCorr = uint8(OCTCorr);

% Plot OCT images before and after correction
figure;
subplot(2,1,1)
imagesc(OCT(1:512,:))
subplot(2,1,2)
imagesc(OCTCorr(1:512,:))
colormap(gray)

% Save calibration file
```

```
phaseSystemEven = phaseSystemE;
phaseSystemOdd = phaseSystemO;
save(calfile, 'phaseSystemEven', 'phaseSystemOdd');

% Plot averaged phase and linear fit.
figure
plot(wavenumber*10^-6,avgPhaseE)
hold on
plot(wavenumber*10^-6,a(2)*k'+a(1));
plot(wavenumber*10^-6,avgPhaseE-(a(2)*k'+a(1)));
xlabel('Wavenumber (rad)');
ylabel('Intensity (a.u.)');
legend('Average measured phase','Robust linear fit','Residual phase');
hold off

%****************************************************%
% Required functions (originally written by Thorlabs) %
%****************************************************%

% Open_File.m
function [file, frame, code] = Open_File()

% Open_File open a .FRG or .IMG file and return its header information
% Call format: [file_head, frame_head] = Open_File();
%
% file_head: a structure contains file header information
```

```
% frame_head: a structure contains frame header information

% Copyright 2009-2010 Thorlabs Inc.
% $Revision: 2.0 $ $Date: 2009/8/21 $

[file_name, file_path, filter] = uigetfile({'*.FRG'; '*.IMG'}, 'Select a .FRG or .IMG File'); % get file name and file path of the fringe data


    if filter == 1;
        file.type = 'FRG';
    elseif filter == 2
        file.type = 'IMG';
    end
    % file location
    file.location = [file_path, file_name];

    % open file and return file handle fid
    file.fid = fopen(file.location, 'rb' );

    % read header of the .FRG data using file handle fid
    file.id = fread(file.fid, 16, '*char'); % File identification string
    file_head = fread(file.fid, 8, 'int32' ); % File_header
    file.nFr = file_head(1); % Number of images saved in the file
    frame.width = file_head(2); % frame width, width = image_width*Average_Num for one channel
```

```
frame.depth = file_head(3); % Image depth
file.nFrp3D = file_head(4); % Number of frames in each 3D volume
file.n3D = file_head(5); % Number of 3D volume, 0 means only 2D movie recorded, 1 means 3D data recorded
frame.FFT_length = file_head(6); % FFT_length for OCT fringe
if frame.FFT_length == 0
    frame.FFT_length = 2*frame.depth;
end
frame.Frame_byte = file_head(7); % Frame size in bytes
frame.Record_length = file_head(8); % Record length

frame.PS_fringe_check = fread( file.fid, 1, 'int16' ); % PS_Fringe_check, 1 is PSOCT Fringe imaging mode, 0 is other modes.
if frame.PS_fringe_check ==[]
   frame.PS_fringe_check = 0;
end

frame.average_number = fread(file.fid, 1, 'int16' ); % Number of A-line numbers for averaging in one frame
if frame.average_number == []
   frame.average_number = 1;
end

frame.imaging_mode = fread(file.fid, 1, 'int16');
if frame.imaging_mode ==[]
   frame.imaging_mode = 0;
end
```

```

file.junk = fread(file.fid,458,'int8'); % Reversed bytes


if (frame.imaging_mode == 0) % Normal imaging mode, .IMG or .FRG format
    frame.num_DAQ_Ch = 1; % Number of DAQ channels for detection of fringes is 1

    if file.type =='FRG'
        frame.pixel_num = frame.width * frame.FFT_length; % FRG frame pixel number
        frame.length_bytes = 40 + frame.pixel_num*2; % FRG frame length in bytes, 40 bytes is sub hearder length in one frame. (one pixel = 2 bytes)
    elseif file.type == 'IMG'

        frame.pixel_num = frame.width * frame.depth; % IMG frame pixel number
        frame.length_bytes = 40 + frame.pixel_num; % IMG frame length in bytes, 40 bytes is sub hearder length in one frame. (one pixel = 1 bytes)
    end
    code = 0;
else % other mode is not provided

    disp('Error message: imgaging mode other than OCT Fringe or intensity is not provided')
```

```
        code = [];
    end
end

% Load_Frame.m
function [frame_2D, frame_info, elapsed_time] = Load_Frame(file, index_frame, frame)

    % Load_Frame Load Thorlabs Swept Source OCT .FRG or .IMG frame
    % at index_frame location. The .FRG frame recorded for
    % spectral fringes in k (wavenumber) domain after the MZI clock calibration.
    % Call format: [frame_2D, frame_info, elapsed_time] = Load_Frame(file_head, index_frame, frame_head)
    %
    % For .FRG file, returned frames of OCT spectral fringe data in a 2D array with
    % format frame_2D(FFT_length, width)
    %
    % For. IMG file, returned frames of images in a 2D array with
    % format frame_2D(depth, width)

    % Copyright 2009-2010 Thorlabs Inc.
    % $Revision: 2.0 $ $Date: 2009/8/21 $


    % read one frame of FRG or IMG data at the position index_frame
    disp(sprintf('...Frame loaded: %d',index_frame))
```

```
    elapsed_time = fread(file.fid, 1, 'int32' ); % 4 bytes of elapsed time
    frame_info = fread(file.fid, 36, 'int8' ); % 4 bytes of System time of current frame + 32 bytes Reserved
    if file.type == 'FRG'
        frame_data = fread(file.fid, frame.pixel_num, 'int16' ); % int16 = 2 bytes = one pixel in FRG frame
        frame_2D = reshape(frame_data, frame.FFT_length, frame.width);
    elseif file.type == 'IMG'
        frame_data = fread(file.fid, frame.pixel_num, 'uint8' ); % uint8 = 1 bytes = one pixel in IMG frame
        frame_2D = reshape(frame_data, frame.depth, frame.width);
    end
end

% Fringe_apodization.m
function Fringe_apodiz = Fringe_apodization(Fringe_k, apodiz_method)

% Fringe_apodization Apodization along depth direction of input spectral fringe
% in the k domain using an apodization method. This is for smoothing the
% fringe to reduce the side lodes of the PSF of the OCT system arising from
% the swept source spectrum
% Calling format: Fringe_apodiz = Fringe_apodization(Fringe_k, apodiz_method)
```

```
%
% Fringe_apodiz: result returned after multiplication of every column of Fringe_k
% by a apodization window specified by the (apodiz_method).
%
% Fringe_k: the input spectral fringe in the k domain
% apodiz_method: option for apodization method. It can be chosen as
% 'Gaussian', 'Hamming', 'Hann', 'Kaiser', 'Cosine', 'super_Gaussian',
% 'Blackman', 'Nuttall', 'Blackman_Harris', 'None'


% Copyright 2009-2010 Thorlabs Inc.
% $Revision: 2.0 $ $Date: 2009/8/21 $

[index_length, width] = size(Fringe_k);

window_band = 0.3*index_length;
depth_index = (1:index_length) - round(index_length/2);

switch apodiz_method
    case 'Kaiser'
        disp('Kaiser window')
        alpha = 2;
        index = (1:index_length)-1;
        v = pi*alpha*sqrt(1 - (2*index/(index_length-1) -1).^2);
        window = (besseli(0,v)./besseli(0,pi*alpha))'*ones(1,width);
    case 'Cosine'
```

```
        %disp('Cosine window')
        window = cos(pi*depth_index./index_length)'*ones(1,width);
    case 'super_Gaussian'
        %disp('super Gaussian window')
        window = exp(-(depth_index./window_band).^4)'*ones(1,width);
    case 'Gaussian'
        %disp('Gaussian window')
        window = exp(-(depth_index./window_band).^2)'*ones(1,width);
    case 'Hamming'
         %disp('Hamming window')
        window =(0.53836 - 0.46164*cos(2*pi*(1:index_length)./(
           index_length-1)))'*ones(1,width); %Hamming
    case 'Hann'
         %disp('Hann window')
         window = (0.5 - 0.5*cos(2*pi*(1:index_length)./(index_length
            -1)))'*ones(1,width); %Hann
    case 'Blackman'
         %disp('Blackman window')
         window =(0.42 - 0.5*cos(2*pi*(1:index_length)./(index_length
            -1)) + ...
            0.08*cos(4*pi*(1:index_length)./(index_length-1)))'*ones
               (1,width); %Blackman
    case 'Nuttall'
         %disp('Nuttal window')
         window =(0.355768 - 0.487396*cos(2*pi*(1:index_length)./(
            index_length-1))+ ...
             + 0.144232*cos(4*pi*(1:index_length)./(index_length-1))-
                 ...
```

```
             0.012604*cos(6*pi*(1:index_length)./(index_length-1)))'*ones(1,width); %Nuttall
    case 'Blackman_Harris'
         %disp('Blackman_Harris window')
         window =(0.35875 - 0.48829*cos(2*pi*(1:index_length)./(index_length-1))+ ...
             + 0.14128*cos(4*pi*(1:index_length)./(index_length-1))- ...
             0.01168*cos(6*pi*(1:index_length)./(index_length-1)))'*ones(1,width); %Blackman_Harris
     otherwise
        %disp('rectangular window')
        window = 1;
end
 Fringe_apodiz = Fringe_k.*window;
end
end
```

A.6.3 Numerical dispersion compensation software

Two versions of numerical dispersion software are presented here. The MATLAB function `correctDispersionVolumetric.m` is used for correcting volumetric data collected with the endoscope using the helical scanning geometry. The second version, `correctDispersionLongBscan.m`, is used when the endoscope collects data in the linear scanning geometry. This geometry is used for Doppler imaging, or any other situation in which several frames are concatenated to form a single, long B-scan.

The `correctDispersionVolumetric.m` function requires a calibration file generated by `generateCalibrationFile.m` described in Sec. A.6.2. The user chooses a `.FRG` file and a directory to save the individual dispersion-corrected frames (saved at TIFF files) and the `list.txt` file for importing in ImageJ (File>Import>Stack From List). This list method is used because ImageJ does not load files in proper alphanumeric order in a directory; the list text file ensures that all frames are loaded in correct order. The resulting stack can be saved as a single, multi-frame TIFF file (this is simpler in ImageJ than in Matlab). The dispersion correction function will automatically grab all `.FRG` files in the same directory. The complete function is reproduced in Code A.3.

The `correctDispersionLongBscan.m` function also requires a calibration file. The user selects a `.FRG` file and a directory to save the dispersion-corrected image and, optionally, the complex dispersion-corrected B-scan data. This function is meant to be used when imaging with a longitudinal scan geometry. This is typically the case during Doppler imaging, which requires high spatial oversampling in the lateral direction. The frames are concatenated to form a single, long B-scan, which is saved at a TIFF image. This should be resized to square pixels for visual inspection (in ImageJ, this can be accomplished by Image>Adjust>Size). Saving the complex B-scan data is optional because the process of saving can take a very long time and produce very large files for highly sampled data. The complex data are saved as a `.mat` file containing the matrix `longBscanComplex`, which is used in `KasaiProcessing.m` described in Appendix B.2.2. The `correctDispersionLongBscan.m` function is provided in Code A.4.

Code A.3: `correctDispersionVolumetric.m`

```matlab
function correctDispersionVolumetric

% Numerical dispersion correction on all .FRG files in a directory.

% Date: April 15, 2016
```

```
% Author: Weston A. Welge

% Correct dispersion using method in Welge and Barton, PLOS ONE e0139396
% (2016).

% Uses calibration file generated using generateCalibrationFile.m to
% correct dispersion on all .FRG files in a directory. The user points to
% the directory containing .FRG files to correct. The user chooses a
% directory to save the dispersion-corrected B-scans from the volumetric
% data. A file 'list.txt' is created with full directories and file names
% for all corrected B-scans in order so that the entire volume can be read
% by ImageJ using File>Import>Stack From List. The entire volume can be
% then saved as a single TIFF file in ImageJ.

% Uses several functions written by Thorlabs, which have been included at
% the end of this function to it can be run without having the other
% function files in the same directory. This function requires a
% calibration file to be in the same directory.

clear variables;

```

```
% Define parameters
apodization = 'Gaussian'; % For use in Fringe_apodization.m
dB_range = 50; % Dynamic range of OCT images in dB.
phaseSystemEven = []; % Needed to load variables in nested function below
phaseSystemOdd = []; % Needed to load variables in nested function below

% Load 'phaseSystemEven' and 'phaseSystemOdd' calibration vectors
load('welge_031215_calibration.mat');

% Let user choose .FRG volumes to process
[file_head,frame_head,fileFull] = OpenAllFiles(); % Extract file header info
exportBscanDirectory = uigetdir('','Choose directory to export Bscans');
txtFileID = fopen([exportBscanDirectory,'/list.txt'],'a');

OCT_maxCorr = zeros(1,file_head(1).nFr);
imax = 0; % Index variable for OCT_maxCorr vector

% Extract frame data, correct dispersion, and determine max value. Only
% using first volume because the global max will likely not differ much
% from the max of the first volume.
for volumeIndex = 1:1%length(file_head)
    % Process all frames in file
```

```
    frame_start = 1;
    frame_stop = file_head(volumeIndex).nFr;
    % Seek start frame
    fseek(file_head(volumeIndex).fid, (frame_start-1)*frame_head(volumeIndex).length_bytes,'cof');
    n = 0;
    for frame_index = frame_start:frame_stop
        n = n+1;
        imax = imax+1;
        [frame_2D,~,~] = Load_Frame(file_head(volumeIndex),...
            frame_index, frame_head(volumeIndex));

        frameNoBGOdd = frame_2D(:,1:2:end) - repmat(mean(frame_2D(:,1:2:end),2),1,size(frame_2D,2)/2);
        frameNoBGEven = frame_2D(:,2:2:end) - repmat(mean(frame_2D(:,2:2:end),2),1,size(frame_2D,2)/2);

        % Generate system dispersion correction terms
        % ***NOTE: If depth resolution is made worse by this code, switch the
        % sign in the following exponential functions***
        phaseCorrEven = exp(1i*phaseSystemEven);
        phaseCorrOdd = exp(1i*phaseSystemOdd);

        % Correct fringes
        correctedFringeEven = 2*frameNoBGEven.*repmat(phaseCorrEven,1,size(frameNoBGEven,2));
        correctedFringeOdd = 2*frameNoBGOdd.*repmat(phaseCorrOdd,1,
```

```
            size(frameNoBGOdd,2));
        % Recombine even and odd fringes
        correctedFringe = zeros(size(frame_2D));
        correctedFringe(:,1:2:end) = correctedFringeOdd;
        correctedFringe(:,2:2:end) = correctedFringeEven;

        % Process corrected fringes to generate B-scans
        [OCT_complexCorr,~] = Compute_Analytical(correctedFringe, frame_head(volumeIndex).FFT_length,...
            frame_head(volumeIndex).depth);
        OCT_IMG_linearCorr = abs(OCT_complexCorr);
        OCT_maxCorr(imax) = max(OCT_IMG_linearCorr(:));
    end
end

% Calculate 98th percentile amplitude value (noise-robust max value)
OCTMax = prctile(OCT_maxCorr(:),98);

% Re-open all files to get file pointers back to beginning of first volume,
% first frame file
[file_head,frame_head] = OpenAllFiles(fileFull); % Extract file header info

% Rerun through volume, this time using OCTMax for setting dynamic range
for volumeIndex = 1:length(file_head)
    % Process all frames in file
```

```
frame_start = 1;
frame_stop = file_head(volumeIndex).nFr;
% Seek start frame
fseek(file_head(volumeIndex).fid, (frame_start-1)*frame_head(
   volumeIndex).length_bytes,'cof');
n = 0;
for frame_index = frame_start:frame_stop
    n = n+1;
    [frame_2DNoApod,~,~] = Load_Frame(file_head(volumeIndex),...
        frame_index, frame_head(volumeIndex));

    frame_2D = Fringe_apodization(frame_2DNoApod,apodization);

    frameNoBGOdd = frame_2D(:,1:2:end) - repmat(mean(frame_2D
       (:,1:2:end),2),1,size(frame_2D,2)/2);
    frameNoBGEven = frame_2D(:,2:2:end) - repmat(mean(frame_2D
       (:,2:2:end),2),1,size(frame_2D,2)/2);

    % Generate system dispersion correction terms
    % ***NOTE: If depth resolution is made worse by this code,
       switch the
    % sign in the following exponential functions***
    phaseCorrEven = exp(1i*phaseSystemEven);
    phaseCorrOdd = exp(1i*phaseSystemOdd);

    % Correct fringes
    correctedFringeEven = 2*frameNoBGEven.*repmat(phaseCorrEven
       ,1,size(frameNoBGEven,2));
```

```
        correctedFringeOdd = 2*frameNoBGOdd.*repmat(phaseCorrOdd,1,
           size(frameNoBGOdd,2));
        % Recombine even and odd fringes
        correctedFringe = zeros(size(frame_2D));
        correctedFringe(:,1:2:end) = correctedFringeOdd;
        correctedFringe(:,2:2:end) = correctedFringeEven;

        % Process corrected fringes to generate B-scans
        [OCT_complexCorr,~] = Compute_Analytical(correctedFringe,
           frame_head(volumeIndex).FFT_length,...
            frame_head(volumeIndex).depth);
        OCT_IMG_linearCorr = abs(OCT_complexCorr);
        OCT_IMG_logCorr = (20*log10(OCT_IMG_linearCorr./OCTMax)+
           dB_range)/dB_range*255;
        OCT_displayCorr = OCT_IMG_logCorr;
        OCT_displayCorr(OCT_displayCorr < 0) = 0;
        OCT_displayCorr = uint8(OCT_displayCorr);

        % Correct "zig-zag" effect from asymmetric sweep spectra
           between
        % adjacent A-scans
        OCTZZCorr = OCT_displayCorr;
        for col = 1:size(OCT_displayCorr,2)-1
            [r,lags] = xcorr(OCTZZCorr(:,col),OCTZZCorr(:,col+1),10,'
               coeff');
            [~,I] = max(r);
            shiftAmount = lags(I);
            OCTZZCorr(:,col+1) = circshift(OCTZZCorr(:,col+1),
```

```
                shiftAmount);
        end

        % Save dispersion and "zig-zag" corrected B-scans as tiffs
        [~,name,~] = fileparts(file_head(volumeIndex).location);
        fileFull = fullfile(exportBscanDirectory,[name,num2str(
            frame_index),'.tif']);
        imwrite(OCTZZCorr,fileFull);
        % Write filename to list text file for loading all tiffs in
            proper
        % order using ImageJ
        fprintf(txtFileID,'%s\n',fileFull);
    end
    fprintf('Volume %s complete\n',name(end-2:end))
end
fclose('all');


%***************************************************%
% Required functions (originally written by Thorlabs) %
%***************************************************%

% OpenAllFiles.m
function [files, frame, fileFull] = OpenAllFiles(fringeFile)

% OpenAllFiles open all .FRG or .IMG files in a directory
% and return header information
% Call format: [file_head, frame_head] = OpenAllFiles();
```

```
%
% file_head: a structure contains file header information
% frame_head: a structure contains frame header information

% Copyright 2009-2010 Thorlabs Inc.
% Edited by Weston A. Welge on Jan. 22, 2016 to load all .frg or .img files
% in the directory initially selected by the user.
% $Revision: 2.0 $ $Date: 2009/8/21 $

if nargin == 0
    [file_name, file_path, filter] = uigetfile({'*.FRG'; '*.IMG'}, 'Select a .FRG or .IMG File'); % get file name and file path of the fringe data
    fileFull = fullfile(file_path,file_name);
else
    [file_path,~,file_extension] = fileparts(fringeFile);
    if strcmpi(file_extension,'.FRG')
        filter = 1;
    elseif strcmpi(file_extension,'.IMG')
        filter = 2;
    else
        error('invalid file type');
    end
end

    if filter == 1;
       type = 'FRG';
```

```
        oldFolder = cd(file_path);
        dirInfo = dir('*.FRG');
        filenames = cell(size(dirInfo));
        locations = cell(size(dirInfo));
        files(length(dirInfo)).location = []; %Initialize struct
        frame(length(dirInfo)).width = [];
        for fileIndex = 1:length(dirInfo)
            filenames{fileIndex} = dirInfo(fileIndex).name;
            locations{fileIndex} = fullfile(file_path,filenames{
                fileIndex});
            files(fileIndex).location = locations{fileIndex};
            files(fileIndex).type = type;
        end

    elseif filter == 2
        type = 'IMG';
        oldFolder = cd(file_path);
        dirInfo = dir('*.IMG');
        filenames = cell(size(dirInfo));
        locations = cell(size(dirInfo));
        files(length(dirInfo)).location = []; %Initialize struct
        frame(length(dirInfo)).width = [];
        for fileIndex = 1:length(dirInfo)
            filenames{fileIndex} = dirInfo(fileIndex).name;
            locations{fileIndex} = fullfile(file_path,filenames{
                fileIndex});
            files(fileIndex).location = locations{fileIndex};
            files(fileIndex).type = type;
```

```
      end
    end

    for fileIndex = 1:length(files)
        % file location
        % file.location = [file_path, file_name];

        % open file and return file handle fid
        files(fileIndex).fid = fopen(files(fileIndex).location, 'rb');

        % read header of the .FRG data using file handle fid
        files(fileIndex).id = fread(files(fileIndex).fid, 16, '*char'); % File identification string
        file_head = fread(files(fileIndex).fid, 8, 'int32' ); % File_header
        files(fileIndex).nFr = file_head(1); % Number of images saved in the file
        frame(fileIndex).width = file_head(2); % frame width, width = image_width*Average_Num for one channel
        frame(fileIndex).depth = file_head(3); % Image depth
        files(fileIndex).nFrp3D = file_head(4); % Number of frames in each 3D volume
        files(fileIndex).n3D = file_head(5); % Number of 3D volume, 0 means only 2D movie recorded, 1 means 3D data recorded
        frame(fileIndex).FFT_length = file_head(6); % FFT_length for OCT fringe
        if frame(fileIndex).FFT_length == 0
```

```
            frame(fileIndex).FFT_length = 2*frame(fileIndex).depth;
        end
        frame(fileIndex).Frame_byte = file_head(7); % Frame size in bytes
        frame(fileIndex).Record_length = file_head(8); % Record length

        frame(fileIndex).PS_fringe_check = fread( files(fileIndex).fid, 1, 'int16' ); % PS_Fringe_check, 1 is PSOCT Fringe imaging mode, 0 is other modes.
        if isempty(frame(fileIndex).PS_fringe_check)
            frame(fileIndex).PS_fringe_check = 0;
        end

        frame(fileIndex).average_number = fread(files(fileIndex).fid, 1, 'int16' ); % Number of A-line numbers for averaging in one frame
        if isempty(frame(fileIndex).average_number)
            frame(fileIndex).average_number = 1;
        end

        frame(fileIndex).imaging_mode = fread(files(fileIndex).fid, 1, 'int16');
        if isempty(frame(fileIndex).imaging_mode)
            frame(fileIndex).imaging_mode = 0;
        end

        files(fileIndex).junk = fread(files(fileIndex).fid,458,'int8'
```

```
          ); % Reserved bytes


        if (frame(fileIndex).imaging_mode == 0) % Normal imaging mode, .IMG or .FRG format
            frame(fileIndex).num_DAQ_Ch = 1; % Number of DAQ channels for detection of fringes is 1

            if strcmp(files(fileIndex).type,'FRG')
                frame(fileIndex).pixel_num = frame(fileIndex).width * frame(fileIndex).FFT_length; % FRG frame pixel number
                frame(fileIndex).length_bytes = 40 + frame(fileIndex).pixel_num*2; % FRG frame length in bytes, 40 bytes is sub hearder length in one frame. (one pixel = 2 bytes)
            elseif strcmp(files(fileIndex).type,'IMG')

                frame(fileIndex).pixel_num = frame(fileIndex).width * frame(fileIndex).depth; % IMG frame pixel number
                frame(fileIndex).length_bytes = 40 + frame(fileIndex).pixel_num; % IMG frame length in bytes, 40 bytes is sub hearder length in one frame. (one pixel = 1 bytes)
            end

        else % other mode is not provided

```

```
            disp('Error message: imgaging mode other than OCT Fringe
                or intensity is not provided')
            %code = [];
        end
    end
cd(oldFolder);
end

% Load_Frame.m

function [frame_2D, frame_info, elapsed_time] = Load_Frame(file,
    index_frame, frame)

% Load_Frame Load Thorlabs Swept Source OCT .FRG or .IMG frame
% at index_frame location. The .FRG frame recorded for
% spectral fringes in k (wavenumber) domain after the MZI clock
    calibration.
% Call format: [frame_2D, frame_info, elapsed_time] = Load_Frame(
    file_head, index_frame, frame_head)
%
% For .FRG file, returned frames of OCT spectral fringe data in a 2D
    array with
% format frame_2D(FFT_length, width)
%
% For. IMG file, returned frames of images in a 2D array with
% format frame_2D(depth, width)

% Copyright 2009-2010 Thorlabs Inc.
```

```
% $Revision: 2.0 $ $Date: 2009/8/21 $


% read one frame of FRG or IMG data at the position index_frame
%disp(sprintf('...Frame loaded: %d',index_frame))
elapsed_time = fread(file.fid, 1, 'int32' ); % 4 bytes of elapsed time
frame_info = fread(file.fid, 36, 'int8' ); % 4 bytes of System time of current frame + 32 bytes Reserved
if file.type == 'FRG'
    frame_data = fread(file.fid, frame.pixel_num, 'int16' ); % int16 = 2 bytes = one pixel in FRG frame
    frame_2D = reshape(frame_data, frame.FFT_length, frame.width);
elseif file.type == 'IMG'
    frame_data = fread(file.fid, frame.pixel_num, 'uint8' ); % uint8 = 1 bytes = one pixel in IMG frame
    frame_2D = reshape(frame_data, frame.depth, frame.width);
end
end

% Compute_Analytical.m

function [OCT_complex,noisyPixels] = Compute_Analytical(Fringe, FFT_length, image_depth)

% Compute_Analytical Return complex OCT image in space domain
% by inverse Fourier transforming along every column(A-line) of the spectral fringe image.
```

```
%
% Calling format: OCT_complex = Compute_Analytical(Fringe, FFT_length, image_depth)
%
% OCT_complex: Complex OCT image in space domain after inverse FFT transforms.
%
% Fringe: Spectral fringe in k(wavenumber) domain recorded after conversion from
% wavelength domain using a MZI clock in the Thorlabs Swept source OCT system.
% FFT_length: Data length for inverse FFT transforming along every column.
% image_depth: the length of the output OCT_complex along the depth diretion.

% Copyright 2009-2010 Thorlabs Inc.
% $Revision: 2.0 $ $Date: 2009/8/21 $

% retrieve complex OCT image by IFFT along every column after padding zero
% to every column to get FFT_length pixels of data
complex_temp = ifft(Fringe,FFT_length);

% returning image_width
[height, image_width] = size(complex_temp);

% declare memory for OCT_complex
```

```
OCT_complex = zeros(image_depth, image_width);

aver_fract = 1/10;
% total number of averaging pixels in one every columns (A-lines) of
    the OCT image
aver_pixel = round(image_depth*aver_fract);

% amplitude of the OCT image
OCT_image = abs(complex_temp(1:image_depth,:));

% (Weston) Extract bottom aver_pixel pixels from each Ascan
noisyPixels = OCT_image((image_depth-aver_pixel):image_depth,:);

%caculate level of noise in the last 1/10*image_depth lines of OCT
    image.
level_noise = sum(OCT_image((image_depth - aver_pixel):image_depth
    ,:))/(aver_pixel+1);
level_noise_matrix = ones(image_depth,1)*(1./level_noise);

% Normalization of every columns of the complex fringe complex_temp
    by the noise
% level of the last (aver_pixel+1) pixels and returning result->
    OCT_complex
OCT_complex = complex_temp(1:image_depth ,:).*level_noise_matrix;

%OCT_complex = complex_temp(1:image_depth ,:);
end

```

```
% Fringe_apodization.m
function Fringe_apodiz = Fringe_apodization(Fringe_k, apodiz_method)

% Fringe_apodization Apodization along depth direction of input spectral fringe
% in the k domain using an apodization method. This is for smoothing the
% fringe to reduce the side lodes of the PSF of the OCT system arising from
% the swept source spectrum
% Calling format: Fringe_apodiz = Fringe_apodization(Fringe_k, apodiz_method)
%
% Fringe_apodiz: result returned after multiplication of every column of Fringe_k
% by a apodization window specified by the (apodiz_method).
%
% Fringe_k: the input spectral fringe in the k domain
% apodiz_method: option for apodization method. It can be chosen as
% 'Gaussian', 'Hamming', 'Hann', 'Kaiser', 'Cosine', 'super_Gaussian',
% 'Blackman', 'Nuttall', 'Blackman_Harris', 'None'


% Copyright 2009-2010 Thorlabs Inc.
% $Revision: 2.0 $ $Date: 2009/8/21 $

[index_length, width] = size(Fringe_k);
```

```

window_band = 0.3*index_length;
depth_index = (1:index_length) - round(index_length/2);

switch apodiz_method
    case 'Kaiser'
        disp('Kaiser window')
        alpha = 2;
        index = (1:index_length)-1;
        v = pi*alpha*sqrt(1 - (2*index/(index_length-1) -1).^2);
        window = (besseli(0,v)./besseli(0,pi*alpha))'*ones(1,width);
    case 'Cosine'
        %disp('Cosine window')
        window = cos(pi*depth_index./index_length)'*ones(1,width);
    case 'super_Gaussian'
        %disp('super Gaussian window')
        window = exp(-(depth_index./window_band).^4)'*ones(1,width);
    case 'Gaussian'
        %disp('Gaussian window')
        window = exp(-(depth_index./window_band).^2)'*ones(1,width);
    case 'Hamming'
         %disp('Hamming window')
        window =(0.53836 - 0.46164*cos(2*pi*(1:index_length)./(index_length-1)))'*ones(1,width); %Hamming
    case 'Hann'
         %disp('Hann window')
         window = (0.5 - 0.5*cos(2*pi*(1:index_length)./(index_length-1)))'*ones(1,width); %Hann
```

```
    case 'Blackman'
         %disp('Blackman window')
         window =(0.42 - 0.5*cos(2*pi*(1:index_length)./(index_length
            -1)) + ...
            0.08*cos(4*pi*(1:index_length)./(index_length-1)))'*ones
               (1,width); %Blackman
    case 'Nuttall'
         %disp('Nuttal window')
         window =(0.355768 - 0.487396*cos(2*pi*(1:index_length)./(
            index_length-1))+ ...
             + 0.144232*cos(4*pi*(1:index_length)./(index_length-1))-
                 ...
             0.012604*cos(6*pi*(1:index_length)./(index_length-1)))'*
                ones(1,width); %Nuttall
    case 'Blackman_Harris'
         %disp('Blackman_Harris window')
         window =(0.35875 - 0.48829*cos(2*pi*(1:index_length)./(
            index_length-1))+ ...
             + 0.14128*cos(4*pi*(1:index_length)./(index_length-1))-
                ...
             0.01168*cos(6*pi*(1:index_length)./(index_length-1)))'*
                ones(1,width); %Blackman_Harris
     otherwise
        %disp('rectangular window')
        window = 1;
end
 Fringe_apodiz = Fringe_k.*window;
end
```

```
end
```

Code A.4: `correctDispersionLongBscan.m`

```
function correctDispersionLongBscan

% Correct dispersion from longitudinal endoscopic imaging with Thorlabs
% OCS1050SS system. Frames are concatenated for form a single long B-scan.
% The user can optionally save the complex concatenated B-scan matrix for
% future Doppler processing.

% Date: April 18, 2016
% Author: Weston A. Welge

% Correct dispersion using method in Welge and Barton, PLOS ONE (2016).
% Concatenates frames to form one long B-scan (used in Doppler image
% processing. Requires a calibration file for the endoscope (made with
% generateCalibrationFile.m) to be in the same directory as this function.

% Define parameters
apodization = 'Gaussian'; % For use in Fringe_apodization.m
dB_range = 50; % Dynamic range of OCT images in dB.
phaseSystemEven = []; % Needed to load variables in nested function
```

```
    below
phaseSystemOdd = []; % Needed to load variables in nested function
    below

% Load 'phaseSystemEven' and 'phaseSystemOdd' calibration vectors
load('welge_031215_calibration.mat');

% Let user choose .FRG volumes to process
[file_head,frame_head] = OpenAllFiles(); % Extract file header info
exportBscanDirectory = uigetdir('','Choose directory to export Bscan'
    );

% Ask user to save complex Bscan data
prompt = 'Save complex B-scan matrix for future Doppler processing? Y
    /N: ';
userResponse = input(prompt,'s');
if strcmpi(userResponse, 'Y')
    saveComplexBscan = 1;
elseif strcmpi(userResponse, 'N')
    saveComplexBscan = 0;
else
    error('Invalid response (use Y or N)');
end

% Pre-allocate space
frame_start = 1;
frame_stop = file_head.nFr;
longBscanComplex = zeros(frame_head.depth,frame_head.width*...
```

```
        (frame_stop-frame_start+1));

% Extract frame data, correct dispersion
for volumeIndex = 1:length(file_head)
    % Process all frames in file
    % Seek start frame
    fseek(file_head(volumeIndex).fid, (frame_start-1)*frame_head(
       volumeIndex).length_bytes,'cof');
    n = 0;
    for frame_index = frame_start:frame_stop
        n = n+1;
        [frame_2DNoApod,~,~] = Load_Frame(file_head(volumeIndex),...
            frame_index, frame_head(volumeIndex));

        frame_2D = Fringe_apodization(frame_2DNoApod,apodization);

        frameNoBGOdd = frame_2D(:,1:2:end) - repmat(mean(frame_2D
           (:,1:2:end),2),1,size(frame_2D,2)/2);
        frameNoBGEven = frame_2D(:,2:2:end) - repmat(mean(frame_2D
           (:,2:2:end),2),1,size(frame_2D,2)/2);

        % Generate system dispersion correction terms
        % ***NOTE: If depth resolution is made worse by this code,
           switch the
        % sign in the following exponential functions***
        phaseCorrEven = exp(1i*phaseSystemEven);
        phaseCorrOdd = exp(1i*phaseSystemOdd);

```

```
    % Correct fringes
    correctedFringeEven = 2*frameNoBGEven.*repmat(phaseCorrEven
       ,1,size(frameNoBGEven,2));
    correctedFringeOdd = 2*frameNoBGOdd.*repmat(phaseCorrOdd,1,
       size(frameNoBGOdd,2));
    % Recombine even and odd fringes
    correctedFringe = zeros(size(frame_2D));
    correctedFringe(:,1:2:end) = correctedFringeOdd;
    correctedFringe(:,2:2:end) = correctedFringeEven;

    % Process corrected fringes to generate B-scans
    [OCT_complexCorr,~] = Compute_Analytical(correctedFringe,
       frame_head(volumeIndex).FFT_length,...
       frame_head(volumeIndex).depth);
    longBscanComplex(:,frame_head.width*(n-1)+1:frame_head.width*
       n) = OCT_complexCorr;
end

% Compute log image using max value from entire volume, rather
   than
% individual frames (this fixes the problem of alternating frame
% brightness)
OCT_IMG_linearCorr = abs(longBscanComplex);
OCT_maxCorr = max(OCT_IMG_linearCorr(:));
OCT_img_logCorr = (20*log10(OCT_IMG_linearCorr./OCT_maxCorr)...
    +dB_range)/dB_range*255;
OCT_displayCorr = OCT_img_logCorr;
OCT_displayCorr(OCT_displayCorr < 0) = 0;
```

```
    OCT_displayCorr = uint8(OCT_displayCorr);

    % Correct "zig-zag" effect from asymmetric sweep spectra between
    % adjacent A-scans
    OCTZZCorr = OCT_displayCorr;
    for col = 1:size(OCT_displayCorr,2)-1
        [r,lags] = xcorr(OCTZZCorr(:,col),OCTZZCorr(:,col+1),10,'coeff');
        [~,I] = max(r);
        shiftAmount = lags(I);
        OCTZZCorr(:,col+1) = circshift(OCTZZCorr(:,col+1),shiftAmount);
    end

    % Save dispersion and "zig-zag" corrected B-scans as tiffs
    [~,name,~] = fileparts(file_head(volumeIndex).location);
    fileFull = fullfile(exportBscanDirectory,[name,'.tif']);
    imwrite(OCTZZCorr,fileFull);
end

if saveComplexBscan
    save(fullfile(exportBscanDirectory,[name,'.mat']),'longBscanComplex','-v7.3');
end
fclose('all');

%**************************************************%
% Required functions (originally written by Thorlabs) %
```

```matlab
%*****************************************************%

% OpenAllFiles.m
function [files, frame, fileFull] = OpenAllFiles(fringeFile)

    % OpenAllFiles open all .FRG or .IMG files in a directory
    % and return header information
    % Call format: [file_head, frame_head] = OpenAllFiles();
    %
    % file_head: a structure contains file header information
    % frame_head: a structure contains frame header information

    % Copyright 2009-2010 Thorlabs Inc.
    % Edited by Weston A. Welge on Jan. 22, 2016 to load all .frg or .img files
    % in the directory initially selected by the user.
    % $Revision: 2.0 $ $Date: 2009/8/21 $

    if nargin == 0
        [file_name, file_path, filter] = uigetfile({'*.FRG'; '*.IMG'}, 'Select a .FRG or .IMG File'); % get file name and file path of the fringe data
        fileFull = fullfile(file_path,file_name);
    else
        [file_path,~,file_extension] = fileparts(fringeFile);
        if strcmpi(file_extension,'.FRG')
            filter = 1;
        elseif strcmpi(file_extension,'.IMG')
```

```
            filter = 2;
        else
            error('invalid file type');
        end
    end

    if filter == 1;
        type = 'FRG';
        oldFolder = cd(file_path);
        dirInfo = dir('*.FRG');
        filenames = cell(size(dirInfo));
        locations = cell(size(dirInfo));
        files(length(dirInfo)).location = []; %Initialize struct
        frame(length(dirInfo)).width = [];
        for fileIndex = 1:length(dirInfo)
            filenames{fileIndex} = dirInfo(fileIndex).name;
            locations{fileIndex} = fullfile(file_path,filenames{
               fileIndex});
            files(fileIndex).location = locations{fileIndex};
            files(fileIndex).type = type;
        end

    elseif filter == 2
        type = 'IMG';
        oldFolder = cd(file_path);
        dirInfo = dir('*.IMG');
        filenames = cell(size(dirInfo));
        locations = cell(size(dirInfo));
```

```
        files(length(dirInfo)).location = []; %Initialize struct
        frame(length(dirInfo)).width = [];
        for fileIndex = 1:length(dirInfo)
            filenames{fileIndex} = dirInfo(fileIndex).name;
            locations{fileIndex} = fullfile(file_path,filenames{
               fileIndex});
            files(fileIndex).location = locations{fileIndex};
            files(fileIndex).type = type;
        end
    end

    for fileIndex = 1:length(files)
        % file location
        % file.location = [file_path, file_name];

        % open file and return file handle fid
        files(fileIndex).fid = fopen(files(fileIndex).location, 'rb'
           );

        % read header of the .FRG data using file handle fid
        files(fileIndex).id = fread(files(fileIndex).fid, 16, '*char'
           ); % File identification string
        file_head = fread(files(fileIndex).fid, 8, 'int32' ); %
           File_header
        files(fileIndex).nFr = file_head(1); % Number of images saved
            in the file
        frame(fileIndex).width = file_head(2); % frame width, width =
            image_width*Average_Num for one channel
```

```
        frame(fileIndex).depth = file_head(3); % Image depth
        files(fileIndex).nFrp3D = file_head(4); % Number of frames in each 3D volume
        files(fileIndex).n3D = file_head(5); % Number of 3D volume, 0 means only 2D movie recorded, 1 means 3D data recorded
        frame(fileIndex).FFT_length = file_head(6); % FFT_length for OCT fringe
        if frame(fileIndex).FFT_length == 0
            frame(fileIndex).FFT_length = 2*frame(fileIndex).depth;
        end
        frame(fileIndex).Frame_byte = file_head(7); % Frame size in bytes
        frame(fileIndex).Record_length = file_head(8); % Record length

        frame(fileIndex).PS_fringe_check = fread( files(fileIndex).fid, 1, 'int16' ); % PS_Fringe_check, 1 is PSOCT Fringe imaging mode, 0 is other modes.
        if isempty(frame(fileIndex).PS_fringe_check)
            frame(fileIndex).PS_fringe_check = 0;
        end

        frame(fileIndex).average_number = fread(files(fileIndex).fid, 1, 'int16' ); % Number of A-line numbers for averaging in one frame
        if isempty(frame(fileIndex).average_number)
            frame(fileIndex).average_number = 1;
        end
```

```matlab

        frame(fileIndex).imaging_mode = fread(files(fileIndex).fid, 1, 'int16');
        if isempty(frame(fileIndex).imaging_mode)
            frame(fileIndex).imaging_mode = 0;
        end

        files(fileIndex).junk = fread(files(fileIndex).fid,458,'int8'); % Reserved bytes


        if (frame(fileIndex).imaging_mode == 0) % Normal imaging mode, .IMG or .FRG format
            frame(fileIndex).num_DAQ_Ch = 1; % Number of DAQ channels for detection of fringes is 1

            if strcmp(files(fileIndex).type,'FRG')
                frame(fileIndex).pixel_num = frame(fileIndex).width * frame(fileIndex).FFT_length; % FRG frame pixel number
                frame(fileIndex).length_bytes = 40 + frame(fileIndex).pixel_num*2; % FRG frame length in bytes, 40 bytes is sub hearder length in one frame. (one pixel = 2 bytes)
            elseif strcmp(files(fileIndex).type,'IMG')

                frame(fileIndex).pixel_num = frame(fileIndex).width * frame(fileIndex).depth; % IMG frame pixel number
```

```
                frame(fileIndex).length_bytes = 40 + frame(fileIndex).pixel_num; % IMG frame length in bytes, 40 bytes is sub hearder length in one frame. (one pixel = 1 bytes)
            end

        else % other mode is not provided

            disp('Error message: imgaging mode other than OCT Fringe or intensity is not provided')
            %code = [];
        end
    end
    cd(oldFolder);
end

% Load_Frame.m
function [frame_2D, frame_info, elapsed_time] = Load_Frame(file, index_frame, frame)

    % Load_Frame Load Thorlabs Swept Source OCT .FRG or .IMG frame
    % at index_frame location. The .FRG frame recorded for
    % spectral fringes in k (wavenumber) domain after the MZI clock calibration.
    % Call format: [frame_2D, frame_info, elapsed_time] = Load_Frame(file_head, index_frame, frame_head)
    %
    % For .FRG file, returned frames of OCT spectral fringe data in a
```

```
        2D array with
    % format frame_2D(FFT_length, width)
    %
    % For. IMG file, returned frames of images in a 2D array with
    % format frame_2D(depth, width)

    % Copyright 2009-2010 Thorlabs Inc.
    % $Revision: 2.0 $ $Date: 2009/8/21 $


    % read one frame of FRG or IMG data at the position index_frame
    %disp(sprintf('...Frame loaded: %d',index_frame))
    elapsed_time = fread(file.fid, 1, 'int32' ); % 4 bytes of elapsed time
    frame_info = fread(file.fid, 36, 'int8' ); % 4 bytes of System time of current frame + 32 bytes Reserved
    if file.type == 'FRG'
        frame_data = fread(file.fid, frame.pixel_num, 'int16' ); % int16 = 2 bytes = one pixel in FRG frame
        frame_2D = reshape(frame_data, frame.FFT_length, frame.width);
    elseif file.type == 'IMG'
        frame_data = fread(file.fid, frame.pixel_num, 'uint8' ); % uint8 = 1 bytes = one pixel in IMG frame
        frame_2D = reshape(frame_data, frame.depth, frame.width);
    end
end

```

```
% Fringe_apodization.m
function Fringe_apodiz = Fringe_apodization(Fringe_k, apodiz_method)

    % Fringe_apodization Apodization along depth direction of input spectral fringe
    % in the k domain using an apodization method. This is for smoothing the
    % fringe to reduce the side lodes of the PSF of the OCT system arising from
    % the swept source spectrum
    % Calling format: Fringe_apodiz = Fringe_apodization(Fringe_k, apodiz_method)
    %
    % Fringe_apodiz: result returned after multiplication of every column of Fringe_k
    % by a apodization window specified by the (apodiz_method).
    %
    % Fringe_k: the input spectral fringe in the k domain
    % apodiz_method: option for apodization method. It can be chosen as
    % 'Gaussian', 'Hamming', 'Hann', 'Kaiser', 'Cosine', 'super_Gaussian',
    % 'Blackman', 'Nuttall', 'Blackman_Harris', 'None'


    % Copyright 2009-2010 Thorlabs Inc.
    % $Revision: 2.0 $ $Date: 2009/8/21 $

```

```
    [index_length, width] = size(Fringe_k);

    window_band = 0.3*index_length;
    depth_index = (1:index_length) - round(index_length/2);

    switch apodiz_method
        case 'Kaiser'
            disp('Kaiser window')
            alpha = 2;
            index = (1:index_length)-1;
            v = pi*alpha*sqrt(1 - (2*index/(index_length-1) -1).^2);
            window = (besseli(0,v)./besseli(0,pi*alpha))'*ones(1,width);
        case 'Cosine'
            %disp('Cosine window')
            window = cos(pi*depth_index./index_length)'*ones(1,width);
        case 'super_Gaussian'
            %disp('super Gaussian window')
            window = exp(-(depth_index./window_band).^4)'*ones(1,width);
        case 'Gaussian'
            %disp('Gaussian window')
            window = exp(-(depth_index./window_band).^2)'*ones(1,width);
        case 'Hamming'
            %disp('Hamming window')
            window =(0.53836 - 0.46164*cos(2*pi*(1:index_length)./(index_length-1)))'*ones(1,width); %Hamming
```

```
        case 'Hann'
            %disp('Hann window')
            window = (0.5 - 0.5*cos(2*pi*(1:index_length)./(index_length-1)))'*ones(1,width); %Hann
        case 'Blackman'
            %disp('Blackman window')
            window =(0.42 - 0.5*cos(2*pi*(1:index_length)./(index_length-1)) + ...
                0.08*cos(4*pi*(1:index_length)./(index_length-1)))'*ones(1,width); %Blackman
        case 'Nuttall'
            %disp('Nuttal window')
            window =(0.355768 - 0.487396*cos(2*pi*(1:index_length)./(index_length-1))+ ...
                + 0.144232*cos(4*pi*(1:index_length)./(index_length-1))- ...
                0.012604*cos(6*pi*(1:index_length)./(index_length-1)))'*ones(1,width); %Nuttall
        case 'Blackman_Harris'
            %disp('Blackman_Harris window')
            window =(0.35875 - 0.48829*cos(2*pi*(1:index_length)./(index_length-1))+ ...
                + 0.14128*cos(4*pi*(1:index_length)./(index_length-1)) - ...
                0.01168*cos(6*pi*(1:index_length)./(index_length-1)))'*ones(1,width); %Blackman_Harris
        otherwise
            %disp('rectangular window')
```

```
        window = 1;
    end
    Fringe_apodiz = Fringe_k.*window;
end

% Compute_Analytical.m
function [OCT_complex,noisyPixels] = Compute_Analytical(Fringe, FFT_length, image_depth)

    % Compute_Analytical Return complex OCT image in space domain
    % by inverse Fourier transforming along every column(A-line) of the spectral fringe image.
    %
    % Calling format: OCT_complex = Compute_Analytical(Fringe, FFT_length, image_depth)
    %
    % OCT_complex: Complex OCT image in space domain after inverse FFT transforms.
    %
    % Fringe: Spectral fringe in k(wavenumber) domain recorded after conversion from
    % wavelength domain using a MZI clock in the Thorlabs Swept source OCT system.
    % FFT_length: Data length for inverse FFT transforming along every column.
    % image_depth: the length of the output OCT_complex along the depth diretion.

```

```
% Copyright 2009-2010 Thorlabs Inc.
% $Revision: 2.0 $ $Date: 2009/8/21 $

% retrieve complex OCT image by IFFT along every column after padding zero
% to every column to get FFT_length pixels of data
complex_temp = ifft(Fringe,FFT_length);

% returning image_width
[height, image_width] = size(complex_temp);

% declare memory for OCT_complex
OCT_complex = zeros(image_depth, image_width);

aver_fract = 1/10;
% total number of averaging pixels in one every columns (A-lines) of the OCT image
aver_pixel = round(image_depth*aver_fract);

% amplitude of the OCT image
OCT_image = abs(complex_temp(1:image_depth,:));

% (Weston) Extract bottom aver_pixel pixels from each Ascan
noisyPixels = OCT_image((image_depth-aver_pixel):image_depth,:);

%caculate level of noise in the last 1/10*image_depth lines of OCT image.
level_noise = sum(OCT_image((image_depth - aver_pixel):
```

```
    image_depth ,:))/(aver_pixel+1);
    level_noise_matrix = ones(image_depth,1)*(1./level_noise);

    % Normalization of every columns of the complex fringe complex_temp by the noise
    % level of the last (aver_pixel+1) pixels and returning result-> OCT_complex
    OCT_complex = complex_temp(1:image_depth ,:).*level_noise_matrix;

    %OCT_complex = complex_temp(1:image_depth ,:);
end


end
```

APPENDIX B

B.1 Submitted manuscript: Endoscopic Doppler OCT imaging

W. A. Welge and J. K. Barton, “In vivo endoscopic Doppler optical coherence tomography imaging of the colon,” (submitted).

Lasers in Surgery and Medicine

In vivo endoscopic Doppler optical coherence tomography imaging of the colon

Journal:	*Lasers in Surgery & Medicine*
Manuscript ID	LSM-16-0097.R1
Wiley - Manuscript type:	Preclinical Reports
Date Submitted by the Author:	n/a
Complete List of Authors:	Welge, Weston; University of Arizona, College of Optical Sciences Barton, Jennifer; University of Arizona,
Key Words:	colorectal cancer, adenoma, image processing, vascular imaging

In vivo endoscopic Doppler optical coherence tomography imaging of the colon

Weston A. Welge, PhD

Jennifer K. Barton, PhD

College of Optical Sciences (WAW, JKB)
The University of Arizona
Tucson, AZ 85721

Department of Biomedical Engineering (JKB)
The University of Arizona
Tucson, AZ 85721

Funding Acknowledgements: This research was supported by the National Cancer Institute and the National Heart, Lung, and Blood Institute of the National Institutes of Health under award numbers R01CA109385 and T32HL007955, respectively, the American Society for Laser Medicine and Surgery Student Research Grant, and the Arizona TRIF Imaging Initiative. The content is solely the responsibility of the authors and does not necessarily represent the official views of the National Institutes of Health.

Correspondence: Jennifer K. Barton, 1657 E. Helen St., Tucson, AZ 85721-0240, phone: 520-626-0314; email: barton@email.arizona.edu

Keywords: colorectal cancer, adenoma, image processing, vascular imaging

Abstract

Background and Objective: Colorectal cancer remains the second deadliest cancer in the United States. Several screening methods exist, however detection of small polyps remains a challenge. Optical coherence tomography has been demonstrated to be capable of detecting lesions as small as 1 mm in the mouse colon, but detection is based on measuring a doubling of the mucosa thickness. The colon microvasculature may be an attractive biomarker of early tumor development because tumor vessels are characterized by irregular structure and dysfunction. Our goal was to develop an endoscopic method of detecting and segmenting colon vessels using Doppler optical coherence tomography to enable future studies for improving early detection and development of novel chemopreventive agents.

Method: We conducted *in vivo* colon imaging in an azoxymethane (AOM)-treated mouse model of colorectal cancer using a miniature endoscope and a swept-source OCT system at 1040 nm with a 16 kHz sweep rate. We applied the Kasai autocorrelation algorithm to laterally oversampled OCT B-scans to resolve vascular flow in the mucosa and submucosa. Vessels were segmented by applying a series of image processing steps: (1) intensity thresholding, (2) two-dimensional matched filtering, and (3) histogram segmentation.

Results: We observed differences in the vessels sizes and spatial distribution in a mature adenoma compared to surrounding undiseased tissue and compared the results with histology. We also imaged flow in four young mice (2 AOM-treated and 2 control) showing no significant differences, which is expected so early after carcinogen exposure. We also present flow images of adenoma in a living mouse and a euthanized mouse to demonstrate that no flow is detected after euthanasia.

Conclusion: We present, to the best of our knowledge, the first Doppler OCT images of *in vivo* mouse colon collected with a fiber-based endoscope. We also describe a fast and robust image processing method for segmenting vessels in the colon. These results suggest that Doppler OCT is a promising imaging modality for vascular imaging in the colon that requires no exogenous contrast agents.

1. Introduction

Colorectal cancer (CRC) is the second deadliest cancer in the United States, with nearly 50,000 estimated deaths in the United States in 2015 (1). Despite the high prevalence of CRC, the mortality rate has been steadily declining over the last four decades owing to the efficacy of many screening methods. When detected at the local stage, the 5-year survival rate of CRC is 90%. However, this rate drops to just 13% at the distant stage (1). This exemplifies the importance of early detection. With an overall five-year survival rate of 65%, there is still much need for improved screening methods.

The recommended CRC screening methods can be broadly divided into two types of tests: stool tests and imaging procedures. The stool tests require little preparation by the patient, are non-invasive, and sometimes do not require an office visit. The fecal occult blood test and fecal immunochemical test have high sensitivity and low specificity or vice versa (2). Stool DNA testing can achieve an area under the receiver operating characteristic (ROC) curve of over 90% given the right combination of tests (3). Stool DNA testing is particularly convenient because the patient can send samples by mail. However, despite the accuracy and convenience of these tests, they can only detect cancer, not localize the lesions. A positive result still requires the patient to undergo an imaging procedure.

Imaging screening methods, such as flexible sigmoidoscopy, colonoscopy, and virtual (CT) colonoscopy are capable of detecting CRC and localizing lesions, but these methods are more invasive than fecal tests. Virtual colonoscopy is the least invasive imaging modality with similar sensitivity as colonoscopy, but polyps cannot be removed without a more invasive procedure and the patient is exposed to ionizing radiation (4). Virtual colonoscopy is especially valuable in rural or isolated regions without easy access to gastroenterologists. Optical imaging is more invasive, but polyps can be removed during the procedure for pathological analysis as the gold standard for diagnosing CRC. Colonoscopy has high sensitivity to mature adenoma, but the miss rate for small polyps (<5 mm diameter) is estimated to be over 15% (5) and as high as 26% (6,7). Flat polyps are particularly easy to miss with white-light imaging.

Optical coherence tomography (OCT) is an attractive modality for CRC imaging because it provides additional information in the form of depth-resolved data. We have demonstrated that it is possible to automatically detect small adenoma in mouse models based on thickening of the mucosa and increased signal attenuation along the depth direction (8). The additional depth information from OCT can make detecting small, flat polyps easier than in traditional optical modalities like colonoscopy. However, this adenoma detection method using OCT still requires at least a doubling of the thickness of the mucosa, based on the results of a study using blinded experts reading OCT images of the mouse colon (9). Recent advancements in microvascular OCT imaging may enable even earlier detection of adenoma.

The microvasculature developed to support tumor growth is markedly different from existing, healthy vessels. In particular, the new vessels have variable diameters, dead ends, and form tortuous paths. Furthermore, the abnormal arterioles lack smooth muscle, which prevents them from dilating and constricting to control the blood flow rate in response to a variety of physiological and environmental stimuli (10). Both the vascular structure and function are potential biomarkers for adenoma detection. Moreover, because the growth of new vessels is one of the earliest morphological changes in the development of adenoma (11), microvascular imaging may improve early polyp detection.

To enable the investigation of the colon microvasculature using OCT, we developed a method of processing the raw data generated from a swept-source OCT system using a lab-built miniature endoscope. The method uses the 2-dimensional Kasai autocorrelation method for measuring bi-directional blood flow (12–14). The flow images are processed using intensity thresholding, 2D matched filtering, and histogram segmentation to extract vessels for further analysis. We tested the method on the azoxymethane (AOM) mouse model of colorectal cancer. We present, to the best of our knowledge, the first endoscopic Doppler OCT images of *in vivo* mouse colon.

2. Materials and Methods

2.1. Imaging System

We previously integrated a lab-built miniature endoscope for mouse colon imaging with a commercial swept-source OCT system (OCS1050SS, Thorlabs, Newton, NJ, USA) (15). The system layout and endoscope schematic are shown in Figure 1. Briefly, the source has a central wavelength of 1040 nm and a bandwidth of 80 nm, which produces an axial resolution of 12 μm in air. The A-scan rate is 16 kHz. The endoscope produces a numerical aperture of 0.14 with a glass spacer, gradient-index lens (GRINTECH, Jena, Germany) and 41° prism. The optics are enclosed by a glass envelope with an outer diameter of 2 mm and a wall thickness of 0.1 mm. These dimensions are robust to breakage during mouse colon imaging. However, a future probe for human imaging would require a safer material, such as a biocompatible, optically transparent plastic. The focus is located about 200 µm outside the envelope and has a spot size of 6.1 µm at focus. The measured power exiting the endoscope is 350 µW. The endoscope is connected to a fiber-optic rotary joint that is interfaced with a rotational motor for selecting the rotational angle for longitudinal imaging. The rotary joint and rotational motor are mounted on a linear translation stage that is moved by a linear actuator to control the motion of the endoscope.

2.2. Animal Model

A mouse model of colorectal cancer was used for *in vivo* imaging. A/J mice (The Jackson Laboratory, Bar Harbor, ME, USA) were treated with the colon-specific carcinogen AOM to develop adenoma (16). Beginning at six weeks of age, the A/J mice were administered 10 mg/kg of AOM for the cancer group and 0.2 mL of saline for the control group via subcutaneous injection weekly for five weeks. These procedures were in accord with a University of Arizona Institutional Animal Care and Use Committee approved protocol.

2.3. Imaging Protocol

Solid food was replaced with a pediatric electrolyte solution 24 hours prior to imaging. Mice were anesthetized for imaging by intraperitoneal injection of 100 mL/kg ketamine and 10 mL/kg xylazine. The colon was flushed with warm saline immediately prior to imaging. Mice were placed on a heating pad during imaging to maintain constant body temperature. Mice were 53 or 13 weeks of age during imaging.

The distal 30 mm of the colon was imaged to produce a single B-scan per mouse. The B-scan consisted of 512,000 A-scans (each with 512 pixels), corresponding to an A-scan spacing of about 58 nm. With a focused spot diameter of 6.1 μm, the number of samples per spot diameter (sampling density) is 104. This oversampling allows the window of measurable flow velocities to be shifted by applying the Kasai autocorrelation to every A-scan, every 2nd A-scan, 3rd A-scan, etc. without undersampling the data in the lateral dimension. Moreover, the high sampling density allows for averaging to reduce artifacts in the flow images due to the swept-source laser phase noise, bulk tissue motion, and vibration in the endoscope. The total imaging time was about 40 seconds.

The 53-week-old mice were euthanized after imaging. The distal 30 mm of the colon was explanted and cut open longitudinally. The tissue was fixed with 10% buffered formalin. Cross sections with 6-μm thickness were cut every 50 μm through the tissue. The sections were stained with hematoxylin and eosin and imaged with a standard laboratory transillumination microscope for histological analysis.

2.4. Image Processing

The raw fringes were recorded linearly in wavenumber. The raw data required numerical dispersion compensation due to an imbalance of dispersive media in the endoscope and the reference arm. We utilized a numerical method that determines the non-linear dispersion by subtracting a linear fit to the phase data as a function of wavenumber (15). After numerical dispersion correction, the data were processed as described in the following subsections. Dispersion compensation is necessary to improve the axial point-spread function so that it closely matches the expected PSF based on the source spectrum. The numerical dispersion compensation does not affect the results of the Doppler flow map beyond improving the axial resolution. The purpose of the image processing is to extract vessels from the surrounding static tissue.

2.4.1. Doppler OCT

The two-dimensional Kasai autocorrelation method (12–14) was used to generate flow images:

$$f_D = \frac{1}{2\pi\Delta T} \arg\left(\sum_{j=1}^{J}\sum_{z=1}^{N} A_{z,j+1}A^*_{z,j}\right) \tag{1}$$

$$v = \frac{\lambda_0 f_D}{2n\cos\theta}\,, \tag{2}$$

where ΔT is the A-scan period, J and N are number of A-scans and depth pixels summed to reduce degradation due to noise, A is the complex A-scan data resulting from the inverse Fourier transform of the fringes after numerical dispersion correction, λ_0 is the central wavelength of the source, f_D is the Doppler frequency, v is the flow velocity, n is the refractive index of the sample, and θ is the Doppler angle (angle between the direction of flow and the OCT beam). We used $J = 4$ and $N = 2$ for the window size and used every sixth A-scan, corresponding to an A-scan period of 375 µs. By using every sixth A-scan, the product of the A-scans in Eq. (1) is $A_{z,j+6}A^*_{z,j}$; however, Eq. (1) is written in the general form. The choice of skipping A-scans for computing the phase change depends on the system (e.g., desired velocity range based on A-scan rate, asymmetric sweep spectra limiting computation of the phase shift on only even or only odd A-scans). The window size was chosen to balance post-processing computation time and noise suppression. The depth window size of 2 pixels reduced the standard deviation of the phase change of stationary 1% Intralipid by about 20%. Further increasing the depth window size showed minimal additional noise suppression and caused a proportional increase in computation time. The larger lateral window size was chosen because phase noise due to synchronization errors between the swept source and the data acquisition manifests across adjacent A-scans. For physiologically relevant flow velocities (< 3 mm/s in mouse colon), applying the Kasai autocorrelation in either axial or transverse directions will accurately measure the flow (14). Due to the asymmetric sweep spectra of the source, the Kasai autocorrelation can only be applied to even or odd A-scans.

With a high sampling density, we can effectively control the range of flow velocities that can be detected. Increasing the A-scan period allows detection of low flow velocities and decreasing the period shifts the flow sensitivity range to higher flow velocities. Because the sampling density is very high, many A-scans can be skipped while still effectively sampling at the same spatial location on the sample. The minimum detectable flow velocity is limited in practice by the phase stability of the imaging system. While a mirror is often chosen as the sample for measuring phase noise, using tissue samples provides a more realistic measure of the system noise due to the decreased SNR of tissue compared to a highly reflective mirror (17). We plotted histograms of regions of interest containing at least 1000 pixels in several vessel-free regions in the muscularis propria. For each region, we measured the full width at half maximum (FWHM). In static tissue, variance in the measured phase ($\arg(\cdot)$ in Eq.(1)) results from system phase noise and bulk motion. The average of the FWHM values was 0.111 rad. If we define the minimum detectable phase change due to flow as 0.111 rad, then this corresponds to a velocity of 17.5 μm/s for $\theta = 0$, $\Delta T = 375$ μs, $\lambda_0 = 1040$ nm, and $n = 1.4$. This value is an order of magnitude lower than typical capillary flow velocity. However, most vessels are not parallel to the beam and so the minimum detectable velocity increases as the Doppler angle approaches 90°. The maximum flow velocity at $\theta = 0$ before phase wrapping is 0.5 mm/s.

A flow phantom was used to measure the experimental minimum detectable flow velocity. The phantom was a glass capillary tube with an inner diameter of 0.45 mm. A 27-gauge needle was inserted into one end of the tube. A syringe pump controlled the flow of 5% Intralipid through the capillary tube. A-scans were collected through the center of the capillary tube at a measured A-scan rate of 15.4 kHz without moving the endoscope. Every 6th A-scan was used for processing. The Doppler angle was 80°. After applying numerical dispersion compensation and computing the Kasai autocorrelation with a window size of 2 pixels in depth and 4 pixels in time, the resulting flow profiles were averaged together. Parabolic flow across the entire inner diameter of the capillary tube was seen at a flow velocity of 0.3 mm/s (52.1 μm/s along the beam axis). The maximum flow velocity before phase wrapping was 1.4 mm/s (0.243 mm/s along the beam axis).

After computing the Kasai autocorrelation, the image was resized to produce square pixels using bicubic interpolation (downsampled from 512 × 512000 to 512 × 7680). Due to the high degree of oversampling in the lateral direction, the downsampling removes most of the motion artifacts due to vibration of the endoscope and mouse respiration. This improvement is demonstrated in Figure 2.

2.4.2. Intensity Thresholding

Signal-void regions produce noisy flow maps when using many Doppler OCT algorithms, including the Kasai method used here. Therefore, we used the structural image intensity to mask the flow image such that signal-void regions are removed. The threshold was 10 dB above the noise floor. Next, a median filter using a 5 × 5 kernel was applied to the image to reduce speckle noise. The noise floor was computed by averaging the bottom 100 rows in the log-intensity image. At this depth (1.61 mm to 2.00 mm), no signal from the tissue could be seen in the structural image. In addition to removing regions where the signal has been greatly attenuated, this masking step also removes flow data from small, non-scattering cavities in the tissue that might otherwise be confused for vessels. Signal from non-colon tissue (e.g., connective tissue, fluid in the colon, endoscope window) was manually removed as needed.

2.4.3. Two-dimensional Matched Filtering

We used a 2D matched filter to reduce the variability of static, non-circular (i.e., vessel cross sectional) features in the flow map. We manually inspected prominent vessels detected from the flow images and found most to have a diameter of about 7 pixels (27μm). We defined a circular template to extract circular features with sizes around 7 pixels. This template was cross-correlated with the flow image. This step may introduce flow artifacts near the boundaries of the tissue introduced by the intensity threshold. Excessive artifacts should be manually removed prior to histogram segmentation to avoid skewing the histogram.

2.4.4. Histogram Vessel Segmentation

A histogram-based segmentation method was then used to extract vessels using velocity thresholds determined by the descriptive statistics of the pixel values with thresholds set at the mean ± 2 standard deviations. This threshold appears to segment vessels in the flow image while also removing or reducing most of any remaining artifacts caused by bulk tissue or endoscope motion. The result of the vessel segmentation is a “quaternary” image consisting of pixels identified as: (1) flow in the positive direction (red), (2) flow in the negative direction (blue), (3) no flow (white), and (4) pixels removed by intensity thresholding (black). The blue and red colors in the quaternary flow maps indicate flow direction only and do not correspond to specific velocity amplitudes.

3. Results

The matched filter improves performance of the histogram segmentation of the vessels. A profile through two vessels before and after applying the matched filter is shown in Figure 3. The signal-to-noise ratio (SNR), defined as the ratio of the signal mean to the background standard deviation, was computed for the profiles through two vessels in Figure 3 before and after the matched filter operation. The matched filter primarily smoothens the background and reduces the background standard deviation. The SNR of the flow map before applying the matched filter for the positive and negative flow are 13.90 and 18.61, respectively. After the matched filter, the positive and negative flow SNR values are 17.93 and 21.84. This is largely due to the 25% reduction in the background standard deviation. Smoothing the background improves the performance of the histogram segmentation step because local fluctuations due to phase noise are reduced. The cross-correlation operation broadens the vessel size by the diameter of the matched filter. However, the amplitude of this broadened region is significantly lower than the actual vessel region and therefore has a small effect on the sizes of the vessel after histogram segmentation.

Example structural and segmented flow images from 13-week-old mice are shown in Figure 4 (saline group) and Figure 5 (AOM group). Vessels are present in the mucosa and submucosa in all four mice. Most vessels are circular, suggesting that the OCT image plane was close to perpendicular to most vessels, though a few larger vessels that are more parallel to the images can be seen. The large blue area on the right side of Figure 5b is an artifact from motion that was partially suppressed by the histogram segmentation.

A comparison of adenoma tissue from a living and a euthanized mouse are shown in Figure 6. Figures 6a and 6b show intensity images of the adenoma, clearly distinguishable as such due to the absence of a visible mucosa-submucosa boundary. The *in* vivo adenoma has a high density of vessels and several arteriole-venule pairs. The motion artifacts on the left and center of Figure 6c have been suppressed in Figure 6e by the histogram segmentation. As expected, the flow images of Figures 6d and 6f show no vessels in the euthanized tissue. Some vertical streaking artifacts from the endoscope motion can be seen in Figure 6d. These artifacts are nearly fully suppressed by histogram segmentation; Figure 6f shows only a small number of (artifactual) flow pixels.

A comparison of an adenoma and surrounding undiseased tissue from a single 53-week-old mouse is shown in Figure 7. The segmented vessels in the undiseased tissue vary in size with a qualitatively uniform distribution of small, medium, and large vessels. However, the vessels in the adenoma are mostly either small or large. The adenoma also has fewer vessels total and the vessels are mostly located in the center and left of center. The large vessel in Figure 7b can be seen in the 4x (Figure 7c) and 10x (Figure 7d) histology images. Very few other vessels were found in the adenoma histology. In contrast, the vessels are homogeneously distributed in the undiseased flow image shown in Figure 7(f) and are located in both the mucosa and submucosa. Some arterioles and venules near the submucosa are denoted with arrows in the corresponding 10x histology image (Figure 7g). Small vessels throughout the depth of the mucosa are shown with arrows in the 20x histology image (Figure 7h).

4. Discussion

The method described here can enable rapid measurements such as total vessel count, 200 vessel density, and extracting flow velocities from individual vessels. Using a standard PC running Matlab (2014b, Mathworks, Natick, MA, USA), all processing steps after the Kasai autocorrelation were completed in about 1 second. Real-time Doppler processing using Kasai autocorrelation in software has been previously demonstrated (18). By implementing the methods described in this paper in a precompiled programming language and using real-time Doppler processing, many vascular measurements could be made in real time.

The matched filter operation smoothens the static tissue regions to improve the performance of the histogram segmentation. This is particularly useful for swept-source lasers because they typically have more phase noise than other OCT sources such as superluminescent diodes. A series of filter templates may enable more accurate vessel detection and orientation (e.g., determining the Doppler angle) at the expense of greater computation time.

The image processing steps described here reduce, but do not completely remove, artifacts due to motion. By oversampling the data in the lateral direction and averaging many A-scans, artifacts from repetitive motions like breathing and endoscope vibration can be reduced or removed. In cases where motion artifacts are not sufficiently suppressed with histogram segmentation, other bulk-motion correction methods (e.g., histogram mean/median or referencing all phase measurements to the tissue surface) may be implemented. Oversampling can be implemented in 3D imaging with a high-speed OCT system (19), and the additional information from surrounding regions can improve the accuracy of vessel detection. Circularly shifting flow values to center the mode of the flow histogram can further reduce bulk motion with a modest increase in computation time (20).

The differences in vascular size and spatial distribution in adenoma and undiseased colon tissue are similar to those reported in the literature. The spatial distribution of vessels is more homogeneous in the undiseased tissue than in the adenoma. Also, the adenoma has a large vessel in the center and a few other small vessels while the undiseased tissue vessels range from small to large. Konerding et al. have shown similar results using corrosion casts of normal and adenoma tissue in the human colon (10). We do not see significant differences in vessel sizes or spatial distribution in the 13-week-old AOM- and saline-treated mice. Based on our previous experience, we would not expect adenomas to develop so shortly after administering AOM. Additionally, it is difficult to ensure that the same location is imaged over multiple imaging sessions without volumetric imaging.

Some challenges exist for translating endoscopic OCT colon imaging to humans. The small diameter of the mouse colon allows for the tissue to remain in contact with the endoscope window. However, the imaging system will need to be modified for imaging in the larger human colon in order to keep the colon within the imaging depth of field. OCT typically uses low numerical aperture probes, so the depth of field is already on the order of the imaging depth imposed by light scattering in the tissue. Two methods could be used to keep the tissue within the depth of field. The first would be to use a balloon catheter inflated to hold the endoscope in the center of the colon, thus maintaining a mostly uniform distance from the probe to the tissue. A second method, termed adaptive ranging (21), would be to design the reference arm to continuously adjust length to keep the zero optical path difference location near the surface of the tissue. Another challenge to clinical translation is optimizing presentation of images and measurements for physicians. Rapid display of volumetric angiograms may enable assessment of tumors based on visual judgment of vessel tortuosity. We have presented, to the best of our knowledge, the first endoscopic *in vivo* Doppler OCT images of the mouse colon and described a simple, robust, and fast image processing method for extracting vessels. Future studies will use volumetric imaging to co-register vessels across multiple time points using a larger mouse population for a statistically significant study. Angiogenesis of dysfunctional vessels form at the earliest stages of pre-malignant tumorigenesis in the colon and many other organs (11,22). Therefore, Doppler OCT may be capable of discriminating pre-malignant tumors based on changes of blood flow in response to vasodilators or vasoconstrictors. The tumors in this AOM-treated mouse model are adenoma and do not progress to malignant adenocarcinoma. Future work will use a model with malignant potential.

References

1. Cancer Facts & Figures 2015 [Internet]. Atlanta: American Cancer Society; 2015. Available from: http://www.cancer.org/acs/groups/content/@editorial/documents/document/acspc-044552.pdf

2. Burch JA, Soares-Weiser K, St. John DJB, Duffy S, Smith S, Kleijnen J, et al. Diagnostic accuracy of faecal occult blood tests used in screening for colorectal cancer: a systematic review. J Med Screen 2007; 14(3):132–137.

3. Yang H, Xia B-Q, Jiang B, Wang G, Yang Y-P, Chen H, et al. Diagnostic value of stool DNA testing for multiple markers of colorectal cancer and advanced adenoma: A meta-analysis. Can J Gastroenterol Hepatol 2013; 27(8):467–475.

4. Pickhardt PJ, Hassan C, Halligan S, Marmo R. Colorectal cancer: CT colonography and colonoscopy for detection—Systematic review and meta-analysis. Radiology 2011; 259(2):393–405.

5. Ahn SB, Han DS, Bae JH, Byun TJ, Kim JP, Eun CS. The miss rate for colorectal adenoma determined by quality-adjusted, back-to-back colonoscopies. Gut Liver 2012; 6(1):64–70.

6. Van Rijn JC, Reitsma JB, Stoker J, Bossuyt PM, van Deventer SJ, Dekker E. Polyp miss rate determined by tandem colonoscopy: a systematic review. Am J Gastroenterol 2006; 101(2):343–350.

7. Pickhardt PJ, Nugent PA, Mysliwiec PA, Choi JR, Schindler WR. Location of adenomas missed by optical colonoscopy. Ann Intern Med 2004; 141(5):352–359.

8. Winkler AM, Rice PFS, Drezek RA, Barton JK. Quantitative tool for rapid disease mapping using optical coherence tomography images of azoxymethane-treated mouse colon. J Biomed Opt 2010; 15(4):041512.

9. Hariri LP, Qiu Z, Tumlinson AR, Besselsen DG, Gerner EW, Ignatenko N, et al. Serial endoscopy in azoxymethane treated mice using ultra-high resolution optical coherence tomography. Cancer Biol Ther 2007; 6(11):1753–1762.

10. Konerding MA, Fait E, Gaumann A. 3D microvascular architecture of pre-cancerous lesions and invasive carcinomas of the colon. Br J Cancer 2001; 84(10):1354–1362.

11. Staton CA, Chetwood ASA, Cameron IC, Cross SS, Brown NJ, Reed MWR. The angiogenic switch occurs at the adenoma stage of the adenoma–carcinoma sequence in colorectal cancer. Gut 2007; 56(10):1426–1432.

12. Kasai C, Namekawa K, Koyano A, Omoto R. Real-time two-dimensional blood flow imaging using an autocorrelation technique. IEEE Trans Sonics Ultrason 1985; 32(3):458–464.

13. Zhang J, Chen Z. In vivo blood flow imaging by a swept laser source based Fourier domain optical Doppler tomography. Opt Express 2005; 13(19):7449–7457.

14. Morofke D, Kolios MC, Vitkin IA, Yang VXD. Wide dynamic range detection of bidirectional flow in Doppler optical coherence tomography using a two-dimensional Kasai estimator. Opt Lett 2007; 32(3):253–255.

15. Welge WA, Barton JK. Expanding functionality of commercial optical coherence tomography systems by integrating a custom endoscope. PLOS ONE 2015; 10(9):e0139396.

16. Papanikolaou A, Wang QS, Papanikolaou D, Whiteley HE, Rosenberg DW. Sequential and morphological analyses of aberrant crypt foci formation in mice of differing susceptibility to azoxymethane-induced colon carcinogenesis. Carcinogenesis 2000; 21(8):1567–1572.

17. Leitgeb RA, Werkmeister RM, Blatter C, Schmetterer L. Doppler optical coherence tomography. Prog Retin Eye Res 2014; 41:26–43.

18. Liu G, Qi W, Yu L, Chen Z. Real-time bulk-motion-correction free Doppler variance optical coherence tomography for choroidal capillary vasculature imaging. Opt Express 2011; 19(4):3657–3666.

19. Choi W, Mohler KJ, Potsaid B, Lu CD, Liu JJ, Jayaraman V, et al. Choriocapillaris and choroidal microvasculature imaging with ultrahigh speed OCT angiography. PLOS ONE 2013; 8(12):e81499.

20. Yang VXD, Gordon ML, Mok A, Zhao Y, Chen Z, Cobbold RSC, et al. Improved phase-resolved optical Doppler tomography using the Kasai velocity estimator and histogram segmentation. Opt Commun 2002; 208(4–6):209–214.

21. Iftimia NV, Bouma BE, de Boer JF, Park BH, Cense B, Tearney GJ. Adaptive ranging for optical coherence tomography. Opt Express 2004; 12(17):4025–4034.

22. Raica M, Cimpean AM, Ribatti D. Angiogenesis in pre-malignant conditions. Eur J Cancer 2009; 45(11):1924–1934.

Figure legends

Figure 1: OCT system diagram and endoscope schematic. (a) The *x*-galvanometer control signal from the OCS1050SS is used to synchronize movement of the endoscope. The red line denotes the beam path in fiber. For the application described in this paper, the linear actuator moves the endoscope along the distal 30 mm of the colon. The rotational motor is used to select the rotational location of the longitudinal B-scan. OCT: OCS1050SS system, SE: synchronization electronics, LA: linear actuator, RM: rotational motor, TS: translation stage, RJ: fiber-optic rotary joint. (b) Schematic of the distal endoscope optics. S: spacer, GL: gradient-index lens, P: 41° rod prism. (c) Photograph of the distal portion of the endoscope.

Figure 2: Comparison of flow map before and after downsampling using bicubic interpolation. (a) A flow map after interpolation, (b) the flow map of the region denoted by the box in (a) prior to downsampling. Note that the repetitive red and blue vertical streaks

due to the stepper motor motion have been averaged out in (a). Scale bar is 1 mm. Color bar is – π to π radians.

Figure 3: Comparison of vessel flow profiles before and after applying 2D matched filter. (a) Flow image prior to matched filter; (b) flow image after applying matched filter; (c) profile along black line in (a); profile along black line in (b); (e) histogram segmentation of (a) with upper and lower thresholds set to mean ± 2 standard deviations, excluding black pixels, (f) histogram segmentation of (b) with upper and lower thresholds set to mean ± 2 standard deviations, excluding black pixels. Scale bar is 1 mm. Color bar is – π to π radians (black pixels denote signal-void regions removed during intensity thresholding) and applies to (a) and (b). The blue and red in (e) and (f) indicate positive and negative flow, but not specific flow velocities.

Figure 4: Structural and segmented flow images from two saline-treated mice. (a,d) Structural OCT images, (b,e) result from matched filter operation after computing Kasai autocorrelation, (c,f) result of histogram segmentation on (b,e). Arrows denote portions of vessels parallel to the image plane and arteriole-venule pairs. Scale bars are 1 mm. Images have been stretched vertically by 25% to improve readability. The blue and red in (c) and (f) indicate positive and negative flow, but not specific flow velocities.

Figure 5: Structural and segmented flow images from two AOM-treated mice. (a,d) Structural OCT images, (b,e) result from matched filter operation after computing Kasai autocorrelation, (c,f) result of histogram segmentation on (b,e). Arrow denotes a partially

suppressed motion artifact. Scale bars are 1 mm. Images have been stretched vertically by 25% to improve readability. The blue and red in (c) and (f) indicate positive and negative flow, but not specific flow velocities.

Figure 6: Comparison of adenoma tissue from living and euthanized mice. (a) and (b) are OCT images from the living and euthanized mouse, respectively. (c) and (d) are the corresponding flow images after intensity thresholding and matched filtering, (e) and (f) are the corresponding flow images after histogram segmentation. Scale bar is 1 mm. Color bar shows the phase shift in radians and applies to (c) and (d). The blue and red in (e) and (f) indicate positive and negative flow, but not specific flow velocities.

Figure 7: Comparison of adenoma and undiseased tissue. (a) Structural OCT image of adenoma, (b) segmented flow image of adenoma, (c,d) histology cross-section of adenoma at 4x and 10x magnification, (e) structural OCT image of undiseased colon tissue, (f) segmented flow image of undiseased tissue, (g,h) histology cross-section of undiseased tissue at 10x and 20x magnification. Arrows denote blood vessels. Scale bars are: 1 mm (a,b,e,f), 0.5 mm (c), 0.2 mm (d,g), and 0.1 mm (h). The blue and red in (b) and (f) indicate positive and negative flow, but not specific flow velocities.

Acknowledgments

We thank Photini Faith Rice and Caitlin Howard for assistance with drug treatment and animal imaging.

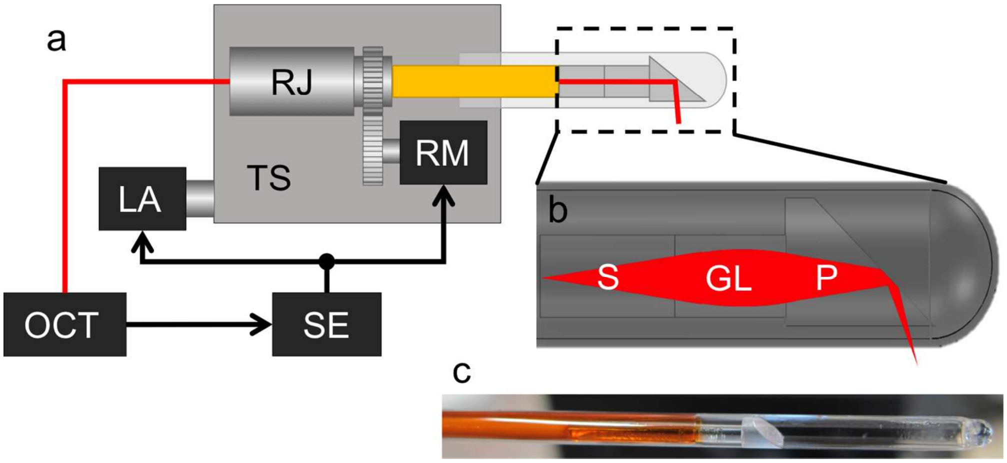

Figure 1: OCT system diagram and endoscope schematic. (a) The x-galvanometer control signal from the OCS1050SS is used to synchronize movement of the endoscope. The red line denotes the beam path in fiber. For the application described in this paper, the linear actuator moves the endoscope along the distal 30 mm of the colon. The rotational motor is used to select the rotational location of the longitudinal B-scan. OCT: OCS1050SS system, SE: synchronization electronics, LA: linear actuator, RM: rotational motor, TS: translation stage, RJ: fiber-optic rotary joint. (b) Schematic of the distal endoscope optics. S: spacer, GL: gradient-index lens, P: 41° rod prism. (c) Photograph of the distal portion of the endoscope.
576x262mm (72 x 72 DPI)

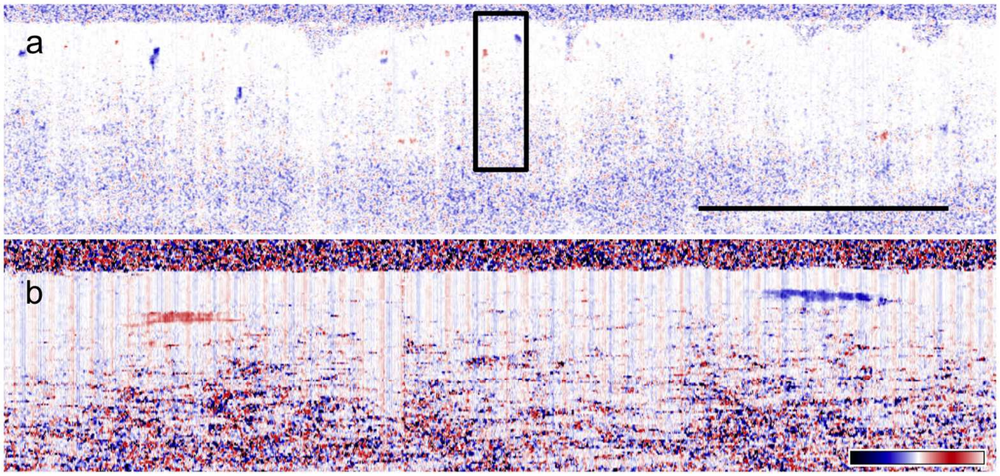

Figure 2: Comparison of flow map before and after downsampling using bicubic interpolation. (a) A flow map after interpolation, (b) the flow map of the region denoted by the box in (a) prior to downsampling. Note that the repetitive red and blue vertical streaks due to the stepper motor motion have been averaged out in (a). Scale bar is 1 mm. Color bar is − π to π radians.
705x335mm (72 x 72 DPI)

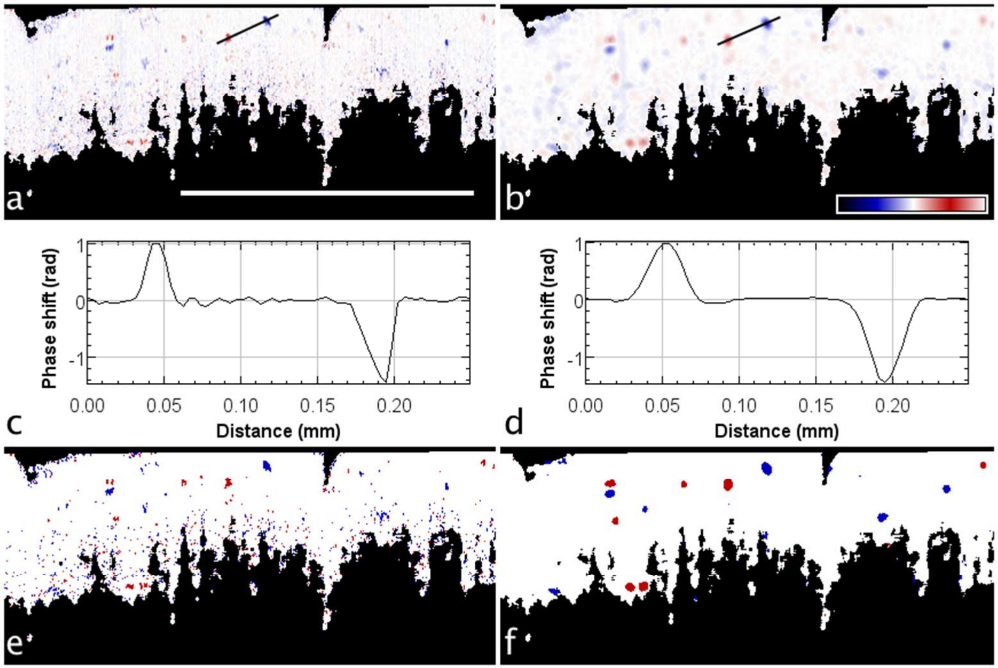

Figure 3: Comparison of vessel flow profiles before and after applying 2D matched filter. (a) Flow image prior to matched filter; (b) flow image after applying matched filter; (c) profile along black line in (a); profile along black line in (b); (e) histogram segmentation of (a) with upper and lower thresholds set to mean ± 2 standard deviations, excluding black pixels, (f) histogram segmentation of (b) with upper and lower thresholds set to mean ± 2 standard deviations, excluding black pixels. Scale bar is 1 mm. Color bar is – π to π radians (black pixels denote signal-void regions removed during intensity thresholding) and applies to (a) and (b). The blue and red in (e) and (f) indicate positive and negative flow, but not specific flow velocities.
307x206mm (72 x 72 DPI)

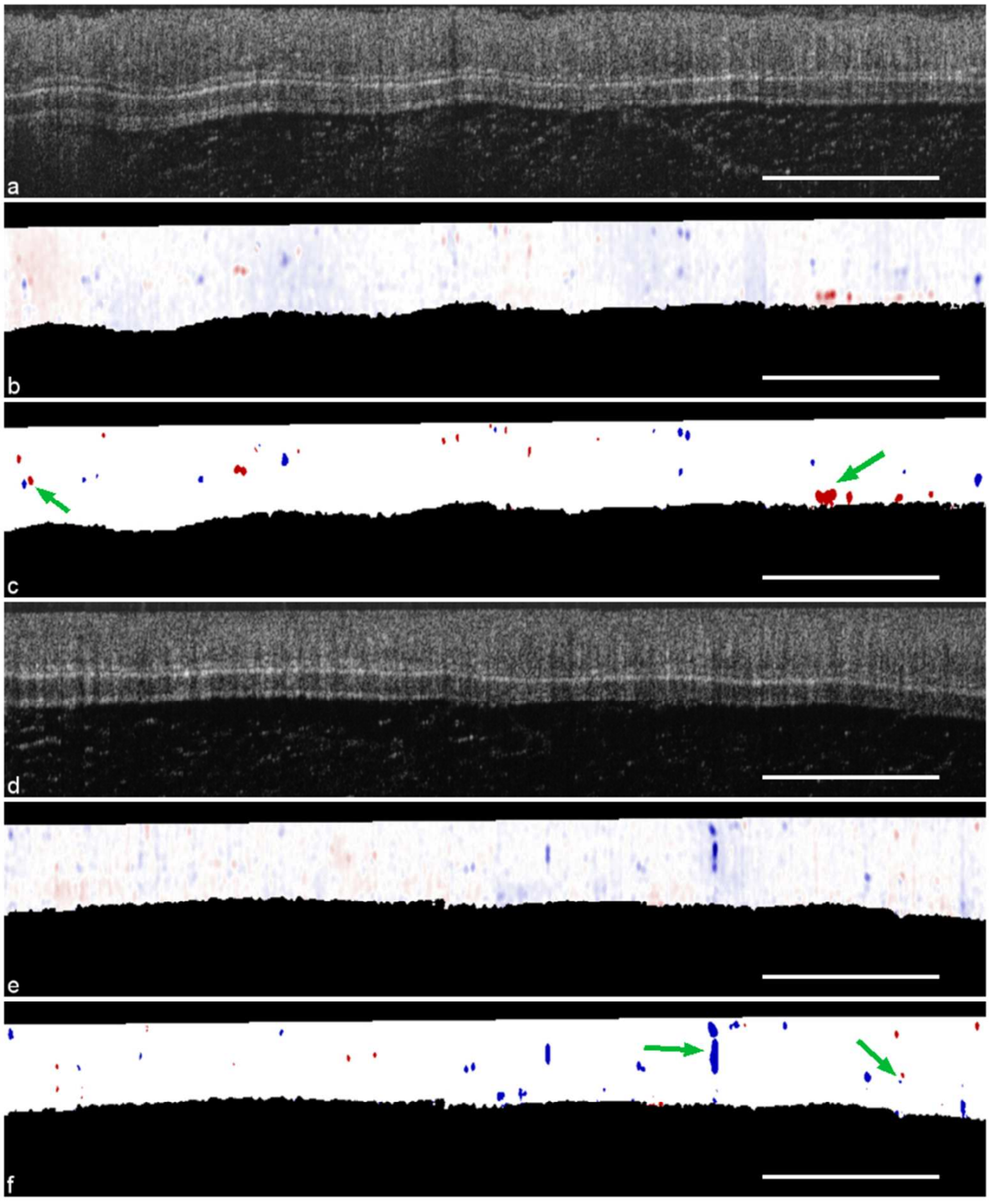

Figure 4: Structural and segmented flow images from two saline-treated mice. (a,d) Structural OCT images, (b,e) result from matched filter operation after computing Kasai autocorrelation, (c,f) result of histogram segmentation on (b,e). Arrows denote portions of vessels parallel to the image plane and arteriole-venule pairs. Scale bars are 1 mm. Images have been stretched vertically by 25% to improve readability. The blue and red in (c) and (f) indicate positive and negative flow, but not specific flow velocities.
93x113mm (300 x 300 DPI)

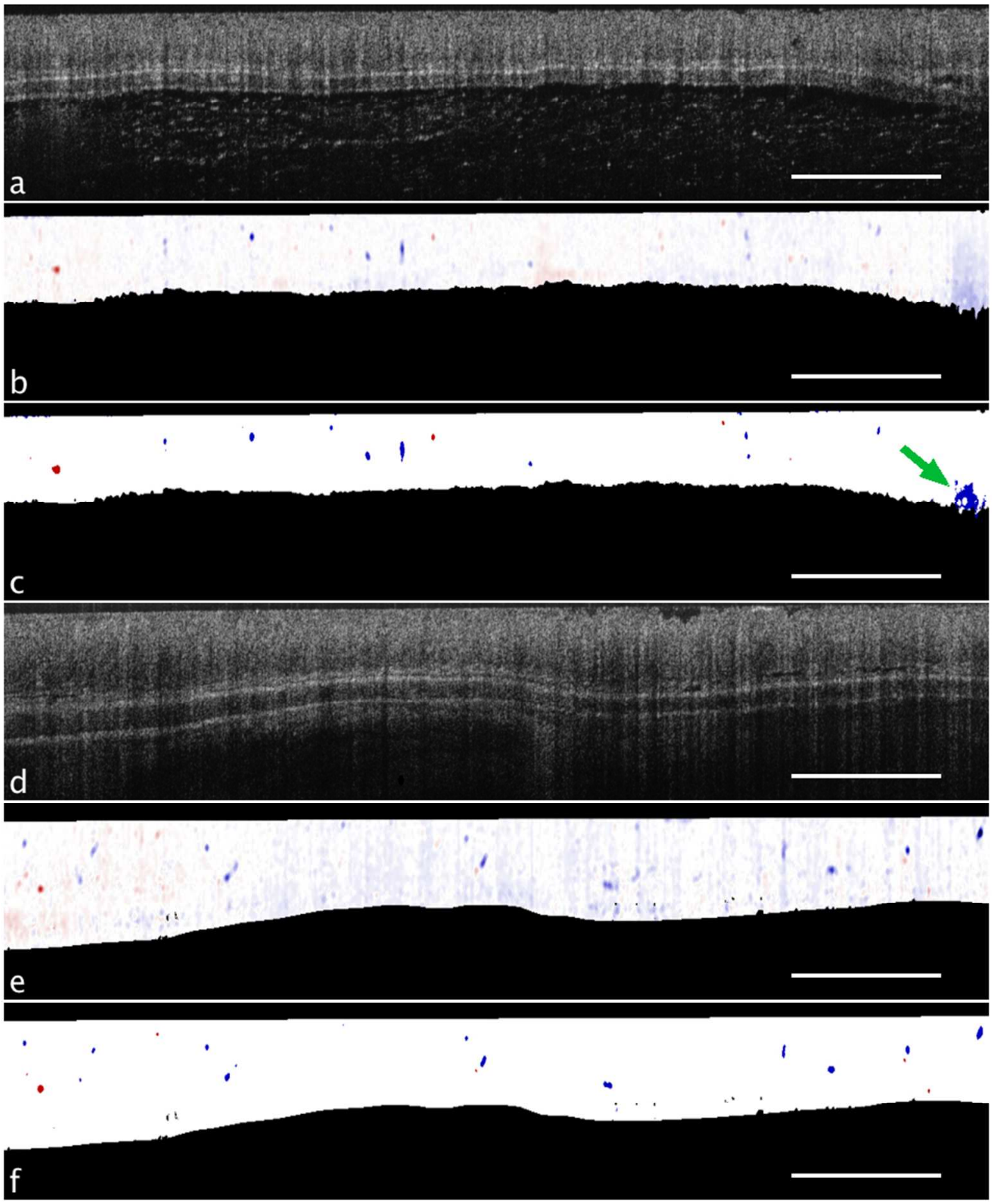

Figure 5: Structural and segmented flow images from two AOM-treated mice. (a,d) Structural OCT images, (b,e) result from matched filter operation after computing Kasai autocorrelation, (c,f) result of histogram segmentation on (b,e). Arrow denotes a partially suppressed motion artifact. Scale bars are 1 mm. Images have been stretched vertically by 25% to improve readability. The blue and red in (c) and (f) indicate positive and negative flow, but not specific flow velocities.
167x152mm (144 x 192 DPI)

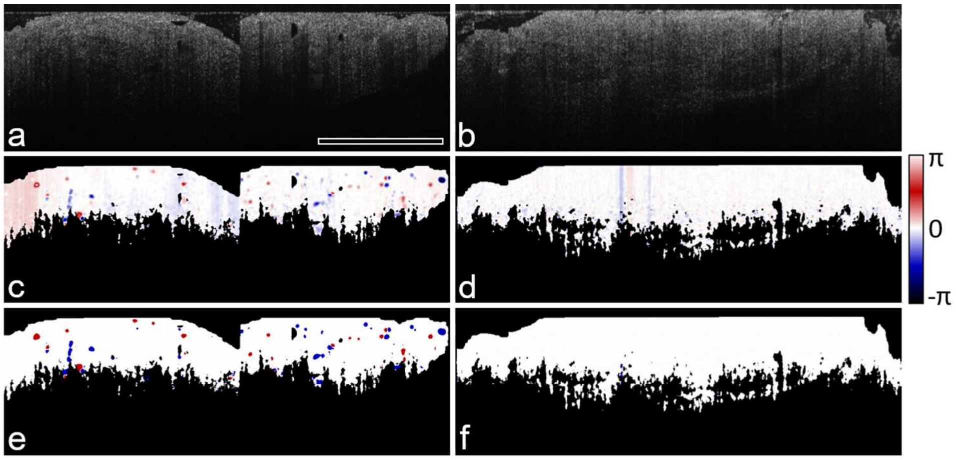

Figure 6: Comparison of adenoma tissue from living and euthanized mice. (a) and (b) are OCT images from the living and euthanized mouse, respectively. (c) and (d) are the corresponding flow images after intensity thresholding and matched filtering, (e) and (f) are the corresponding flow images after histogram segmentation. Scale bar is 1 mm. Color bar shows the phase shift in radians and applies to (c) and (d). The blue and red in (e) and (f) indicate positive and negative flow, but not specific flow velocities.
474x225mm (72 x 72 DPI)

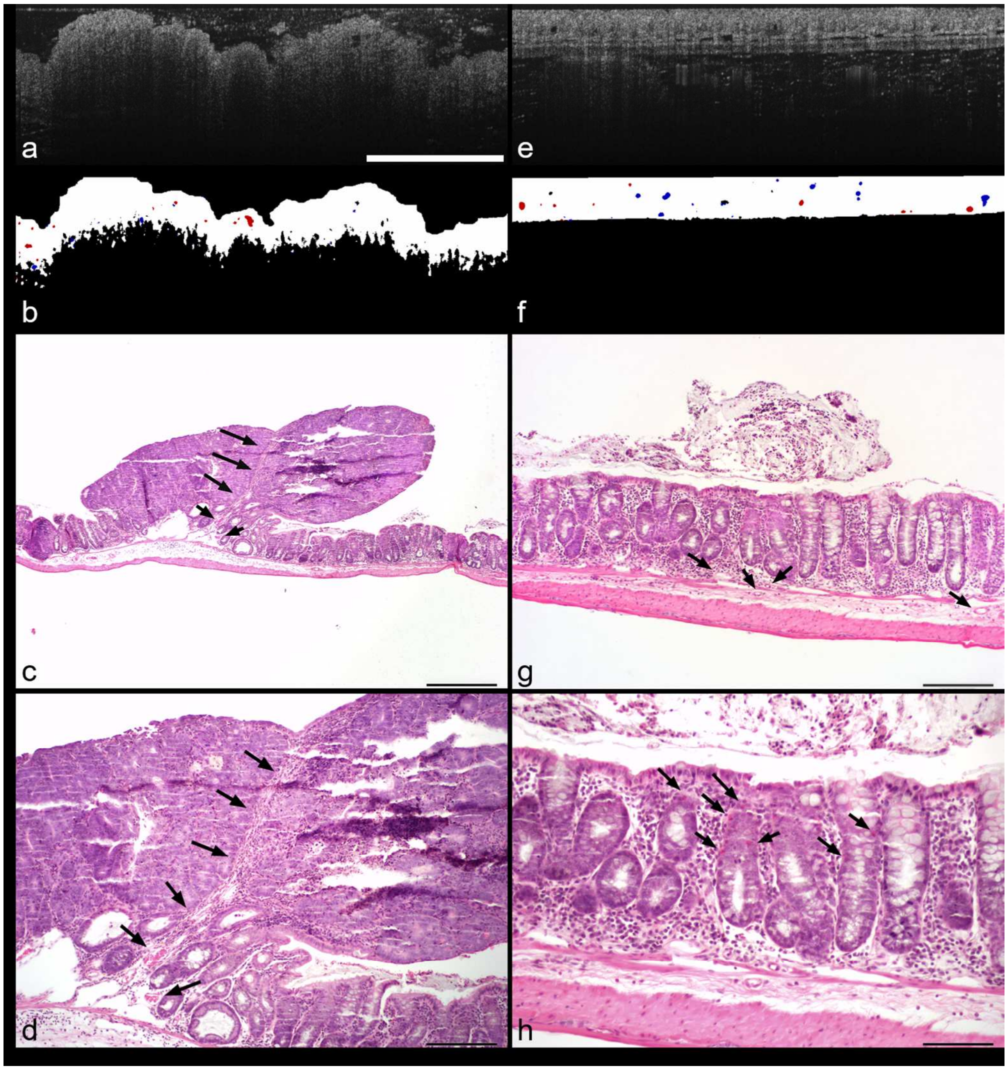

Figure 7: Comparison of adenoma and undiseased tissue. (a) Structural OCT image of adenoma, (b) segmented flow image of adenoma, (c,d) histology cross-section of adenoma at 4x and 10x magnification, (e) structural OCT image of undiseased colon tissue, (f) segmented flow image of undiseased tissue, (g,h) histology cross-section of undiseased tissue at 10x and 20x magnification. Arrows denote blood vessels. Scale bars are: 1 mm (a,b,e,f), 0.5 mm (c), 0.2 mm (d,g), and 0.1 mm (h). The blue and red in (b) and (f) indicate positive and negative flow, but not specific flow velocities.
258x273mm (150 x 150 DPI)

B.2 Kasai autocorrelation

I used the two-dimensional Kasai autocorrelation (also known as phase-resolved optical Doppler tomography) method for estimating the frequency shift of the scattered sample-arm light due to moving particles in tissue. This method estimates the average phase shift of adjacent A-scans. The derivation of the autocorrelation as an estimator of the phase shift is described in Sec. 1.3.3. Like many Doppler OCT algorithms, the user has freedom to adjust some parameters. The two-dimensional Kasai autocorrelation algorithm averages over a user-defined number of pixels in depth and lateral dimensions. The choice for these parameters is through trial and error and aims to balance the tradeoff between reducing noise, maintaining a physiologically relevant range of detectable flow velocities, and keeping computation time reasonable. I describe the parameters used for collecting the images with the Thorlabs OCS1050SS system, the parameters used in the software for computing the Kasai autocorrelation, and the details of the image processing steps for generating a map of the vasculature in Sec. B.2.1. The MATLAB code listed in Sec. B.2.2.

B.2.1 Method and parameters

To generate high-quality OCT images sensitive to capillaries, current Doppler algorithms call for two or more sequential B-scans collected at the same location on the tissue. Ideally the beams scans rapidly over the same line on the sample without any translation in the orthogonal direction until the desired number of overlapping B-scans are acquired to maximize correlation of static tissue in each B-scan. However, continuous movement of the beam along the slow scan axis is acceptable so long as the pitch between adjacent B-scans is sufficiently small relative to the beam size. This simplifies control of the slow scanning motor because synchronization of motion with each B-scan is not necessary.

For endoscopic Doppler imaging, the linear motor is programmed to move at a velocity of 0.0287 in/s (0.7290 mm/s) and no rotational motion was used. The data was collected as a 3D volume using the OCT software. In post-processing, each frame was concatenated to form a single, long B-scan. At an A-scan rate of 16 kHz and the above velocity, the A-scan separation is 45.56 nm. However, there is a brief period of time between each frame where the fringe data are saved to the hard drive. The data presented here were collected using 2000 A-scans per frame and 216 frames per volume. Using these settings, the OCT system typically finishes imaging within 1 second of the linear motor reaching 30 mm of travel. Based on the empirical performance of the system, the average A-scan separation can be computed as the total distance of travel (30 mm) divided by the total number of A-scans ($2000 \times 216 = 432000$), which is 69.44 nm. Using this separation, the sampling density is

$$SD \equiv \frac{\text{beam diameter}}{\text{A-scan separation}} = \frac{6.1\,\mu\text{m/spot}}{69.44\,\text{nm/A-scan}} = 87.85\,\text{A-scans/spot.} \tag{B.1}$$

This high sampling density demonstrates that even though no adjacent A-scans are collected at exactly the same location on the sample, there is a high degree of overlap of adjacent scans due to the finite diameter of the beam.

The asymmetric sweep spectrum of the OCS1050SS tunable laser affects the processing of the A-scans in Doppler imaging. When comparing adjacent A-scans (rather than adjacent B-scans in a helical scan), even and odd scans must be processed separately. This results in an effective halving of the sampling density. If scanning in a helical geometry and comparing adjacent B-scans for high sensitivity to low flow velocity, this is no longer necessary because even A-scans will automatically be compared to other even A-scans and likewise for odd A-scans.

A high sampling density allows for shifting the maximum detectable flow without phase wrapping by computing the Kasai autocorrelation for every N A-scans, where N is an integer for helical scanning geometry or $2N$ or $2N-1$ for even and odd A-scans in longitudinal scanning geometry, respectively. So long as the sampling density remains sufficiently high, this is effectively equivalent to adjusting the A-scan period T in the maximum velocity equation (assuming Doppler angle is zero),

$$v_{\max} = \pm\frac{\lambda_0}{4nT}. \tag{B.2}$$

There is no exact definition of sufficiently high sampling density. The data reported in Sec. B.1 used every 6th A-scan. At this reduced sampling density, the vessels still did not usually phase wrap and the computation time was of course reduced by a factor of 3 compared to taking every other A-scan. Determining optimal sampling density will reduce the image acquisition time and reduce the large file sizes.

The two other parameters that can be chosen for Kasai autocorrelation processing are the number of pixels to average in the lateral and axial dimensions. Previously reported literature for intensity-based Doppler variance[1] used window sizes of 4 in both axial and lateral direction [43, 79, 80]. I found that reducing the depth window size to 2 pixels had a subjectively minimal affect on the flow images and greatly reduced computation time.

After estimating the phase difference between adjacent A-scans using the Kasai autocorrelation, a series of image processing steps were applied to generate the vessels maps reported in Sec. B.1. These steps are

1. Intensity thresholding to mask out regions of low reflectance signal from the tissue,
2. (*optional*) Manual removal of the endoscope glass envelope and tissue beyond the colon (connective tissue or other organs),
3. Applying a two-dimensional matched filter using a circular template to amplify circular flow signal from vessels,

---

[1] The equation used for computing the intensity-based Doppler variance is similar to the Kasai autocorrelation. The numerator differs by taking the magnitude of the A-scans and a denominator is included that is the sum of the square moduli of adjacent A-scans.

4. Histogram segmentation to discriminate vessels from static tissue, and
5. (*optional*) Add vertical lines to divide the flow map into equal-size regions of interest (ROIs) for manually analyzing the data.

The script `KasaiProcessing.m` is comprised of cells that compute these steps (including optional steps) individually. ImageJ is recommended for manual removal of the envelope and undesired tissue. The histogram segmentation is optimized for the "union jack" colormap in ImageJ to maximize contrast between positive- and negative-velocity flow, static tissue, and signal-free regions.

Intensity thresholding is used to remove signal-free regions from the flow map. Any signal in tissue-free regions, or regions deep enough into tissue that no singly scattered light can return, is comprised solely of noise. The noise is characterized by broad phase changes between adjacent pixels and erroneously produces flow maps showing high positive and negative flow. To mask out these regions, the software defines a map based on the noise floor of the intensity image. The software first checks for the existence of the variable `longBscanComplex`, which is a matrix computed as the inverse fast Fourier transform of the raw fringe data, transformed along the k (vertical) axis after numerical dispersion compensation. This is generated using the `correctDispersionLongBscan.m` function. The log of the normalized amplitude is first computed to transform the data to a decibel scale that is used for display. The noise is computed as the average of rows 400–500, corresponding to the bottom 20% of rows. At this depth, any reflectance from colon tissue is fully attenuated. The intensity threshold is defined as 10 dB above this noise value. The OCT image is then resized to have square pixels using the `imresize` function, which uses bicubic interpolation by default. Each pixel is then compared to the threshold to generate a binary image, which is saved as a template using a user-defined filename.

The next two cells in the software compute the Kasai autocorrelation and save the results. The results are saved to avoid having to recompute the autocorrelation, which has a long computation time for highly sampled data.

The next step runs a matched filter on the autocorrelation after resizing for square pixels. The software currently computes all future steps for three binary circular templates of 5, 7, and 9 pixels in diameter. Determining the optimal filter diameter or implementing a dynamic matched filter remain as future work. The matched filter is cross-correlated with the autocorrelation data and the result is normalized. This matrix is again resized for square pixels because the cross-correlation increases the size of the input matrix by the radius of the template. Finally, the filtered matrix is masked using the intensity threshold computed earlier. The matched filter operation increases contrast of circular features with similar radii to the template compared to static regions. This step assists in effectively applying histogram segmentation for vessel discrimination. The images are saved after the completion of this step.

At this point, the user may choose to remove the endoscope glass window or connective tissue to improve the performance of the histogram segmentation. I found that the Kasai autocorrelation consistently estimated negative phase shifts in the signal from the endoscope glass window. Without removing the window, the histogram will be skewed to lower values. Connective tissue also tends to produce phase changes that are highly negative or highly positive due to the structure of the connective tissue. Finally, severe bulk tissue motion can produce vertical bands of flow signal even after downsampling to square pixels. Bulk motion bands should be removed to produce effective histograms for vessel segmentation. To remove these undesired features, the user can load the image saved from the previous step into an image processing program such as ImageJ. The user should “paint” the undesired regions with the same value as the masked out signal-free regions and save the result as a TIFF image. The `KasaiProcessing.m` script recommends saving the polygon mask used to remove the envelope so that the exact same pixels can be masked out in the intensity image for generating high-quality structural images with an overlaid flow map for presentation or publication.

The next step is to generate "quaternary" flow maps using histogram segmentation. These are images where each pixel can have one of four values corresponding to background, static tissue, positive flow, or negative flow. I found by investigating the histograms of the flow maps that the flow signal is symmetric and typically has small variance if bulk motion, glass envelope, and connective tissue are removed. I qualitatively determined that a threshold of the histogram mean ± two standard deviations segmented most vessels without severe misclassification (identifying static regions as having flow). This cell in the script assigns non-zero valued pixels to be 0.25 for negative flow, 0.5 for static tissue, and 0.75 for positive flow. These values were chosen to maximize the contrast using the "union jack" colormap in ImageJ. When this colormap is applied to the quaternary image, the signal-void regions appear black, static tissue is white, negative flow is blue, and positive flow is red.

The quaternary images are vessel masks and can be used for various forms of analysis. The number of discrete vessels can be counted over the whole image or within specific ROIs. An optional function, `addROILines.m` can be applied to the quaternary image to add vertical bars at equally spaced, user-defined distances for manual vessel counting. The actual flow velocity can be measured by applying the quaternary image as a mask to the Kasai autocorrelation output. It should be noted that the velocity cannot be accurately known without knowing or estimating the Doppler angle. However, the autocorrelation output can be used for measuring the change in flow in response to stimuli such as heat or chemical vasodilators/vasoconstrictors.

B.2.2 Kasai autocorrelation software

The Kasai autocorrelation function `KasaiLongitudinal.m` takes as input the complex OCT image in the form of a single B-scan. This is generated using the `correctDispersionLongBscan.m` script listed in Code A.4. The Kasai software here is only meant for computing a single B-scan. The variables must be modified if this is to be applied to a standard volumetric dataset comparing adjacent B-scans. The image processing steps for generating quaternary flow masks is listed in Code B.2, including the optional `addROILines.m` function (Code B.3).

Code B.1: `KasaiLongitudinal.m`

```
function R = KasaiLongitudinal(longBscanComplex)

BscanOdd = longBscanComplex(:,1:2:end);
clear longBscanComplex
M = 2;
m = 1:M;
N = 4;
n = 1:N;
Rmax = size(BscanOdd,1)-M;
Cmax = size(BscanOdd,2)-N-1;
R = zeros(Rmax,Cmax);
for row = 1:Rmax
    for col = 1:Cmax
        R(row,col) = angle(sum(sum(BscanOdd(row+m-1,col+n).*conj(...
            BscanOdd(row+m-1,col+n-1)))));
    end
end
end
```

Code B.2: `KasaiProcessing.m`

```
% Script of various steps for processing Kasai autocorrelation data
   from
```

```
% longitudinal scan using OCS1050SS.

% Author: Weston A. Welge
% Date: February 9, 2016
% Required functions: KasaiLongitudinal.m (for generating longBscanComplex
% matrix), addROILines.m

% This script contains several cells that process the data to ultimately
% produce the "quarternary" image data presented in WA Welge and JK Barton,
% "In vivo endoscopic Doppler optical coherence tomography imaging of the
% colon," (submitted).

% Filename definitions
transparencyMaskFilename = 'Ms358AOMTP2_030416_transparencyMask.tif';
KasaiFilename = 'Ms358AOM030416_kasai_row2col4_raw.mat';
circFiltered5DiaFilename = 'Ms4AOM030416_R_filtered_5diameter.tif';
circFiltered7DiaFilename = 'Ms4AOM030416_R_filtered_7diameter.tif';
circFiltered9DiaFilename = 'Ms4AOM030416_R_filtered_9diameter.tif';
FilteredThreshed5DiaFilename = 'Ms358AOM030416_R_filteredThreshed_5diameter.tif';
FilteredThreshed7DiaFilename = 'Ms358AOM030416_R_filteredThreshed_7diameter.tif';
FilteredThreshed9DiaFilename = 'Ms358AOM030416_R_filteredThreshed_9diameter.tif';
```

```
quarternary5DiaFilename = 'Ms358AOM030416_quarternary_5dia_2SD.tif';
quarternary7DiaFilename = 'Ms358AOM030416_quarternary_7dia_2SD.tif';
quarternary9DiaFilename = 'Ms358AOM030416_quarternary_9dia_2SD.tif';
quarternaryROIBorders5DiaFilename = 'Ms358AOM030416_quarternary_ROI5mm_5dia_2SD.tif';
quarternaryROIBorders7DiaFilename = 'Ms358AOM030416_quarternary_ROI5mm_7dia_2SD.tif';
quarternaryROIBorders9DiaFilename = 'Ms358AOM030416_quarternary_ROI5mm_9dia_2SD.tif';

% Requires longBscanComplex variable in workspace.
if ~exist('longBscanComplex','var')
    error(['longBscanComplex not found in working directory. This file',...
        ' is generated using correctDispersionLongBscan.m']);
end

% Generate mask based on structural image intensity.
longBscan = abs(longBscanComplex);
m = max(longBscan(:));
longBscan = 20*log10(longBscan./m);
noiseFloor = mean(mean(longBscan(400:500,:)));
thresh = noiseFloor + 10; % in dB
longBscanResized = imresize(longBscan, [512 7680]);
threshedResized = longBscanResized;
threshedResized(threshedResized<thresh) = -100;
threshedResized = medfilt2(threshedResized,[5 5]);
%se = strel('square', 5);
```

```
%temp = imdilate(threshedResized, se);
%temp = imerode(threshedResized, se);
%template = temp;
template = threshedResized;
template(template>-100) = 1;
template(template==-100) = 0;
imwrite(template,transparencyMaskFilename)

%% Flow image processing
% Generate Kasai flow map
R = KasaiLongitudinal(longBscanComplex);
%% Save raw Kasai autocorrelation output
save(KasaiFilename,'R')

%%
% Matched filter using template
RResized = imresize(R, [510 7680]);
% Circular templates
% 9-diameter
circTemplate9 = [0 0 0 0 0 0 0 0 0 0 0
                 0 0 0 0 1 1 1 0 0 0 0;
                 0 0 0 1 1 1 1 1 0 0 0;
                 0 0 1 1 1 1 1 1 1 0 0;
                 0 1 1 1 1 1 1 1 1 1 0;
                 0 1 1 1 1 1 1 1 1 1 0;
                 0 1 1 1 1 1 1 1 1 1 0;
                 0 0 1 1 1 1 1 1 1 0 0;
                 0 0 0 1 1 1 1 1 0 0 0;
```

```
                0 0 0 0 1 1 1 0 0 0 0;
                0 0 0 0 0 0 0 0 0 0 0];

% 7-diameter
circTemplate7 = [0 0 0 0 0 0 0 0 0
                0 0 0 1 1 1 0 0 0;
                0 0 1 1 1 1 1 0 0;
                0 1 1 1 1 1 1 1 0;
                0 1 1 1 1 1 1 1 0;
                0 1 1 1 1 1 1 1 0;
                0 0 1 1 1 1 1 0 0;
                0 0 0 1 1 1 0 0 0;
                0 0 0 0 0 0 0 0 0];

% 5-diameter
circTemplate5 = [0 0 0 0 0 0 0;
                0 0 1 1 1 0 0;
                0 1 1 1 1 1 0;
                0 1 1 1 1 1 0;
                0 1 1 1 1 1 0;
                0 0 1 1 1 0 0;
                0 0 0 0 0 0 0];

% circTemplate5 = [102 143 173 149 105;
% 108 144 181 167 115;
% 114 167 228 207 126;
% 105 158 228 204 123;
% 91 124 167 155 111];
```

```

filteredR5 = xcorr2(RResized, circTemplate5);
filteredR5 = filteredR5-min(filteredR5(:));
filteredR5 = filteredR5./max(filteredR5(:));
imwrite(filteredR5,circFiltered5DiaFilename);
filteredR7 = xcorr2(RResized, circTemplate7);
filteredR7 = filteredR7-min(filteredR7(:));
filteredR7 = filteredR7./max(filteredR7(:));
imwrite(filteredR7,circFiltered7DiaFilename);
filteredR9 = xcorr2(RResized, circTemplate9);
filteredR9 = filteredR9-min(filteredR9(:));
filteredR9 = filteredR9./max(filteredR9(:));
imwrite(filteredR9,circFiltered9DiaFilename);
%threshedR = filteredR;
%RFiltered = imread('Ms1AOM061915_post10_R_filtered.tif');
filteredR5 = imresize(filteredR5, [512 7680]);
filteredR7 = imresize(filteredR7, [512 7680]);
filteredR9 = imresize(filteredR9, [512 7680]);
% Threshold based on intensity
threshedR5 = filteredR5.*template;
imwrite(threshedR5,FilteredThreshed5DiaFilename);
threshedR7 = filteredR7.*template;
imwrite(threshedR7,FilteredThreshed7DiaFilename);
threshedR9 = filteredR9.*template;
imwrite(threshedR9,FilteredThreshed9DiaFilename);

%% Generate quarternary image for manually corrected images
% Use this cell when manually removing envelope, connective tissue,
```

```
and
% motion artifacts to generate a more accurate threshold based on the flow
% histogram for generating quaternary images.
% Steps:
% (1) Load filtered and thresholded image in ImageJ and use the polygon
% select tool to select the envelope if fully separted from tissue. After
% drawing polygon, make sure edges of polygon extend to the edges of the
% image. Then save mask: Edit->Selection->Create Mask.
% (2) Manually remove motion artifacts and connective tissue now and save
% resulting image, or do that after generating quaternary image (experience
% shows that vast majority of noise comes from envelope).
% (3) Run the code in this cell to generate a quarternary image.
% (4) Manually remove connective tissue and bulk-motion noise artifacts.
% (5) Quantitatively analyze resulting code (e.g., run vesselStats.m).
flow = imread('Ms4AOM062215_post10_R_filteredThreshed_7diameter.tif');
mask = imread('7dia_post10_envelopeMask.tif');
mask = mask./255; % normalize
threshedR7 = flow.*mask;
threshedR7 = double(threshedR7); % need double for std computation
```

```
avg7 = mean(threshedR7(threshedR7~=0)); % Ignore black (removed) regions
std7 = std(threshedR7(threshedR7~=0));
threshLow7 = avg7-2*std7; % Segmentation thresholds = mean +- 2*SD
threshHigh7 = avg7+2*std7;
% Generate quaternary image optimized for ImageJ's union jack colormap
qR7 = threshedR7;
qR7(qR7 <= threshLow7 & qR7 > 0) = 0.25;
qR7(qR7 >= threshHigh7) = 0.75;
qR7(qR7 < threshHigh7 & qR7 > threshLow7) = 0.5;
imwrite(qR7,'Ms4AOM062215_post10_quarternary_7dia_2SD_noiseRemoved.tif')

%% Generate flow image optimized for union jack LUT in ImageJ
% Note: run only if no need to manually remove envelope and noisy regions

% The output will consist of 4 values:
% 0: Areas removed by intensity thresholding (appears black)
% 64: Areas below lower threshold (negative flow direction; appears blue)
% 192: Areas above upper threshold (positive flow direction; appears red)
% 128: Everything else (appears white)
% The thresholding here is based on the histogram statistics of the
% intensity-thresholded image, ignoring the 0 values from the thresholding.
```

```
% The lower threshold is 2 standard deviations below the mean and the
    upper
% threshold is 2 standard deviations above the mean.

% ************************************************************
% Use this section if motor stopped before reaching end of scan
% startpoint = 40; % First row to use (for removing endoscope)
% endpoint = 5680; % Last A-scan before motor stopped moving
% tempR5 = threshedR5;
% tempR7 = threshedR7;
% tempR9 = threshedR9;
% threshedR5 = threshedR5(startpoint:end,1:endpoint);
% threshedR7 = threshedR7(startpoint:end,1:endpoint);
% threshedR9 = threshedR9(startpoint:end,1:endpoint);
% ************************************************************

avg5 = mean(threshedR5(threshedR5~=0)); % 0 are intensity thresholded
avg7 = mean(threshedR7(threshedR7~=0));
avg9 = mean(threshedR9(threshedR9~=0));
std5 = std(threshedR5(threshedR5~=0));
std7 = std(threshedR7(threshedR7~=0));
std9 = std(threshedR9(threshedR9~=0));
threshLow5 = avg5 - 2*std5;
threshLow7 = avg7 - 2*std7;
threshLow9 = avg9 - 2*std9;
threshHigh5 = avg5 + 2*std5;
threshHigh7 = avg7 + 2*std7;
threshHigh9 = avg9 + 2*std9;
```

```
% Generate quarternary images
qR5 = threshedR5;
qR5(qR5 <= threshLow5 & qR5 > 0) = 0.25;
qR5(qR5 >= threshHigh5) = 0.75;
qR5(qR5 < threshHigh5 & qR5 > threshLow5) = 0.5;
qR7 = threshedR7;
qR7(qR7 <= threshLow7 & qR7 > 0) = 0.25;
qR7(qR7 >= threshHigh7) = 0.75;
qR7(qR7 < threshHigh7 & qR7 > threshLow7) = 0.5;
qR9 = threshedR9;
qR9(qR9 <= threshLow9 & qR9 > 0) = 0.25;
qR9(qR9 >= threshHigh9) = 0.75;
qR9(qR9 < threshHigh9 & qR9 > threshLow9) = 0.5;

% Use this section if motor stopped before end of scan *********
% qR5 = [qR5 tempR5(startpoint:end,endpoint+1:end)];
% qR5 = [qR5; tempR5(1:startpoint-1,:)];
% qR7 = [qR7 tempR7(startpoint:end,endpoint+1:end)];
% qR7 = [qR7; tempR7(1:startpoint-1,:)];
% qR9 = [qR9 tempR9(startpoint:end,endpoint+1:end)];
% qR9 = [qR9; tempR9(1:startpoint-1,:)];
% *************************************************************

%% Save quarternary images without ROI borders
imwrite(qR5,quarternary5DiaFilename)
imwrite(qR7,quarternary7DiaFilename)
imwrite(qR9,quarternary9DiaFilename)
```

```

%% Add ROI border lines
qR5ROI = addROILines(qR5,5);
qR7ROI = addROILines(qR7,5);
qR9ROI = addROILines(qR9,5);

%% Save quarternary images with ROI borders
imwrite(qR5ROI,quarternaryROIBorders5DiaFilename);
imwrite(qR7ROI,quarternaryROIBorders7DiaFilename);
imwrite(qR9ROI,quarternaryROIBorders9DiaFilename);
```

Code B.3: `addROILines.m`

```
function outputImage = addROILines(inputImage, ROILength)
% ADDROILINES Add vertical bars to image to denote ROIs.
% outputImage = ADDROILINES(inputImage, ROILength) adds columns of
    value
% 255 separated along the image at ROILength in mm (assuming input
    image
% is 30 mm long in longitudinal dimension).

% Author: Weston A. Welge
% Date: February 9, 2016

imgLength = 30; % Longitudinal length of OCT image in mm.

pxLength = imgLength/size(inputImage,2); % Longitudinal pixel
    dimension in mm
ROILengthInPixels = round(ROILength/pxLength);
```

```
numROIs = floor(30/ROILength); % Number of ROI borders to draw

outputImage = inputImage;
for ROIIndex = 1:numROIs
    outputImage(:,(ROIIndex*ROILengthInPixels)-5:...
        (ROIIndex*ROILengthInPixels)) = 255; % White vertical line
end
end
```

B.3 Preliminary use of other Doppler OCT methods and future work

In addition to the Kasai autocorrelation method described above, I have implemented several other Doppler OCT methods and tested them on flow phantoms and, in some cases, applied them to animal data. Some of these methods were used on the 890 nm SD-OCT system, the TD-OCT system, and the OCS1050SS system. This section describes my progress on those efforts and my opinion on their value, at least applied to the OCS1050SS system. Furthermore, I will describe ideas for future work on these methods. My Matlab software can be found on the lab server at `\People\Weston\Doppler_OCT_Project\`.

Swept sources typically exhibit greater phase noise than superluminescent diodes, and this is the case with the OCS1050SS source compared to our Superlum sources. The ability to resolve low flow velocity is limited by the phase noise of the source. This noise can be estimated by repeatedly imaging a stationary target without moving the beam, computing the phase change between adjacent A-scans (remembering to only compute the phase change between even or odd A-scans when using the OCS1050SS), and averaging the phase changes over all A-scans. Low phase noise sources, as reported in the literature, typically have a phase change standard deviation of 1 mrad to 10 mrad. I measured the phase noise in the OCS1050SS by averaging the phase shift in a region of colon submucosa without apparent vessels as a realistic indicator of actual performance when imaging *in vivo*. The resulting average phase shift full width at half maximum was about 100 mrad. The high phase noise in this situation makes amplitude-only Doppler algorithms particularly attractive because much of the phase information, particularly for low flow rates and vessels nearly perpendicular to the beam, is noise.

Intensity-based Doppler variance (IBDV) is the amplitude-only Doppler algorithm I worked with. This method is based on phase-resolved Doppler variance, but operates only on the amplitude of the complex A-scan data, rather than working with the complex representation of the data [43, 79, 80]. The formula for the Doppler variance is

$$\sigma^2 = \frac{1}{T^2}\left[1 - \frac{\sum_{j=1}^{J}\sum_{z=1}^{N}\left(|A_{j,z}|\,|A_{j+1,z}|\right)}{\sum_{j=1}^{J}\sum_{z=1}^{N}\frac{1}{2}\left(|A_{j,z}|^2 + |A_{j+1,z}|^2\right)}\right], \tag{B.3}$$

where T is the period between the adjacent A-scans used in the algorithm, A is the complex A-scan data after Fourier transformation of the fringe data, j is the A-scan index, z is the depth index, and J and N are the lateral and depth window sizes, respectively. Like in the Kasai autocorrelation, larger window sizes improves SNR at the expense of computation time and spatial resolution. The primary benefits of IBDV are reduced sensitivity to bulk motion, improved sensitivity to near perpendicular flow, and reduced sensitivity to source phase noise. The reduced sensitivity to bulk motion is based on the assumption that bulk motion is slowly varying, so changes in velocity of a small range of adjacent A-scans is small. This may be true for physiological bulk motion from respiration, but this is not the case for vibration in an endoscope, as demonstrated in Figure 2 in Section B.1. Therefore, I believe oversampling and averaging to reduce endoscope vibration is necessary for successful implementation of IBDV, and this should be the first step when attempting to use this method in the future.

The major disadvantages of IBDV are the difficulty of obtaining accurate velocity measurements, insensitivity to direction (positive/negative) of flow, and shadowing artifacts beneath vessels. Conversion of variance values to velocities requires a calibration procedure to map variances to known velocities [79]. However, accurate measurements are also affected by the Doppler angle. The variance has been reported to not affect the IBDV measurements for angles less than about 12°, with a linear increase in variance as the angle increases thereafter [80]. Therefore, there will be loss of accuracy due to ambiguity for flow nearly perpendicular to the beam. Finally, vessel shadowing can make quantitative measures difficult. This artifact is not uncommon in Doppler OCT. It appears as vertical streaks beneath vessels and erroneously hides regions of actual flow beneath the most superficial vessels. With sufficient contrast of flow compared to static tissue, angiograms may still be generated by taking the maximum intensity projection along the depth direction [80]. My preliminary angiograms using the OCS1050SS on mouse colon are not as good as those in the literature; however, I did not apply any intensity thresholding, Gaussian blurring, or other image processing techniques to improve flow contrast.

I have produced four IBDV MATLAB scripts: `IBDV_SSOCT.m`, `IBDVLongitudinal.m`, `IBDVFast.m`, and `angioIBDV.m`. These are located on the lab server at `\People\Weston\Doppler_OCT_Project\Matlab files\` and copies are stored on the server at `\Software\Doppler OCT software\`. The first script, `IBDV_SSOCT.m` was mostly used for prototyping the method and contains code to handle processing of `.FRG` files saved by the OCS1050SS. The next two scripts, `IBDVLongitudinal.m` and `IBDVFast.m` require the complex A-scan data (after dispersion correction if needed) to be loaded in the workspace and are used for highly sampled, longitudinal scanning with the endoscope and with a 3D volume data collected with the handheld probe, respectively. The “Fast” refers to applying the algorithm along the fast-scanning axis of the raster scanning commercial probe. Due to the system A-scan rate, applying the IBDV algorithm along the slow scanning direction is typically not recommended as the B-scan period will likely be around 100 ms. At such a long period, virtually any flow results in saturation and even static tissue has relatively high measured variance such that the contrast between moving and static scatterers is low. The last script, `angioIBDV.m` is a modified version of the `angioCDV.m` code written by Ahhyun Nam and Benjamin Vakoc (described below). This version of the script is modified to use the IBDV algorithm in place of the original complex differential variance algorithm used by the original authors. My motivation for using this script is to see how filtering affects the IBDV results.

Complex differential variance (CDV) is another Doppler algorithm I applied to data collected using the OCS1050SS. In contrast to Kasai autocorrelation and IBDV, the CDV method uses both amplitude and phase information to generate angiograms while rejecting bulk motion [45]. The CDV formula can be considered to be a ratiometric combination of the Kasai autocorrelation and the IBDV formulas:

$$f_{\mathrm{CDV}}(z) = \sqrt{1 - \frac{\left|\sum\limits_{k=-L}^{L} w(k) R(z-k,1) R^*(z-k,2)\right|}{\sum\limits_{k=-L}^{L} w(k) \frac{1}{2} \left[|R(z-k,1)|^2 + |R(z-k,2)|^2 \right]}}, \qquad \text{(B.4)}$$

where $R(z-k,1)$ is the complex A-scan data at depth $z-k$ (the 1 and 2 refer to the two adjacent A-scans used in the computation), $w(k)$ is a window function (e.g., Hanning window) with length $2L+1$. The numerator is similar to the Kasai autocorrelation, but with summing only in the depth direction. The denominator is the same as the IBDV denominator, but again only summing along the depth direction. The authors compared CDV to the IBDV and power intensity differential methods and found to have greater separation in the histogram of the distributions corresponding to static and flowing scatterers [45].

I tested the CDV algorithm using the `angioCDV.m` and `angioProjection.m` scripts written by Nam and Vakoc.[2] I wrote two scripts, `generateCDVinput.m` and `generateCDVinput2.m`, to manipulate the OCS1050SS complex A-scan data into the correct geometric format to work with the `angioCDV.m` script. The difference between my two scripts is that one has no overlap between adjacent B-scans, where the width of the B-scan is determined by the sampling density of the collected data, and the other version produces B-scans that are shifted by a single A-scan. The data collection method in the corresponding article [45] involved acquiring several A-scans at the same location. This is not possible with the OCS1050SS. The best approximation is to highly oversample the data. This can be accomplished using the commercial probe by increasing the "Averaging" parameter. The number of fringes to be saved per frame will be the number of x pixels multiplied by the averaging parameter. The endoscope gives the user complete control over longitudinal motor speed. I have not attempted to apply the `CDFFast.m` script to the longitudinal oversampled colon images, so that would be worth trying.

I used the `angioCDV.m` script on mouse ear data collected using the commercial probe. An example median projection is given in Fig. B.1. This figure clearly show vascular structure. However, the inability to sample at exactly the same spatial location is likely the main contributor to decreased quality of the angiogram compared to results published in [45]. Similar to IBDV, vertical streaking beneath vessels is present in the mouse CDV results.

I also attempted to determine the affect of A-scan period on the CDV values using a flow phantom. As in IBDV, the variance is non-linearly proportional to the flow velocity. I computed the average of the central region of a 2-mm inner diameter transparent tube with 10% Intralipid solution flowing with velocities controlled by a syringe pump. I highly sampled the data so that I could skip integer numbers of A-scans to effectively increase the A-scan period while still sampling

---

[2] These scripts and the user manual can be downloaded from `http://octresearch.org/resources/downloads/`.

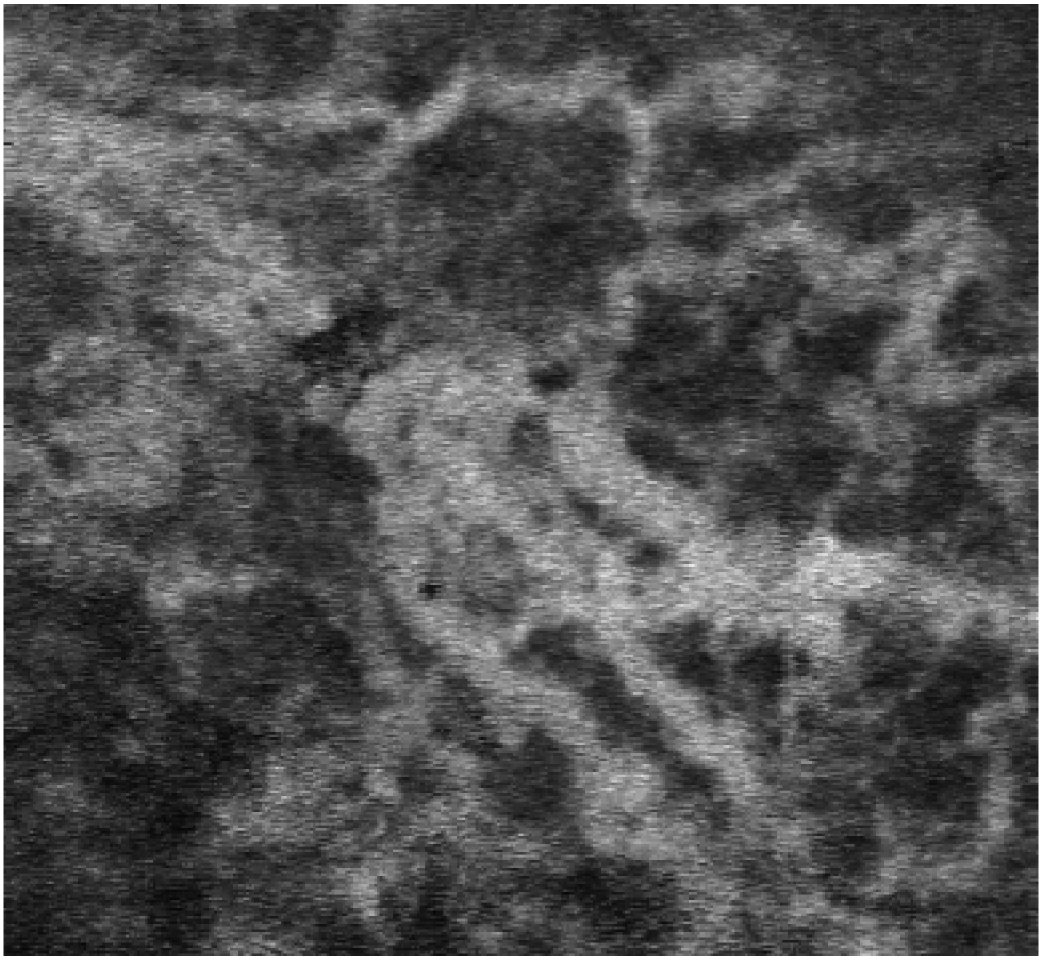

Figure B.1: Angiogram of mouse ear using complex differential variance algorithm. Size is 1 × 1 mm.

in nearly the same spatial location (this could be improved in the future by using a smaller capillary tube and using M-mode imaging). The results are plotted in Fig. B.2. The figure shows that increasing A-scan interval monotonically increases the average CDV values for flow velocities ranging from 1 mm/s to 5 mm/s. For all velocities *except 3 mm/s*, the variance increases with velocity. This outlier could have been due to user error in setting the syringe pump and another flow phantom study should be conducted. The average CDV value for a region outside the tube (air) was also computed for each velocity and timing parameter. As expected, there was no correlation of CDV in signal-void regions with the fluid flow velocity or A-scan period. Therefore, this CDV level can be considered the maximum possible CDV value. It also appears that the CDV values of the flowing solution are approaching the signal-void variance. These data suggest that an A-scan period of 625 µs produces the greatest spread in CDV values over then range of flow velocities. Future work should be to determine the ideal imaging parameters (i.e., degree of oversampling, A-scan period) for generating high-quality CDV angiograms.

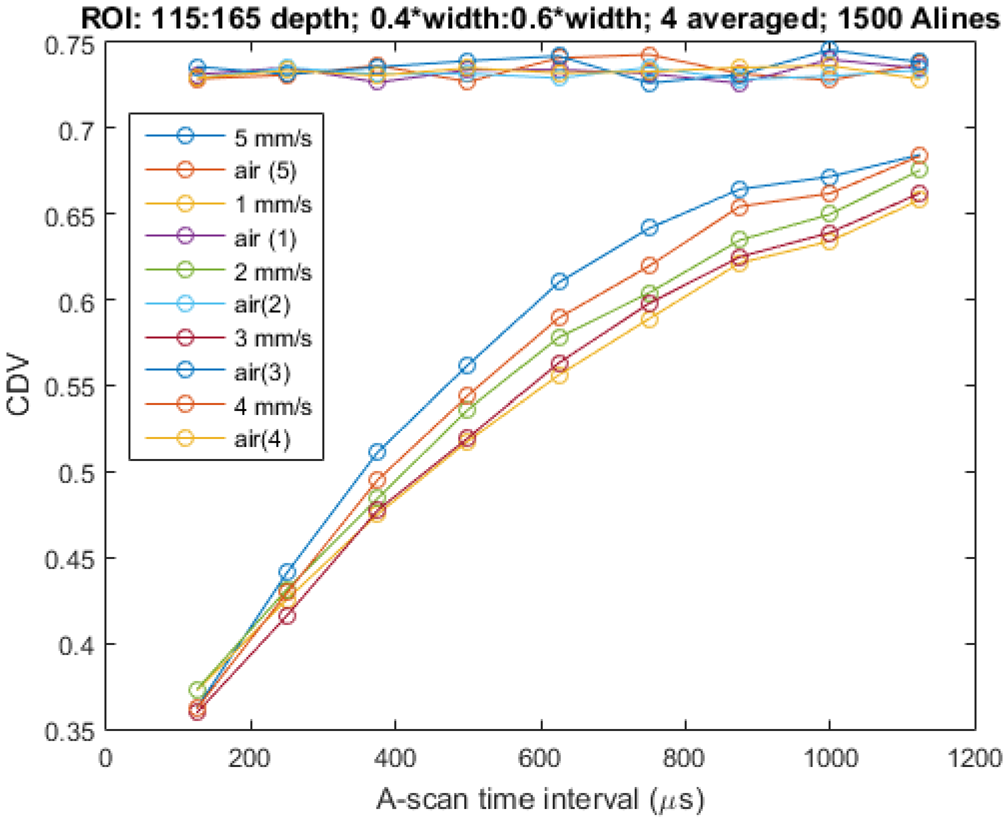

Figure B.2: CDV values versus A-scan period over a range of flow velocities.

APPENDIX C

C.1 Conference proceedings: Colon crypt imaging using OCT

W. A. Welge and J. K. Barton, “Optical coherence tomography imaging of colonic crypts in a mouse model of colorectal cancer,” Proc. SPIE **9691**, 96910V (2016).

Optical coherence tomography imaging of colonic crypts in a mouse model of colorectal cancer

Weston A. Welge[a] and Jennifer K. Barton[a,b]

[a]College of Optical Sciences, Univ. of Arizona, 1630 E. University Blvd., Tucson, AZ, USA 85721

[b]Department of Biomedical Engineering, Univ. of Arizona, 1657 E. Helen St., Tucson, AZ, USA 85721

ABSTRACT

Aberrant crypt foci (ACF) are abnormal epithelial lesions that precede development of colonic polyps. As the earliest morphological change in the development of colorectal cancer, ACF is a highly studied phenomenon. The most common method of imaging ACF is chromoendoscopy using methylene blue as a contrast agent. Narrow-band imaging is a contrast-agent-free modality for imaging the colonic crypts. Optical coherence tomography (OCT) is an attractive alternative to chromoendoscopy and narrow-band imaging because it can resolve the crypt structure at sufficiently high sampling while simultaneously providing depth-resolved data. We imaged *in vivo* the distal 15 mm of colon in the azoxymethane (AOM) mouse model of colorectal cancer using a commercial swept-source OCT system and a miniature endoscope designed and built in-house. We present *en face* images of the colonic crypts and demonstrate that different patterns in healthy and adenoma tissue can be seen. These patterns correspond to those reported in the literature. We have previously demonstrated early detection of colon adenoma using OCT by detecting minute thickening of the mucosa. By combining mucosal thickness measurement with imaging of the crypt structure, OCT can be used to correlate ACF and adenoma development in space and time. These results suggest that OCT may be a superior imaging modality for studying the connection between ACF and colorectal cancer.

Keywords: colonic crypts, aberrant crypt foci, adenoma, optical coherence tomography, colorectal cancer, endoscopy

1. INTRODUCTION

Aberrant crypt foci (ACF) are abnormal epithelial lesions thought to precede carcinogenesis in the colon.[1] ACF is thought to be the earliest neoplastic lesion in colorectal cancer. Because colorectal cancer is the second deadliest cancer in the United States,[2] the study of ACF has the potential to improve early detection of dysplasia in the colon, increase our understanding of the natural history of colorectal cancer, and help with the development and analysis of chemopreventive and chemotherapeutic drugs.

Two of the most common modalities for imaging ACF are magnifying chromoendoscopy[1,3,4] and narrow-band imaging.[3,4] Magnifying chromoendoscopy uses dyes such as indigo carmine or methylene blue to stain the colon epithelium and improve contrast of the colonic crypts. Kudo first determined that the crypt patterns can be used to differentiate hyperplastic (totally benign) and adenomatous (benign with potential to become malignant) polyps.[5] Chromoendoscopy is effective at resolving crypt structure, but the use of non-FDA-approved dyes is non-ideal for routine human screening.

Narrow-band imaging systems illuminate the colon with a series of narrow bandwidth wavelength spectra corresponding to absorption peaks of hemoglobin.[6] Longer wavelengths penetrate deeper into tissue, so a combination of illumination bandwidths can be used that are highly absorbed by blood vessels at various depths in the tissue. A composite of these images can provide some degree of depth resolution in the resulting image.

Further author information: (Send correspondence to J.K.B.)
W.A.W.: E-mail: wwelge@email.arizona.edu, Telephone: 1 520 626 4463
J.K.B.: E-mail: barton@email.arizona.edu, Telephone: 1 520 621 4116

Endoscopic Microscopy XI; and Optical Techniques in Pulmonary Medicine III, edited by Guillermo J. Tearney, Thomas D. Wang, Melissa J. Suter, Stephen Lam, Matthew Brenner, Proc. of SPIE Vol. 9691, 96910V · © 2016 SPIE · CCC code: 1605-7422/16/$18 · doi: 10.1117/12.2211963

Although blood absorption is the primary source of contrast in narrow-band imaging, the crypt structure can be clearly seen in the images. Accuracy of adenoma detection based on classifying the crypt structure based on Kudo's criteria using narrow-band imaging is better than standard white-light endoscopy, but only after significant experience is gained by the user.[7]

Optical coherence tomography (OCT) is an attractive alternate imaging modality for investigating colonic crypt patterns and detecting polyps. OCT requires no exogenous dyes and provides greater depth resolution than narrow-band imaging, but it is typically a slower imaging modality owing to its point-scanning operation, and OCT cannot be as easily integrated with standard colonoscopes. As OCT imaging speeds increase, however, we can increase the number of A-scans taken in a reasonable amount of time and therefore increase the tissue sampling density. By scanning in two dimensions, *en face* projections depicting the colonic crypt patters can be generated. To date, *en face* OCT colonic crypt imaging has been demonstrated in the rabbit,[8] human,[9] and mouse[10] colon. The ability to image over 1.5 mm in depth with OCT provides additional important information relevant to colorectal cancer, such as epithelial thickness and light absorption. This information has already been used to identify adenoma in a mouse model of colorectal cancer.[11] Because small adenoma can be accurately identified using non-destructive, *in vivo* imaging, OCT is a powerful modality for studying the link between ACF and adenoma.

We present *in vivo* OCT images of mouse colon, including *en face* projections for investigating the crypt patterns. We describe qualitative differences between the colons of healthy and diseased mice using the azoxymethane (AOM) mouse model of colorectal cancer. The crypt patterns are markedly different in healthy and adenoma tissue. These pilot data suggest that OCT may be an effective modality for studying the development of ACF and its correlation to adenoma growth, as well as a useful tool for developing and monitoring chemopreventive and chemotherapeutic drugs.

2. METHODS

2.1 Imaging system

We previously integrated a lab-built miniature endoscope for mouse colon imaging with a commercial swept-source OCT system (OCS1050SS, Thorlabs, Newton, NJ, USA).[10] The endoscope, shown in Fig. 1, consists of single mode fiber pigtailed to a glass spacer, gradient-index lens (GRINTECH, Jena, Germany), and 41° rod prism, enclosed in a glass envelope with an outer diameter of 2 mm. The optics produce a numerical aperture of 0.14 and a diffraction-limited spot size of 6.1 µm at a distance of 200 µm outside the glass envelope.

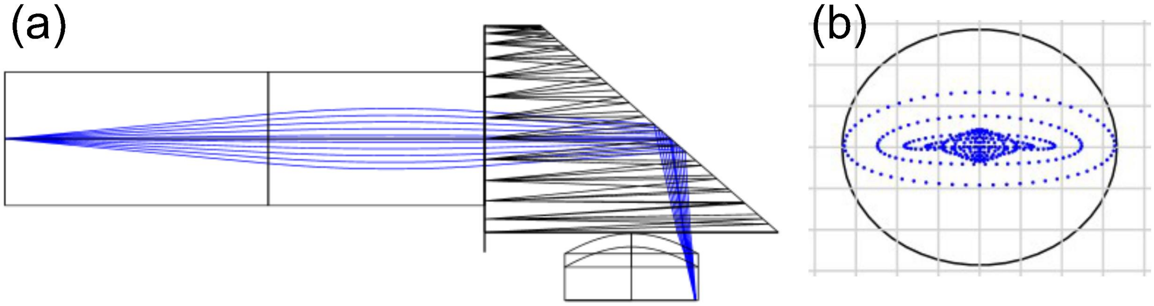

Figure 1. Zemax (a) ray trace and (b) spot diagram of the endoscope. The cylindrical glass window is responsible for the astigmatism seen in the spot diagram. However, the beam is still within the diffraction-limited circle drawn in black.

The endoscope scans in a helical geometry. The endoscope is connected to a fiber optic rotary joint (Princetel, Hamilton, NJ, USA) to enable free rotation. Rotation is achieved by a stepper motor interfaced with the rotary joint. The endoscope and rotary joint are mounted on a linear translation stage that is controlled by a linear actuator. During imaging, the endoscope glass envelope remains stationary in the mouse colon.

The OCT system has a central wavelength of 1040 nm and an 80 nm bandwidth, producing an axial resolution of 12 µm in air and 9 µm in water. The A-scan rate is 16 kHz.

2.2 Animal Model

A mouse model of colorectal cancer was used for *in vivo* imaging of the colonic crypts. A/J mice (The Jackson Laboratory, Bar Harbor, ME, USA) were treated with the colon carcinogen azoxymethane (AOM) to develop ACF and adenoma.[12] Beginning at six weeks of age, the A/J mice were administered 10 mg/kg of AOM for the cancer group and 0.2 mL of saline for the control group via subcutaneous injection weekly for five weeks. This protocol was in accordance with the University of Arizona Institutional Animal Care and Use Committee.

2.3 Imaging Protocol

Mice were anesthetized for imaging by intraperitoneal injection of 100 mL/kg ketamine and 10 mL/kg xylazine. Mice were placed on a heating pad during imaging to maintain body temperature. Mice were either 6 or 35 weeks of age during imaging. The young mice were imaged prior to the first AOM or saline injections.

Three-dimensional OCT volumes of the distal 15 mm were collected with 2000 A-scans per frame (B-scan) and 2400 frames per volume. The distance between adjacent A-scans at the surface of the colon was 3.1 µm. The distance between adjacent frames was 6.3 µm. Total imaging time was approximately 6 minutes. This is slower than expected with an A-scan rate of 16 kHz because the PC required time to save the raw fringe data after acquisition of each frame.

2.4 Image Processing

The raw fringe data required numerical dispersion compensation. We utilized a numerical method that determines the non-linear dispersion by subtracting a linear fit to the phase data as a function of wavenumber.[10]

A variety of *en face* projections were tested to produce best contrast of the colonic crypts. We found standard deviation and sum projections to be the most effective. The projections used slices beginning about 50 µm beneath the colon surface. For sum projections, we used 50 slices, corresponding to a thickness of 195 µm. For standard-deviation projections, we used 300 slices, or a thickness of 1.2 mm.

3. RESULTS AND DISCUSSION

En face standard-deviation projections of 35-week-old mice are shown below. A healthy mouse is shown in Fig. 2. The magnified inset shows crypts with mostly the same size and a relatively uniform crypt density. The AOM mouse colon in Fig. 3 shows adenoma, which have been outlined with dashed lines. The magnified view of the inset shows irregular crypt size, shape, and distribution. Fig. 4 shows representative magnified (0.47 mm×0.93 mm) regions of 5-week-old mice prior to their first AOM or saline injections.

The crypt structure differs greatly from normal on the surface of adenoma, shown in Fig. 3(b). The pit pattern looks elongated and branching, particularly in the upper-left region. This pattern is similar to the gyrus pattern described by Kudo that are seen in tubulovillous adenoma.[5] In some regions of the adenoma, it is difficult to see any crypt pattern. Kudo reports a correlation between non-pit patterns and invasive carcinoma.[5] It is unclear whether a pit pattern exists in some of the adenoma OCT images or if the pattern is simply difficult to see with the current projection parameters.

Regions of healthy tissue in both the AOM-treated and saline-treated mice show round crypts (note that the images reported here are stretched horizontally due to non-square pixels). Round, uniform-sized crypts are characteristic of healthy colon tissue.[5]

We have previously defined criteria for automatically identifying adenoma using OCT B-scans.[11] Others have developed algorithms for automatic crypt segmentation using 3D OCT data.[13] Combining these efforts could result in robust software capable of early detection of ACF and adenoma.

We have shown that OCT is capable of resolving the crypt structure in the mouse colon and that the crypt patterns differ between healthy and adenoma tissue. Future work will be to study the changes in the crypts of the AOM mouse model of colorectal cancer and to develop quantitative measures of the crypt patterns for discriminating healthy and adenoma tissue.

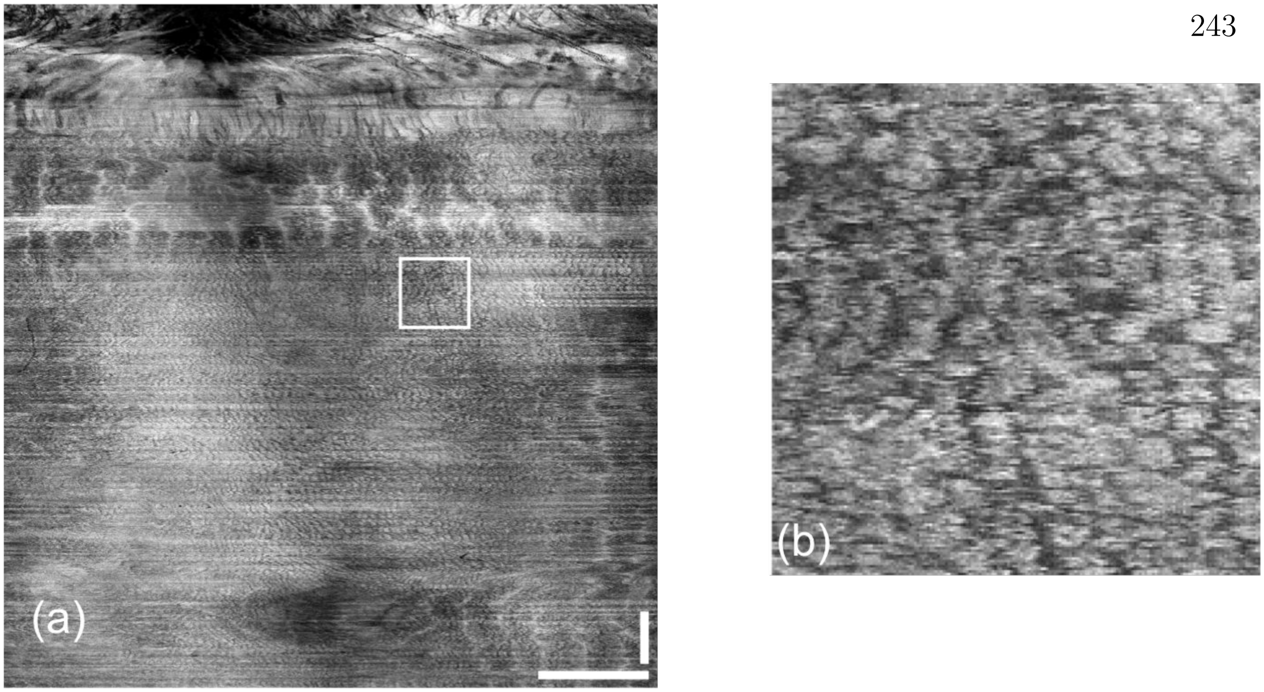

Figure 2. Saline-treated mouse at 35 weeks of age. (a) *En face* standard-deviation projection that shows the crypt structure. (b) Magnification of the inset in (a) showing mostly uniform crypt size, structure, and density. Scale bars are 1 mm.

ACKNOWLEDGMENTS

We thank Photini Faith Rice for assistance with drug treatment and animal imaging. This research was supported by the National Cancer Institute and the National Heart, Lung, and Blood Institute of the National Institutes of Health under award numbers R01CA109385 and T32HL007955, respectively, and the American Society for Laser Medicine and Surgery Student Research Grant. The content is solely the responsibility of the authors and does not necessarily represent the official views of the National Institutes of Health.

REFERENCES

[1] Alrawi, S. J., Schiff, M., Carroll, R. E., Dayton, M., Gibbs, J. F., Kulavlat, M., Tan, D., Berman, K., Stoler, D. L., and Anderson, G. R., "Aberrant crypt foci," *Anticancer Res.* **26**(1A), 107–119 (2006).

[2] "Cancer facts & figures 2015," tech. rep., American Cancer Society, Atlanta (2015).

[3] Tischendorf, J., Wasmuth, H., Koch, A., Hecker, H., Trautwein, C., and Winograd, R., "Value of magnifying chromoendoscopy and narrow band imaging (NBI) in classifying colorectal polyps: a prospective controlled study," *Endoscopy* **39**(12), 1092–1096 (2007).

[4] Su, M.-Y., Hsu, C.-M., Ho, Y.-P., Chen, P.-C., Lin, C.-J., and Chiu, C.-T., "Comparative study of conventional colonoscopy, chromoendoscopy, and narrow-band imaging systems in differential diagnosis of neoplastic and nonneoplastic colonic polyps," *Am. J. Gastroenterol.* **101**(12), 2711–2716 (2006).

[5] Kudo, S., Hirota, S., Nakajima, T., Hosobe, S., Kusaka, H., Kobayashi, T., Himori, M., and Yagyuu, A., "Colorectal tumours and pit pattern.," *J. Clin. Pathol.* **47**(10), 880 (1994).

[6] Gono, K., Obi, T., Yamaguchi, M., Ohyama, N., Machida, H., Sano, Y., Yoshida, S., Hamamoto, Y., and Endo, T., "Appearance of enhanced tissue features in narrow-band endoscopic imaging," *J. Biomed. Opt.* **9**(3), 568–577 (2004).

[7] Rogart, J. N., Jain, D., Siddiqui, U. D., Oren, T., Lim, J., Jamidar, P., and Aslanian, H., "Narrow-band imaging without high magnification to differentiate polyps during real-time colonoscopy: improvement with experience," *Gastrointest. Endosc.* **68**(6), 1136–1145 (2008).

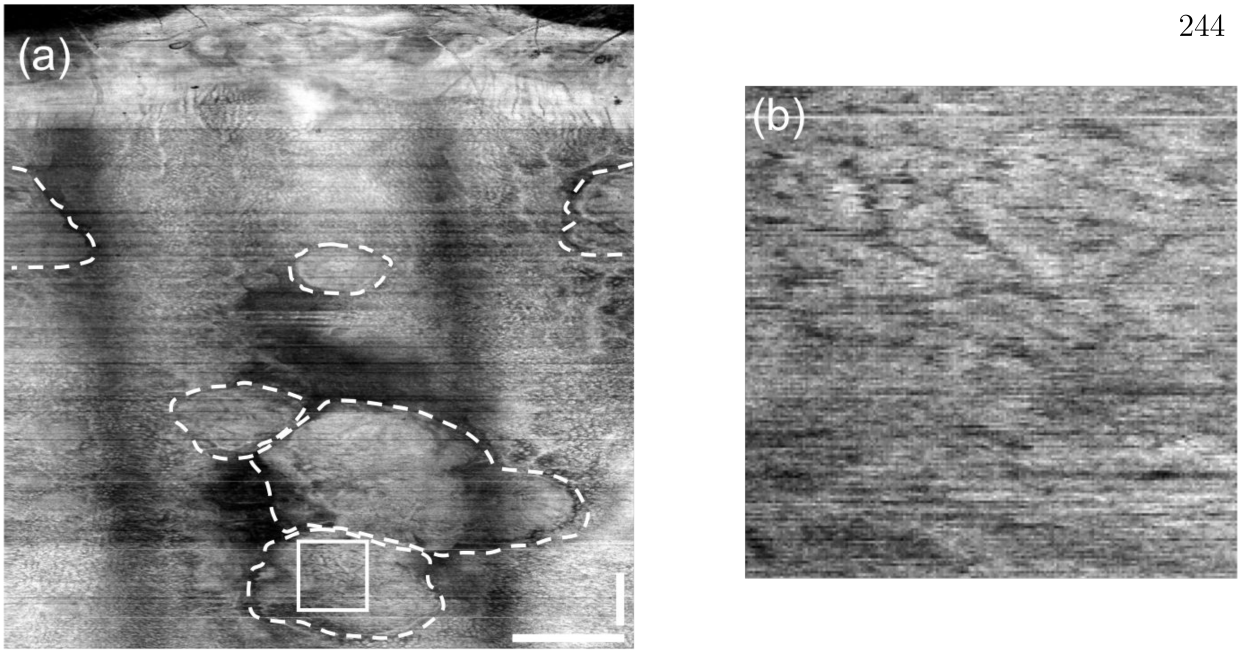

Figure 3. AOM-treated mouse at 35 weeks of age. (a) *En face* standard-deviation projection that shows the crypt structure and prominent adenoma. (b) Magnification of the inset in (a) showing irregular crypt size, structure, and density. Scale bars are 1 mm.

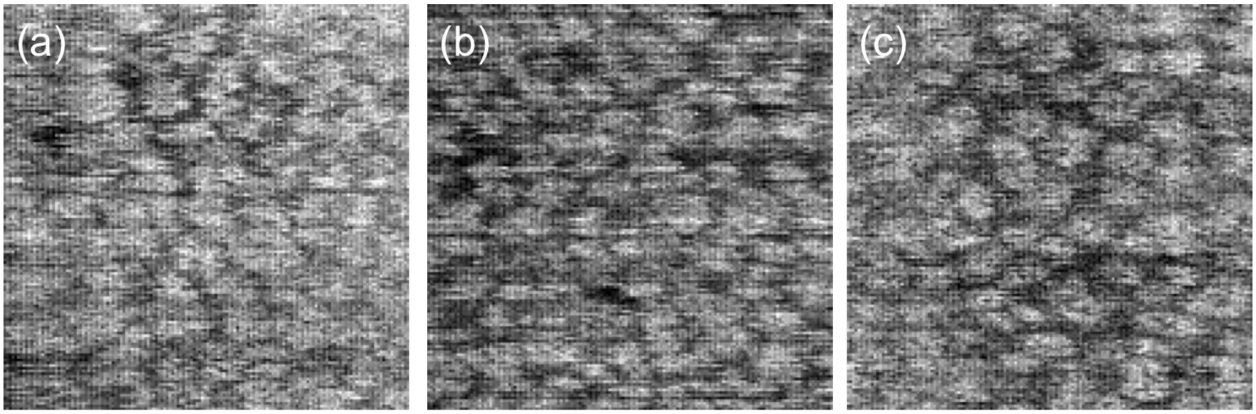

Figure 4. Magnified regions from 5-week-old mice showing regular crypt structure. Image dimensions are 0.47 mm (horizontal) and 0.93 mm (vertical). All images were taken prior to first AOM (a,b) or saline (c) injections.

[8] Adler, D. C., Chen, Y., Huber, R., Schmitt, J., Connolly, J., and Fujimoto, J. G., "Three-dimensional endomicroscopy using optical coherence tomography," *Nat. Photon.* **1**(12), 709–716 (2007).

[9] Adler, D. C., Zhou, C., Tsai, T.-H., Schmitt, J., Huang, Q., Mashimo, H., and Fujimoto, J. G., "Three-dimensional endomicroscopy of the human colon using optical coherence tomography," *Opt. Express* **17**(2), 784 (2009).

[10] Welge, W. A. and Barton, J. K., "Expanding functionality of commercial optical coherence tomography systems by integrating a custom endoscope," *PLoS ONE* **10**(9), e0139396 (2015).

[11] Winkler, A. M., Rice, P. F. S., Drezek, R. A., and Barton, J. K., "Quantitative tool for rapid disease mapping using optical coherence tomography images of azoxymethane-treated mouse colon," *J. Biomed. Opt.* **15**(4), 041512–041512–10 (2010).

[12] Papanikolaou, A., Wang, Q. S., Papanikolaou, D., Whiteley, H. E., and Rosenberg, D. W., "Sequential and morphological analyses of aberrant crypt foci formation in mice of differing susceptibility to azoxymethane-induced colon carcinogenesis," *Carcinogenesis* **21**(8), 1567–1572 (2000).

[13] Qi, X., Pan, Y., Hu, Z., Kang, W., Willis, J. E., Olowe, K., Sivak, Michael V., J., and Rollins, A. M., "Automated quantification of colonic crypt morphology using integrated microscopy and optical coherence tomography," *J. Biomed. Opt.* **13**(5), 054055–054055–11 (2008).

REFERENCES

[1] American Cancer Society, “Cancer Facts & Figures 2015,” Tech. rep., American Cancer Society, Atlanta (2015).

[2] W. A. Welge and J. K. Barton, “Optical coherence tomography imaging of colonic crypts in a mouse model of colorectal cancer,” Proceedings of SPIE **9691**, 96910V (2016).

[3] W. A. Welge and J. K. Barton, “Expanding Functionality of Commercial Optical Coherence Tomography Systems by Integrating a Custom Endoscope,” PLOS ONE **10**, e0139396 (2015).

[4] A. M. Winkler, P. F. S. Rice, R. A. Drezek, and J. K. Barton, “Quantitative tool for rapid disease mapping using optical coherence tomography images of azoxymethane-treated mouse colon,” J. Biomed. Opt **15**, 041512–041512–10 (2010).

[5] S. LeGendre-McGhee, P. S. Rice, R. A. Wall, K. J. Sprute, R. Bommireddy, A. M. Luttman, R. B. Nagle, E. R. Abril, K. Farrell, C.-H. Hsu, D. J. Roe, E. W. Gerner, N. A. Ignatenko, and J. K. Barton, “Time-serial Assessment of Drug Combination Interventions in a Mouse Model of Colorectal Carcinogenesis Using Optical Coherence Tomography,” Cancer Growth Metastasis **8**, 63–80 (2015).

[6] M. R. Keenan, S. J. Leung, P. S. Rice, R. A. Wall, and J. K. Barton, “Dual optical modality endoscopic imaging of cancer development in the mouse colon,” Lasers Surg. Med. **47**, 30–39 (2015).

[7] J. L. Carbary-Ganz, W. A. Welge, J. K. Barton, and U. Utzinger, “In vivo molecular imaging of colorectal cancer using quantum dots targeted to vascular endothelial growth factor receptor 2 and optical coherence tomography/laser-induced fluorescence dual-modality imaging,” J. Biomed. Opt. **20**, 096015–096015 (2015).

[8] A. M. Winkler, P. F. S. Rice, J. Weichsel, J. M. Watson, M. V. Backer, J. M. Backer, and J. K. Barton, “In Vivo, Dual-Modality OCT/LIF Imaging Using a Novel VEGF Receptor-Targeted NIR Fluorescent Probe in the AOM-Treated Mouse Model,” Mol Imaging Biol **13**, 1173–1182 (2011).

[9] L. P. Hariri, Z. Qiu, A. R. Tumlinson, D. G. Besselsen, E. W. Gerner, N. Ignatenko, B. Povazay, B. Hermann, H. Sattmann, J. McNally, A. Unterhuber, W. Drexler, and J. K. Barton, "Serial endoscopy in azoxymethane treated mice using ultra-high resolution optical coherence tomography," Cancer Biology & Therapy **6**, 1753–1762 (2007).

[10] A. R. Tumlinson, B. Povaay, L. P. Hariri, J. McNally, A. Unterhuber, B. Hermann, H. Sattmann, W. Drexler, and J. K. Barton, "In vivo ultrahigh-resolution optical coherence tomography of mouse colon with an achromatized endoscope," J. Biomed. Opt **11**, 064003–064003–8 (2006).

[11] A. R. Tumlinson, L. P. Hariri, U. Utzinger, and J. K. Barton, "Miniature Endoscope for Simultaneous Optical Coherence Tomography and Laser-Induced Fluorescence Measurement," Appl. Opt. **43**, 113–121 (2004).

[12] R. A. Wall and J. K. Barton, "Fluorescence-based surface magnifying chromoendoscopy and optical coherence tomography endoscope," J. Biomed. Opt **17**, 0860031 (2012).

[13] S. J. Alrawi, M. Schiff, R. E. Carroll, M. Dayton, J. F. Gibbs, M. Kulavlat, D. Tan, K. Berman, D. L. Stoler, and G. R. Anderson, "Aberrant Crypt Foci," Anticancer Res **26**, 107–119 (2006).

[14] J. A. Burch, K. Soares-Weiser, D. J. B. St. John, S. Duffy, S. Smith, J. Kleijnen, and M. Westwood, "Diagnostic accuracy of faecal occult blood tests used in screening for colorectal cancer: a systematic review," J Med Screen **14**, 132–137 (2007).

[15] H. Yang, B.-Q. Xia, B. Jiang, G. Wang, Y.-P. Yang, H. Chen, B.-S. Li, A.-G. Xu, Y.-B. Huang, and X.-Y. Wang, "Diagnostic value of stool DNA testing for multiple markers of colorectal cancer and advanced adenoma: A meta-analysis," Can J Gastroenterol Hepatol **27**, 467–475 (2013).

[16] P. J. Pickhardt, C. Hassan, S. Halligan, and R. Marmo, "Colorectal Cancer: CT Colonography and Colonoscopy for DetectionSystematic Review and Meta-Analysis," Radiology **259**, 393–405 (2011).

[17] S. B. Ahn, D. S. Han, J. H. Bae, T. J. Byun, J. P. Kim, and C. S. Eun, "The Miss Rate for Colorectal Adenoma Determined by Quality-Adjusted, Back-to-Back Colonoscopies," Gut Liver **6**, 64–70 (2012).

[18] J. C. van Rijn, J. B. Reitsma, J. Stoker, P. M. Bossuyt, S. J. van Deventer, and E. Dekker, “Polyp miss rate determined by tandem colonoscopy: a systematic review,” Am. J. Gastroenterol. **101**, 343–350 (2006).

[19] P. J. Pickhardt, P. A. Nugent, P. A. Mysliwiec, J. R. Choi, and W. R. Schindler, “Location of Adenomas Missed by Optical Colonoscopy,” Ann Intern Med **141**, 352–359 (2004).

[20] D. Huang, E. A. Swanson, C. P. Lin, J. S. Schuman, W. G. Stinson, W. Chang, M. R. Hee, T. Flotte, K. Gregory, C. A. Puliafito, and J. G. Fujimoto, “Optical coherence tomography,” Science **254**, 1178–1181 (1991).

[21] J. F. de Boer, B. Cense, B. H. Park, M. C. Pierce, G. J. Tearney, and B. E. Bouma, “Improved signal-to-noise ratio in spectral-domain compared with time-domain optical coherence tomography,” Optics Letters **28**, 2067 (2003).

[22] M. Choma, M. Sarunic, C. Yang, and J. Izatt, “Sensitivity advantage of swept source and Fourier domain optical coherence tomography,” Opt. Express **11**, 2183–2189 (2003).

[23] R. Leitgeb, C. Hitzenberger, and A. Fercher, “Performance of fourier domain vs time domain optical coherence tomography,” Optics Express **11**, 889 (2003).

[24] M. Leahy, J. Hogan, C. Wilson, H. Subhash, and R. Dsouza, “Multiple reference optical coherence tomography (MR-OCT) system,” Proc SPIE **8580**, 85800L (2013).

[25] P. M. McNamara, C. O’Riordan, S. Collins, P. O’Brien, C. Wilson, J. Hogan, and M. J. Leahy, “Development of a miniature multiple reference optical coherence tomography imaging device,” Proc SPIE **9699**, 969909 (2016).

[26] M. J. Leahy, C. Wilson, J. Hogan, P. OBrien, R. Dsouza, K. Neuhaus, D. Bogue, H. Subhash, C. ORiordan, and P. M. McNamara, “The how and why of a $10 optical coherence tomography system,” Proc SPIE **9697**, 96970T (2016).

[27] R. Dsouza, H. M. Subhash, K. Neuhaus, J. Hogan, C. Wilson, and M. Leahy, “3D nondestructive testing system with an affordable multiple reference optical-delay-based optical coherence tomography,” Applied Optics **54**, 5634 (2015).

[28] R. Dsouza, H. Subhash, K. Neuhaus, J. Hogan, C. Wilson, and M. Leahy, “Dermascope guided multiple reference optical coherence tomography,” Biomedical Optics Express **5**, 2870 (2014).

[29] A. Zam, R. Dsouza, H. M. Subhash, M.-L. O'Connell, J. Enfield, K. Larin, and M. J. Leahy, "Feasibility of correlation mapping optical coherence tomography (cmOCT) for anti-spoof sub-surface fingerprinting," J. Biophoton. **6**, 663–667 (2013).

[30] S. R. Chinn, E. A. Swanson, and J. G. Fujimoto, "Optical coherence tomography using a frequency-tunable optical source," Optics Letters **22**, 340 (1997).

[31] W. Y. Oh, S. H. Yun, G. J. Tearney, and B. E. Bouma, "115 kHz tuning repetition rate ultrahigh-speed wavelength-swept semiconductor laser," Optics Letters **30**, 3159 (2005).

[32] R. Huber, M. Wojtkowski, and J. G. Fujimoto, "Fourier Domain Mode Locking (FDML): A new laser operating regime and applications for optical coherence tomography," Optics Express **14**, 3225 (2006).

[33] W. Wieser, B. R. Biedermann, T. Klein, C. M. Eigenwillig, and R. Huber, "Multi-Megahertz OCT: High quality 3d imaging at 20 million A-scans and 45 GVoxels per second," Optics Express **18**, 14685 (2010).

[34] I. Grulkowski, J. J. Liu, B. Potsaid, V. Jayaraman, J. Jiang, J. G. Fujimoto, and A. E. Cable, "High-precision, high-accuracy ultralong-range swept-source optical coherence tomography using vertical cavity surface emitting laser light source," Optics Letters **38**, 673 (2013).

[35] J. G. Fujimoto and W. Drexler, "Introduction to OCT," in "Optical Coherence Tomography," , W. Drexler and J. G. Fujimoto, eds. (Springer International Publishing, 2015), pp. 3–64.

[36] J. A. Izatt, M. D. Kulkarni, S. Yazdanfar, J. K. Barton, and A. J. Welch, "In vivo bidirectional color Doppler flow imaging of picoliter blood volumes using optical coherence tomography," Opt. Lett. **22**, 1439–1441 (1997).

[37] Z. Chen, T. E. Milner, S. Srinivas, X. Wang, A. Malekafzali, M. J. C. van Gemert, and J. S. Nelson, "Noninvasive imaging of in vivo blood flow velocity using optical Doppler tomography," Optics Letters **22**, 1119 (1997).

[38] Y. Zhao, Z. Chen, C. Saxer, S. Xiang, J. F. de Boer, and J. S. Nelson, "Phase-resolved optical coherence tomography and optical Doppler tomography for imaging blood flow in human skin with fast scanning speed and high velocity sensitivity," Opt. Lett. **25**, 114–116 (2000).

[39] H. Ren, K. M. Brecke, Z. Ding, Y. Zhao, J. S. Nelson, and Z. Chen, "Imaging and quantifying transverse flow velocity with the Doppler bandwidth in a phase-resolved functional optical coherence tomography," Optics Letters **27**, 409 (2002).

[40] R. K. Wang, S. L. Jacques, Z. Ma, S. Hurst, S. R. Hanson, and A. Gruber, "Three dimensional optical angiography," Opt. Express **15**, 4083–4097 (2007).

[41] J. Barton and S. Stromski, "Flow measurement without phase information in optical coherence tomography images," Opt. Express **13**, 5234–5239 (2005).

[42] A. Mariampillai, B. A. Standish, E. H. Moriyama, M. Khurana, N. R. Munce, M. K. Leung, J. Jiang, A. Cable, B. C. Wilson, I. A. Vitkin, and V. X. D. Yang, "Speckle variance detection of microvasculature using swept-source optical coherence tomography," Opt Lett **33**, 1530–1532 (2008).

[43] G. Liu, W. Qi, L. Yu, and Z. Chen, "Real-time bulk-motion-correction free Doppler variance optical coherence tomography for choroidal capillary vasculature imaging," Opt. Express **19**, 3657–3666 (2011).

[44] D. Morofke, M. C. Kolios, I. A. Vitkin, and V. X. D. Yang, "Wide dynamic range detection of bidirectional flow in Doppler optical coherence tomography using a two-dimensional Kasai estimator," Opt. Lett. **32**, 253–255 (2007).

[45] A. S. Nam, I. Chico-Calero, and B. J. Vakoc, "Complex differential variance algorithm for optical coherence tomography angiography," Biomed Opt Express **5**, 3822–3832 (2014).

[46] Y. Zhao, Z. Chen, C. Saxer, Q. Shen, S. Xiang, J. F. de Boer, and J. S. Nelson, "Doppler standard deviation imaging for clinical monitoring of in vivo human skin blood flow," Optics Letters **25**, 1358 (2000).

[47] C. Kasai, K. Namekawa, A. Koyano, and R. Omoto, "Real-Time Two-Dimensional Blood Flow Imaging Using an Autocorrelation Technique," IEEE Transactions on Sonics and Ultrasonics **32**, 458–464 (1985).

[48] Nelson J, Kelly KM, Zhao Y, and Chen Z, "Imaging blood flow in human port-wine stain in situ and in real time using optical doppler tomography," Arch Dermatol **137**, 741–744 (2001).

[49] Y. Zhao, K. M. Brecke, H. Ren, Z. Ding, J. S. Nelson, and Z. Chen, "Three-dimensional reconstruction of in vivo blood vessels in human skin using phase-resolved optical Doppler tomography," IEEE Journal of Selected Topics in Quantum Electronics **7**, 931–935 (2001).

[50] B. R. White, M. C. Pierce, N. Nassif, B. Cense, B. H. Park, G. J. Tearney, B. E. Bouma, T. C. Chen, and J. F. de Boer, "In vivo dynamic human retinal blood flow imaging using ultra-high-speed spectral domain optical Doppler tomography," Optics Express **11**, 3490 (2003).

[51] R. A. Leitgeb, L. Schmetterer, W. Drexler, A. F. Fercher, R. J. Zawadzki, and T. Bajraszewski, "Real-time assessment of retinal blood flow with ultrafast acquisition by color Doppler Fourier domain optical coherence tomography," Optics Express **11**, 3116 (2003).

[52] J. Zhang and Z. Chen, "In vivo blood flow imaging by a swept laser source based Fourier domain optical Doppler tomography," Opt. Express **13**, 7449–7457 (2005).

[53] B. J. Vakoc, S. H. Yun, J. F. de Boer, G. J. Tearney, and B. E. Bouma, "Phase-resolved optical frequency domain imaging," Opt Express **13**, 5483–5493 (2005).

[54] R. Motaghiannezam and S. Fraser, "Logarithmic intensity and speckle-based motion contrast methods for human retinal vasculature visualization using swept source optical coherence tomography," Biomedical Optics Express **3**, 503 (2012).

[55] S. Makita, Y. Hong, M. Yamanari, T. Yatagai, and Y. Yasuno, "Optical coherence angiography," Opt. Express **14**, 7821–7840 (2006).

[56] E. Jonathan, J. Enfield, and M. J. Leahy, "Correlation mapping method for generating microcirculation morphology from optical coherence tomography (OCT) intensity images," J. Biophoton. **4**, 583–587 (2011).

[57] Y. Jia, O. Tan, J. Tokayer, B. Potsaid, Y. Wang, J. J. Liu, M. F. Kraus, H. Subhash, J. G. Fujimoto, J. Hornegger, and D. Huang, "Split-spectrum amplitude-decorrelation angiography with optical coherence tomography," Optics Express **20**, 4710 (2012).

[58] M. Szkulmowski, A. Szkulmowska, T. Bajraszewski, A. Kowalczyk, and M. Wojtkowski, "Flow velocity estimation using joint Spectral and Time domain Optical Coherence Tomography," Optics Express **16**, 6008 (2008).

[59] R. K. Wang, "Optical Microangiography: A Label-Free 3-D Imaging Technology to Visualize and Quantify Blood Circulations Within Tissue Beds In Vivo," IEEE J Sel Top Quantum Electron **16**, 545–554 (2010).

[60] A. H. Bachmann, M. L. Villiger, C. Blatter, T. Lasser, and R. A. Leitgeb, "Resonant Doppler flow imaging and optical vivisection of retinal blood vessels," Optics Express **15**, 408 (2007).

[61] B. Angelsen, "Instantaneous Frequency, Mean Frequency, and Variance of Mean Frequency Estimators for Ultrasonic Blood Velocity Doppler Signals," IEEE Transactions on Biomedical Engineering **BME-28**, 733–741 (1981).

[62] H. H. Barrett and K. J. Myers, *Foundations of Image Science* (John Wiley & Sons, Hoboken, NJ, 2004).

[63] E. Swanson, "Clinical translation in OCT: Role of research, funding, and entrepreneurism (Presentation Video)," Proceedings of SPIE **8934**, 89342E (2014).

[64] B. Cense, N. Nassif, T. Chen, M. Pierce, S.-H. Yun, B. Park, B. Bouma, G. Tearney, and J. de Boer, "Ultrahigh-resolution high-speed retinal imaging using spectral-domain optical coherence tomography," Opt. Express **12**, 2435–2447 (2004).

[65] M. Wojtkowski, V. J. Srinivasan, T. H. Ko, J. G. Fujimoto, A. Kowalczyk, and J. S. Duker, "Ultrahigh-resolution, high-speed, Fourier domain optical coherence tomography and methods for dispersion compensation," Optics Express **12**, 2404 (2004).

[66] D. L. Marks, A. L. Oldenburg, J. J. Reynolds, and S. A. Boppart, "Digital algorithm for dispersion correction in optical coherence tomography for homogeneous and stratified media," Appl. Opt. **42**, 204–217 (2003).

[67] A. F. Fercher, C. K. Hitzenberger, M. Sticker, R. Zawadzki, B. Karamata, and T. Lasser, "Dispersion compensation for optical coherence tomography depth-scan signals by a numerical technique," Optics Communications **204**, 67–74 (2002).

[68] S. Kudo, S. Hirota, T. Nakajima, S. Hosobe, H. Kusaka, T. Kobayashi, M. Himori, and A. Yagyuu, "Colorectal tumours and pit pattern." Journal of Clinical Pathology **47**, 880 (1994).

[69] X. Qi, Y. Pan, Z. Hu, W. Kang, J. E. Willis, K. Olowe, J. Sivak, Michael V., and A. M. Rollins, "Automated quantification of colonic crypt morphology using integrated microscopy and optical coherence tomography," J. Biomed. Opt **13**, 054055–054055–11 (2008).

[70] C. A. Staton, A. S. A. Chetwood, I. C. Cameron, S. S. Cross, N. J. Brown, and M. W. R. Reed, "The angiogenic switch occurs at the adenoma stage of the adenomacarcinoma sequence in colorectal cancer," Gut **56**, 1426–1432 (2007).

[71] M. Raica, A. M. Cimpean, and D. Ribatti, "Angiogenesis in pre-malignant conditions," European Journal of Cancer **45**, 1924–1934 (2009).

[72] D. Hanahan and R. Weinberg, "Hallmarks of Cancer: The Next Generation," Cell **144**, 646–674 (2011).

[73] X. Sun, L. Xing, C. C. Ling, and G. C. Li, "The effect of mild temperature hyperthermia on tumour hypoxia and blood perfusion: relevance for radiotherapy, vascular targeting and imaging," Int J Hyperthermia **26**, 224–231 (2010).

[74] R. J. Griffin, R. P. Dings, A. Jamshidi-Parsian, and C. W. Song, "Mild temperature hyperthermia and radiation therapy: Role of tumour vascular thermotolerance and relevant physiological factors," Int J Hyperthermia **26**, 256–263 (2010).

[75] C. W. Song, H. J. Park, C. K. Lee, and R. Griffin, "Implications of increased tumor blood flow and oxygenation caused by mild temperature hyperthermia in tumor treatment," Int J Hyperthermia **21**, 761–767 (2005).

[76] C. W. Song, "Modification of blood flow," in "Blood perfusion and microenvironment of human tumors," , M. Molls and P. Vauple, eds. (Springer, Berlin, 1998), pp. 193–207.

[77] V. L. Chamary, M. Loizidou, P. B. Boulos, I. Taylor, and G. Burnstock, "Changes in vasoconstrictor and vasodilator neurotransmitters in nerves supplying arterioles in developing colorectal polyps," Colorectal Disease **8**, 230–234 (2006).

[78] A. M. Winkler, "Optical methods for molecular sensing: Supplementing imaging of tissue microstructure with molecular information," Dissertation, The University of Arizona, Tucson, AZ (2010).

[79] G. Liu, W. Jia, V. Sun, B. Choi, and Z. Chen, "High-resolution imaging of microvasculature in human skin in-vivo with optical coherence tomography," Opt. Express **20**, 7694–7705 (2012).

[80] G. Liu, A. J. Lin, B. J. Tromberg, and Z. Chen, "A comparison of Doppler optical coherence tomography methods," Biomedical Optics Express **3**, 2669 (2012).